Gas-Phase Terahertz Spectroscopy and the Study of Complex Interstellar Chemistry

Thesis by

Rogier Braakman

In Partial Fulfillment of the Requirements

for the Degree of

Doctor of Philosophy

California Institute of Technology

Pasadena, California

2010

(Defended 20 August 2009)

Aan mijn familie

Acknowledgements

The last seven years at Caltech and in LA have been a rich experience, with much personal and scientific growth, and as it is coming to a close there are many people I wish to thank. First I would like to thank my advisor, Geoff, for giving me the opportunity to come to Caltech on an internship prior to grad school and later to join the group. His support, guidance and broad scientific knowledge and curiosity have allowed me to learn much about spectroscopy and astrochemistry, while at the same time always keeping an eye on how the research we pursue in the lab connects to the 'bigger picture' and what future directions it could lead to. I am also grateful for his support in allowing me to explore outside of the realms of research in our group as part of trying to figure out my own path in science.

I would also like to thank other (current and former) members of the Blake group. Susanna for showing me the ropes when I first arrived at Caltech, and in particular Matt and Dan for sharing our office and labs in the basement of Beckman Institute, and the many scientific discussions, adventures in observing and attending conferences and of course the many jokes and pranks over the years that always lightened the mood. Many thanks also to the members of the molecular spectroscopy group at the Jet Propulsion Laboratory, in particular Brian Drouin, for many enjoyable collaborations and for teaching much about the details of rotational spectroscopy, and John Pearson for collaboration on the spectroscopy of methanol and learning about "interstellar weeds".

Also thanks to the many people providing support for our activities in lab, Leticia and Sarah for processing our many, many orders over the years, Tom in the electronics shop, Mike and Steve at the machine shop and Rick at the glass shop for the many different parts they made (not uncommonly designed without consideration for the difficulty) and the problems they helped solve. To the several people in the division office that helped me out with various organizational aspects of being a Caltech grad student, Dianne, Anne, Agnes. I would particularly also like to thank Jim, Athena and Marjorie at the international student offices, for always helping me with any visa issues or other questions and especially for organizing the internal student orientation each year in which I participated twice as a student and several times as a volunteer. The great and supportive atmosphere during this period was a great way to get started at Caltech and is where I met many of my closest friends.

I also owe a debt of gratitude to Ewine van Dishoeck at the Sterrenwacht in Leiden for giving me my first research opportunity in astrochemistry and to Rens Waters at the Anton Pannekoek Institute for Astronomy in Amsterdam for supporting in further explorations in this field during my undergraduate years. These initial exposures were a great introduction to the field and eventually led to my graduate studies at Caltech.

On a personal level it is hard to express enough gratitude to the many great friends I have made here over the years, Lily, Aaron, Nitzan, Manu, Mel, Ivan, Maria, Anusha, Victor, Roshan, Sean, Waheb, and too many more to do them all justice. They know who they are. They have made the tough times bearable and the good times truly enjoyable. I would also like to thank everyone that played on the Lucky Bastards over the years, basketball was always one of my favorite outlets and I had many great teammates.

Finally, I would like to thank my family, without whose love and support I would not

have gotten to where I am today. To my parents, Dick and Ireen, for giving me life and always being there for me with support and advice and for creating a great family bond and atmosphere. To my brothers Martijn and Niels for being the greatest brothers anyone could want, and to Zaïda and Charlotte for making my brothers happy and generally just being awesome additions to our family.

Abstract

Terahertz spectroscopy holds great promise in the advancement of the field of astrochemistry. The sensitive observation of interstellar THz radiation is expected to lower detection limits and allow the study of larger and more complex species than is currently possible at millimeter wavelengths, which will place further constraints on chemical models and permit a direct comparison to the organic compounds seen in carbonaceous chondrites. With the successful recent launch of the Herschel Space Telescope, which will give high-fidelity access to interstellar THz radiation for the first time, and the completion of the Atacama Large Millimeter Array (ALMA) by 2013, the THz astronomy era is upon us. Unfortunately, laboratory THz spectroscopy presents significant challenges and will be soon be lagging behind the newly available observational platforms. Technologies to extend the capabilities of high-resolution spectroscopic systems into the THz domain are actively being pursued on many fronts, but affordable systems that are broadly tunable, sensitive and achieve the necessary resolution are not yet available. The work in this thesis should therefore be seen as part of the effort in the transition from centimeter-/millimeter-wave to THz spectroscopy that is currently taking place in the astrochemistry community.

As part of this thesis, observational searches for the complex organics hydroxyacetone (CH_3COCH_2OH), 2-cyanoethanol ($OHCH_2CH_2CN$) and methoxyacetonitrile (CH_3OCH_2CN) were attempted at millimeter wavelengths. The unsuccessful nature of these searches high-

light the current limits of studying interstellar chemistry using pure rotational spectroscopy. The characterization of the laboratory spectra of these molecules is nonetheless important as it will aid in the assignment and description of the rotational substructure and band shapes of their THz torsional spectra, features that may allow their interstellar detection; and this thesis presents methods by which such complex spectra may be rapidly and efficiently collected and fit using automated spectrometers and modern software tools.

The description of the spectrum of hydroxyacetone is furthermore of interest due to the presence of the very low barrier to internal rotation in this molecule. Many interstellar compounds, both known and potential future targets, have functional groups capable of internal rotation in their structure; and so the effort in understanding the complex effects of the low barrier rotor in this case will benefit the general effort to further understand internal rotation.

In searching for new interstellar molecules, both at millimeter wavelengths and at higher THz frequencies, characterization of the complete spectra of known interstellar molecules is of great importance to allow substraction of their contribution to observational spectra. In this thesis, the ground-state rotational spectrum of methanol, the most important "interstellar weed", is catalogued and described in detail through most of the THz region that will be accessible with Herschel and ALMA.

Lastly, as part of the effort to increase the sensitivity of THz spectrometers, the use of Fabry-Perot cavities at these frequencies is explored. Such resonant cavities hold the potential to significantly increase the possible path lengths in spectroscopic system and to allow novel and sensitive detection techniques. Optimal configurations and the limits on achievable path lengths and Q-factors of such cavities are discussed, as are the possible extensions of Fourier Transform MicroWave (FT-MW) techniques to THz frequencies.

Contents

List of Figures

List of Tables

Chapter 1

Introduction

1.1 Historical Background

Curiosity about and observations of the natural environment in which we live is one of the defining characteristics of human existence. History abounds with evidence of humans peering into the night skies and attempting to explain the views above, back as far as the first annals of recorded thought. Fueled by technological advancement, the last few centuries have seen a rapid acceleration in our capabilities to describe and understand the celestial objects and patterns we see. The first technologically aided observations, and arguably the birth of the modern scientific method, date back to the efforts of Galileo starting four hundred years ago in 1609, when he constructed telescopes with a magnification of $\times 3$ and, later, with magnification of $\times 30$ (all based on descriptions of a similar instrument constructed in the Netherlands the previous year) and used them to study a variety of astronomical objects. His description of the moons of Jupiter, the existence of phases of Venus similar to the Moon, other bodies and phenomena in the solar system, and the first description of the Milky Way [3] confirmed the heliocentric model of the solar system developed by Nicholas Copernicus a century before and forever changed the way we think of our place in Nature. Galileo's use of mathematics to describe his observations was also one

the earliest and clearest examples showing that the workings and organization of nature could be described by mathematical rules. This work was thus at the forefront of the scientific revolutions of the 17th century that culminated with the efforts of Isaac Newton, work that emphatically drove this point home [4].

In the four centuries since those first telescopic studies, an ever expanding mountain of observational data has been gathered, and we now know our place in the Universe to be rather insignificant. We live on a planet around an unremarkable star in a remote location in one of the spiral arms of the Milky Way, which is thought to contain some 200-400 billion stars; and which in turn is only one of $\gtrsim$80 billion galaxies thought to exist in the observable universe. These numbers are so staggering it is difficult to fully comprehend their meaning, but it is clear that our contributions to the universe are near vanishing in terms of size and mass, and humbling to say the least.

Observational astronomy has thus changed our perception from living at the center of the universe with poorly understood points of light in the night skies, to a much grander view where we live in a vast universe with countless numbers and wide varieties of galaxies, stars and planets. Much of the history of observational astronomy, however, was limited to research in the visible part of the spectrum. Although this allows the study of the characteristics, dynamics and evolution of luminous structures such as stars and galaxies, it is limited in its potential to study chemistry in the interstellar medium (ISM) – the apparent void between the stars. The advent of high-resolution spectroscopy allowed some access to this domain of study, as electronic transitions of selected atomic and molecular species occur at visible wavelengths. In fact, the first molecular species observed in the interstellar medium, CH, CH^+ and CN, were detected using high-resolution spectroscopy at optical wavelengths [5, 6, 7]. The visible part of the spectrum lends itself best to the study of

electronic transitions in molecules with unpaired electrons, pi-bonds or ionic species, and is less ideal for saturated molecules, however, thus limiting the range of chemical species that can be observed at these wavelengths. Furthermore, as we now know, the chemical evolution toward species of higher complexity is generally limited to the interiors of dense molecular clouds that are impenetrable to visible photons [8, 9]. In diffuse interstellar clouds and parts of the ISM with still lower densities, the harshness of the radiation environment tends to destroy the molecular bonds of most organics, limiting the scope of possible chemical reaction networks [8, 9]. A notable exception are the polycyclic aromatic hydrocarbons (PAHs), whose large pi-clouds and linked molecular topologies are thought to allow them to survive even under the harsh conditions of the diffuse ISM [10].

Dense molecular clouds provide the conditions necessary for molecules of higher complexity to form and survive. Several factors work together in the formation of these clouds, which are opaque to visible and ultraviolet light and provide an environment in which the complexity of chemical species can increase. The short wavelengths of visible photons (sub-micrometer) makes them prone to scatter off of interstellar dust grains as the size of these particles approaches the size of the wavelength of the photons. In diffuse interstellar clouds, which are part of the larger domain termed the Cold Neutral Medium (CNM), the median grain size is of order $\sim$0.1 micron, and their number (and column) density is low – resulting in limited scattering at visible wavelengths. Inevitable variations and fluctuations in the density of the interstellar medium, however, result in some regions where the amount of scatter is higher, which results in a lower temperature. The lower temperature and decreased radiation pressure further allows the density to increase and more material to condense onto dust grains. Increases in density, decreases in temperature, the growth of grains, and an increase in the amount of scattering of visible photons are thus part of

an inter-linked positive feedback mechanism. Furthermore, at these higher densities, lower temperatures and more shielded conditions, a larger fraction of matter will be in molecular form. Molecules can in turn provide further mechanisms for shielding and cooling of the cloud environment.

The first and most dominant molecular species to form, molecular hydrogen (H_2), is a product of grain surface catalysis, and can self-shield itself against photodissociating UV radiation. In the wake of the formation of molecular hydrogen, carbon also transitions from ionized atomic carbon (C^+) to neutral atomic carbon (C) to carbon monoxide (C≡O), which after H_2 is the most abundant molecule in dense clouds. Unlike H_2, however, CO has a permanent electric dipole moment, which makes it capable of rotational de-excitation after collisional excitation, providing another cooling mechanism in the dense cloud environment. Once temperatures reach sufficiently low levels, CO and other volatile species will increasingly freeze out onto dust grains, encasing the core of silicate and other metal-oxides and -carbides with a growing ice mantle. Grain growth further increases the amount of scattering of visible photons (until they are well beyond a micron in size), and so on. Eventually the result of this complex feedback mechanism is that only the outer most layers of the clouds can be penetrated by visible photons, creating a dense ($> 10^4$ cm^{-3}), cold (T $\sim$ 10-50 K) and mild radiation environment, where chemistry of higher complexity than any other region of the interstellar medium can occur (for further details on the classification and evolution of interstellar clouds, see [8]). However, the same conditions that allow such chemistry to occur make it impossible to study it in the visible part of the spectrum. Well into the 20th century, large parts of the physical and chemical evolution of the interstellar medium, leading up to and including the birth and evolution of young stellar and planetary systems, were therefore shrouded in mystery.

With the emergence of radio astronomy in the middle of the 20th century, a technique that does allow one to look inside dense clouds, observational astronomy was therefore ripe for another leap forward. Because the wavelength of microwave radiation is much longer than that of visible light (centimeters to millimeters versus sub-micrometers), these photons are largely immune to the scattering off dust-grains and can thus penetrate into even the densest cores where stars are being formed – allowing researchers to map and study these regions in detail for the first time. Furthermore, at cm- to mm-wavelengths, mainly rotational motions of molecules are active, which offers several advantages over the electronic transitions probed at visible wavelengths. The only requirement for a molecule to have strongly allowed transitions at these wavelengths is that a permanent charge displacement (an electric dipole moment) exists in the molecule which, outside of the most highly symmetric molecules (e.g. H_2, benzene, C_{60}), is the case for the majority of species.

Molecules also tend to have a rich and unique spectral fingerprint in these regions, which allows for unambiguous identifications and the extraction of much useful information from high resolution spectroscopic observations. At the low temperatures and densities that characterize the dense ISM, the widths, shapes and shifts of individual transitions are indications of both the local velocity and global velocity distributions of the gas in which the molecules resides. This makes it possible to study the kinematics of interstellar clouds across many length scales. The relative intensity of different transitions of a single species allows the determination of both the abundance and temperature of this species, and the relative abundance of different species gives insights into the chemistry that occurs. Spatially resolved, sensitive observations at microwave frequencies thus gives an extremely dynamic data set that can be used to gain many insights into the chemistry and physics of dense interstellar clouds.

The maturation of high-resolution microwave spectroscopy in the footsteps of the first detections of interstellar microwave radiation therefore resulted in an explosion of information about the matter and processes inside dense molecular clouds. The first interstellar polyatomic molecules water, ammonia and formaldehyde were discovered in 1968 and 1969 [11, 12, 13], and by 1975 nearly 40 molecules had been detected. In the four decades since those first discoveries, the tally has risen to 151 molecules (as of this writing), the majority of which are organic in nature [14, 15]. The revolutionary impact of these discoveries on astronomy and our understanding of physical and chemical processes in the interstellar medium cannot be overstated. The different phases and global evolution of the Cold Neutral Medium, from diffuse to translucent and then to dense clouds; the physico-chemical evolution in dense clouds, from pre-stellar cores to the birth of massive stars and low-mass stars akin to our sun; and the emergence of proto-planetary disks and eventually planets have, to varying degrees, been both qualitatively and quantitatively described as a result of the marriage between high-resolution microwave spectroscopy and observational astronomy.

1.2 The Transition from Microwave to Terahertz Spectroscopy

While these dogged pursuits in identifying newer and larger molecules in the ISM have led to the large numbers of new detections, they have also made it difficult to maintain the overall pace of discovery. Whereas earlier molecular identifications could be undertaken using the most intense features in observational spectra, later detections have come from increasingly weaker signals. As species in the dense ISM increase in size, not only do their spectra become weaker due to progressively lower abundances, their rotational energy is also spread over a larger number of states – which both increases the spectral density and decreases the average strength of the signal. As a result, the detection limit for any given observational sensitivity

floor invariably becomes higher and higher as the molecular complexity is increased. Further complicating matters is that the higher density of states in larger species shifts the peak of their Boltzmann distribution to lower frequencies (see Fig. 1.1). For molecules at the size of current detection limits the Boltzmann peaks overlap strongly at millimeter wavelengths, leading to a dense and highly complex observational spectrum at the weakest signal levels. The high degree of line blending and spectral confusion combined with the weaker and more complex spectra of new and larger molecules thus makes it increasingly difficult to positively identify individual transitions belonging to a particular species, and the situation cannot be ameliorated by simply improving the observational sensitivity. This, in turn, requires more elaborate methods to identify new interstellar molecules from observational spectra (which are often appropriately referred to as 'confusion limited').

As a result, the field has increasingly been pushed towards sensitive spectral line surveys over broad frequency ranges and careful modeling of the spectra of the molecules known to exist in the targeted source. An important part of this effort is the detailed spectral characterization of known interstellar molecules, as these are likely to have significant spectral contributions beyond the transitions that have been mapped or detected to date. In particular, abundant species with dense spectra are likely to play a 'weed'-like role in observational spectra, whose weakest features (either from excitation or isotopic substitution) must be well understood in order to search for more complex molecules. This issue will be addressed in more detail in the next Chapter, which considers the rotational spectrum of methanol, the most important 'interstellar weed'.

Another important effort in lowering current detection limits at cm-to-mm wavelengths lies in increasing the spatial resolution of observational studies. The chemistry and physical state of dense molecular clouds are intertwined, and by increasing the spatial resolution

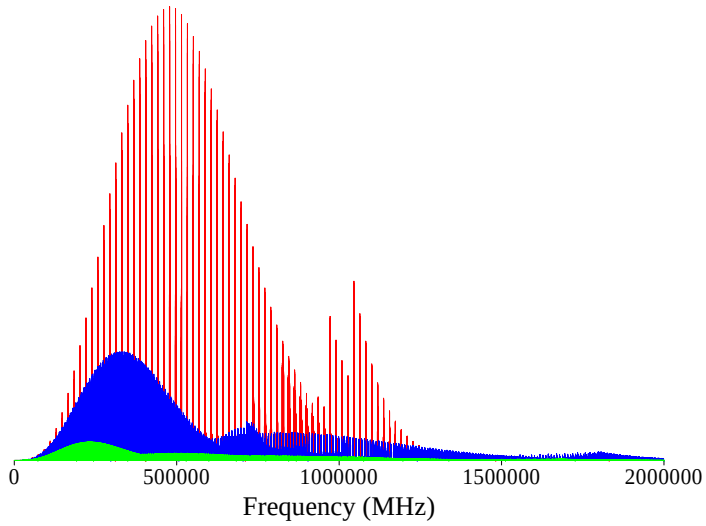

Figure 1.1: The simulated rotational spectra of CH_3CN (red), C_2H_5CN (blue) and C_3H_7CN (green) at 200 K (typical of hot core molecules) illustrating the various aspects of spectral confusion. The closer spacing of the energy levels due to the increase in size of the molecules significantly increases the partition function and results in a denser and weaker spectrum, while the larger moments of inertia also cause a shift of the Boltzman peak to lower frequencies. The trend in the spectra shows that the overlap and confusion is greatest at millimeter wavelengths.

with which molecular emission and absorption signals are probed (along with that of the thermal emission from dust grains), researchers can gain a more refined sense of the local physics in the different regions of the cloud. Through a careful selection of the target cloud and spatial resolution, it is therefore possible to highlight regions of complex chemistry. The commissioning of the Atacama Large Millimeter Array (ALMA) [16], as well as the maturation of the Combined Array for Research in Millimeter-wave Astronomy (CARMA) [17], will provide dramatic improvements on this front as their interferometric operations allow telescope separations – and thus a spatial resolution – that are orders of magnitude better than is possible with a single dish. ALMA in particular is expected to achieve a spatial resolution that will be nearly 10 times better than the Hubble Space Telescope (HST), which will allow researchers to resolve length scales on the order of a few times the orbit of terrestrial planets in our solar system for the first time. Unlike Hubble, ALMA

operates at mm-wavelengths, which as previously mentioned gives access to the densest cores inside molecular clouds. These interferometric observatories are thus expected to be a major boon to the study of complex molecules in the dense ISM. They will further allow the verification that molecular signals associated with a newly detected species arise from the same spatial location, which provides a powerful constraint on new detections. The spatial filtering of molecular signals with arrays should also decrease the spectral confusion due to line blending while simultaneously improving our understanding of the cloud structure, both of which should lead to substantially lowered detection limits.

Perhaps the biggest increase in our understanding of interstellar chemistry will come, however, not from ground based arrays but by moving beyond the mm-wave region and into the high frequency THz regime. Defined most broadly, THz radiation extends roughly from 0.1-10$\times 10^{12}$ Hz, or 3-333 cm^{-1}, and thus includes mm-wave radiation. The shorter wavelengths of photons from, say, 1-10 THz offer several advantages over those at microwave and millimeter wavelengths that make them ideal in the pursuit of newer and larger interstellar molecules, and in the associated understanding of their chemistry. At frequencies $\gtrsim$1 THz, the spectra of molecules transition from the domain of rotational motions to torsional/large amplitude vibrational motions. The low-energy vibrations/torsions in the THz (far-infrared) regime are generally more global in nature, typically involving the entire molecular framework or whole groups rather than the more isolated bending or stretching of individual bonds that is characteristic of the mid- or near-infrared frequency ranges. Increasing in the size of a molecule thus shifts the low energy end of the vibrational spectrum towards lower frequencies. For organics, the nature of these modes generally also makes them significantly more intense than rotational modes for the same molecule since the matrix elements are similar and the Einstein A-coefficients scale steeply with frequency.

For perpendicular transitions, the intense Q-branch features that are generated coalesce many lines into a compact region, and this effect acts to offset the increase in the partition function for complex species. Furthermore, moving above the mm-wave Boltzman peak for large molecules should drive the confusion limit to lower noise levels. All of these features act in concert to lower the detection limit for a given molecule at a given noise level, and together these advantages are expected to significantly lower detection limits and extend the size range of detectable molecules by several atoms. This in turn would allow further constraints to be placed on current chemical models and deepen our understanding of the chemistry in dense clouds leading up to the earliest stages of star and planet formation.

1.2.1 Terahertz: The *Double* Spectral Gap

Unfortunately, THz spectroscopy currently suffers from several limitations that makes it a more challenging spectral region in the pursuit of science than either of its bordering electromagnetic windows – the infrared and microwave regions. From the perspective of observations of interstellar THz radiation, the biggest obstacle is the atmosphere that lies between ground-based observatories and the ISM. Water has quite intense transitions throughout the THz region, making the atmosphere practically opaque above 1 THz, with only a few atmospheric windows even at the best sites on Earth. It is possible to partially circumvent this problem by building observatories at high altitudes and under dry conditions, such as at the summit of Mauna Kea in Hawaii or in the Atacama desert of Chile where many current (sub-)millimeter observatories exist. The illustration in Fig. 1.2 shows that even at such sites this effect cannot be completely eliminated, however, especially above $\sim$1 THz, where transitions of water are most intense, without moving above the atmosphere altogether. The successful launch of the Herschel space-based THz platform [18] is therefore of

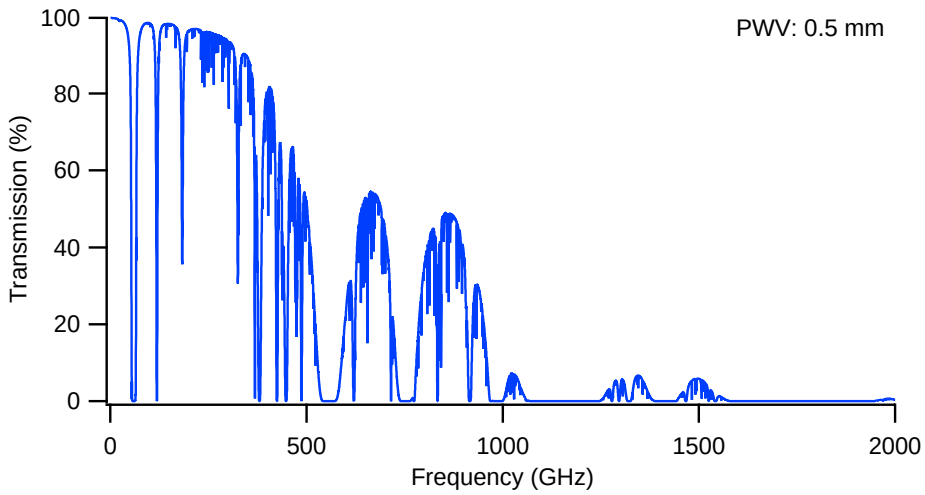

Figure 1.2: Atmospheric transmission on Mauna Kea at a precipitable water vapor level of 0.5 mm. The plot very clearly shows the opacity of the atmosphere due to water, especially above 1 THz, where virtually no radiation is transmitted. Generated at [1].

tremendous importance as it gives full access to interstellar THz radiation for the first time. Once fully operational in the fall of 2009, this instrument, working in tandem with ALMA, is expected to result in another major leap forward in our understanding of the chemistry in the interstellar medium.

To detect any new interstellar species at THz frequencies, laboratory reference spectra of the target molecule are needed to compare against the observational data. Laboratory THz spectroscopy presents significant technical challenges not encountered in observational THz spectroscopy. When observing interstellar THz signatures, the radiation is provided by stellar or interstellar objects, which are contrasted against the very low thermal background of interstellar space (ultimately that of the Cosmic Microwave Background, with T_{CMB}=2.7 K). The significantly higher thermal background levels in laboratory settings thus provide significant constraints on the detection system versus observational studies. Furthermore, in generating photons to use as a light source, THz spectroscopy cannot easily borrow from techniques used in the more mature microwave and infrared regions. At microwave frequencies, electronic oscillators are generally used to generate radiation, but extensions

of this technique to THz frequencies must overcome the severe parasitic losses in typical oscillator designs. Even in the most promising devices, such as Backward Wave Oscillators, the power output in most cases is reduced to insignificant levels above 1-2 THz.

Furthermore, the coherent photonic techniques used at infrared wavelengths also do not extend to lower frequency, as the lifetimes for spontaneous emission are inversely correlated with frequency, eventually causing this type of device to stop radiating unless the material can be fabricated with near atomic level precision [19]. The main sources for high resolution access over broad THz ranges at present are thus up-conversion of microwave radiation through harmonic multiplication and difference frequency generation through photomixing of two near-infrared lasers. Both methods have limited efficiency, however, necessitating other approaches to increasing the sensitivity of the system. One obvious route lies in increasing the sensitivity of detection schemes, and the other is by increasing the relative level of the molecular signal. A technique of particular interest is therefore the use of resonant cavities, which can significantly increase the path length of the spectroscopic system and allow for other means of decreasing noise. The last chapter of this thesis will therefore address the potential of Fabry-Perot resonators at THz frequencies.

1.3 Complex Chemistry in the Interstellar Medium

The observational efforts over the last four decades, combined with the complementary studies of theorists and experimentalists has led to a wealth of knowledge about the chemistry of the interstellar medium. As mentioned before, “complex” chemistry is generally confined to the interiors of dense molecular clouds. The shielded, dense, and cold conditions of these clouds allow molecules to form more easily and survive longer than is possible in more diffuse regions of the ISM. The chemistry that operates under such conditions is a unique combina-

tion of reactions in the gas phase, on the surfaces of, and in the icy mantles on dust grains. The coupling between these two domains varies depending on the local conditions in the cloud, with virtually no coupling in the coldest, most quiescent regions and strong coupling at sites of star formation where the heat and shocks from the young star drive chemical species from the grain surface/mantle into the gas phase. Gas phase chemistry, particularly in the quiescent domains of dense clouds, is dominated by exothermic ion-neutral reactions (and supplemented by a few very low barrier neutral-neutral reactions), often initiated by the key species H_3^+ [20]. Gas phase reactions alone, however, are limited in their potential in creating molecules larger than a few atoms in size within dense clouds, indicating that grain surface pathways or a combination of these two routes are needed to explain the large variety of complex molecules observed in regions of star formation.

Interstellar dust grains consist of a core of silicates and other oxides or carbides, surrounded by a mantle of ice consisting of 'volatile' species such as H_2O and CO. In quiescent regions of dense clouds many types of chemical reactions are inhibited on dust grains as most species are immobilized by the low temperatures ($\sim$10 K) of the grains. In fact, at these temperatures, only atomic hydrogen will have any significant mobility because its low mass allows it to tunnel across the surface of the dust grains (though in some rare cases the migration of first row atoms such as C, N or O can play important roles in the synthesis of larger species). It was therefore thought that dust grain chemistry in quiescent regions of clouds was limited to reactions initiated by hydrogen tunneling through unsaturated bonds of molecules such as CO, followed by subsequent additions of other single atoms without a reaction barrier [21, 22]. The species formed through these processes were then thought to participate in further ion-neutral gas phase reactions as the ice evaporates near sites of star-formation. More elaborated models of complex reactions between larger radical species were

developed [23], but the hypothesized methods of initiating these pathways were considered less likely under low temperature conditions.

In recent years, however, it has been realized that energetic cosmic-rays likely also play an important role in driving complex chemistry in icy grain mantles. These particles are too energetic to initiate chemistry directly, but upon collision with dust grains/mantles can release a cascade of supra-thermal electrons that are capable of driving new chemical pathways. Both experiments [24, 25] and models [26, 27] have shown that reactions initiated by the processing of interstellar ice by electrons after collisions of cosmic-rays likely play an important role in dust grain chemistry. In these pathways, larger radical species are created through the cleavage of molecular bonds of species trapped in the ice by the electrons, which allows the pathways considered in [23] to be revisited [26]. Cosmic rays can further contribute to the chemistry in dense regions through collisions with H_2 which provide the primary source of ionization and energy input into molecular clouds, and which can generate a secondary UV field that can both process molecules in the ice of dust grains and photo-ionize molecules in the gas phase.

Beyond the addition of cosmic-ray driven reactions to the arsenal of chemical pathways, it has also been realized that as grains enter regions of star-formation, rather than undergoing an instantaneous jump in temperature that promptly releases the icy mantle into the gas phase, grains are more likely to undergo gradual heating as the star matures [28]. Such gradual heating of the grains allows increased mobility of the larger radical species formed through tunneling reactions and cosmic-ray processing, further driving dust grain chemistry. It also results in the vaporization of different species at different times during the formation of a star and any attendant planetary system. For a more detailed and excellent overview of the formation of complex interstellar organic molecules, see [9].

In addition to ongoing experimental and modeling efforts to understand these different processes in the creation of complex molecules, the continued observation of known and the search for new complex molecules is of vital importance in the understanding of complex interstellar chemistry. The systematic comparison of structurally related molecules places further constraints onto chemical models by giving insights into the relative contributions of different pathways. This is the topic of Chapter 6, which explores observational searches for related cyanide molecules.

1.4 Technical Considerations

In order to detect new molecules in the interstellar medium and determine their temperature, abundance and role in interstellar chemistry, characterization of the laboratory spectrum of the target species is a crucial (first) step. Thanks to the dense spectra of molecular clouds, a species cannot be detected in the ISM if the frequencies of its spectral transitions are not accurately known, and an accurate quantum mechanical description of its spectrum further allows the extraction of information such as abundance and temperature. For smaller molecules both the millimeter and THz regions are the domain of their rotational spectra, whereas for larger species the pure rotational transitions shift more towards the millimeter region with vibrational spectra shifting down from the infrared toward the THz region. In describing the torsional modes of large molecules at THz frequencies, understanding their pure rotational spectra is still of great importance as high resolution spectra will resolve the rotational sub-structure of the torsion/vibration bands. An accurate description of the pure rotational spectra of larger molecules will therefore help in the assignment of the THz torsional bands. The next section describes the general principles of rotational spectroscopy as much of this thesis revolves around the characterization of rotational degrees of

freedom of various molecules. This section is followed by a description of the experimental techniques used in acquiring the spectra studied in this thesis.

1.4.1 Rotational Spectroscopy

The rotational spectrum of nonlinear molecules can be treated using an effective Hamiltonian that describes the rotations along the principal axes (a, b, c) of the molecule. In the rigid rotor approximation, this leads to the following form of the Hamiltonian:

$$H = AP_a^2 + BP_b^2 + CP_c^2 \tag{1.1}$$

where P_a, P_b and P_c are the angular momentum operators along the principal axes. A, B and C are the rotational constants, which are simply the inverse of the moment of inertia along the principle axes according to:

$$A = \frac{\hbar}{4\pi c I_A} \tag{1.2}$$

where I_A is the moment of inertia along the a axis of the molecule. When the moments of inertia along all three axes are different, which is the most common class of molecules, a species is classified as an 'asymmetric top', and this requires a more complex treatment. The matrix of the effective Hamiltonian in a given basis set must be diagonalized to find the energy eigenvalues and eigenstates. This leads to a Hamiltonian of the following form:

$$\begin{aligned} H = &\left(\frac{B+C}{2}\right)P^2 + \left(A - \frac{B+C}{2}\right)P_a^2 + \left(\frac{B-C}{4}\right)(P_b^2 - P_c^2) - \Delta_J P^4 \\ &- \Delta_{JK} P^2 P_a^2 - \Delta_K P_a^2 - 2\delta_J P^2 (P_b^2 - P_c^2) - \delta_K \{P_a^2, (P_b^2 - P_c^2)\} \end{aligned} \tag{1.3}$$

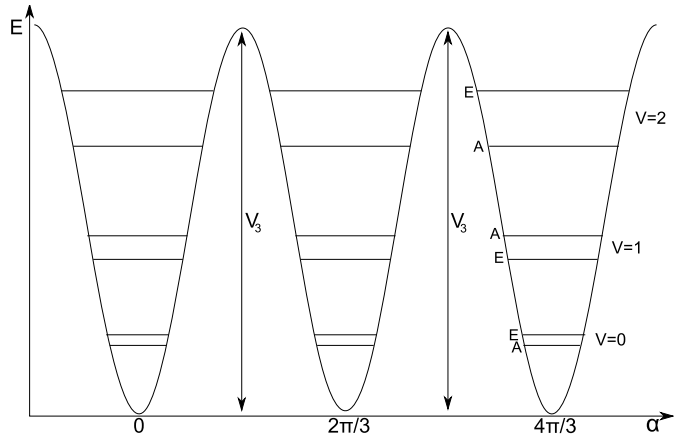

Figure 1.3: Rotational potential energy curve of a hindered internal rotor. The angle of rotation, α, of the methyl top is shown along the x-axis, and the resulting potential energy lies along the y-axis, with maxima at the barrier to rotation, V_3, every $2\pi/3$. Tunneling of the hydrogen atoms through the barrier results in splitting of the torsional levels, ν, into A- and E- sublevels.

where $P^2 = P_a^2 + P_b^2 + P_c^2$, and Δ_J, Δ_{JK}, Δ_K, δ_J and δ_K are the first order centrifugal distortion constants that follow from a perturbation treatment on the zeroth order (rigid rotor) Hamiltonian. Higher order centrifugal distortion corrections also exist, but their contribution is decreasingly significant in magnitude. Nonetheless, for weaker, high quantum number states at high frequencies these corrections can lead to shifts on the order of MHz or more – large enough to lead to errors in assignment given the complex nature of dense cloud spectra. This indicates the need to measure or accurately predict the rotational spectrum of an observational target across the observational windows to be studied astronomically and describing the laboratory spectrum in detail. For large frequency jumps from millimeter wavelengths into the THz regime (such as will occur with spectral line surveys undertaken by Herschel) this is of great importance.

In addition to the basic rotational treatment of asymmetric molecules above, further complications to the spectrum can arise due to the contribution of low-energy, large-amplitude vibrational motions, in particular the internal rotation of a methyl (CH_3) group. A repulsive interaction caused by the overlap of the hydrogen atom electrons in the methyl

group with the rest of the framework of the molecule leads to a periodic contribution in the potential energy, which is shown in Fig. 1.3. In a barrier of finite size, the hydrogen atoms are capable of tunneling through the torsional barrier, which leads to a splitting of the rotational levels into A- and E-state sublevels. The magnitude of the splitting depends on the size of the barrier, with a large splitting for low barriers and a small splitting for high barriers. In the case of very high barriers the A-E splitting in the spectrum can essentially be treated as a perturbation correction to the rotational Hamiltonian; whereas at negligible barriers, the splitting can be treated as a free-rotor problem [29]. Both of these limits simplify the treatment of the problem. At low to intermediate levels, however, significant coupling between the torsional motion of the top and the rotational motion of the molecule can occur, leading to significant perturbations. This leads to a zeroth-order Hamiltonian of the general form:

$$H = H_{rot} + (1/2)V_3(1 - cos3\gamma) + F(P_\gamma + \rho P_a)^2 \tag{1.4}$$

where the first term is the pure rotational Hamiltonian of the form in equation (1.3), the second term accounts for the periodic contribution to the potential energy, and the third term accounts for the coupling between the torsional and rotational motions of the molecule. V_3 is the barrier to internal rotation, γ the angle of internal rotation, P_γ is the angular momentum operator of the methyl top, ρ is the projection of the moment of inertia of the top onto that of the molecule, and F is the reduced rotational constant for the methyl top. Higher order terms in the Hamiltonian, i.e. centrifugal distortion constants, higher order torsional constants, and their cross-products, arise in treatments where a power series expansion of the various angular momenta are used, since there are products of these

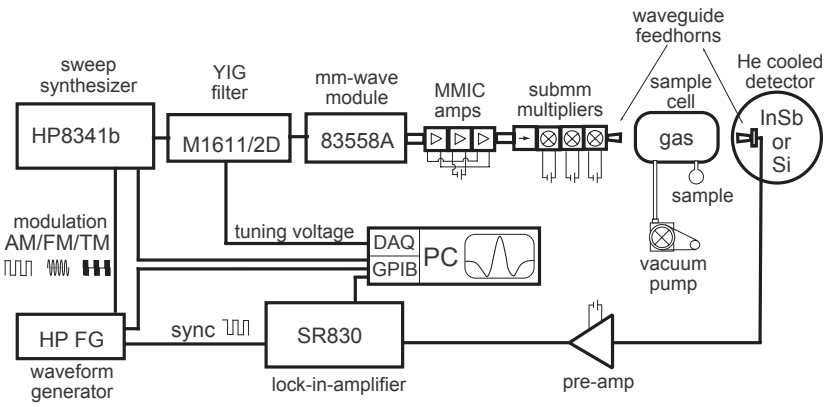

Figure 1.4: Block diagram of the JPL frequency multiplier flow cell spectrometer, taken from [2]. Details on the system can be found in the text.

terms with the torsional potential term in the effective Hamiltonian. For further details on rotational spectroscopy and the effects of internal rotation, see [30, 29]. The next two Chapters of this thesis deal with rotational spectra that show the effects of internal rotation. In the case of methanol (Chapter 2), the barrier is of intermediate value, and only represents a challenging but fairly well understood problem due to its long history of study. Hydroxyacetone (Chapter 3) has a low barrier to internal rotation, which thus represents a challenging spectroscopic problem, and one that can now be solved with modern numerical approaches to the spectroscopy of internal rotation.

1.4.2 Experimental Techniques

The majority of the laboratory data in this thesis are high resolution millimeter and THz spectra acquired using similar flow cell spectrometers both at the JPL Molecular Spectroscopy lab and at Caltech. A layout of the JPL system is shown in Fig. 1.4. An HP sweep synthesizer (0-20 GHz) locked to a highly stable external reference signal is sent through a co-tuned YIG filter to suppress spurious and harmonic frequency content of the output. The resulting signal is sent through a frequency sextupler to generate radiation in

the 71 - 115 GHz (3 mm) band. The signal is then sent through a series of amplifiers to provide sufficient power to drive the subsequent series of harmonic multipliers. Different combinations of multipliers are capable of almost continuous coverage from 0.07 - 1.28 THz and from 1.55 - 1.75 THz. A last tripler is capable of reaching the 2.57 - 2.65 THz window, albeit with significantly lower power than the other frequency windows. The millimeter or THz radiation is then sent through molecular gas contained in a cell that can be run in either a static or flow mode by a combination of needle valves controlling a vacuum pump and sample flask connected to the cell. The radiation passing through the cell is then sampled with either a room temperature diode detector or a liquid helium cooled Si or InSb detector, sent through a preamplifier, and recorded using a lock-in amplifier in either Amplitude Modulated (AM, for absolute power) or Frequency Modulation (FM) mode. Further details on this system can be found in [2].

The Blake group flow cell spectrometer is similar in layout to the JPL system with a few exceptions. A Wiltron rather than a HP synthesizer is used to generate the microwave radiation and is run without the use of a YIG filter. The microwave radiation is then sent through a active frequency doubler, amplifier, and passive Virginia Diodes (VDI) tripler to generate radiation in the 75 - 120 GHz band. The 1 mm band (225 - 360 GHz) is then accessed by following the 3 mm output with an amplifier and a second passive VDI tripler. The signal is similarly recorded either using a liquid helium cooled InSb bolometer detector or a room temperature diode detector and lock-in amplifier combination. The JPL system was used, in particular, for measurements of the methanol spectrum across all accessible bands as described in the next Chapter, and the Caltech system was used in recording the hydroxyacetone (Chapter 3), cyanoethanol (Chapter 4) and methoxyacetonitrile (Chapter 5) spectra.

At lower THz frequencies and for molecules such as methanol that are easy to vaporize and have intense spectra, a system of the type described above is of more than sufficient sensitivity. For more elusive species that are difficult to generate in large quantities or difficult to vaporize, as well as in higher frequency bands where significant levels of THz power are difficult to generate, methods to increase sensitivity are desirable. Toward this goal, we further use the Caltech multiplier chain and detection system to investigate the principles and quality factors of Fabry-Perot cavities at THz frequencies. As will be discussed in the final Chapter of this thesis, we have shown that using wire-grid polarizer as input and output coupling mirrors for the Fabry-Perot resonator has the promise to allow the development of a Fourier Transform-THz (FT-THz) system with a senstivity only slightly below that of current FT-MW machines, and with tuneability over the entire THz range as sources of increased power become available.

1.5 Thesis Overview

The next Chapter of this thesis presents the THz rotational spectrum of the ground torsional state of methanol. As discussed, this species is one of the most abundant 'interstellar weeds' and the detailed cataloguing of its spectrum is of great importance to future observational efforts in studying interstellar chemistry, both at millimeter wavelengths using current or near-future ground based observatories and at THz frequencies using the Herschel space observatory, the Stratospheric Observatory for Infrared Astronomy (SOFIA, a 2.7m telescope in a 747-SP aircraft), or other future missions. Chapter 3 covers the rotational spectrum of hydroxyacetone, which was the target of several unsuccessful observational searches in the interstellar medium. The complex spectral effects of the lower barrier internal methyl rotor in the molecule makes the description of its millimeter wave spectrum an important

contribution nonetheless, as this represents a benchmark in the study of low barrier internal rotors. Chapter 4 and 5 discuss the millimeter wave rotational spectra of 2-cyanoethanol and methoxyacetonitrile, both of which have a significantly simpler asymmetric rotor spectrum then either methanol or hydroxyacetone, further illustrating the complexities added by the presence of an internal rotor. Chapter 6 subsequently covers the observational searches for both cyanoethanol and methoxyacetonitrile in an attempt to assess the chemistry of molecules containing a cyanide group. The searches did not lead to a successful detection, but the upper limits determined still provide useful constraints on coupled gas-grain chemical models. Both the descriptions of these two species and of hydroxyacetone will further be of use as detection limits drop due to the increased spatial resolution of millimeter wave arrays/observatories and in the description of their torsional spectra and observational searches at THz frequencies. Finallly, Chapter 7 discusses the principles and fundamental limits of Fabry-Perot resonators at THz frequencies. Such cavities show significant promise in helping to achieve sensitivities at THz frequencies similar to existing microwave systems. Together these topics form a representative view of the current limits of gas phase spectroscopy at microwave and millimeter wavelengths and the transition to THz spectroscopy in the study of complex chemistry within the dense interstellar medium.

Chapter 2

Methanol and the Interstellar Weed Problem

2.1 Introduction

As noted in Chapter 1, the identification of new interstellar molecules has required increasingly elaborate methods in recent years. In particular, toward regions of high-mass star formation, where the majority of complex species have been detected, the challenge of finding new and larger species is significant. The high degree of line blending and spectral confusion at the weakest signal levels combined with the lower expected abundances for larger molecules makes it increasingly difficult to positively identify individual transitions belonging to a particular species. This has led to some disputes about claimed detections (in particular concerning the search for the simplest amino acid, glycine [31]), and has led to a debate within the astronomy community as to what constitutes proof of detection of a new molecule. The currently accepted procedure requires the meeting of several criteria, including [31, 32, 33]: (1) the accurate knowledge of rest frequencies for the species being searched for, (2) the observation of clean, unobstructed lines that match the given rest frequencies at a known, well-determined velocity for the source, and (3) not a single absence of any predicted transitions from a local thermodynamic equilibrium (LTE) model of the

target molecule in the observational data. These requirements, in particular the latter, has put an emphasis on acquiring highly sensitive, broad coverage frequency surveys of sources or regions of interest combined with detailed modeling of known species in the source, to allow the systematic investigation of the data at the weakest signal levels for new species.

The continued classification of known interstellar molecules is also of great importance [9]. In particular, the detailed spectral characterization of so-called "interstellar weeds" has an important role in minimizing or eliminating erroneous assignments of new species to spectral features in observational data. Asymmetric molecules with dense spectra and high fractional abundances in so called 'hot cores' (warm, dense regions of molecular clouds adjacent to or surrounding luminous protostars) such as dimethyl ether (CH_3OCH_3), methylformate ($HCOOCH_3$), methanol (CH_3OH) and ethyl cyanide (C_2H_5CN), are often referred to as weeds due to their omnipresence in observational spectra. Approximately half of all identified interstellar spectral lines up to 700 GHz emanate from weed molecules [34, 35], and these molecules often dominate observational spectra not just at the level of the most intense features, but at all signal levels. However, in many cases, both high J- and K-states, as well as low-lying vibrational states and/or common isotopologues of such molecules have not been studied in detail, resulting in a lack of identification of weaker features that may significantly contribute to the 'grass' in any observational survey. The presence of many unidentified features in observational studies, in some case up to 50-60% of the lines in the spectrum [32, 9], highlights the importance of such efforts. Furthermore, the recent successful launch of the Herschel Space Telescope and the upcoming commissioning of SOFIA, both platforms that will allow the first observational studies at THz frequencies – where such species are even less well studied – provides a sense of urgency for this work.

Of the interstellar weeds, methanol in particular is a central player. Its abundance

is often significantly higher than all other weed molecules [9], and it has an intrinsically strong spectrum, which is further complicated due to the presence of an intermediate barrier internal rotor. The moments of inertia of the 'top' (CH_3) and the 'frame' (OH) are close to each other, resulting in very effective coupling between the internal rotation of the methyl group and the overall rotation of the molecule. This causes large shifts/perturbations of the K-stacks throughout the THz region in addition to the *A*-*E* splitting of individual lines. Here, the detailed cataloguing of the ground state rotational spectrum of methanol is described.

2.2 History

Methanol is the simplest intermediate barrier internal rotor. This, combined with its astronomical relevance, have provided an extensive history of spectroscopic study. The first part of this history was focused on the acquisition and analysis of the microwave spectrum, in an attempt to understand the torsion-rotation problem. The first high-resolution spectra were of the K = 2-1 E-state Q branch in the microwave region in 1948 [36], and the next two decades provided a series of further studies of the cm-wave spectrum (e.g. [37, 38]. The first study of the millimeter spectrum of methanol was published in 1968 [39], and this research provided a breakthrough in the global analysis of the spectrum through the assignment of ^{a}R-branches to J = 4 in the first four torsional states, in addition to several additional Q-branches and *b*-type transitions. Over the next two decades, the main driving force behind the continued study of the rotational spectrum of methanol came from the radioastronomy community, for reasons described above. The first models capable of fitting the data to experimental accuracy were achieved only around 1990, but required separate fits for the *A*- and *E*-states [40, 41]. Global fits of the *combined* *A*- and *E*-states were subsequently

achieved in the ranges of J $\leq$ 20, K $\leq$ 12 in the first two torsional states [42]. Several studies on individual states also extended assignments up to higher J's in specific frequency ranges (e.g. [43, 44]), and a highly detailed methanol atlas based on FTIR spectroscopy was published that provided much further detail on high quantum number states (although to lower frequency accuracy) [45]. The energy levels published in this atlas provided an extremely useful reference against which to compare the frequency of individual high J and K lines measured here.

The goal of the present work is to catalogue in detail the rotational spectrum of the ground state of methanol across the frequency ranges accessible to the heterodyne spectrometer for the far-infrared (HIFI) aboard the Herschel Space Telescope. This will allow an extension of the global analysis of the rotational-torsional problem to higher quantum numbers, but more importantly to provide a observational database of the THz spectrum of methanol. The latter will allow the identification of methanol transitions in both Herschel and SOFIA data, as well as unidentified lines in existing data, even in the absence of a fully quantum mechanical model describing the complete spectrum.

2.3 Data Set

The data set in this study is a compilation from several different sources. Much of the spectral line frequencies were recently acquired at the Jet Propulsion Laboratory (JPL) on a new instrument [2] that uses many of the technologies originally developed for HIFI and the heterodyne instruments under development for SOFIA. Data from the JPL spectrometer covers nearly the complete 0.3 - 1.2 THz region, as well as the 1.55 - 1.66 THz interval, and several windows around 1.7, 1.8 THz and 2.5 THz. A representative scan is shown in Fig. 2.1, in which both the density and the dynamic range of the rotation-torsion signals

can be seen. Ground state transitions in these ranges were assigned and verified using a variety of techniques that will be described in more detail below. Briefly, initial assignments were made using a prediction from a previous high-resolution study in the 0.5 - 1.2 THz region [46]. For high J- and K- transitions, these assignments were expanded on using the energy levels listed in the methanol atlas [45], in addition to close analysis of the spacing of individual lines within Q-branches, as well the use of energy power series expansions in individual K-stacks and line-loop calculations. Ground state transitions from studies outside of the JPL frequency ranges were compiled from a variety of sources and checked for correctness in similar fashion as the new data. These various sets were then combined to give a global database of THz transitions for the ground state of methanol. This database contains almost 3900 total transitions, including nearly 2000 that were newly assigned from the JPL data set. Quantum number coverage in this database is significant and goes beyond any previous study, with transitions up to J = 45 and K = 18 being assigned. Except for the most extreme sources, the present analysis should be sufficient to characterize ground state methanol emission from the warm, dense gas associated with star and planet formation, and so represents a significant advance over previous work.

2.4 Analysis

Before attempting to fit the data set to a global rotational-torsional model, it is important to check for the correctness of the assignments. Mistaken assignments can lead to a subtle shift away from the global minimum of the Hamiltonian model that can be difficult to detect when working with very large data sets as is the case here. This step is critically important for transitions that play central roles in the model, such as those connecting different K stacks, and that are sparsely represented in the data set. Several methods are available to check if

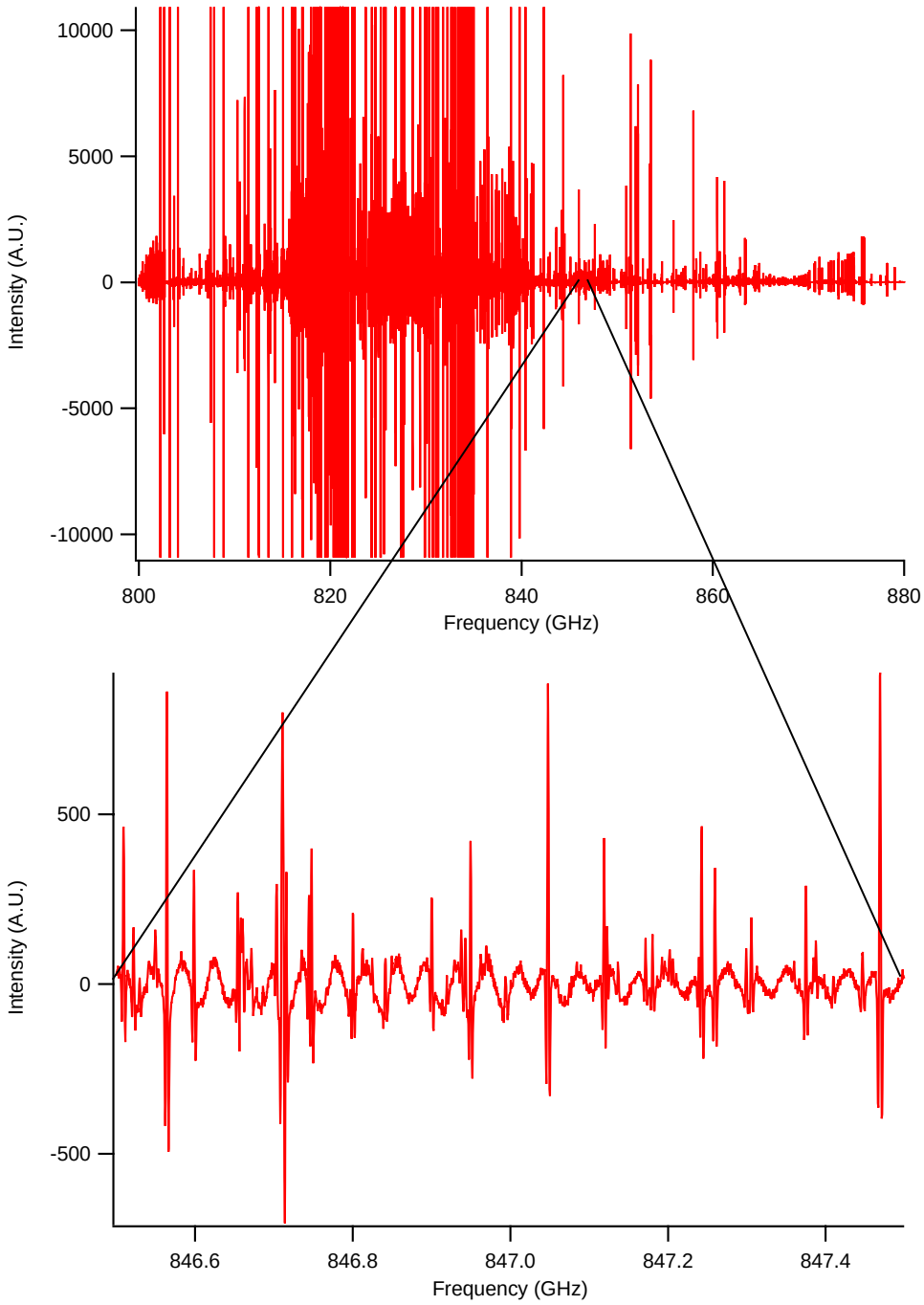

Figure 2.1: A scan of the methanol rotational spectrum in the 800-880 GHz region. These graphs show both the density and the large dynamic range of the molecular signals. The settings in the spectrum in the top plot were chosen such that many of the strongest transitions are saturated. This was done to allow measurement of transitions at the weakest levels given the available data acquisition capabilities of the instrument. The bottom plots illustrate the dynamic range of the spectrum, including the expansion of a section with "weaker" features that reveals them to still have significant signal-to-noise ratios. Many still weaker features can be seen at or above the noise level/standing wave level achieved.

an assignment is correct. The first step is paying close attention to the initial assignment, taking into account the location of both the assigned and alternative features compared to a prediction, as well as the intensity of the transition. As mentioned, initial assignments were done here using a prediction from a previous high-resolution study that extended to moderately high frequencies, and covering states up to J = 25 and K = 8 [46]. For quantum numbers outside of this range, the prediction was generally still close to a spectral feature up to about J $\sim$ 30-35 and K $\sim$ 11 and paying close attention to the intensity progression of the transitions, assignments were made with reasonable confidence. Beyond these states, the energy levels from the methanol atlas [45] proved invaluable. Even though the spectra in that work were of significantly lower resolution then the data analyzed here, the extremely large data set ($\sim$19000 transitions were included) allowed the fitting of individual levels to many transitions, thus increasing the accuracy. Predictions from this atlas were generally within a few MHz of the spectral feature assigned using the multiplier chain THz data acquired here. Furthermore, it is possible to trace the pattern within an individual branch to extend assignments to higher J levels. In particular, with Q-branches that are closely spaced in specific parts of the spectrum we were able to look at the progression of the spacing and intensity of individual lines and use this to extend assignments to high J thanks to the wide coverage and good absolute intensity calibration of the JPL spectrometer.

After the initial identification of a transition using these methods, the assignments were further checked by using basic models and calculations. It is possible to break the global fitting problem down into smaller sub-models, fitting the individual K-stacks as vibrational states separated by an energy term. This method is not particularly useful in the global description of the problem as these models cannot simply be tied together, but does provide a valuable means of checking the assignments within K-stacks. The A state levels were

treated as a symmetric top and E state levels as a linear molecule, which for many states permitted fitting to high J (but with a few exceptions). In the A state, the K = 9 levels diverge above J∼25 due to a perturbative interaction that occurs with K = 5 in $\nu_t = 1$, and in both the A and E state low values of K diverge at the highest J's due to several interactions between these states. The strengths of these repulsive interactions are inversely proportional to the ΔK between the states, with a single unique interaction term describing each ΔK interaction. The mapping of these level crossings is thus important in the global modeling of the spectrum as it allows prediction and fitting of further interactions of similar ΔK that are currently not part of the measured data set.

Ultimately, the only way to determine if a spectral assignment is absolutely correct is by calculating the sum over closed combination-difference loops, in which the individual transitions in the loop have all been measured. Several examples of such loops are shown in Fig. 2.2. If the lines in the loop have equal measurement uncertainties, $\Delta\nu_{meas}$, one would expect the loop to sum to zero within a factor of $\Delta\nu_{meas}\sqrt{N}$. Since it is highly unlikely that all lines in the loop have been assigned incorrectly such that the errors cancel, especially as many connected loops are calculated, this technique can generally be considered the final word on the correctness of an assignment. Calculating the sums over many loops of $N =$ 3,4,5,6 lines, and in a few select cases up to N= 10 lines, we managed to include ∼ 63% of all ground state transitions in loops. The various aspects in assembling and checking the database of assigned lines can be thought of as different levels of description of the energy level landscape with increasing levels of accuracy. The loop-sum calculations are the final aspect of fully weaving together the landscape in great detail. Thus, even though not all transitions were included in loops, the large fraction of included lines in addition to the other methods gives a high level of confidence in the set and that the few incorrect

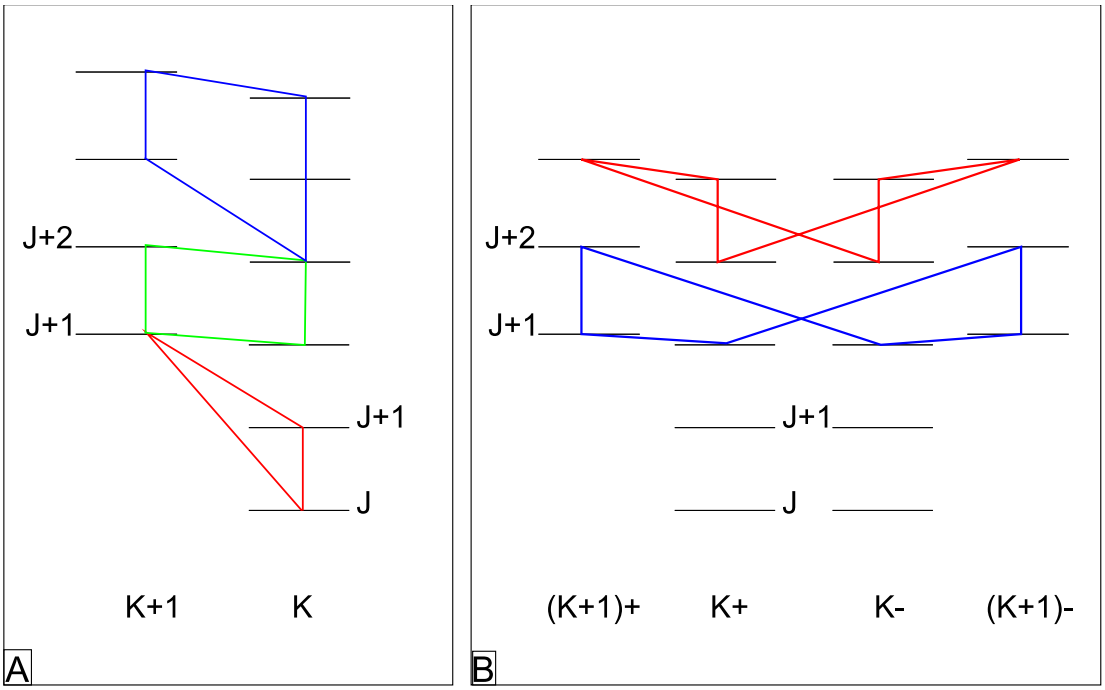

Figure 2.2: Graphs explaining the principles of loop calculations. The colored lines are the rotational transitions that connect the different energy levels in the diagrams. In the calculation, a closed loop must be formed by a series of transitions, and the error in the sum of the transition frequencies should not surpass the sum in the expected uncertainties. Panel A) represents the case when no asymmetry splitting is present, and examples of 3-, 4- and 5-line loops are shown. Panel B) shows the situation in the presence of asymmetry splitting, in which case symmetry selection rules must be obeyed. Two examples of 6-line loops are shown.

assignments left in the set will be identified by the computerized fitting procedure.

In work related to that presented here for the ground state, the THz and microwave data set for the ground state were combined with similar data sets for the first and second excited torsional states to create a global data set for the first three torsional states (ν_t = 0,1,2). Where appropriate, high resolution infrared data were also included, resulting in a global model up to J $\leq$ 30, K $\leq$ 14. This work was published recently [47], and will be briefly described here. The program used in the fitting procedure was obtained from I. Kleiner, available on the web [48]. The general approach involves fitting a rotational Hamiltonian to which the large amplitude internal rotational motion of the vibrational motion has been

transferred. The zeroth-order Hamiltonian has the following form:

$$H = F(P_\gamma + \rho P_a)^2 + (1/2)V_3(1 - cos3\gamma) + AP_a^2 + BP_b^2 + CP_c^2 + D_{ab}(P_aP_b + P_bP_a) \quad (2.1)$$

where γ is the angle of internal rotation, P_γ is its conjugate momentum, V_3 is the barrier to internal rotation, and P_a, P_b and P_c are the rotational angular momentum operators. Higher-order terms are generated by taking products of a power series of the momenta $P_\gamma^p P_a^q P_b^r P_c^s$ with terms (1 - cos3γ) in the Fourier expansion of the internal rotation potential function. Group theory and time reversal is then used to eliminate symmetry-forbidden terms. The program was modified in some ways to take maximum advantage of the present fit, the details of which can be found in [47]. The approximately 25000 total methanol lines were fit to 119 parameters, and the fit reaches the experimental uncertainty of the infrared line frequencies and about twice the experimental uncertainty for the microwave and THz lines. The Hamiltonian include rotational, torsional and rotational-torsional cross terms up to 10th order, whereas previous fits only extended to 6th order.

2.5 Discussion

From the results of the laboratory scans and spectral assignments carried out here, a THz database for rotational lines in the ground state of methanol has been compiled which includes nearly 3900 transitions and quantum number coverage up to J = 45 and K = 18. The database includes nearly 2000 new measurements throughout the THz region, and represents an unprecedented mapping of the $\nu_t = 0$ state of methanol, including transitions ranging from the most intense features in the spectrum to lines that barely rise above the noise level achieved in the lab. A subset of these transitions, almost 3000 lines with quantum

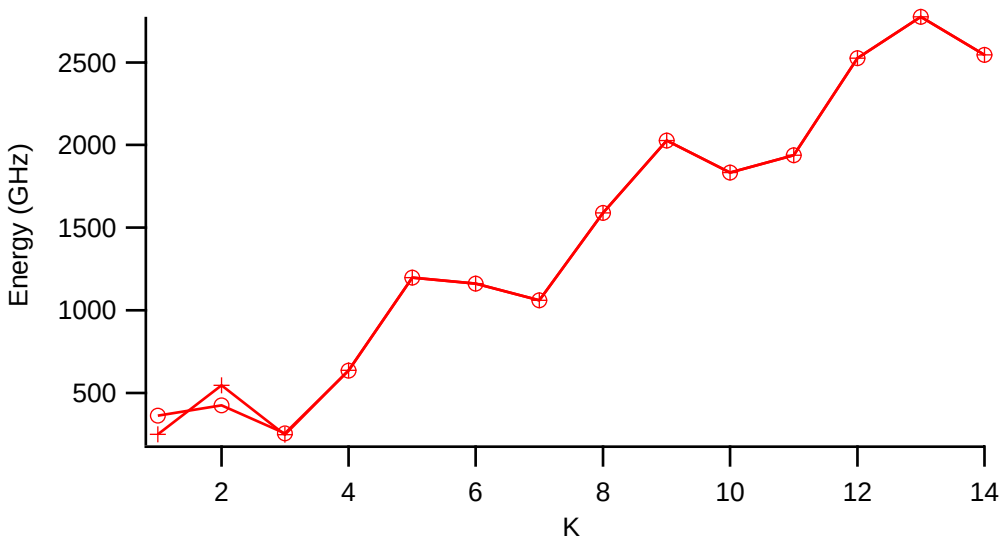

Figure 2.3: Energy progressions, $\Delta E_{(K+1)-K}$, of the J = 16 levels in the A state, showing the torsional shifts of the K stacks superimposed on the overall rise of the potential energy. + symbols represent states with K+ symmetry, ∘ symbols represent states with K- symmetry, and it can be seen that the symmetry splitting for the J = 16 levels is lifted by K = 4.

numbers up to J $\leq$ 30, K $\leq$ 14 were included in a global fit with transition from both the first and second excited torsional states as well as a large suite of high resolution infrared lines. This fit significantly improves the description of the rotational-torsional behavior of methanol to high frequencies. A good example of the quality of the description can be seen in Fig. 2.3, which shows the energy progression of the J = 16 levels in the A state of methanol. By fitting up to K = 14, it can be seen that several periods of the torsional potential are mapped, superimposed on the general rise in the rotational potential. This improved mapping to high J and K gives an accurate description of the distortion effects in the molecule, and the combined mapping of both the E and A states further increases the description of the rotational-torsional coupling. Further included in the fit are several of the repulsive interactions as described in the previous section: the interaction between K = 9 in $\nu_t = 0$ and K = 5 in $\nu_t = 1$ in the A state, and the interactions between the low K stacks at high J's in both the A and E states.

The quality global fit (for all three torsional states) allows predictions be be made with high confidence that extend beyond the quantum numbers included in the fit up (to J $\leq$ 35, K $\leq$ 15). These predictions can be found in the electronic supplementary material of [47]. However, for the ground state, the THz database we describe here extends further beyond these limits. The extensive analysis performed, including the careful analysis of individual assigned lines and branches along with a power series fitting of the energies within K stacks, allow us to make this claim. Further, the extensive loop calculations performed include transitions up to J values in the high 30's, bolstering the robustness of the assignment(s). Nonetheless, extending the global model for the ground state to the quantum number levels measured in this study is an important next step in describing the rotational spectrum of the ground state of methanol.

Chapter 3

Extended Analysis of Hydroxyacetone in the Torsional Ground State

3.1 Introduction

It has become increasingly clear that a stronger coupling between dust grain and gas phase chemistry is needed to explain the complex chemistry observed in dense molecular clouds. Furthermore, much remains to be understood about the relative contributions of various energetic pathways that drive the chemical processing of ices. One idea that has received increasing attention over the past few years is the formation of radical species in the quiescent, pre-collapse phase of an interstellar cloud, followed by reactions between these species as the grains are heated in the warm-up phase associated with core collapse and star-formation [28, 26]. One route by which more complex species are formed is by single atom additions to CO molecules, initiated by the tunneling of hydrogen atoms, a process previously argued to be the only significant grain-surface pathway in quiescent clouds due the very low temperatures that prevail [22].

The second process now also thought to play an important role in the formation of radical species is the cleavage of molecular bonds by supra-thermal electrons that are released in

the collision of highly energetic (>MeV) cosmic rays with dust grains. Both the models that include these two processes [28, 26] and experimental studies of the processing of ice analogs with thermal electrons [24] have shown, for example, an overabundance in the formation of methyl formate versus its structural isomers acetic acid and glycolaldehyde, a trend that is not well explained by gas phase chemical models yet widely observed in the interstellar medium (ISM) [49]. In order to disentangle the relative contributions of these and other pathways (e.g. UV photolysis) and better understand the complex web of reactions that drive interstellar chemistry, further observations and systematic comparisons of structurally related molecules are needed. The focus of this Chapter is hydroxyacetone ($HOCH_2COCH_3$), a structural intermediate between glycolaldehyde ($HOCH_2COH$) and the 3C sugar dihydroxyacetone ($HOCH_2COCH_2OH$, DHA), a compound widely observed in the soluble organic fraction of carbonaceous chondrites. Both glycoaldehyde and DHA have been the focus of previous observational studies [50, 51, 52, 53], and we began preliminary laboratory/observational work on hydroxyacetone with these motivations in mind [54, 55].

Our initial, fairly shallow observational search for hydroxyacetone at 1.3 mm with the Caltech Submillimeter Observatory (CSO, atop Mauna Kea) was unsuccessful [55], and while further work on the molecule was ongoing at Caltech a detailed 3 mm survey using the SubMillimeter Telescope (SMT, at Mount Graham) confirmed it to be below detection limits [56]. After an initial tentative detection [52], a similarly detailed study of DHA showed this molecule to be undetected as well [53]. Thus, not much can be currently said about the chemistry of these species, other than the constraints on chemical models provided by the observational upper limits. As noted in the introductory Chapter, however, the detection limits for complex species using the Herschel, ALMA, and SOFIA platforms are expected to be substantially lower than those achievable with ground-based 10m single dishes, and

so these new facilities may well permit the detection of hydroxyacetone/DHA and related species (and thus permit a reconsideration of their chemistry).

The very high frequencies to which Herschel and ALMA have access place stringent demands on the quality of laboratory fits to the spectra of molecules such as hydroxyacetone. Thus, even though a previous millimeter-wave study of this molecule characterized the spectrum to $J_{max} = 30$ and $K_{a,max} = 12$ in the ground torsional state, an extrapolation of this analysis of the rotational-torsional spectrum of hydroxyacetone to the higher frequencies and quantum numbers that characterize transitions in the Herschel/ALMA submillimeter windows is fraught with uncertainty. Indeed, even a modest extension of the previous analysis from 3 to 1 mm, where the lines are expected to be substantially stronger, results in line uncertainties that are larger than the typical spacing between features in the spectra of molecule rich hot cores such as Sgr B2(N).

The barrier to internal rotation of the methyl top in hydroxyacetone is only 65 cm^{-1}, which gives a reduced barrier of s = 5.5 (s = $4V_3/9F$, where F is the rotational constant of the methyl top). In this low-barrier regime, the $A - E$ splitting is on the order of the spacing between rotational levels, and in combination with asymmetry splitting, can make even assignments challenging – much less quantitative fits of the spectrum to experimental precision. In addition, the low barrier drives an effective coupling between the internal rotation of the top and overall rotation of the molecules, leading to many higher order off-diagonal terms in the Hamiltonian [29]. The combination of these effects makes the analysis of the torsion-rotation spectrum of hydroxyacetone a compelling spectroscopic problem, one that can aid in the continued quest of understanding the effects of internal rotation on rotational spectra of asymmetric molecules.

In our initial characterization of the spectrum of hydroxyacetone, difficulties in fitting

the transitions of the E state led to ambiguous observational results [55]. In a recent study [56], henceforth AP06, several microwave transitions from the initial microwave work on this molecule [57] were remeasured. The new frequencies led to significant revisions in the microwave assignments, and allowed a global fit to experimental accuracy for low to moderate J-values, and created an opportunity for us to revisit the problem. Furthermore, we have used hydroxyacetone as a test case to make several modifications to the SPFIT/SPCAT program suite developed by H.M. Pickett at JPL in order to simplify the internal axis modeling of low-barrier internal rotation problems. This general and highly flexible program suite forms the core of the most widely used THz catalog available to astronomers and atmospheric scientists, and so an improved model and fitting procedure for low barrier internal rotors has much wider applicability than simply the present study of one compound.

The front-end program IAMCALC (Internal Axis Method Calculator) has recently been released as part of the CALPGM program suite (see `http://spec.jpl.nasa.gov` for further details). This program creates torsion-rotation operators through periodic solutions to the Mathieu equation which are then represented in the SPFIT/SPCAT programs as Fourier series (in energy and rotation operators) and off-diagonal torsional couplings (between specifically defined states whose symmetries match the torsional levels and sublevels) from user defined values such as barrier height and ρ value. These parameters are then adjusted iteratively through both programs to optimize both the spectral fit and the periodic solutions of the torsional problem. Used in tandem the IAMCALC/SPFIT programs are similar to the BELGI (BELGian Internal rotor) program developed by. I. Kleiner [58], but there are a number of notable differences that must be considered when comparing results from these two packages. First, the open definition of parameters in IAMCALC/SPFIT allows very high order interactions to be modeled, whereas BELGI is limited to a pre-defined

set of input parameters. Next, the IAMCALC basis may be chosen to be simple functions of K, rather than the Fourier expansions, thus allowing an accurate sampling of energy values near avoided crossings and/or cusps. Finally, the programs utilize separate definitions for the fundamental torsional operator, P_γ, which, in IAMCALC, is always Hermitian, $P_\gamma - \rho P_a$, but used in this form only for the definition of F in BELGI – higher order terms in BELGI truncate the expression by elimination of ρP_a. This latter difference requires either special parameter definitions for consistency between BELGI and IAMCALC, or a post-fit parameter transformation to compare the fitted values.

3.2 Experimental Section

Scans covering several millimeter and sub-millimeter spectral bands were measured as part of this work, providing a more extensive data set of the rotation-torsion spectrum of hydroxyacetone. The 91-120 GHz and 275-350 GHz regions were recorded on the Caltech flow cell spectrometer; while the 230-250 GHz, 425-435 GHz regions, and a small window around 360 GHz were recorded using the JPL flow cell spectrometer. Both instruments are similar in general setup and have been described in detail elsewhere [2, 59]. Briefly, both consist of a fully computer controlled, swept frequency microwave (12-20 GHz) synthesizer followed by a series of fixed tuned harmonic multipliers and amplifiers that upconvert the microwave radiation into the desired band. The high frequency harmonics are then sent through a gas cell through which the sample flows at constant pressure. Radiation exiting the cell is then sampled with either a room temperature Schottky diode detector or a LHe-cooled InSb detector. The signal is ultimately recorded as a 2nd derivative lineshape using a lock-in amplifier set to the 2nd harmonic of the frequency modulation. In both experiments a flask of high purity hydroxyacetone, purchased from Sigma-Aldrich, was attached to the flow cell,

and a sample pressure of 10-30 mTorr was maintained in a slow, but steady, flow.

3.3 Results and Data Analysis

Data were assigned in a boot-strap method using the IAMCALC/SPFIT/SPCAT program suite [60], in conjunction with the Sub-Millimeter Analysis Program (SMAP, also available at [60]). Further assignments were later made using Loomis-Wood visualization plots in the Computer Aided Assignment of Asymmetric Rotor Spectra (CAAARS) program suite [61]. The spectrum of hydroxyacetone exhibits several interesting trends, mainly due to asymmetry and internal rotation (A-E) splittings, that both aided in our assignment of the spectrum and give indications of the underlying physics of the rotation-torsion motions of the molecule. The first and most obvious of these trends is a series of collapsing quartets, similar to other asymmetric molecules with large dipole moments along two or more principle axes, such as lactic acid [62]. Both hydroxyacetone and lactic acid, for example, have significant dipole moments along the a- and b-inertial axes (lactic acid: μ_a=1.44 D, μ_b=1.83 D [62], hydroxyacetone: μ_a=2.22 D, μ_b=2.17 D [57]), and both molecules possess nearly degenerate pairs of K_a levels at low K_a. This results in two, overlapping, a- and b-type asymmetry doublets, together making up the prominent quartet feature. The asymmetry splitting in these quartets decreases with J for a given K_a, giving a single intense line at high J. Additionally, the asymmetry splitting increases with K_a, resulting in the collapse of the quartet at increasingly higher values of J. This eventually makes it impossible to trace the quartet pattern in the spectrum, here K_a = 6,7 is the highest K_a for which this pattern is still obvious in our data. At higher values of K_a, the splitting becomes so large that it is now pairs of K_c levels with the same value of K_a that become nearly degenerate, giving the more traditional asymmetry doublets with patterns opposite from before: the splitting

increases with J and decreases with K_a. In this case, a- and b-type doublets no longer overlap, giving somewhat less prominent, though still distinctive and intense, doublets.

The second main pattern in the spectrum is the A-E splitting arising from the internal rotation of the methyl top. Due to the low barrier of hydroxyacetone, the A-E splitting is quite large, often significantly larger than the asymmetry splitting. Nevertheless, the general patterns of the E state spectrum are similar to that of the A state, with collapsing quartets also being the most prominent features identifiable, albeit with smaller splitting(s). The E quartet splitting is consistently ∼60-65 % of that in the A state, allowing a relatively straight-forward mapping of the E state transitions relative to the A state transitions once the latter are assigned. The A-E splitting increases regularly with K_a, from ∼40-50 MHz for the K_a=0,1 quartet to approximately 1 GHz at K_a=6,7, with relatively small variations as a function of J within the K_a stacks.

In addition to using these patterns to confirm the assignment of the majority of the lines in the fit, the CAAARS program and its Loomis-Wood visualization was used to further expand the data set, in particular for transitions of high J where the quartet pattern is no longer apparent and for assignment of various Q branches throughout the spectrum.

In all, over 1100 new transitions in the ground state rotation-torsion spectrum of hydroxyacetone, up to frequencies of 430 GHz, were assigned using the methods described above. The full data set includes a-type transitions up to $J = 75$ and $K_a = 16$ and b-type transitions up to $J = 75$ and $K_a = 18$ in the A state, and $J = 75$, $K_a = 13$ and $J = 75$, $K_a = 10$ for a-type and b-type transitions, respectively, in the E state. The increased torsional interaction in the E state make it more difficult to characterize, hence the smaller range in K_a. This is also the reason 'only' 472 new lines were assigned in the E state versus 677 new lines in the A state. The new data set also includes several nearly complete Q branches

up to $K_a = 10$ for both the A and E states in the 91-120 GHz region that were previously unassigned [56], and represents a significant increase in quantum number coverage. Previous spectral analyses of hydroxyacetone were limited to values of $J = 30$ and $K = 12$, including only a handful of transitions above $K = 7$ for $b-$types in the A state, and only 2 transitions above $K = 5$ in the E state [56]. The newly assigned lines were ultimately combined with the AP06 set to give a total of 2300 transitions. In AP06, the line list from Kattija-Harmony (1980) was reassessed, and assignments that were determined to be incorrect were either reassigned or removed from the set. Two additional transitions, left out of the AP06 fit, were reassigned here and added to the list: the 30997.800 MHz line was identified as the $5_{1,5}$ - $4_{1,4}$ E state transition, and the 34514.380 MHz line was identified as the $8_{3,5}$ - $8_{2,6}$ E state transition [57].

Fitting was done using the SPFIT/SPCAT program suite, including the IAMCALC front-end that uses the Internal Axis Method (IAM) to analyze the effects of internal rotation. Initial fits utilized the parameter and data set of AP06 [53] as a starting point. This allowed further assignment and expansion of the analysis through an iterative process. Although the IAM basis used in this procedure includes excited torsional states implicitly, the transitions predicted for these states did not conform to any recognizable patterns in the unassigned portions of the recorded spectra. It is likely that the extremely low barrier of hydroxyacetone makes it a poor choice for a global torsional analysis such as that performed recently on methanol [47] (see also Chapter 2) or acetaldehyde [63]. In these latter two studies the global torsional analysis is valid up to approximately $\nu_t = 3$, at which point the higher torsional states transition to a free-rotor situation instead of a low-barrier hindered rotor. Similarly, we believe that assignment of the $\nu_t > 0$ states of hydroxyacetone will require a different basis than that presented here and in AP06 [53].

We have fit a total of 39 parameters, shown in Table 3.1. The numerical results of the fit are complied in Table 3.2, which also lists the results of the AP06 fit for comparison. Table 3.1 is in the format of [64] to show the order progression of the operators we fit. Due to the differences in parameter definitions as described in the introduction (in the AP06 study the BELGI program suite was used) the parameters have been transformed to allow direct comparison. Lines with an obs-calc error of larger than 7 times the experimental uncertainty were removed from the fit. This truncation excluded approximately 60 transitions from the final fit, and resulted in a global rms of 120 kHz for the remaining lines, close to experimental uncertainty of ∼100 kHz. The factor of 7 in the truncation was chosen somewhat arbitrarily, but was an attempt to balance the inclusion of as many lines as possible while simultaneously excluding those transitions for which the model was clearly breaking down. The excluded lines were consistently the highest J transitions within K_a stacks for a particular type of transition, with the onset first appearing around J = 50-55 for the K_a=4,5 quartets and the divergence occurring at subsequently lower values of J for increasing K_a. Because the error progression in the divergence is smooth and also because these transitions were assigned using Loomis-Wood plots, we believe this to be due to breakdown in the model at high quantum numbers rather than a misassignment of lines. The great difficulty in assigning Q branches above K_a = 10, where K_a = 18-17 Q branch in the A state is the only exception, also supports this conclusion. The excitation energies at which these divergences occur are at least 300 - 500 cm^{-1}, depending on K_a, and so all lines likely to be strong under hot core conditions are now predicted to essentially experimental precision. Based on the results of the fit, an entry for hydroxyacetone was created for the JPL spectral line catalog, and can be found at `http://spec.jpl.nasa.gov`.

Table 3.1: Rotational, torsional and cross-terms determined for hydroxyacetone

Rotational operator	Torsional operator								
	1	$\tilde{P}_\gamma^2$	$\tilde{P}_\gamma P_a$	1 - cos 3γ	$\{\tilde{P}_\gamma^2$, c$\}$	$\{\tilde{P}_\gamma P_a$, c$\}$	1 - cos 6γ	$\tilde{P}_\gamma^3 P_a$	P_γ^4
1		F	-$2\rho F$	$V_3/2$				k_3	
P^2	$\frac{B+C}{2}$	G_v	L_v	F_v				k_{3J}	
P_a^2	$A - \frac{B+C}{2}$		k_1	k_5				k_{3K}	
$P_b^2 - P_c^2$	$\frac{B-C}{4}$	c_1	c_4	c_2		c_{3a}		c_{3b}	
$\{P_a, P_b\}$	D_{ab}	Δ_{ab}	δ_{ab}	d_{ab}					
P^4	$-\Delta_J$	g_v		f_v					
$P^2 P_a^2$	$-\Delta_{JK}$								
P_a^4	$-\Delta_K$		l_k						
$2P^2(P_b^2 - P_c^2)$	$-\delta_J$								
$\{P_a^2, (P_b^2 - P_c^2)\}$	$-\delta_K$								
$P_a^2\{P_a, P_b\}$	D_{abK}								
P^6	Φ_J								
$P^4 P_a^2$	Φ_{JK}								
$P^2 P_a^4$	Φ_{KJ}								
P_a^6	Φ_K								
$2P^4(P_b^2 - P_c^2)$	ϕ_J								
$P^2\{P_a^2, (P_b^2 - P_c^2)\}$	ϕ_{JK}								
$\{P_a^4, (P_b^2 - P_c^2)\}$	ϕ_K								

3.4 Discussion

The rotational spectrum of the ground vibrational state of hydroxyacetone has been characterized up to 435 GHz. A total of 2300 lines in both A and E states were fit to a global model with 39 parameters. This is a significant increase in the number of parameters compared to previous studies [56], and is mainly required due to the large increase in both J and K_a coverage. This has allowed us to determine the rotational, torsional and rotational-torsional cross terms in the Hamiltonian to 8th order. As can be seen in Table 3.1, higher order terms were added in a consistent manner, always exhausting lower order possibilities before including higher order terms.

As to the breakdown of the model at higher J within K_a stacks, there are several possible reasons for this. First to consider are the excited torsional/vibrational states, which can interact with and perturb the ground state if they sufficiently low in energy. Hydroxyacetone has several low-lying excited states, most importantly the methyl torsion, which has been calculated to lie near 65 cm^{-1} (but which is too weak to have been observed in Raman spectra), and the CH_2OH torsion that has been measured at 80 cm^{-1} [65]. Additional low-lying bands that are experimentally observed are the OCC in plane bending mode at 276 cm^{-1} and the OH torsion at 330 cm^{-1} [65], both of which could potentially impact the rotational spectrum of the ground state. The importance of these low-lying excited states is confirmed by the presence of many unassigned lines in our data with similar or larger intensity than the ground state. As these lines are currently unassigned, interactions with the excited states have not been explicitly included in our model. IAMCALC does assume a basis set including several excited states in predicting the parameters for the rotational Hamiltonian, but these are predicted internally in the program mainly as a consistency

Table 3.2: Spectroscopic parameters for the ground vibrational state of hydroxyacetone

Operator	Parameter (Units)	Value	
		This work	AP06
$\frac{1}{2}(1-cos3\gamma)$	V_3 (cm^{-1})	65.3038	65.3560
P_γ^2	F (MHz)	158942	159118.2
$P_\gamma P_a$	ρ (unitless)	0.0587318	0.0587793
P^2	*(B + C)/2* (MHz)	3434.434(62)	3439.8048
P_a^2	*A - (B + C)/2* (MHz)	6460.209(41)	6439.3312
$P_b^2 - P_c^2$	*(B - C)/4* (MHz)	285.733(33)	286.5946
$\{P_a, P_b\}$	D_{ab} (MHz)	1097.364(213)	1089.287
$(1-cos3\gamma)P^2$	F_V (MHz)	-5.512(167)	-1.772
$(1-cos3\gamma)P_a^2$	k_5 (MHz)	20.221(70)	26.585
$(1-cos3\gamma)(P_b^2 - P_c^2)$	c_2 (MHz)	-0.704(88)	-1.746
$(1-cos3\gamma)\{P_a, P_b\}$	d_{ab} (MHz)	2.80(60)	12.696
$P_\gamma^2 P^2$	G_v (MHz)	-0.3396(168)	
$P_\gamma^2 P_a^2$	k_2 (MHz)		0.9809
$P_\gamma^2(P_b^2 - P_c^2)$	c_1 (MHz)	0.0205(88)	-0.03229
$P_\gamma^2\{P_a, P_b\}$	Δ_{ab} (MHz)	-0.392(65)	0.4800
$P_\gamma P_a P^2$	L_V (MHz)	0.01772(19)	-0.00053
$P_\gamma P_a^3$	k_1 (MHz)	0.0128(57)	0.00174
$P_\gamma P_a(P_b^2 - P_c^2)$	c_4 (MHz)	-0.0119(43)	-0.00015
$P_\gamma P_a\{P_a, P_b\}$	δ_{ab} (MHz)	-0.03239(228)	-0.08554
$P_\gamma^3 P_a$	k_3 (MHz)	2.331(117)	-0.1730
P^4	-Δ_J (kHz)	-0.8350(74)	-0.8399
$P^2 P_a^2$	-Δ_{JK} (kHz)	9.91(40)	8.984
P_a^4	-Δ_K (kHz)	-27.19(62)	-29.58
$P^2(P_b^2 - P_c^2)$	-δ_J (kHz)	-0.2515(37)	-0.24274
$\{P_a^2, (P_b^2 - P_c^2)\}$	-δ_K (kHz)	2.743(150)	2.599
$P_a^2\{P_a, P_b\}$	D_{abK} (kHz)	16.85(59)	18.41
$\{P_\gamma P_a, (1-cos3\gamma)\}(P_b^2 - P_c^2)$	c_{3a} (kHz)	-0.01368(54)	
$P_\gamma^3 P_a P^2$	k_{3J} (kHz)	11.27(64)	
$P_\gamma^3 P_a^3$	k_{3K} (kHz)	-47.4(34)	
$P_\gamma^3 P_a(P_b^2 - P_c^2)$	c_{3b} (kHz)	-8.697(192)	
$(1-cos3\gamma)P^4$	f_v (kHz)	-0.04695(110)	
$P_\gamma^2 P^4$	g_v (Hz)	2.907(58)	
$P_\gamma P_a^5$	l_k (kHz)	0.0536(43)	
P^6	Φ_J (Hz)	0.004223(168)	
$P^4 P_a^2$	Φ_{JK} (Hz)	-0.0298(77)	
$P^2 P_a^4$	Φ_{KJ} (Hz)	1.337(49)	
P_a^6	Φ_K (Hz)	-1.396(61)	
$2P(P_b^2 - P_c^2)$	ϕ_J (Hz)	0.002134(84)	
$P^2\{P_a^2, (P_b^2 - P_c^2)\}$	ϕ_{JK} (Hz)	-0.0432(33)	
$\{P_a^4, (P_b^2 - P_c^2)\}$	ϕ_K (Hz)	1.1845(297)	

check, and more explicit assignments may be needed. Early on we attempted to include several of the remaining intense transitions into the fit; and while it was possible to assign several branches based on quartet patterns and using Loomis-Wood plots, the fit did not converge when these additional series were included. Additionally, the predictions for the excited state transitions using our first order model were not close to the spectral features observed, making the identification of the states to which the lines belong difficult. A more profitable route would likely be to return to the microwave region in order to measure the lowest J, K_a lines in the excited states before attempting to fit the (sub)mm-wave lines.

A second effect that can also cause line shifts is due to local repulsive interactions when different K stacks in a given torsional state approach or cross each other. With the high density of states for hydroxyacetone, this is certainly not an unlikely scenario. However, it is the consistent and more general breakdown of the model that leads us to believe this 'internal' K stack effect is likely less important in characterizing the full rotational spectrum than are the excited torsional/vibrational states. Once the excited states have been included and the fit has been stabilized, further analysis and refinement should allow identification of K stack effect if it does indeed occur.

Even with the limitations of the model as discussed above, the present results provide a significant improvement in the overall description of the rotational-torsional spectrum of hydroxyacetone compared to previous studies; and demonstrate that the recent extensions of the SPFIT/SPCAT program suite now permit the quantitative analysis of low barrier (single) internal rotor spectra. The pure rotational assignments in the ground torsional state have been extended from $J = 30$ and $K_a = 12$ up to $J = 75$ and $K_a = 18$ in this study, and the rotational-torsional terms have been refined and extended up to 8th order, making hydroxyacetone one of the few asymmetric molecule/low barrier internal rotors for

which such an extensive rotation-centrifugal distortion analysis exits. As noted above, the expanded fit is also a significant milestone in the use of SPFIT/SPCAT to study such systems, as the program suite proved capable, indeed highly successful, of fitting both A and E states in a single, global, model.

Finally, from an observational perspective, this study catalogs the vast majority of the important lines under hot core conditions by extending the assignments from 180 GHz up to 435 GHz. Thus, most of the windows available to CSO and other similar (ground-based) observatories can now be used to search for the emission lines of hydroxyacetone. As has been discussed previously (e.g.[59, 66], simply predicting the frequencies of even the most well described transitions can lead to unacceptable errors when large frequency extrapolations are required. These laboratory characterization are therefore a crucial first step in exploring observational windows at $\lambda < 1$ mm. However, with both our initial attempts [55] and subsequent efforts at longer wavelengths (AP06) providing only upper limits on the column density, new single dish telescope observations over large spatial scales are not likely to meet with success. Given the compact nature of most hot core sources, interferometric observations with either CARMA in the short term or, especially, ALMA once it comes on-line in 2013 (shared risk observations with roughly a quarter of ALMA will begin in 2011) should provide much better detection limits through their larger collecting area and ability to spatially filter out the extended emission from simpler molecules. Alternatively, the line confusion can be largely reduced by moving to THz frequency observations with Herschel or SOFIA. If such observations ultimately do lead to a detection of torsionally excited hydroxyacetone, the present analysis will be of use in further detailed laboratory analyses of the torsional spectrum and in the global fitting of confusion-limited surveys that provide the best platform for the identification of new species [67].

Chapter 4

The Millimeter-Wave Spectrum of 2-Cyanoethanol

4.1 Introduction

The study of star forming regions and the feedback between observations and models has taught us much about the chemistry that occurs as protostars begin to fuse hydrogen and warm their surrounding. This transitional phase of star- and planet-formation is particularly interesting because it is the interval over which chemistry can occur in the relatively gentle conditions between the first evaporation of icy dust grain mantles as the environment heats up and the eventual incorporation of volatile species into larger bodies or their destruction by the intense UV field from the star as the dust clears. Understanding the chemistry of this phase can thus lead to insights about the general evolution of molecular complexity from an interstellar setting into that characteristic of planetary systems. More specifically, the properties of embedded protostars set the initial stage against which the records from dust, comets and asteroids in our own solar system can be compared, with a long term view towards establishing a better understanding of the chemical environment of the early Earth from which life spontaneously arose.

Early models of protostellar chemical evolution focused largely on isolated models of

gas or grain mantle chemistry, but it has recently become increasingly clear that there must be substantial coupling of the gas phase and dust grain reaction networks, especially as the (proto)star approaches the main sequence [28, 26]. In their studies, Garrod et al. showed that the inclusion of various additional chemical pathways on the grain before sufficient warming occurred to drive the icy mantles into the gas phase was necessary to explain the observed abundance ratios of certain molecules seen toward sites of (massive) star formation. Specifically, instead of only mobile H and heavier first row atoms reacting with larger structures on cold grains [22], larger reactive species that are created by the cosmic-ray processing of interstellar ices were now also allowed to participate in similar mechanisms as temperatures of the grains increase near forming stars [28, 26].

We would like to further explore this hypothesis by looking at molecules containing cyano-groups. Cyano-containing molecules are almost always highly polar, and so have strongly allowed rotational spectra. Further, under the conditions prevalent in planetesimals, aqueous alteration of cyano-groups can lead to a wide variety of carboxylic acids. Such compounds are abundant in carbonaceous chondrites, and have unusual isotopic signatures that suggest an interstellar inheritance for these compounds or their organic precursors. For example, Belloche et al. recently published a detection of aminoacetonitrile (NH_2CH_2CN) in the galactic center cloud, SgrB2(N), and discussed its significance as a potential precursor to interstellar (or nebular) glycine, one of the holy grails of observational astronomy [32].

The main mechanisms by which the reactive species participate in the scheme of Garrod et al. is through bond-cleavage of larger species by the supra-thermal electrons that result from the collisions of cosmic-rays with the dust grains on which these species reside; as well as by mobile hydrogen atoms tunneling through higher order bonds such as in CO. The set of species that are thus considered for cosmic-ray induced dissociation in-

cludes H_2O, CH_4, NH_3, HCO, H_2CO and CH_3OH. There is no reason, however, why other species that may reside in the ice prior to star-formation should not participate in this kind of scheme. By expanding the set of observational targets containing cyano-groups it should be possible, if detected, to examine wether this class of molecules follows the same general rules as described by Garrod et al. We selected the two isomeric species 2-cyanoethanol ($OHCH_2CH_2CN$) and methoxyacetonitrile (CH_3OCH_2CN) as observational targets, which can then be compared with aminoacetonitrile and preliminary studies of other cyano-molecules that are ongoing (personal comm. Belloche), to see what the abundance ratios say about the chemical pathways that operate on grain surfaces.

Here we describe the millimeter-wave spectrum of 2-cyanoethanol. The millimeter-wave spectrum of methoxyacetonitrile will be described in the subsequent Chapter (to be submitted as [68]). Hydroxyacetonitrile ($HOCH_2CN$) would have been another natural target, but is highly volatile and extremely toxic (as is aminoacetonitrile) with an LD50 of 5 mg/kg or the inhalation of <250 ppm vapor for a few hours. In addition to its astronomical/cosmochemical relevance, 2-cyanoethanol serves as a testbed for another challenging aspect of mm-wave/THz complex molecule spectroscopy. In the case of hydroxyacetone, the major hurdle concerned accurate fits to the complex spectrum provided by the low barrier to the internal rotation of the methyl group. For 2-cyanoethanol the challenge, as we shall see, is provided by the large number of conformers and low-lying excited torsional/vibrational states that are populated at room temperature. With modern mm-wave spectrometers it is possible to collect hundreds of GHz of spectra in a hands off, automated fashion in a matter of only a few days, resulting in the acquisition of tens of thousands of line frequencies for complex molecules. Assigning these spectra in an efficient manner will be critical to sustaining adequate throughput to meet the needs of the Herschel and ALMA observatories. The

former in particular has a limited lifetime of only 3-4 years before its cryogen is exhausted.

Assignments in the microwave region are often simpler than those near the Boltzman peak, and for that reason we have relocated the original Balle-Flygare FT-MW machine to Caltech and refurbished the electronics/computer control system. Here, the necessary microwave data for 2-cyanoethanol are available from a previous study by Marstokk and Mollendal [69], who assigned transitions belonging to three separate conformers and several excited states in the 18.0-39.6 GHz spectral region. The *gauche* conformer was found to be the global minimum for this molecule, lying 2.7 kJ/mole below the *anti* I conformer, and for this reason has the most intense features in the spectrum and the most easily identifiable excited states [69]. In the present work we identified the *gauche* conformer and three of its excited states as well as the ground state of the *anti* I conformer, but not the *anti* II conformer. The relative energies of the different conformers and the torsional bands can be seen in Fig. 4.1. Results of the assignments and fitting of the spectrum are discussed below.

4.2 Experimental Section

Millimeter data for 2-cyanoethanol were measured over the entire 225-360 GHz spectral window in our flow cell spectrometer. In the setup, millimeter-wave radiation emanates from a room temperature, solid state multiplier chain driven by a 0.01-20 GHz Wiltron microwave source, passes through a 9 foot glass flow cell, and is received on a Virginia Diodes Shottky diode detector. Scans were done in single pass, but the setup is capable of a double-pass configuration. The pressure and flow rate were controlled through a series of needle valves and a rotary vacuum pump. The signal is recorded as a 2nd derivative lineshape using a Stanford lock-in amplifier.

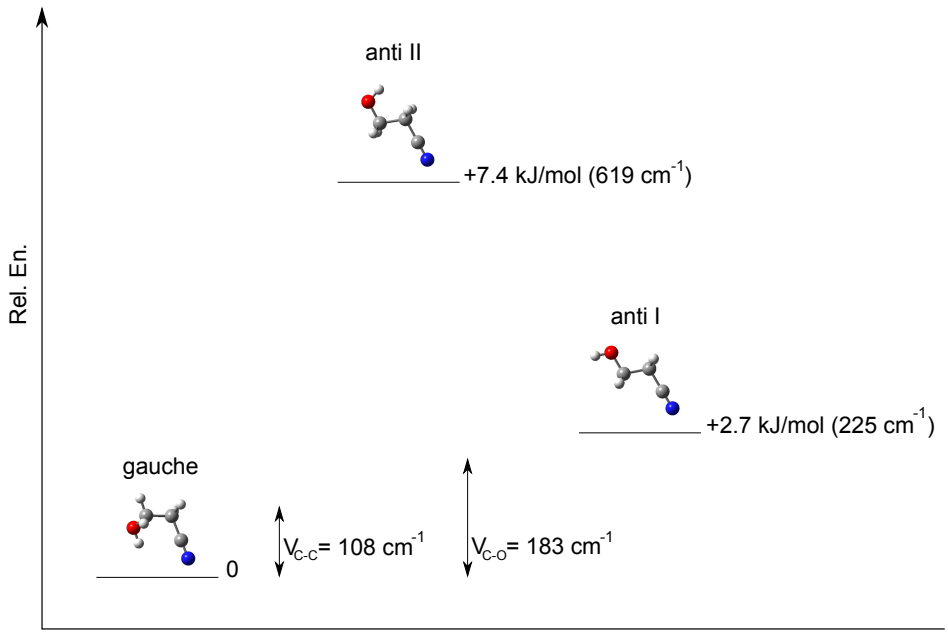

Figure 4.1: The relative energies of the three lowest energy conformers of cyanoethanol. The global minimum for this species is the *gauche*-conformer, with the *anti*-I conformer 2.7 kJ/mol above it and the *anti*-II conformer an additional 4.7 kJ/mol higher in energy. Also indicated are the relative energies of the first two torsional modes of the *gauche*-conformer, the torsion along the central C-C bond at 108 cm^{-1} and the torsion along the C-O bond (i.e. torsion of the OH group) at 183 cm^{-1}. We identified ground state rotational transitions for both the *gauche*- and *anti*-I conformers in this study, but not the *anti*-II conformer. In addition we identified transitions from the fundamental and first overtone of the C-C torsional mode and the fundamental of the C-O torsion.

2-Cyanoethanol was obtained commercially from Sigma Aldrich. It is a clear, slightly yellow, liquid with a very high vapor pressure, and as a result is easily placed into the gas phase. In fact, some care was needed to maintain a sufficiently low pressure so as to not collisionally broaden the lines and saturate the detector for individual transitions. Only by barely opening the controlling needle valves to the flask containing the sample and maximizing the pumping speed could we maintain the flow cell pressure in the 30-60 mTorr range, thereby minimizing the pressure broadening and permitting the acquisition of the entire spectrometer range in one single scan. The data contains many thousands of lines from both the true ground state conformer as well as several excited torsional/vibrational

states along with the ground state of a second conformer, the details of which will be described in the following section.

4.3 Results and Data Analysis

The data were assigned using the SPFIT/SPCAT programs and the SMAP visualization tools [60] discussed in Chapter 3, in combination with the CAAARS program suite [61]. In particular, going back and forth between the easy navigability of the direct data in SMAP and the Loomis-Wood plots in CAAARS proved extremely useful. The main R and Q branches of greatest intensity were generally assigned using CAAARS, followed up by a more methodical walk-through of the data in SMAP to assign as many, especially weaker, transitions as we could to achieve wide J- and K- coverage of the rotational spectrum. We were able to assign transitions belonging to the ground vibrational state of the *gauche* conformer of 2-Cyanoethanol, as well as three excited states and the ground state of the *trans* conformer. In total over 6000 transitions have been assigned in this region, and the details of the spectrum and the fit for the various states are described in more detail next. Based on these fits, an entry for both *gauche*- and *anti*-2-Cyanoethanol was created for the JPL spectral line catalog, and can be found at `http://spec.jpl.nasa.gov`.

4.3.1 Ground Vibrational State for *Gauche*- and *Anti*-2-Cyanoethanol

The *gauche* conformer of 2-cyanoethanol is the global minimum on the potential energy landscape of this species, and for observational purposes the *gauche* conformer is thus most important as it provides the most intense lines in the spectrum. This is even more so the case at the lower temperatures (∼100-200 K) that characterize the rotational excitation conditions in most hot cores. In total, some 2502 transitions (including blends) were assigned

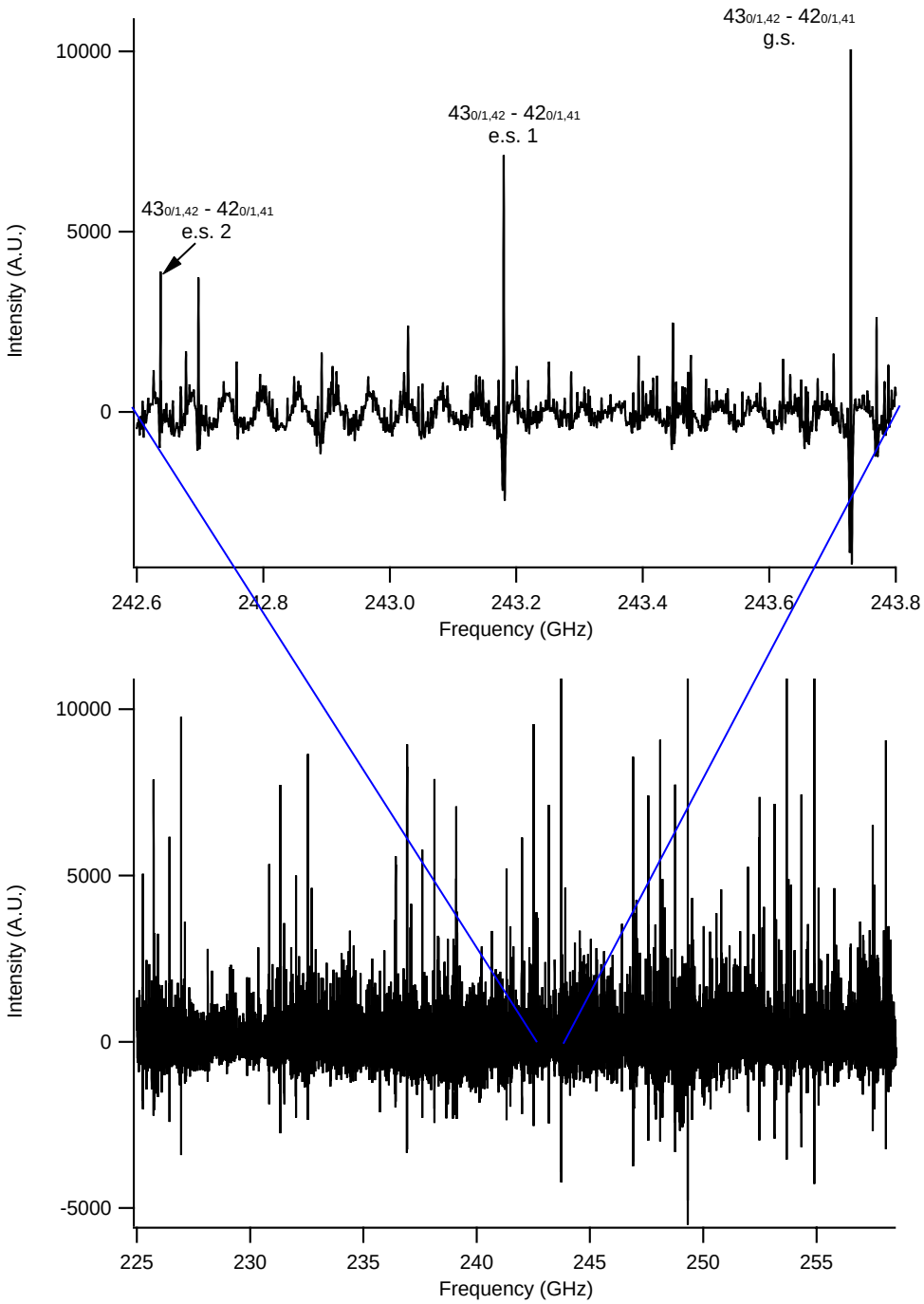

Figure 4.2: A scan of the rotational spectrum of 2-cyanoethanol from 225 to 258 GHz. Strong ^{a}R branches can be seen every ∼5.6 GHz, with red-shifted excited states clearly visible as well. The excitation pattern for the $43_{0/1,42}$ - $42_{0/1,41}$ transition is shown more closely in the inset. The high line density at weakest signal levels seen in the inset is indicative for this species, where much of the room temperature spectrum is essentially a line 'continuum.' The remaining sinusoidal baseline fluctuations are caused by etalons between the optical components of the spectrometer.

to 1454 spectral lines for the ground state of the *gauche* conformer, covering a continuous range in J from 11 to 84 and in K from 0 to 40. Another 61 transitions previously measured in the 15-40 GHz region [69] were included to anchor the fit at the low frequency end and to ensure that predicted frequencies of transitions between these regions have the required accuracy for observation. The rms of the fit was 92.9 kHz, which closely matches our expected experimental uncertainty of ∼100 kHz. Due to the density of the spectrum – some parts of the spectrum form essentially a line continuum – blending of lines has to be carefully considered in the fitting procedure. Even when a line looks clean and symmetric it can still hide blending underneath, for which the linewidth can then be used as an indicator. Generally, lines in the spectrum are about ∼1.2-1.3 MHz wide, so when a line with a width closer to ∼1.8-2.0 MHz (or wider) is seen it is likely to the combination of several, blended, transitions.

Fortunately, the extremely wide coverage of the data and the many intense lines enables an accurate fit to be made. Obvious blends can be excluded "by eye", and an option in SPFIT to leave out transitions that are more than a certain number of standard deviation removed from the experimental uncertainty can be further eliminated. We chose 3 standard deviations, so lines frequencies more than 0.3 MHz removed from their predicted values were excluded as well. Using this method only 22 out of the 2502 newly measured lines were excluded, showing the quality of the data and the fit. Closer visual inspection of the excluded transitions showed in each case that blending is indeed likely and resulted in only small errors relative to the prediction (generally under 0.5 MHz). Thus, the predictions of the fit to the *gauche* conformer can be considered to be accurate over the entire millimeter region up to 360 MHz for the full range of J's and K's we have covered here. This coverage extends well beyond the Boltzmann peak, and so the lines most likely to be detected toward

Table 4.1: Spectroscopic parameters for the ground vibrational state of 2-cyanoethanol

	gauche-conformer		*trans*-conformer	
Parameter	This work	Marstokk85	This work	Marstokk85
# of transitions	2502	220	755	19
A	10726.45630(108)	10726.4535(36)	26656.85(43)	26627.8(243)
B	3432.310915(279)	3432.3084(11)	2336.58835(235)	2336.5773(39)
C	2815.606794(305)	2815.6978(15)	2208.81951(218)	2208.8476(39)
-Δ_J(kHz)	4.878082(108)	4.8684(54)	0.448541(212)	0.449(27)
-Δ_{JK}(kHz)	-29.02150(101)	-29.091(46)	-16.1429(42)	-15.46(70)
-Δ_K(kHz)	80.2471(48)	80.212(24)	479.0(208)	
-δ_J(kHz)	1.4945691(280)	1.4939(34)	0.056395(266)	
-δ_K(kHz)	10.56645(109)	10.61(12)	2.483(34)	
H_J(Hz)	0.0147946(138)	0.0434(41)	0.0004893(174)	
H_{JK}(Hz)	0.070757(301)	0.379(72)	-0.04604(185)	
H_{KJ}(Hz)	-1.09796(143)	-0.369(53)	0.7218(162)	
H_K(Hz)	2.9708(85)	2.698(36)	1348.0(2940)	
h_J(Hz)	0.0067636(35)		0.0001392(225)	
h_{JK}(Hz)	-0.017433(191)			
h_K(Hz)	1.46446(266)			
L_{JK}(mHz)	-0.0007870(214)			
L_{JJK}(mHz)	-0.011141(173)			
L_{KJ}(mHz)	0.07166(45)			
L_K(mHz)	-0.1445(48)			

dense clouds are now well characterized.

The spectrum contains several interesting general patterns that were used as a guide in assignments and can play a similar role in observational studies. The b-dipole of *gauche* 2-cyanoethanol, at 2.544 D, is the largest component of the permanent dipole moment, but is followed closely by the a-dipole projection at 1.844 D [69]. Thus, the low-K a- and b-R transitions are the strongest lines in the spectrum, with the R branches spaced by ∼5.7 GHz throughout the entire region scanned. Assymetry splitting plays a prominent role in these transitions, as the low K energy levels adjacent in K_a move toward each other and eventually become fully degenerate as J increases. This causes a highly characteristic collapsing quartet pattern in the spectrum, and as the levels become fully degenerate the transitions merge into a single line with a summed intensity from the individual components. Aspects of this line merging process are illustrated in Fig. 4.3. The point at which these transitions merge

occurs at higher frequencies and higher values of J as K increases. In theory, this general pattern combined with the location of the Boltzmann peak should give the lowest detection limits at higher millimeter-wave frequencies. However, since spectral line confusion in hot cores leads to difficulty in assigning new transitions, the 3 mm spectral window might prove better suited to 2-cyanoethanol searches than the 1 mm atmospheric spectral window. Lastly, the large b-dipole also causes strong Q branches with easily recognizable branch heads that are spaced by ∼15 GHz throughout the millimeter-wave region.

The spectrum was fit to a standard Watson A-type assymetric top Hamiltonian. The high J and K coverage in the data sets allowed us to determine distortion constants up to the octic level with good confidence. The results of the fit are shown in Table 4.1, and as can be seen they match the results of the original microwave studies quite well.

The *anti* or *trans* conformer of 2-cyanoethanol can also be seen in the spectrum. This conformer was determined to lie 2.7 kJ/mole higher in energy than the ground state, but has several advantages over its *gauche* counterpart in terms of assigning and fitting the spectrum. The *anti* conformer is a nearly symmetric top (the Ray's asymmetry parameter, κ, is -0.99), with the dipole almost exclusively along the a-axis (μ_a estimated at 3.5 D versus 0.2 D for μ_b). The result is a relatively intense yet simple spectrum characterized by a-R branches that pile up at medium to high values of K. We were able to assign 755 such transitions ranging in J from 49 to 75 and K from 0 to 22. These transition were fit to a standard Watson-A type asymmetric Hamiltonian including distortion up to sextic order, with an rms of 105 kHz, again closely matching our expected experimental uncertainty. The results of the fit are shown in Table 4.1.

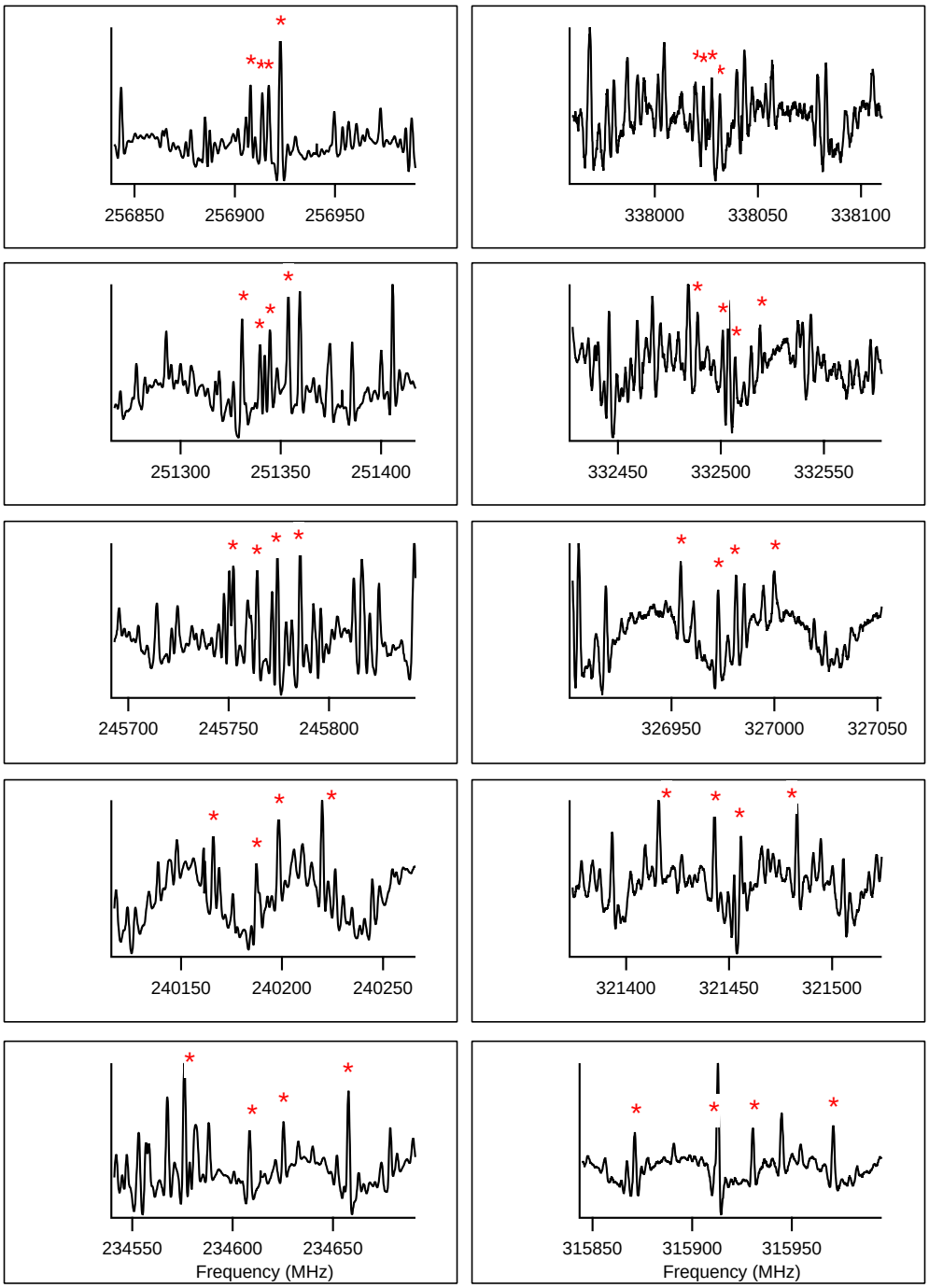

Figure 4.3: Loomis Wood plots of the K_a = 3,4 asymmetry quartet from J_{upper} = 39 to 43 (left panels), and of the K_a = 5,6 quartet from J_{upper} = 52 to 56 (right panels). These plots show the increase in asymmetry splitting with K_a, which cause the quartets to collapse at higher J values and higher frequencies for higher K_a values.

4.3.2 Excited States

Many intense lines beyond those assigned to the ground state exist in the spectrum, and using similar patterns to those described above for the ground state and predictions based on the study of Marstokk and Mollendal [69] we were able to assign a large fraction of the remaining transitions to several excited states. The lowest lying vibrational state has been assigned to torsions along the CH_2-CH_2 bond (with the OH and CN groups rocking relative to eachother) and estimated to lie at 108 ± 10 cm^{-1} [69]. Using a prediction from [69], we were able further assign 1877 new transitions to 1132 lines in the spectrum. Again fitting these to a Watson A-type assymetric top Hamiltonian, we were able to determine distortion constants up to octic order similar to the ground state and a rms to the fit of 113.6 kHz. As before, a cut-off line position error was chosen, this time at 4 standard deviations, to exclude blended lines. This led to only 11 transitions being left out of the final suite of assignments, once again showing the quality of the data. The results of the fit are shown in Table 4.2, which includes the results for each of the excited states assigned in this work.

As can be seen in Table 4.2, we were able to assign significantly fewer lines and achieve lower quality fits for higher excited states. Several factor contribute to this result. An important aspect is obviously the generally decreased intensity of the transitions from these states, which makes clear assignments, especially for the more weakly allowed transitions for each state, increasingly difficult in the highly congested and blended room temperature spectrum. Another important factor however, is that there appears to be an interaction between the first overtone of the C-C torsional state and the fundamental of the C-O torsional mode. For a rough comparison, doubling the energy of the fundamental C-C torsional mode at 108 ± 10 cm^{-1} puts it close to the estimated energy for the fundamental C-O torsional mode at 183 ± 30 cm^{-1}, with considerable overlap between the error bars.

Table 4.2: Spectroscopic parameters for excited vibrational states of *gauche*-2-cyano-ethanol

Parameter	grnd. st.	C-C tors.	1st overt. C-C tors.	C-O tors.
# of transitions	2502	1877	223	593
A(MHz)	10726.45630(108)	10810.29832(202)	10895.7756(171)	10729.13158(285)
B(MHz)	3432.310915(279)	3423.69001(71)	3414.518(37)	3435.0401(46)
C(MHz)	2815.606794(305)	2808.86935(84)	2802.5872(80)	2817.5944(55)
-Δ_J(kHz)	4.878082(108)	4.72291(33)	4.6776(42)	4.81110(181)
-Δ_{JK}(kHz)	-29.02150(101)	-29.08890(166)	-30.335(58)	-29.6994(70)
-Δ_K(kHz)	80.2471(48)	84.0032(123)	89.189(146)	81.9921(127)
-δ_J(kHz)	1.4945691(280)	1.447993(106)	1.35697(285)	1.47973(130)
-δ_K(kHz)	10.56645(109)	10.9491(84)	12.632(46)	13.451(47)
H_J(Hz)	0.0147946(138)	0.012810(58)	0.03427(62)	-0.00506(40)
H_{JK}(Hz)	0.070757(301)	0.07125(215)	-0.381(39)	-0.1634(98)
H_{KJ}(Hz)	-1.09796(143)	-1.1518(86)	-1.423(74)	-0.745(39)
H_K(Hz)	2.9708(85)	3.2498(315)	4.655(224)	4.0383(314)
h_J(Hz)	0.0067636(35)	0.0058271(220)		-0.001413(234)
h_{JK}(Hz)	-0.017433(191)	-0.03515(211)		0.5071(126)
h_K(Hz)	1.46446(266)	1.435(42)		-1.241(196)
L_J(mHz)				
L_{JK}(mHz)	-0.0007870(214)			
L_{JJK}(mHz)	-0.011141(173)	-0.00884(40)		
L_{KJ}(mHz)	0.07166(45)	0.06949(111)		
L_K(mHz)	-0.1445(48)	-0.1652(280)		

The spectrum also shows clear evidence of repulsive interactions for both states, and we were not able to fit either state to high accuracy using only a single state/asymetric-top Hamiltonian including centrifugal distortion. Many of the branches we did manage to successfully assign can be seen to diverge rapidly away from the basic prediction, and due to low intensity of many of these lines and the congested conditions of the spectrum we did not manage to fully describe the suspected interaction between the two excited torsional states. Detailed, multi-state fits are also beyond the scope of this paper, as these lines are of much lower intensity and thus of lesser importance for observational searches. Excluding assigned transitions beyond the point where they diverge from the prediction(s), we were able to fit the basic patterns of both states; including both a- and b-R transitions with $K_a \leq 4$, several series of b-R transitions with $8 \leq K_a \leq 14$ for each excited state, as well as the full set of Q branches with $15 \leq K_a \leq 22$ for the C-O torsional mode. The results of both

fits are shown in Table 4.2. In total, we assigned 2693 lines belonging to excited states, compared to 181 in the original study by Marstokk and Mollendal [69]

4.4 Discussion

The rotational spectrum of 2-cyanoethanol has been characterized up to 350 GHz. Over 6000 new assignments were made as part of this study, and they include transitions assigned to both the *gauche* and *anti* conformers for this molecule. Assignments further include several excited states for the lowest lying conformer, *gauche* 2-cyanoethanol: the C-C torsional fundamental mode and its first overtone as well as the C-O torsional fundamental mode. All states were fit to a standard Watson-A assymetric top Hamiltonian, and we were generally able to describe most of the spectrum to experimental accuracy including only effects due to distortion. The main exception is for the first overtone of the C-C torsional mode and the fundamental C-O torsional mode, the spectra of which show evidence of repulsive interactions between these two states. This interaction was not fully described, but the general description of the rotational spectrum presented here is more than sufficient as a guide for observational searches for 2-cyanoethanol. Observational studies of this molecule in the galactic center region SgrB2 are now underway, and the preliminary results from this search will be presented in Chapter 6.

Looking toward future THz studies in the laboratory and with Herschel (or SOFIA), the torsional modes of 2-cyanoethanol should provide intense bands between 100 and 200 cm^{-1} that lie within the range accessible by the Photodetector Array Camera and Spectrometer (or PACS). The doppler widths of individual lines at these frequencies will be substantially larger than those for the hot bands studied here, leading to an even more blended spectrum than that presented here. As a result, the present work provides rotational and distortion

constants for the excited states that are $\sim$10$\times$ more precise than those which can be obtained with direct studies in the far-infrared. Combined fits, in which the band origins and state interactions are fixed by THz measurements and the rotation-distortion constants by microwave through millimeter-wave pure rotational spectroscopy, will provide the most robust characterization of the structure and large amplitude dynamics in 2-cyanoethanol.

Chapter 5

The Millimeter-Wave Spectrum of Methoxyacetonitrile

5.1 Introduction

As part of an effort to study the chemistry of molecules containing a cyano (CN) group in regions of star formation, we undertake here an analysis of the microwave → millimeter-wave spectrum of methoxyacetonitrile (CH_3OCH_2CN). Methoxyacetonitrile is a structural isomer of 2-Cyanoethanol ($OHCH_2CH_2CN$), the spectrum of which we presented in Chapter 4 (and in [70]). By comparing observational results for these and related molecules, the hope is to improve our understanding of the chemistry of cyano-molecules and to examine wether this class of molecules follows the same general patterns as has been proposed for other classes of molecules in the models of Garrod et al. on the coupled gas-grain chemistry in the warm-up phase of star formation [28, 26]. These models do not consider cyano-molecules in much detail, so expanding the range of such species could lead to an interesting test of the principles proposed therein and a more detailed exploration of the set of reactants and reactions that are involved in the chemistry of icy grain mantles. For example, methoxyacetontrile substitutes a methyoxy group for the amino group in the detected interstellar molecule amniocetonitrile [32]. Ammonia and methanol are abundant components of grain mantles,

and so a comparison of the abundances of aminoacetonitrile and methoxyacetonitrile should shed light on the production and relative reactivity of radicals in ices.

The microwave spectrum of methoxyacetonitrile had been previously studied between 8-40 GHz, and was found to have both *gauche* and *trans* conformations in the gas phase [71]. Like 2-cyanoethanol, the *gauche* conformer was found to be the global minimum, lying 5.7 kJ/mole lower in energy than the *trans* conformer, one of several similarities between these two molecules. Several excited states for the *gauche* conformer were also found in the original study, and all of these results were used as a basis for the starting the investigations outlined in this Chapter. The relative energies of the two conformers and the torsional mode can be seen in Fig. 5.1. We extended the assignments through the 1 mm window and identified both conformers as well two excited states of *gauche* conformer. The results of the assignments and fitting of the spectrum are discussed below.

5.2 Experimental Section

Millimeter data for methoxyacetonitrile were measured over the entire 225-360 GHz spectral window of our flow cell spectrometer. The instrumental configuration we used was the same as for our study of cyanoethanol [70]. Methoxyacetonitrile was obtain commercially from Sigma Aldrich, and is a clear liquid with a very high vapor pressure. As a result it was easy to obtain a gas phase spectrum, balancing a very slightly opened needle valve to the flask with the full pumping speed of the vacuum system. Sample pressure in the 60-100 mTorr range was maintained, optimizing signal while minimizing pressure broadening. Like cyanoethanol, the data for methoxyacetonitrile contains many thousands of spectral lines, the general features of which are described in the following section.

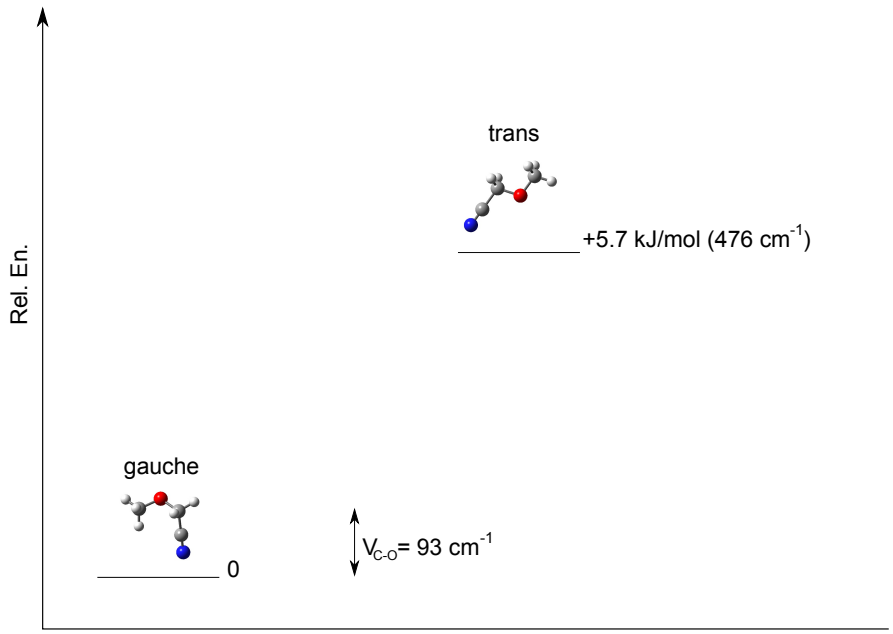

Figure 5.1: The relative energies of the two lowest energy conformers of cyanoethanol. The global minimum for this species is the *gauche*-conformer, with the *trans*-conformer 5.7 kJ/mol higher in energy. Also indicated is the relative energy of the first torsional mode of the *gauche*-conformer, the torsion along the central C-C bond at 93 cm^{-1}. We identified ground state rotational transitions for both the *gauche*- and *anti*-I conformers in this study. In addition we identified transitions from the fundamental and first overtone of the C-C torsional mode.

5.3 Results and Data Analysis

Methoxyacetonitrile contains a methyl group, but with a high barrier(at 810 cm^{-1} [72]) and no *A*-*E* splittings were observed, which is consistent with the lack of splittings at microwave frequencies for this species [71]. Thus, the analysis proceeded much as described for 2-cyanoethanol in Chapter 4. A combination of the SPFIT/SPCAT programs with the SMAP visualization tool [60] and the CAAARS program suite [61] were used to assign the data. The main R and Q branches were generally first assigned in CAAARS due to the useful feature of the Loomis-Wood plots, followed by a more methodical walk-through using SMAP where finer details of the spectrum are more easily accessible. We were able to assign a total of nearly 7400 transitions to 3380 spectral features, belonging to both *gauche* and

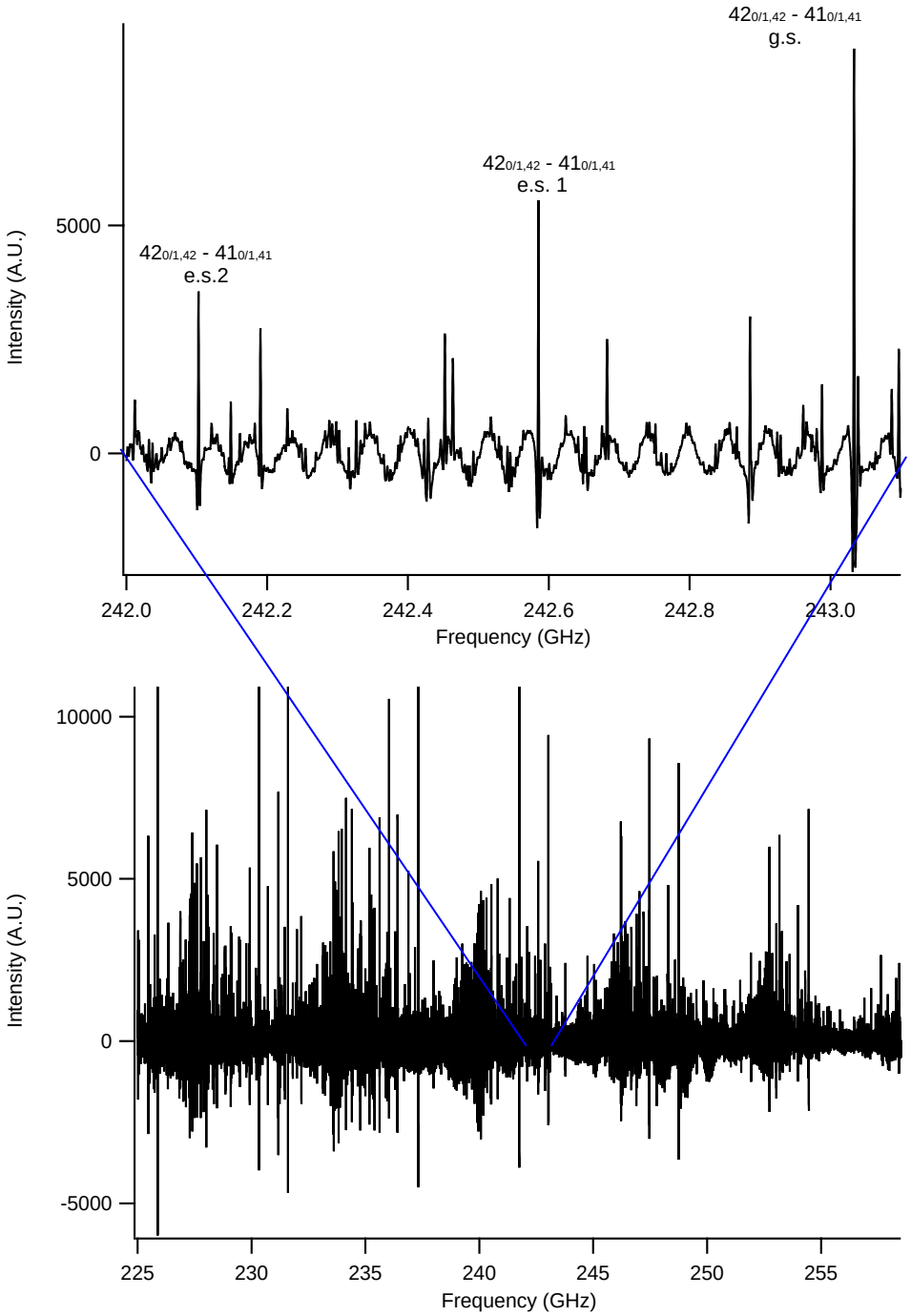

Figure 5.2: A section of the rotational spectrum of methoxyacetonitrile from 225 to 258 GHz. Strong ^{a}R branches can be seen every ∼5.8 GHz, with the distinctive branch head patterns at mid-K to the left of the most intense low-K transitions. Red-shifted excited states are clearly visible as well, with the excitation pattern for the $43_{0/1,42}$ - $42_{0/1,41}$ shown more closely in the inset. As with cyanoethanol, much of the spectrum of methoxyacetonitrile is essentially a line continuum. The characteristic high line density at weak signal levels can be seen in the inset, along with the residual instrumental fringing pattern.

trans conformers and several excited states. The spectrum has a high line density, in many parts forming essentially a line continuum, which leads to blending of many spectral lines. Combined with a high degree of degeneracy due to the lifting of asymmetry splitting, this leads to the high observed ratio of transitions assigned to relatively fewer spectral features. The features of each state and the fits are described in more detail below. Based on these fits, an entry for both *gauche*- and *anti*-2-Cyanoethanol was created for the JPL spectral line catalog, and can be found at `http://spec.jpl.nasa.gov`.

5.3.1 Ground State of *Gauche*- and *Trans*-Methoxyacetonitrile

From an observational perspective the ground state *gauche* conformer of methoxyacetronitrile is most important as it is will display the most intense lines under the conditions prevailing in dense clouds. Indeed, the relative difference between the ground and excited state conformers will be enhanced at the lower temperatures prevailing in most hot cores (T$\sim$100-200 K) as compared to the room temperature spectrum we obtained in the lab. Over 3200 new transitions were assigned to the *gauche* conformer, covering a range in J from 10 to 75 and K_a from 0 to 43. The assigned data were fit to a standard Watson A asymmetric top Hamiltonian with distortion constants up to 8^{th} order. Due to the large amount of line blending in the spectrum, some care had to be taken in the fitting process. Obvious blends resulting in asymmetric line shapes can easily be identified by eye, but blending can also be hidden under a symmetric, apparently clean transition. As before with our analysis of the 2-cyanoethanol spectrum, we use the linewidth as a discriminator by assuming that lines with a width significantly higher than the standard FWHM$\sim$1.2-1.4 MHz are due to blending. SPFIT also has an automated option that allows one to exclude probable blends by excluding lines that are more than a certain number of standard deviations off from

the estimated laboratory uncertainty, which in our case is ∼0.1 MHz. Setting the cutoff at 3σ, only 68 out of 3260 lines were excluded from the fit, giving a final rms of 102.5 kHz. The small amount of exclusions and the matching of the rms to the expected experimental uncertainty are indications of the high quality of the fit. The parameters determined in the fit are shown in Table 5.1 and show a good match to the rotational constants and low order centrifugal distortion terms obtained in the microwave fit of [71].

As with the 2-cyanoethanol analysis, the methoxyacetonitrile spectrum contains several characteristic patterns that were both useful in assignment of the laboratory spectrum and that could be similarly useful from an observational point of view. Since the a-dipole for methoxyacetonitrile is the largest of the three projections, this leads to a-R branches being the dominant features in the spectrum. At low K_a these transitions are spread out over a fairly wide frequency range, with very clear asymmetry splitting patterns due to nearly degenerate K_a levels for low K_a. As J increases, the asymmetry splitting decreases and eventually the levels become fully degenerate. Similar to cyanoethanol [70], this results in a characteristic collapsing quartet patterns for these low K_a aR-branch transitions. An example of this is shown in Fig. 3.1. As K_a increases, the value of J at which the levels become degenerate also increases, leading to a larger asymmetry splitting with increasing K_a. For medium to high values of K_a, this pattern is no longer apparent and instead transitions pile up and form an obvious branch head pattern around K_a = 20-22. These general features repeat approximately every 6.3 GHz. A second characteristic feature is the appearance of Q branches, also with obvious branch heads, that are spaced by approximately 17 GHz. Since the b-dipole for this molecule is only about half the magnitude of the a-dipole, these Q branch are significantly (×4) weaker than the a-R branches, but still form a characteristic presence in the spectrum at sufficient signal-to-noise.

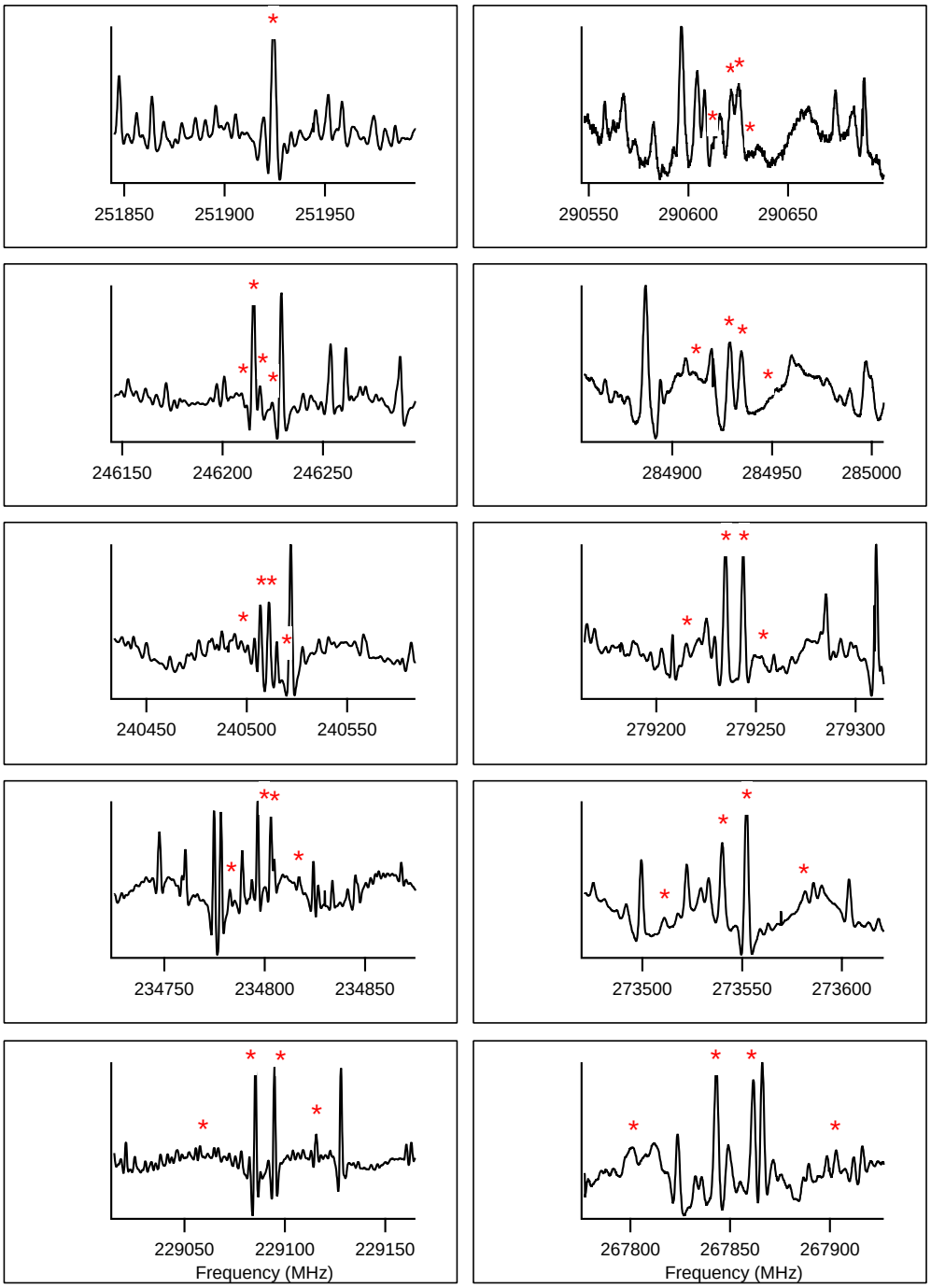

Figure 5.3: Loomis-Wood plots of the K_a = 2,3 asymmetry quartet from J_{upper} = 38 to 42 (left panels), and of the K_a = 3,4 quartet from J_{upper} = 44 to 48 (right panels). These plots show the increase in asymmetry splitting with K_a, which cause the quartets to collapse at higher J values and higher frequencies for higher K_a values. The intrinsically weaker *b*-type transitions (the marked outer pair) are increasingly difficult to distinguish at higher frequency due to a lower S/N.

Table 5.1: Spectroscopic parameters for the ground vibrational state of *gauche* and *trans* conformers of methoxyacetonitrile

	gauche-conformer		*trans*-conformer	
Parameter	This work	Kewley74	This work	Kewley74
# transitions	3263	34	203	38
rms (kHz)	102.5	330	221.7	not given
A	11893.73683(123)	11893.36(5)	29621.28(139)	29610(90)
B	3423.36198(41)	3423.26(2)	2470.96295(105)	2470.96(2)
C	2871.47309(42)	2871.53(2)	2348.09188(116)	23480.07(2)
-Δ_J(kHz)	3.424161(272)	2.93(40)	0.435632(137)	0.433(96)
-Δ_{JK}(kHz)	-23.90946(91)	-23.3(4)	-17.45084(155)	-17.9(2)
-Δ_K(kHz)	101.0630(56)		3087(86)	
-δ_J(kHz)	1.061232(88)			
-δ_K(kHz)	10.4079(46)			
H_J(Hz)	0.006565(85)			
H_{JK}(Hz)	0.05723(133)			
H_{KJ}(Hz)	-1.0446(49)			
H_K(Hz)	4.2132(79)			
h_J(Hz)	0.0027027(178)			
h_{JK}(Hz)	-0.03933(118)			
h_K(Hz)	1.3265(309)			
L_J(mHz)	-0.0000802(101)			
L_{JK}(mHz)				
L_{JJK}(mHz)	0.010014(162)			
L_{KJ}(mHz)	0.07135(38)			
L_K(mHz)				

The *trans* conformer of methoxyacetonitrile lies significantly higher in energy than the *gauche* conformer, so although the a-dipole for this conformer was previously estimated to have a large value (roughly 4.0 D, [71]), the spectrum of this conformer is significantly weaker than that arising from the ground state. Combined with the high density of the spectrum, it makes this spectrum more difficult to assign. We were finally able to start new assignments by locating the characteristic a-R branch heads consisting of the pileup of medium K_a transitions in the branches. Once these assignments, in the range of K_a from 6 to 14 and covering about 20 such branch heads were made, we were then able to 'pull in' many of the lower $K_a$transitions, extending the assigned range down to $K_a = 2$. Due the very low intensity and the spread out nature of these lowest K_a transitions, however, we

Table 5.2: Spectroscopic parameters for excited vibrational states of *gauche*-methoxy-acetonitrile

Parameter	grnd. st.	1	2
# transitions	3263	2814	1110
rms (kHz)	102.5	132.7	188.6
A	11893.73683(123)	11981.59685(216)	12078.6198(148)
B	3423.36198(41)	3415.67921(48)	3406.58195(78)
C	2871.47309(42)	2866.12194(49)	2860.37141(69)
-Δ_J(kHz)	3.424161(272)	3.503377(217)	3.581041(300)
-Δ_{JK}(kHz)	-23.90946(91)	-25.47488(154)	-27.2119(44)
-Δ_K(kHz)	101.0630(56)	113.3731(169)	129.722(236)
-δ_J(kHz)	1.061232(88)	1.091722(112)	1.120991(182)
-δ_K(kHz)	10.4079(46)	11.3381(79)	12.3434(129)
H_J(Hz)	0.006565(85)	0.005760(44)	0.004654(65)
H_{JK}(Hz)	0.05723(133)	0.09159(266)	0.1148(37)
H_{KJ}(Hz)	-1.0446(49)	-1.4437(101)	-1.3416(166)
H_K(Hz)	4.2132(79)	6.101(54)	15.49(162)
h_J(Hz)	0.0027027(178)	0.0026428(241)	0.002159(37)
h_{JK}(Hz)	-0.03933(118)	-0.05348(208)	-0.0802(33)
h_K(Hz)	1.3265(309)	1.827(65)	2.235(87)
L_J(mHz)	-0.0000802(101)		
L_{JK}(mHz)			
L_{JJK}(mHz)	0.010014(162)	-0.01260(33)	0.0519(76)
L_{KJ}(mHz)	0.07135(38)	0.11191(102)	-0.7315(237)
L_K(mHz)		-0.502(61)	14.4(40)

were not able to confidently extend all the way down to $K_a = 0$. The approximately 200 new assignments we made this way were again fit to a standard Watson A asymmetric top Hamiltonian, with only three distortion constants to 4th order included. The rms of the fit was 221.7 kHz and the results are shown alongside the *gauche* conformer in Table 5.1.

5.3.2 Excited States of *Gauche*-Methoxyacetonitrile

The first excited state of methoxyacetonitrile is the torsion along the O-CH_2 bond, and was found to lie at approximately 93 cm^{-1} [71]. Because of this low value, the first excited torsional state is significantly populated at room temperature. Indeed, the intensity of the pure rotational spectrum of the 93 cm^{-1} hot band is about 60-65 % of that of the ground state. As a result, we were able to assign a great amount of detail in the spectrum of this

state. Over 2800 new transitions were assigned, with similar J and K coverage as the ground state, namely J running from 11 to 72 and K_a from 0 to 38. The lines were again fit to a standard Watson A asymmetric top Hamiltonian, including distortion constants up to 8th order. Setting the cutoff for exclusion of blends this time to 4 standard deviations, only 62 of the cataloged lines were not included in the final fit. A rms of 132.7 kHz was achieved, again close to our experimental uncertainty although not as good as that achieved for the ground state. The results of the fit are shown in Table 5.2.

The second excited state is the overtone of O-CH_2 torsional fundamental, with intensities now only approximately 35% of the ground state lines at room temperature. The lower signal-to-noise prevented the same level of detail in assignments as the first excited state, but we were still able to assign over 1100 new transitions, with the J coverage extending from 10 to 60, that for K_a from 0 to 29. The fit for this state includes distortion up to 8th order, and a rms of 188.6 kHz was achieved. The results for this fit are also presented in Table 5.2. The spectral patterns for both excited states are similar to that of the ground state for this conformer, and unlike the situation for the higher excited states of 2-cyanoethanol there are no apparent interactions between states for methoxyacetonitrile.

5.4 Discussion

The rotational spectrum of CH_3OCH_2CN has been characterized up to 350 GHz. Nearly 7400 new transitions were assigned, belonging to the ground state *gauche* and the excited state *trans* conformers, as well as 2 excited torsional states for the *gauche* conformer. No repulsive interactions between states were apparent in the spectrum, and all states were fit to standard Watson-A asymmetric top Hamiltonians. The fit is close to experimental accuracy for the ground state of the *gauche* conformer, with RMS values that increase gradually

for the excited torsional states and the *trans* conformer. The characterization presented here is more than sufficient as a guide for microwave → millimeter-wave observational searches for this molecule, which are currently underway for the galactic center region hot core SgrB2(N) and which will be presented in Chapter 6. Finally, the high precision rotational and distortion constants for the excited states will be of great utility in combined THz/millimeter-wave studies of the far-infrared torsional bands of this molecule. Such bands offer a new route to searching for complex species in the interstellar medium, now that the Herschel Space Telescope is safely on its way to the L2 point beyond the Earth's orbit.

Chapter 6

Search for Interstellar Cyanoethanol and Methoxyacetonitrile: Insights into Cyano-Chemistry

6.1 Introduction

It has become increasingly clear in recent years that the inclusion of a variety of different pathways and effects are needed to give a coherent explanation of the patterns of complex organic chemistry seen in the dense cores of molecular clouds where stars are born. Beyond the gas phase and solid-state dust grain chemical pathways in quiescent clouds that have been the subject of study for nearly four decades, the driving potential of both UV photons and highly energetic cosmic-rays and the coupling between gas phase and solid state processes need to be considered. In particular, it has become clear that the coupling between gas phase and dust grain chemistry is stronger and more complex than previously thought. Instead of two essentially independent reservoirs with a sudden onset of coupling when the star 'switches on' and dust grain volatiles enter the gas phase, the warming of the dust grains as the star is being formed is likely a more gradual event that steadily increases the temperature of the dust grains, affecting both the chemistry in and on the grain and

the coupling between solid and gas phases [28, 26]. A slower, more gradual increase of the grain temperature allows increased mobility and reactivity of a variety of chemical species, resulting in an increased opportunity for chemical maturation of dust grain species prior to entering into the gas phase. Ongoing waves of star formation can mix the material from one region of dense clouds to another, further driving the levels of molecular complexity that can be attained long before planetary surfaces are made.

Furthermore, even the 'simple' solid-state dust grain chemistry in isolated, cold dense clouds is no longer thought to be limited to the tunneling of mobile hydrogen atoms through the barriers associated with stable molecules such as carbon monoxide (and the subsequent reaction with additional atoms [22]), but to also include cosmic-ray driven processes. The energy ($\sim$MeV) of these particles is too high to couple directly to the chemistry on dust grains, but their collision with a dust grain can release a cascade of thermal electrons at milder energies ($\sim$keV) that have been experimentally shown to be capable of affecting dust grain chemistry by cleaving molecular bonds and creating reactive intermediates that can then form new species [24]. These species can then react with each other (and with species formed through traditional tunneling processes) either in the pores left behind in the ice as the cosmic-ray travels through the dust grain [25], or as they become mobile with increasing grain temperature [28].

Chemical models of star forming regions that include such processes and a gradual rather than sudden heating have shown to be capable of predicting the abundance ratios of molecular isomers that were previously difficult to explain with either gas phase reaction networks alone or the 'prompt' injection of simple, first generation icy grain mantle products into the gas phase [28, 26]. In addition, experimental studies on the processing of mixed ices with supra-thermal electrons found similar isomeric ratios as those predicted by the

revised gas-grain models [24]. These result show that cosmic-ray driven activation followed by diffusion and reaction as the ice heats up are likely to play a crucial role in the complex organic chemistry of star-forming regions. The next step in modeling the chemistry will be to expand the set of species and reactions included in these studies and the systematic comparison of observational results for structurally related molecules.

The pathways included in the latest full version of the warm-up chemical models are limited to radical species resulting from bond cleavage of the major ice components H_2O, CH_3OH and NH_3, as well as hydrogen tunneling additions to CO [26]; but there is no reason larger species resulting from similar processes should not also participate in grain mantle chemistry. Indeed, recent detections of the cyano-molecules aminoacetonitrile (NH_2CH_2CN) [32] and *n*-propyl cyanide ($CH_3CH_2CH_2CN$) [27], have prompted the expansion of a subset of pathways to more closely focus on cyanide chemistry. In these latest models, various pathways emanating from either CN or larger radicals containing a cyanide group were included in an attempt to explain the observed relative abundances of these and previously observed cyano-molecules. The version of the model that best explains the relative abundances of these molecules is that where the incorporation of CN into the growing structure is one of the *first* steps in the pathway, whereas the addition of the CN radical to larger structures is deemed unlikely [27].

In this study we investigate further expanding the set of potential pathways involving molecules containing a cyanide group by searching for the molecules 2-cyanoethanol ($OHCH_2CH_2CN$) and methoxyacetonitrile (CH_3OCH_2CN), and comparing the search results with the abundances of other cyano-containing molecules seen in dense molecular clouds. The rotational spectra of both 2-cyanoethanol and methoxyacetonitrile were recently characterized [70, 68] and are used as the basis for these observational searches. In

addition, potential chemical pathways and expected abundance are discussed and compared with observational and theoretical results.

6.2 Cyano-Chemistry

In the models of Belloche et al. [27], both aminoacetonitrile and n-propyl cyanide are suggested to be predominantly formed in pathways starting from CH_2CN, by addition of the NH_2 radical in the case of aminoacetonitrile and by the sequential addition of CH_2 and CH_3 in the case of n-propyl cyanide. To test these models, we consider these pathways in a broader chemical context. In particular, we focus here on the potential cross-linking of these pathways with the products of cosmic-ray induced photo-ionization of methanol. If the assumed pathways to amino acetonitrile and *n*-propyl cyanide [27] are correct, then there is no reason that such cross linking should not happen and in fact would seem likely as methanol is one of the major components of the ice mantles of interstellar dust grains. The two most likely pathways emanating from CH_2CN and cross-linked with methanol derivatives would be:

$$CH_3O + CH_2CN \rightarrow CH_3OCH_2CN \tag{6.1}$$

$$CH_2OH + CH_2CN \rightarrow OHCH_2CH_2CN \tag{6.2}$$

The two structural isomers formed in reactions (6.1) and (6.2), methoxyacetonitrile (CH_3OCH_2CN) and cyanoethanol ($OHCH_2CH_2CN$), therefore make for good subjects to test these models, as their relative ratio should be a reflection of the ratio of the photolysis/cosmic ray dissociation products of methanol. Experimental studies on the processing

of mixed CO:CH_3OH ices with supra-thermal electrons were not able to measure the ratio of CH_3O:CH_2OH directly, but did find an overproduction of methyl formate (CH_3OCHO) versus its isomer glycolaldehyde ($OHCH_2CHO$) by a factor of ∼55 [24] – indicating that CH_3O is the dominant dissociation product. This is in accordance with observational results that have found a ratio of methyl formate to glycolaldehyde of ∼52:1 [49]. If both of the molecules studied here are indeed formed by the pathways outlined above, we would therefore expect a similar overabundance of methoxyacetonitrile versus cyanoethanol.

Furthermore, the pathways to these molecules are very similar to the pathway leading to aminoacetonitrile (all are thought to be formed in reactions with CH_2CN as a starting material), and a comparison to the abundance of this molecule would thus provides a second test of the proposed scheme. The abundances of ammonia and methanol in interstellar ices are generally found to be within a factor of a few of each other [73, 74, 75, 76]. If CH_3O is indeed the dominant product of the photolysis of or supra-thermal electron driven dissociation of methanol, one would thus expect a similar fractional abundance of methoxyacetonitrile and amino acetonitrile. In fact, because the diffusion barrier of CH_3O (1250 K) is significantly lower than that of NH_2 (1978 K) [26], it may well be possible that methoxyacetonitrile could achieve a higher peak abundance than amino acetonitrile for sources in which methanol is a substantial grain mantle component.

There are, of course, other potential processes that can affect the abundances of these molecules, including alternative formation as well as destruction pathways that might favor one over another of these species. One set of potential alternative grain pathways to methoxyacetonitrile and cyanoethanol involve reactions of the CN radical with the photolysis products of dimethyl ether and ethanol:

$$CH_3OCH_2 + CN \rightarrow CH_3OCH_2CN \tag{6.3}$$

$$OHCH_2CH_2 + CN \rightarrow OHCH_2CH_2CN \tag{6.4}$$

In this scenario, the relative abundances of methoxyacetonitrile and 2-cyanoethanol would reflect the abundances of the isomers dimethyl ether and ethanol. Although the models of Belloche et al 2009 [27] deemed reactions involving the incorporation of the CN group into larger structures at a late stage unlikely versus pathways that include early incorporation, these reactions cannot be excluded offhand. Indeed, testing these models with an expanded set of both pathways and observational targets such as suggested here would make these claims more robust. Inclusion of the photolysis products of dimethyl ether and ethanol has also not considered previously, but there is no reason to assume that these molecules would be immune to bond cleavage by supra-thermal electrons. Systematic expansion of chemical models towards larger and more complex species would allow for more quantitative statements on the chemistry considered here; and in future should become one the main paths forward in better understanding the complex chemistry in star forming regions, particularly as observational data from next generation telescopes such as Herschel space observatory and the Atacama Large Millimeter Array (ALMA) becomes available. The searches in this study represent a qualitative first attempt at investigating whether species as complex as methoxyacetonitrile and 2-cyanoethanol can be detected at millimeter-wave frequencies using ground based single dish telescopes.

Table 6.1: Spectroscopic parameters of cyanoethanol and methoxyacetonitrile

Parameter	Cyanoethanol Value	Methoxyacetonitrile
A (MHz)	10726.45630(108)	11893.73683(123)
B (MHz)	3432.310915(279)	3423.36198(41)
C (MHz)	2815.606794(305)	2871.47309(42)
-Δ_J(kHz)	4.878082(108)	3.424161(272)
-Δ_{JK}(kHz)	-29.02150(101)	-23.90946(91)
-Δ_K(kHz)	80.2471(48)	101.0630(56)
-δ_J(kHz)	1.4945691(280)	1.061232(88)
-δ_K(kHz)	10.56645(109)	10.4079(46)
H_J(Hz)	0.0147946(138)	0.006565(85)
H_{JK}(Hz)	0.070757(301)	0.05723(133)
H_{KJ}(Hz)	-1.09796(143)	-1.0446(49)
H_K(Hz)	2.9708(85)	4.2132(79)
h_J(Hz)	0.0067636(35)	0.0027027(178)
h_{JK}(Hz)	-0.017433(191)	-0.03933(118)
h_K(Hz)	1.46446(266)	1.3265(309)
L_J(mHz)		-0.0000802(101)
L_{JK}(mHz)	-0.0007870(214)	
L_{JJK}(mHz)	-0.011141(173)	0.010014(162)
L_{KJ}(mHz)	0.07166(45)	0.07135(38)
L_K(mHz)	-0.1445(48)	

6.3 Observations and Data Analysis

The two hot core regions Sgr B2(N) and Sgr B2(M) were observed with the IRAM 30 m telescope on Pico Valeta, Spain, over the course of a year, in January 2004, September 2005, and January 2005. A complete spectral survey of the 3 mm atmospheric window from 80 to 116 GHz was carried out, along with associated surveys in the 1.3 mm window between 201.8 and 204.6 GHz and between 205.0 and 217.7 GHz. Selected spectra in the 2 mm window and 1 mm window between 219 and 268 GHz were also obtained. The coordinates of the observed position for Sgr B2(N) are $\alpha_{J2000} = 17^h47^m20^s.0$, δ_{J2000} = -28 °22′19.0″ with a systemic velocity V_{lsr} = 64 km s^{-1} and $\alpha_{J2000} = 17^h47^m20^s.4$, δ_{J2000} = -28 °23′07.0″ with a systemic velocity V_{lsr} = 62 km s^{-1} for Sgr B2(M). Additional details about the observational setup and data reduction can be found in [32]. An rms noise level of 15-20

mK on the $T_a^\star$ scale was achieved below 100 GHz, 20-30 mK between 100 and 114.5 GHz, about 50 mK between 114.5 and 116 GHz, and 25-60 mK in the 2 mm atmospheric window. At 1.3 mm, the confusion limit was reached for most of the spectra obtained toward Sgr B2(N).

A central goal of the survey was to characterize as best as possible the molecular content of Sgr B2(N) and (M). The careful modeling of the emission of all known molecules in detail also facilitates the search for new species. The broadband nature of the data allows this to be done with high accuracy, because the emission of a target molecule can be modeled and compared with the observational data over the entire frequency space with the global model of known molecules as a reference. Claiming a detection of a new molecule is thus possible if all lines emitted by the target species are present in the data at the right intensity according to the model. The absence of even a single line in the observed spectrum signifies a non-detection for the species in question. In this case, an upper limit on the column density can be determined using the noise (or confusion) level at the line positions accurately known from previous laboratory work. The emission of both the known molecules and new targets are modeled using the XCLASS software (see [77]) in the local thermodynamic equilibrium (LTE) approximation, with source size, temperature, column density, velocity linewidth, and velocity offset with respect to the systemic velocity of the source as the free parameters (for more details on the modeling and analysis see [32, 27]).

6.4 Upper Limits of Methoxyacetonitrile and Cyanoethanol

The full millimeter-wave rotational spectra of both methoxyacetonitrile and cyanoethanol were recently characterized [70, 68], and these results were used as the basis for the observational study here. For both molecules the *gauche* conformer is lowest in energy by a

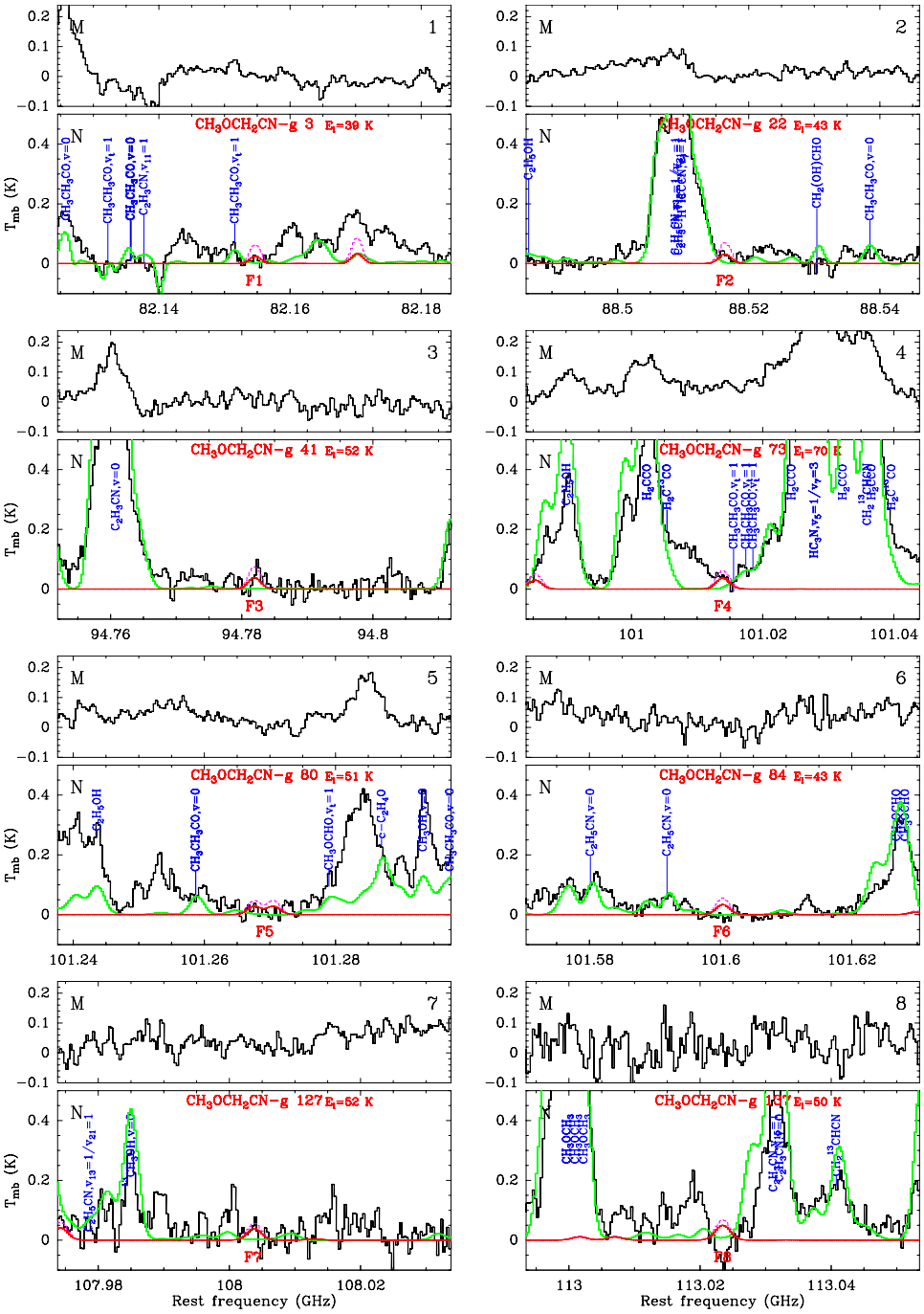

Figure 6.1: Transitions of the *gauche*-conformer of methoxy acetonitrile (CH_3OCH_2CN-g) tentatively detected with the IRAM 30 m telescope or missing. Each panel consists of two plots and is labeled in black in the upper right corner. The lower plot shows in black the spectrum obtained toward Sgr B2(N) in main-beam brightness temperature scale (K), while the upper plot shows the spectrum toward Sgr B2(M). The rest frequency axis is labeled in GHz. The systemic velocities assumed for Sgr B2(N) and (M) are 64 and 62 km s^{-1}, respectively. The lines identified in the Sgr B2(N) spectrum are labeled in blue. The top red label indicates the CH_3OCH_2CN-g transition centered in each plot (numbered like in Col. 1 of Table 6.2), along with the energy of its lower level in K (E_l/k_B). The bottom red label is the feature number (see Col. 8 of Table 6.2). The green spectrum shows our LTE model containing all identified molecules, but not CH_3OCH_2CN-g. The LTE synthetic spectrum of CH_3OCH_2CN-g alone is overlaid in red, and its opacity in dashed violet. All observed lines which have no counterpart in the green spectrum are still unidentified in Sgr B2(N).

Table 6.2: Transitions of the *gauche*-conformer of methoxy acetonitrile tentatively detected or missing toward Sgr B2(N) with the IRAM 30 m telescope.

N^a	Transition	Frequency (MHz)	Unc.^{b} (kHz)	$E_l{}^c$ (K)	$S\mu^2$ (D^2)	σ^d (mK)	F^e	τ^f	$I_{obs}{}^g$ (K km s^{-1})	$I_{mod}{}^g$ (K km s^{-1})	$I_{all}{}^g$ (K km s^{-1})	Comments
(1)	(2)	(3)	(4)	(5)	(6)	(7)	(8)	(9)	(10)	(11)	(12)	(13)
3	$13_{6,8} - 12_{6,7}$	82154.546	8	39	59	19	1	0.06	0.16(08)	0.19	0.14	Candidate group, partial blend with CH_3CH_3CO, v_t=1
4	$13_{6,7} - 12_{6,6}$	82154.817	8	39	59	19	1	–	–	–	–	–
22	$14_{6,9} - 13_{6,8}$	88516.044	8	43	66	17	2	0.07	0.65(07)	0.25	0.37	Candidate group, partial blend with C_2H_5CN, v_{13}=1/v_{21}=1 and $H^{13}CCCN$, v_7=1
23	$14_{6,8} - 13_{6,7}$	88516.682	8	43	66	17	2	–	–	–	–	–
41	$15_{7,9} - 14_{7,8}$	94781.913	8	52	68	28	3	0.07	0.44(12)	0.29	0.01	Candidate group
42	$15_{7,8} - 14_{7,7}$	94781.948	8	52	68	28	3	–	–	–	–	–
73	$16_{9,7} - 15_{9,6}$	101013.914	9	70	63	21	4	0.06	0.65(08)	0.28	0.21	Candidate group, partial blend with U-line and CH_3CH_3CO, v_t=1
74	$16_{9,8} - 15_{9,7}$	101013.914	9	70	63	21	4	–	–	–	–	–
75	$31_{5,27} - 30_{6,25}$	101015.693	19	157	7	21	4	–	–	–	–	–
80	$16_{6,11} - 15_{6,10}$	101267.615	8	51	79	21	5	0.05	0.32(10)	0.42	0.07	Candidate group, uncertain baseline
81	$16_{6,10} - 15_{6,9}$	101270.538	8	51	79	21	5	–	–	–	–	–
84	$16_{4,13} - 15_{4,12}$	101600.336	8	43	86	16	6	0.06	-0.03(06)	0.25	0.01	Missing line, but uncertain baseline?
127	$17_{5,12} - 16_{5,11}$	108003.802	9	52	89	46	7	0.06	0.46(17)	0.28	0.08	Candidate line, noisy
137	$18_{3,16} - 17_{3,15}$	113023.465	9	50	100	40	8	0.07	-0.04(15)	0.37	0.57	Missing line, but uncertain baseline?

Notes: ^{a} Numbering of the observed transitions associated with a modeled line stronger than 20 mK (see Table A.1). ^{b} Frequency uncertainty. ^{c} Lower energy level in temperature units (E_l/k_B). ^{d} Calculated rms noise level in T_{mb} scale. ^{e} Numbering of the candidate or missing features. ^{f} Peak opacity of the modeled feature. ^{g} Integrated intensity in T_{mb} scale for the observed spectrum (Col. 10), the methoxy acetonitrile model (Col. 11), and the model including all molecules except methoxy acetonitrile (Col. 12). The uncertainty in Col. 10 is given in parentheses in units of the last digit.

significant margin over the next lowest conformer, 5.7 kJ mol^{-1} in the case of methoxy-acetonitrile [71] and 2.7 kJ mol^{-1} in the case of cyanoethanol [69]. These conformers are therefore the focus of the present observational searches toward Sgr B2.

Both molecules have large dipole moments ($\mu_a = 1.8$ and $\mu_b = 2.5$ for cyanoethanol, $\mu_a = 2.4$ and $\mu_b = 1.4$ for methoxyacetonitrile) resulting in exceptionally rich and dense spectra. Because these molecules are strongly prolate tops (κ = -0.844 for cyanoethanol and κ = -0.878 for methoxyacetonitrile) and effects of internal rotation are not present, both spectra are well-behaved and can be accurately described using the parameters shown in Table 6.1. The rotational partition function merits some extra attention here due to the fact that both molecules have several low-lying torsional states. Accordingly, the inclusion of these states in the partition function is known to be important in correctly modeling the spectral

intensities of the room temperature laboratory spectra [70, 68]. Although the rotational excitations temperatures of typical hot core molecules are significantly lower than the 300 K conditions under which the laboratory spectra were measured, the inclusion of the excited torsional states has a significant impact on the magnitude of the partition function even at these temperatures. For example, the partition function for methoxyacetonitrile is 4.716×10^4 and 1.216×10^4 at 150 and 75 K, respectively, numbers that would be reduced to 2.864×10^4 and 1.013×10^4 if excited vibrational states are not considered. For cyanoethanol, the partition function is 5.371×10^4 and 1.265×10^4 at 150 and 75 K, respectively (3.042×10^4 and 1.076×10^4 if the far-infrared torsional states are excluded).

Although several possible spectral features associated with both molecules are seen in the observational data, the absence or marginal presence of many other spectral features leads us to conclude that neither of the two molecules were detected at the sensitivity levels achieved in this study. Results of the searches are listed in Tables 6.2 and 6.3. Searches were conducted by modeling the emission spectra of both molecules in the local thermodynamic (LTE) approximation, and the parameters we varied in the search were the rotational temperature and source size. The spectra were predicted assuming either a compact hot core emission (angular size = $2''$, as common for most hot core molecules) at both high and low rotational temperatures (T_{rot} = 200 K, 100 K, respectively) or an extended cold emission more commonly associated with a shocked region surrounding the dense molecular cloud (angular size = $60''$, T_{rot} = 15 K, as has been found for glycoaldehyde). None of the assumed conditions led to the detection of either of the species in Sgr B2(N) or (M), and upper limits were therefore determined for each set of conditions. The noise level, T_{MB}, was measured at each spectral position and a $\sim 3\sigma$ upper limit was calculated using Eq.

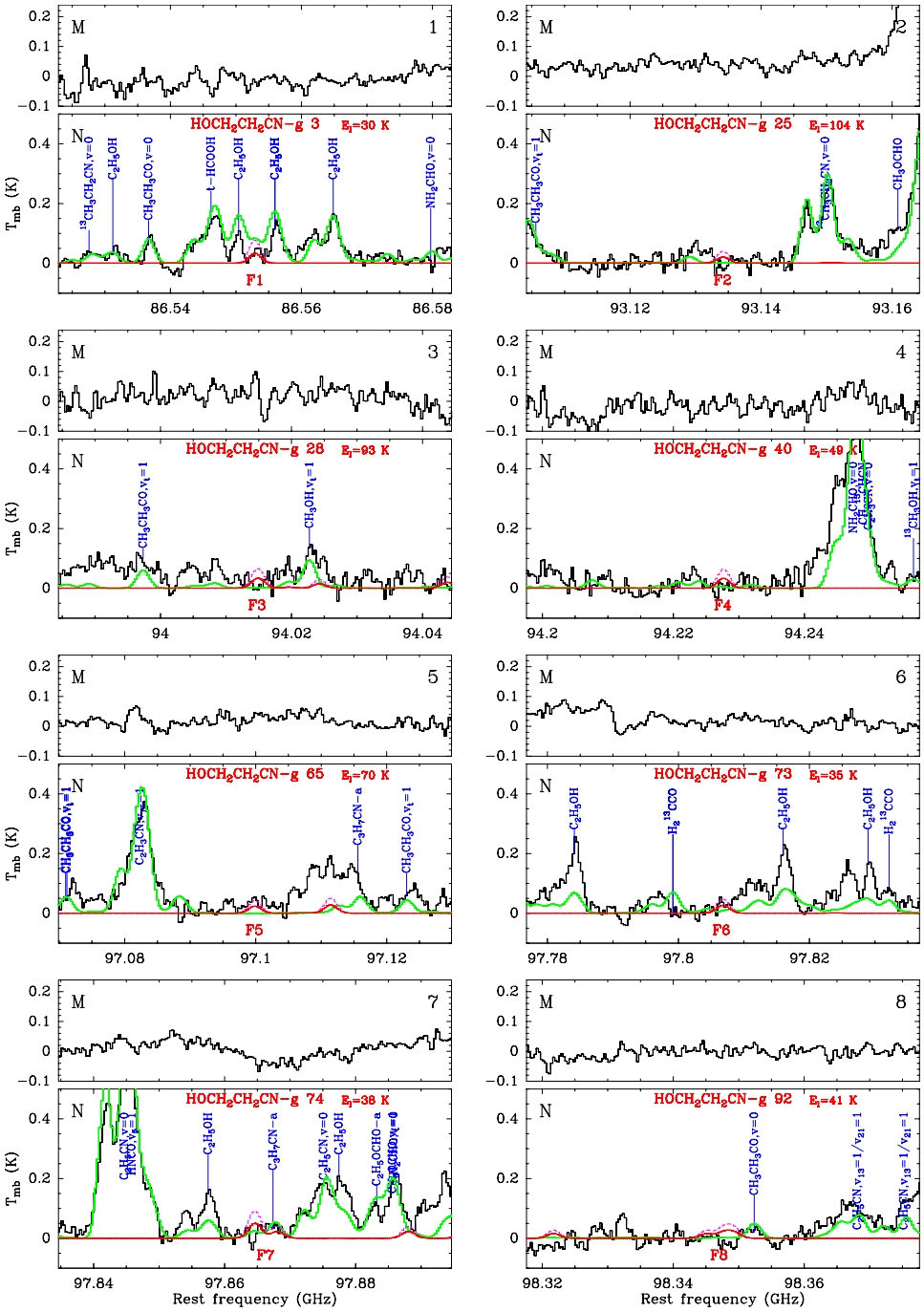

Figure 6.2: Transitions of the *gauche*-conformer of 2-cyanoethanol ($HOCH_2CH_2CN$-g) tentatively detected with the IRAM 30 m telescope or missing. Each panel consists of two plots and is labeled in black in the upper right corner. The lower plot shows in black the spectrum obtained toward Sgr B2(N) in main-beam brightness temperature scale (K), while the upper plot shows the spectrum toward Sgr B2(M). The rest frequency axis is labeled in GHz. The systemic velocities assumed for Sgr B2(N) and (M) are 64 and 62 km s^{-1}, respectively. The lines identified in the Sgr B2(N) spectrum are labeled in blue. The top red label indicates the $HOCH_2CH_2CN$-g transition centered in each plot (numbered like in Col. 1 of Table 6.3), along with the energy of its lower level in K (E_l/k_B). The bottom red label is the feature number (see Col. 8 of Table 6.3). The green spectrum shows our LTE model containing all identified molecules, but not $HOCH_2CH_2CN$-g. The LTE synthetic spectrum of $HOCH_2CH_2CN$-g alone is overlaid in red, and its opacity in dashed violet. All observed lines which have no counterpart in the green spectrum are still unidentified in Sgr B2(N).

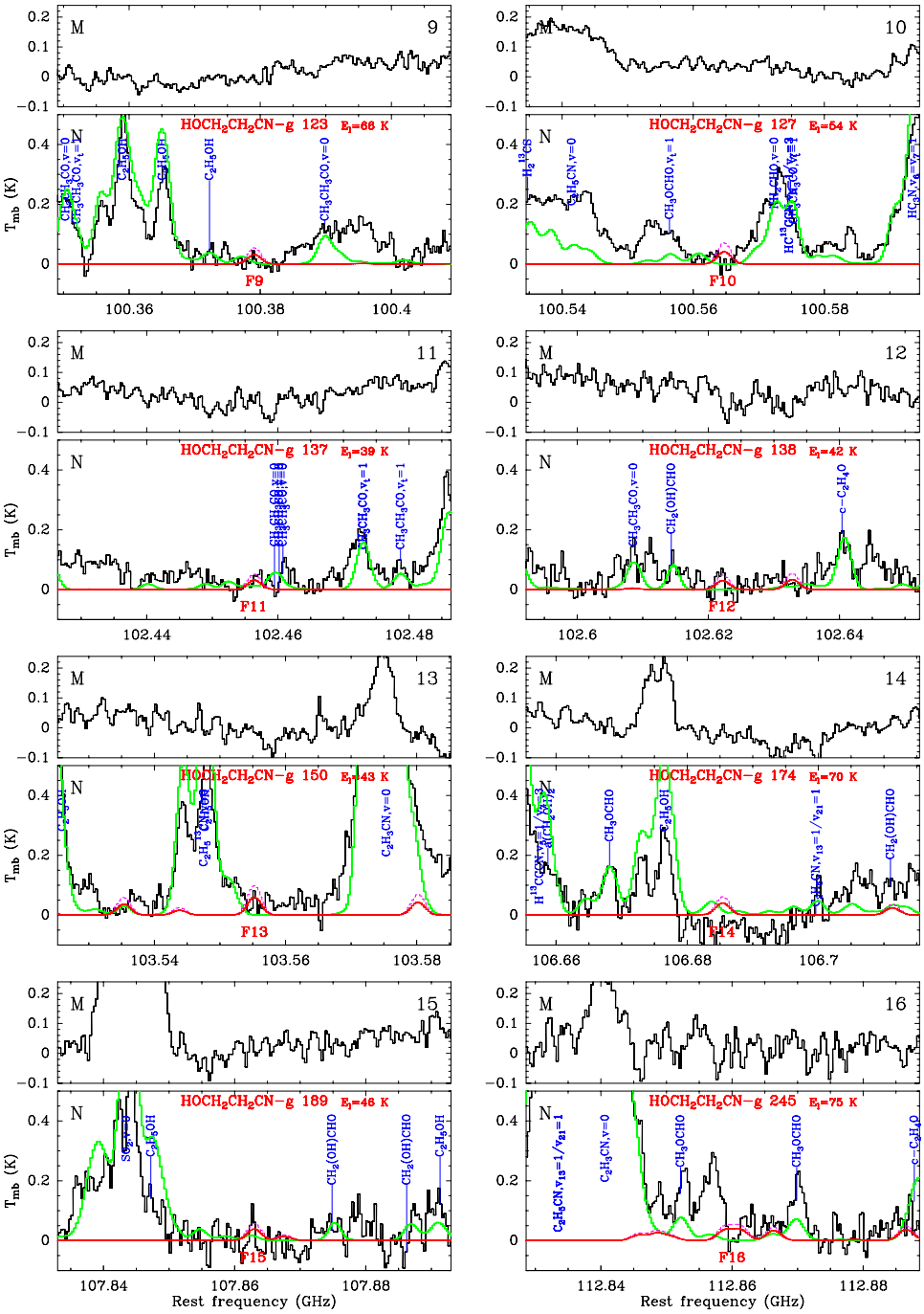

Figure 6.2: (continued)

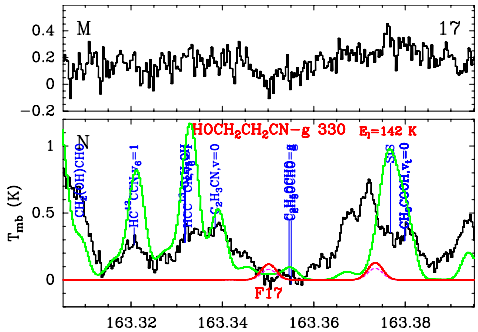

Figure 6.2: (continued)

(A5) of [31]:

$$ln\left(\frac{N_u}{g_u}\right) = ln\left(\frac{1.67W_T \times 10^{14}}{S\mu^2 B\nu}\right) = -\frac{E_u}{T_{rot}} + ln\left(\frac{N_T}{Q_r}\right) \tag{6.5}$$

where W_T is the integrated intensity in K km s^{-1} in main-beam brightness temperature scale, $S\mu^2$ is the line strength times the dipole moment squared in D^2, B the beam filling factor, ν the frequency in GHz, E_u the energy of the upper state in K, T_{rot} the rotational temperature in K, N_T the molecular column density in cm^{-2}, and Q_r the partition function. Even with the broad frequency coverage of the IRAM 30 m Sgr B2 surveys, there are only a handful of windows in which the intrinsic noise level of the scans are reached. More typically, limits to the possible fluxes of methoxyacetonitrile and 2-cyanoethanol lines must be found in the presence of substantial molecular emission from the myriad species that are present toward these hot cores.

Since neither molecule was detected in this study, the integrated intensities were approximated as arising from a line at the $\sim 3\sigma$ level, i.e. $3 \times T_{MB}$. We assumed the same line width (7.0 km s^{-1}) as the recently detected molecules aminoacetonitrile [32], n-propyl cyanide, and ethyl formate [27]. W_T was then calculated assuming a gaussian line shape, that is, $W_T = 1.064\ (3{\times}T_{MB})\ \Delta\nu$. The rotational temperature and the source size (which affects the so-called beam filling factor) were then varied as mentioned above, and the up-

Table 6.3: Transitions of the *gauche*-conformer of 2-cyanoethanol tentatively detected or missing toward Sgr B2(N) with the IRAM 30 m telescope.

N^a	Transition	Frequency (MHz)	Unc.^{b} (kHz)	$E_l{}^c$ (K)	$S\mu^2$ (D^2)	σ^d (mK)	F^e	τ^f	$I_{obs}{}^g$ (K km s^{-1})	$I_{mod}{}^g$ (K km s^{-1})	$I_{all}{}^g$ (K km s^{-1})	Comments
(1)	(2)	(3)	(4)	(5)	(6)	(7)	(8)	(9)	(10)	(11)	(12)	(13)
3	$15_{0,15} - 14_{1,14}$	86552.902	8	30	85	17	1	0.08	0.48(07)	0.25	1.43	Candidate group, blend with C_2H_5OH, uncertain baseline
4	$25_{17,8} - 26_{16,11}$	86554.133	15	199	6	17	1	–	–	–	–	–
5	$25_{17,9} - 26_{16,10}$	86554.133	15	199	6	17	1	–	–	–	–	–
25	$24_{7,17} - 24_{6,18}$	93134.179	11	104	87	22	2	0.04	0.10(09)	0.15	0.01	Missing line, but noisy and uncertain baseline?
28	$15_{13,2} - 14_{13,1}$	94014.420	7	93	13	31	3	0.07	0.31(13)	0.27	0.02	Missing group, uncertain baseline?
29	$15_{13,3} - 14_{13,2}$	94014.420	7	93	13	31	3	–	–	–	–	–
30	$28_{7,22} - 28_{6,23}$	94014.809	11	136	106	31	3	–	–	–	–	–
31	$15_{12,3} - 14_{12,2}$	94015.384	7	84	18	31	3	–	–	–	–	–
32	$15_{12,4} - 14_{12,3}$	94015.384	7	84	18	31	3	–	–	–	–	–
40	$15_{7,9} - 14_{7,8}$	94227.567	7	49	40	26	4	0.06	0.11(11)	0.25	0.09	Missing group, but uncertain baseline?
41	$15_{7,8} - 14_{7,7}$	94227.738	7	49	40	26	4	–	–	–	–	–
65	$19_{7,13} - 19_{6,14}$	97099.887	10	70	63	21	5	0.04	0.52(08)	0.17	0.00	Candidate line, blend with U-line?
73	$15_{3,12} - 14_{3,11}$	97806.800	7	35	49	20	6	0.05	0.50(08)	0.20	0.18	Candidate line, blend with C_2H_5CN, v_{13}=1/v_{21}=1 and C_2H_5OH
74	$17_{0,17} - 16_{1,16}$	97864.630	8	38	98	20	7	0.09	0.62(10)	0.54	0.63	Missing group, blend with C_3H_7CN
75	$16_{7,10} - 16_{6,10}$	97867.370	11	54	1	20	7	–	–	–	–	–
76	$16_{7,9} - 16_{6,10}$	97868.051	11	54	50	20	7	–	–	–	–	–
92	$13_{7,7} - 13_{6,7}$	98347.596	11	41	1	18	8	0.05	-0.07(10)	0.40	0.14	Missing group, blend with U-line and CH_3CH_3CO, uncertain baseline
93	$13_{7,6} - 13_{6,7}$	98347.629	11	41	36	18	8	–	–	–	–	–
94	$13_{7,7} - 13_{6,8}$	98349.265	11	41	36	18	8	–	–	–	–	–
95	$13_{7,6} - 13_{6,8}$	98349.298	11	41	1	18	8	–	–	–	–	–
123	$16_{9,8} - 15_{9,7}$	100379.093	7	66	37	24	9	0.05	0.02(10)	0.24	0.17	Candidate group, blend with CH_3CH_3CO, v_t=1, uncertain baseline
124	$16_{9,7} - 15_{9,6}$	100379.093	7	66	37	24	9	–	–	–	–	–
127	$16_{7,10} - 15_{7,9}$	100564.513	7	54	44	20	10	0.07	0.31(08)	0.31	0.08	Missing group, uncertain baseline?
128	$16_{7,9} - 15_{7,8}$	100564.925	7	54	44	20	10	–	–	–	–	–
137	$16_{2,14} - 15_{2,13}$	102456.406	7	39	53	30	11	0.05	0.36(12)	0.24	0.37	Candidate line, partial blend with CH_3CH_3CO
138	$16_{4,12} - 15_{4,11}$	102622.206	7	42	51	37	12	0.05	0.11(14)	0.22	0.00	Candidate line
150	$18_{1,18} - 17_{0,17}$	103555.237	8	43	104	27	13	0.10	0.93(11)	0.45	0.24	Candidate line, noisy
174	$17_{9,9} - 16_{9,8}$	106685.426	7	70	42	34	14	0.06	-0.65(13)	0.30	0.39	Missing group, blend with CH_3CH_3CO, uncertain baseline
175	$17_{9,8} - 16_{9,7}$	106685.426	7	70	42	34	14	–	–	–	–	–
189	$18_{2,17} - 17_{2,16}$	107863.000	8	46	60	46	15	0.06	-0.02(17)	0.29	0.15	Candidate line, blend with C_3H_7CN, noisy
245	$19_{8,12} - 19_{7,12}$	112858.588	11	75	1	40	16	0.05	2.18(17)	0.53	0.13	Missing group, uncertain baseline?
246	$19_{8,11} - 19_{7,12}$	112858.852	11	75	59	40	16	–	–	–	–	–
247	$18_{12,6} - 17_{12,5}$	112861.107	8	98	34	40	16	–	–	–	–	–
248	$18_{12,7} - 17_{12,6}$	112861.107	8	98	34	40	16	–	–	–	–	–
249	$18_{16,2} - 17_{16,1}$	112861.973	8	139	13	40	16	–	–	–	–	–
250	$18_{16,3} - 17_{16,2}$	112861.973	8	139	13	40	16	–	–	–	–	–
330	$26_{11,16} - 25_{11,15}$	163350.130	8	142	73	38	17	0.08	0.83(12)	0.88	1.03	Missing group, blend with C_2H_5OCHO, uncertain baseline?
331	$26_{11,15} - 25_{11,14}$	163350.132	8	142	73	38	17	–	–	–	–	–

Notes: ^{a} Numbering of the observed transitions associated with a modeled line stronger than 20 mK (see Table B.1). ^{b} Frequency uncertainty. ^{c} Lower energy level in temperature units (E_l/k_B). ^{d} Calculated rms noise level in T_{mb} scale. ^{e} Numbering of the candidate or missing features. ^{f} Peak opacity of the modeled feature. ^{g} Integrated intensity in T_{mb} scale for the observed spectrum (Col. 10), the 2-cyanoethanol model (Col. 11), and the model including all molecules except 2-cyanoethanol (Col. 12). The uncertainty in Col. 10 is given in parentheses in units of the last digit.

Table 6.4: Column density upper limits

Cyanoethanol			
Source SgrB2	Source size	T_{rot} (K)	Upper limit N_T (cm^{-2})
(N)	2″	200	1×10^{17}
	2″	100	5×10^{16}
	60″	15	8×10^{13}
(M)	2″	200	1×10^{17}
	2″	100	5×10^{16}
	60″	15	6×10^{13}
Methoxyacetonitrile			
Source SgrB2	Source size	T_{rot} (K) (K)	Upper limit N_T (cm^{-2})
(N)	2″	200	8×10^{16}
	2″	100	3×10^{16}
	60″	15	1.2×10^{14}
(M)	2″	200	5×10^{16}
	2″	100	2.5×10^{16}
	60″	15	4×10^{13}

per limits on the column density calculated for both molecules toward Sgr B2(N) and (M). These results are shown in Table 6.4. As the table shows, assuming a hot core emission angular size and a rotational temperature similar to that of aminoacetonitrile (100 K), we find column density upper limits of 3×10^{16} cm^{-2} for methoxyacetonitrile and 5×10^{16} cm^{-2} for cyanoethanol in Sgr B2(N).

6.5 Discussion

In the present search for the molecules 2-cyanoethanol and methoxyacetonitrile, we cannot claim a detection based on the observational data. Several predicted spectral features for both molecules did match features in the observational data, but other features were not present leading to only upper limits being obtained. A closer inspection of the observational data indicates that although both species were not detected, the possibility exists that they

may not be very far below the detection limit. The high degree of line blending in some regions of the spectra can make it difficult to find the emission-free channels that are needed to establish the baseline against which the molecular fluxes are determined, which adds considerable uncertainty to the estimated line fluxes near the RMS levels of the survey. Indeed, looking both in Figures 6.1 and 6.2 and the corresponding tables, in basically all cases where a line was found missing there was some uncertainty as to the true level of the baseline. It if it were slightly lower for those regions where lines were found missing, the predicted spectra would still be compatible with the observational data. Furthermore, for most frequencies it is the emission from other, more abundant species that sets the confusion floor against which any new molecular features must be sought. In such cases, additional integration time or more sensitive detectors are of no use in improving the chances of detecting additional species in the star-forming cores of dense clouds.

What, then, is to be done? The Sgr B2(N) and (M) hot cores are among the highest column density regions known, but are quite distant (lying adjacent to the Galactic Center) and are characterized by complex emission and absorption line profiles. Molecular line surveys toward additional hot cores, especially those with narrower emission line profiles, would be useful in determining whether the results obtained here apply more generally. Even so, single dish surveys, with their large beam sizes, necessarily blend the molecular features from a range of cloud environments. Thus, the present results provide yet another example of the great advantages of interferometric observations in the search for new interstellar molecules. By combining the signals from many radio telescopes spread over a range of distributions on the ground, aperture synthesis observations allows for both higher and tailored spatial resolution of the data than is possible in single dish experiments, which has several advantages. As was shown in the case of aminoacetonitrile [32], confirming

that the emissions associated with a newly detected molecule are indeed coming from the same spatial location provide a powerful verification of the detection. Furthermore, by concentrating on the longest baselines available in the interferometric data, it is possible to 'filter out' the smooth molecular emission from more common species. In most sources this leads to a significant reduction in the line confusion. As interferometric observatories such as CARMA reach their full capabilities and, in particular, once ALMA comes online, the detection of larger molecules such as those searched for here, but that are severely hindered by line blending, may well become possible. For example, ALMA will consist of fifty 12 m antennas at a site markedly superior to that at Pico Valeta (or CARMA). The resulting raw sensitivity will improve by a factor of $\sim$20 over the IRAM 30 m, and the ALMA correlator will be able to process 16 GHz of spectral line data in a single local oscillator setting. Thus, surveys at least a factor of ten deeper than those reported here will be possible in a matter of hours, and when searching for emission from compact hot cores the expectation is that the line confusion will be reduced by similar factors.

Nonetheless, the upper limits measured here still give some information about grain mantle chemistry. The previously measured column density for aminoacetonitrile was 2.8×10^{16} cm^{-2} at a rotational temperature of 100 K. If we assume the same rotational temperature for methoxyacetonitrile, then the upper limit measured here, 3×10^{16} cm^{-2}, indicates that this species does not achieve a higher peak abundance than aminoacetonitrile, as might be expected based on the relative abundances of ammonia and methanol in typical interstellar ices and the diffusion barriers of their derivatives. If the rotational temperature of methoxyacetonitrile were higher than that for aminoacetonitrile, this possibility still exists, as the upper limit at 200 K is 8×10^{16} cm^{-2}, which is more than a factor 2 higher than the measured value for aminoacetonitrile. Since neither of the species searched for here

were detected, the upper limits determined cannot yet tell us much about their relative chemistry, neither do they insubstantiate the suggested cross-linking between methanol and cyanide pathways. The higher upper limit for cyanoethanol is mainly an indication of its slightly larger partition function and the somewhat weaker transitions that result.

Methoxyacetonitrile and 2-cyanoethanol also provide excellent examples of the importance of extending the observational window into the currently inaccessible THz region. The successful launch of the Herschel Space Telescope will change this situation markedly as it becomes operational in the fall of 2009. In addition to moving away from the Boltzmann peak of many large molecules at millimeter wavelengths, thus reducing the problem of line confusion, the THz window also allows the observation of low lying torsional or vibrational states. Both methoxyacetonitrile and cyanoethanol have torsional states in the THz window, the lowest one at approximately 93 cm^{-1} for methoxyacetonitrile [71], and at approximately 108 cm^{-1} for cyanoethanol [69]. These torsions lie along the path to interconversion between the *gauche* and *anti* conformers for both molecules. In both cases *gauche* and *anti* conformers have large but differently oriented dipole moments [71, 69], indicating that these torsional modes should have significant intensity. These bands for both molecules lie above the window for the high-resolution heterodyne instrument HIFI, but right in range for the lower-resolution but highly sensitive instrument PACS that covers wavelengths from 57 – 210 μm at a spectral resolving power of $\gtrsim$1500. Thus, the laboratory measurement of these bands is of high priority, and possible means of improving the sensitivity of THz spectrometers is the subject of the next Chapter.

Chapter 7

The Principles and Promise of Fabry-Perot Resonators at THz Frequencies

7.1 Introduction

THz spectroscopy has been rapidly expanding over the last two decades and has applications in a great variety of fields, from remote sensing in astronomical and atmospheric settings, to biological and medical sciences, to homeland security [19, 78, 79]. Time-domain techniques in particular have seen great advancements in the sensitivity that can be achieved [79], but these approaches are typically limited in their spectral resolution. In THz Time Domain Spectroscopy (THz TDS), for example, a broadband THz field is generated by the illumination of photoconducting devices or suitable nonlinear optical materials with ultra-short femtosecond (fs) near-infrared laser pulses. The THz field is then recorded in the time-domain using small portions of the same fs pulses, typically with beamsplitters and an optical delay line; and the achievable spectral resolution is limited either by the length of the delay line or, ultimately, the repetition rate of the laser –usually on the order $\gtrsim$80 MHz for Ti:Sapphire oscillators.

High resolution continuous wave (CW) systems that generate THz radiation either by

up conversion through harmonic multiplication of microwave radiation, or down-conversion through difference frequency mixing of two narrow bandwidth IR lasers on a photo-mixing chip. These methods, however, are currently limited to power levels on the order of $\lesssim 10\ \mu$W or (typically much) less at higher THz frequencies [80, 81], necessitating sensitive detectors and other techniques to improve overall system sensitivity.

These limitations are especially central to the study of chemical species relevant to interstellar settings, where THz spectroscopy is expected to greatly advance our understanding in the coming years. Conditions in the interstellar medium allow for the existence and survival of compounds that can be difficult to create in the gas phase on Earth, for example transient species such as complex ions or radicals, or molecules that are difficult to volatilize such as large organic acids. Various laser or high temperature induced reactions/vaporization techniques combined with supersonic molecular beam expansions that decrease the reaction or interaction opportunities do, in some cases, allow such difficult targets to be studied. However, due to the low concentrations of the species under investigation, all methods to increase sensitivity should be explored.

Fabry-Perot cavity resonators provide an attractive method to increase the sensitivity of a spectroscopic system, as they allow a major increase in the path length and thus the fraction of light a medium can absorb. In addition, cavities ultimately allow most laboratory measurements to be moved from the frequency domain into the time-domain, for example either with cavity ring down approaches or via the free-induction decay of molecular transitions excited by a coherent radiation field. Cavity ring down spectroscopy is now widely applied at visible and infrared wavelengths, while in the microwave region it is the latter technique that now serves as the basis for most of the highly sensitive FT-MW systems used around the globe.

In this Chapter, we will explore the use of resonant Fabry-Perot cavities at millimeter and THz frequencies. The ultimate goal of this work is to build towards a THz analog of the "Balle-Flygare" (or FT-MW) systems that are commonly used at microwave frequencies, in which the free induction decay of the rotational or low-energy torsional transitions are recorded as a time-domain signal using heterodyne detection and Fourier Transformed to a high resolution frequency domain THz signal (or FT-THz). In achieving such a system, the cavity is of central importance, as the nature and quality of its performance will impact or limit various aspects of any spectroscopic system, including path length, detector requirements (sensitivity, bandwidth), source power levels, etc.

As will be discussed in a subsequent section, however, THz frequencies provide unique challenges to the use of Fabry-Perot resonators in cavity-enhanced spectroscopic techniques. Due to the wavelengths typically encountered, for example, the input/output coupling schemes that are commonly used at IR or MW frequencies are unworkable (or impossible). Here, we investigate the use of wire grid polarizers as input and output coupling mirrors. In addition, due to the nature of the optics being used and the low powers that are available at THz frequencies, accurate consideration of the Gaussian nature of the radiation and the coupling of the beam(s) to the various spectrometer optics is necessary. In this Chapter we present a short discussion of these various optical considerations along with the configurations of the cavities investigated to date. Following a presentation of the preliminary results obtained near 300 GHz, the Chapter concludes with a discussion of the fundamental limitations of THz cavities and how they might best be used in future spectroscopic setups.

7.2 Cavity Configuration

Resonant Fabry-Perot cavities are commonly used in spectroscopic setups over a wide range of frequencies. The two most closely related electromagnetic domains that we will consider here for suggestions on how to extend cavity-based spectroscopic techniques into the THz range are the neighboring MW and IR regions. At infrared wavelengths, input/output coupling mirrors generally consist of dielectric stacks that are composed of multiple thin layers of materials with alternating refractive indices. These dielectric mirrors function on the principle of constructive interference, with the thickness and refractive index of the different layers chosen such that the reflected light from different layers constructively interfere, which allows the design of mirrors with very high reflectivity (R>0.9999) and very low loss per pass (<ppm). Due to the much longer wavelengths, this is technologically difficult to achieve at THz frequencies, and no such dielectrics currently exist in this regime. Metallic mirrors, with only a small conductance loss in the surface, provide a material that is principle capable of achieving the high reflectivity required for the type of experiments discussed here. However, metallic mirrors do not transmit any radiation, thus requiring another method of coupling the radiation into and out of the cavity. At microwave frequencies, this problem is surmounted by coupling the radiation into the cavity using either an antenna inside the cavity, or a waveguide butted against an iris in one of the mirrors. Because the wavelengths at THz frequencies are two orders of magnitude shorter than at MW frequencies, however, these coupling methods can severely impact the quality factor of the cavity. Further, both THz strip lines and waveguides are exceedingly difficult to manufacture and have high loss.

These factors lead us to explore THz cavities using wire-grid polarizers as input/output

coupling mirrors. Electric field components parallel to a thin metal wire cause the flow of electrons in the wire, turning the wire into a reflective/diffractive element. A wire-grid polarizer consists of an array of such conducting metal wires, with both the spacing between the wires, g, and the diameter of the wires, $2a$, significantly less than half the wavelength: $g << \lambda/2$, $2a < g$. Under these conditions, the reactive shunt impedance of the grid is significantly less than the characteristic impedance of free space, resulting in almost complete reflection of the power in the incident electric field parallel to the grid [82]. A small amount of radiation still leaks through the grid, however, giving us exactly the characteristics needed for coupling radiation in to and out of a cavity. Use of a wire-grid does affect the configuration of the cavity, as it provides a flat surface rather than the spherical mirrors used in traditional microwave confocal cavities.

The simplest configuration we attempted is shown in Figure 7.1, and consists of a semi-confocal arrangement, with the wire-grid polarizer serving as both the input and the output coupling mirror. In this case, the beam waist is positioned at the polarizer, and the distance between the polarizer and the spherical mirror, L, is equal to the effective focal length (EFL) of the mirror. This ensures that the radius of curvature of the mirror matches that of the THz field at its minimum, and gives several straightforward relationships that fix the characteristics of beam and the optics, allowing for a simple design process:

$$\omega_0 = \left(\frac{\lambda L}{\pi}\right)^{0.5} \tag{7.1}$$

$$\omega(L) = \sqrt{2}\omega_0 \tag{7.2}$$

where ω_0 is the beam waist at the polarizer, $\omega(L)$ is the beam radius at the spherical mirror

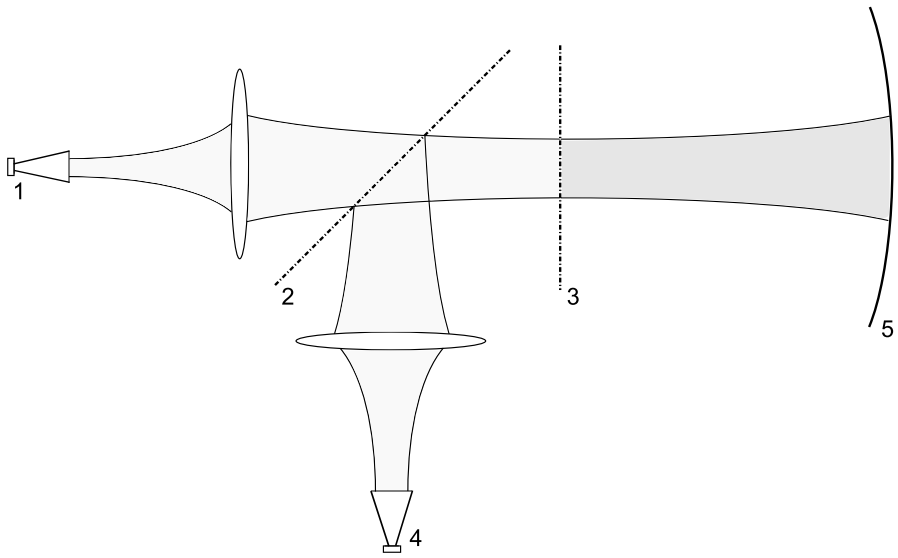

Figure 7.1: THz cavity consisting of a semi-confocal Fabry-Perot resonator. In grey is the resonantly enhanced THz beam. The radiation is coupled into and out of the cavity through the same wire grid polarizer and the outgoing beam is redirected towards the detector by a 50:50 beam splitter. The accompanying spectrum can be seen in Fig. 7.3. Components of the system include: (1) THz radiation source; (2) 50:50 beam splitter, wire grid polarizer angled at 45 ° relative to the field; (3) Input coupling mirror, Microtech Instruments wire-grid polarizer, G45×10; (4) THz receiver, combined with lock-in amplifier recording in AM mode; (5) Gold spherical mirror, of Effective Focal Length, or EFL = 12″.

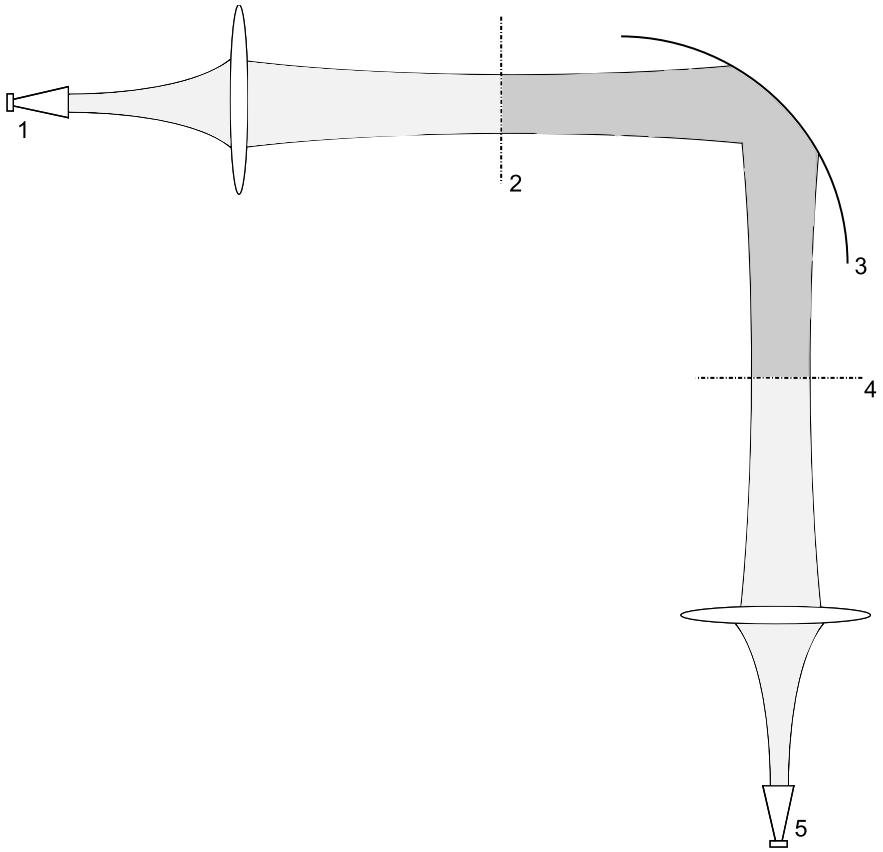

Figure 7.2: THz cavity consisting of an off-axis Fabry-Perot resonator. In dark grey is the resonantly enhanced THz beam. The radiation is coupled into and out of the cavity through two different wire-grid polarizers. This results in a mode-filtering effect by the cavity that allows only the fundamental TEM_{00} modes to reach the detector, resulting in a much cleaner and simpler (transmitted) spectrum, that can be seen in Fig. 7.4. The components of the system are: (1) THz radiation source; (2) Input coupling mirror, Microtech Instruments, G50×20; (3) Off-axis parabolic mirror, EFL = 12″; (4) Output coupling mirror, Microtech Instruments wire-grid polarizer, G45×10; (5) THz receiver, combined with lock-in amplifier in AM mode.

and λ is the wavelength. Due to the gaussian nature of the beam, the diameter of the optics (in this case that of the polarizer and the spherical mirror) need to be $D > 4\omega$ to ensure that diffraction losses are practically eliminated relative to other losses in the system. A 50:50 beam splitter between the radiation source and the cavity allows the redirection of the beam transmitted by the cavity to the detection system.

The second configuration we attempted is shown in Figure 7.2, and can be thought of as two semi-confocal cavities arranged at 90 °, with an off-axis parabolic mirror instead of a spherical mirror connecting the two arms. In this arrangement, the distance from one

polarizer to the mirror is still equal to the effective focal length of the mirror, but the total length of the cavity is now twice this distance. The beam waist thus changes to:

$$\omega_0 = \left(\frac{\lambda L}{2\pi}\right)^{0.5} \tag{7.3}$$

The main reason for this arrangement versus the simple semi-confocal arrangement outlined above is that the cavity now acts essentially as a frequency selective transmitter, one in which only the fundamental cavity modes should reach the detector. In the former arrangement, since the path for direct reflection off the cavity input mirror and the emission from the cavity are the same, it can be difficult to distinguish the fundamental modes of the cavity if the power coupling reaches steady-state. Under cavity illumination with a pulsed radiation source this would not be an issue if the decay of the cavity (or molecular emission) could be monitored, but the alignment and optimization of the cavity would still be significantly impeded. Furthermore, if the cavity is used in combination with a swept CW source, simply as a method to increase the path length, the direct reflection/cavity out-coupled confusion problem would not be eliminated as the sweep-rate of the source would generally be slower than the ring down time of the cavity. Going to a configuration where the input and output coupling mirrors are separate from each other solves this problem. The second advantage of the 90° arrangement is that it eliminates the need for the 50:50 beam splitter that redirects the cavity emission to the detector. Since 50 % of the power is waisted on each pass through the beam splitter, only a maximum of 25 % of the source power can be recovered in the arrangement in Figure 1. In the situation arrangement shown in Figure 2, however, the maximum amount of input power that can be recovered is 50 % if the reflectivity of the input and output coupling mirrors are equal (i.e. 50 % emission from

both polarizers in steady-state). It is possible to choose a different reflectivity for the two mirrors and essentially 'tune' the fraction of power reaching the detector from the cavity, although such a parameter study is not pursued here.

7.3 Experimental Studies

Both of the cavity configurations described above were investigated using a swept frequency source at wavelengths near 1 mm (= 300 GHz). The source consisted of a 12.5-20 GHz Wiltron microwave source followed by a room-temperature solid state multiplier chain ($\times 2 \times 3 \times 3$) that outputs radiation from 225-360 GHz. The signal is detected by the combination of a Virginia Diodes Shottky diode detector and Stanford lock-in amplifier. The experiment is run in AM mode to record the signal as absolute power versus frequency.

The two cavity arrangements we tested are shown in Figures 7.1 and 7.2. The semi-confocal cavity shown in Figure 7.1 was assembled using a $4''$ diameter polarizer (model G45$\times$10) from Microtech Instruments, consisting of an array of Tungsten wires with a width of 10 μm and a spacing of 45 μm, and a $12''$ diameter gold spherical with a $12''$ effective focal length. The polarizer has a quoted reflectivity of $\sim$0.999 at 300 GHz. With this set of optics, the beam radius is 19.7 mm at the polarizer and 27.8 mm at the mirror, ensuring that diffraction losses in the cavity are negligible compared to the conductance loss in tungsten or reflection losses at the polarizer. The beam waist as emitted from the radiation source was transformed to match the beam waist of the cavity fundamental mode at the input plane of the polarizer using a single lens. Similarly, a second lens was used to transform the beam emitted by the cavity to match the beam waist at the detector.

The 90° off-axis configuration shown in Figure 7.2 consists of two similar $4''$ diameter polarizers from Microtech Instruments, the input polarizer (model G50$\times$20) consisting of

wires with a width of 20 μm and a spacing of 50 μm and a quoted reflectivity of $\sim$0.9997 at 300 GHz, for the output polarizer these numbers were 10, 45, and $\sim$0.999, respectively. The off-axis parabolic mirror had a diameter of a 6$''$ and a focal length of 6$''$, giving a beam radius of 13.9 mm at the polarizers and 19.7 mm at the parabolic mirror.

7.4 Results

The spectrum resulting from the cavity arrangement of Figure 7.1 is shown in Figure 7.3. Several features can be seen in this spectrum, including both the fundamental TEM_{00} and higher order TEM_{mn} modes. However, as mentioned previously, it is not immediately clear which are the fundamental modes and which are the higher order modes. One's first intuition might be to assume that the strong features in absorption arise from the fundamental TEM_{00} modes, but in fact these modes should couple most effectively into and out of the cavity. Thus, once the cavity reaches steady state the difference between reflection off the input mirror and re-emission by the cavity should be smallest for the fundamental modes. It will furthermore be difficult in reality to completely eliminate diffraction losses, minor phase shifts and other losses due to an imperfect system. These effects differ between the various TEM_{mn} families, resulting in the somewhat different shapes of each mode. As such, is not clear from inspection which are the fundamental modes and which are the higher order modes. The expected spacing of the fundamental modes is given by $\nu_0 = c/2L$, which for a cavity length of 12$''$ equals $\nu_0 = 492$ MHz. The spacing between similar features in the spectrum shown is 472 MHz for each set, indicating the actual cavity length is 31.8 cm in this case. In addition to the sharp cavity modes, broader fluctuations in the baseline can also be seen. These features are likely etalon effects resulting from interactions between various optics in the system, and further complicate the spectrum.

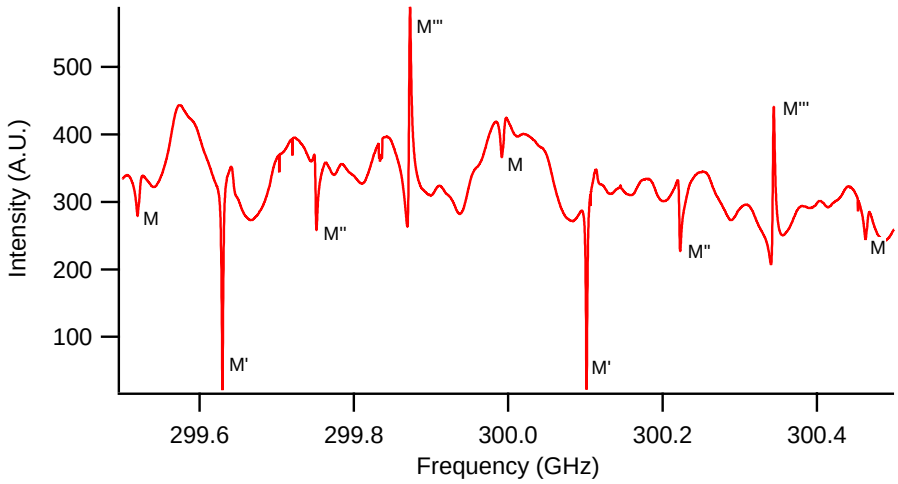

Figure 7.3: AM frequency spectrum corresponding to the cavity arrangement seen in Fig. 7.1. Cavity resonances are labeled M, and several different modes (both the fundamental TEM_{00} and higher order TEM_{mn}) can be seen, with some uncertainty as to which are the TEM_{00} modes. In steady-state for this cavity arrangement, one would expect the difference between reflection off the input mirror and emission of the cavity mode to be smallest for the fundamental mode, which should couple in and out of the cavity most effectively. However, the modes are also affected by small phase shifts and other imperfections of the cavity, with a varying impact across the modes, so that further analysis would be needed to determine which are the TEM_{00} modes. The variable effect of the phase shifts can also be seen in the different shapes and spacing of the different modes. The free spectral range is consistent across modes, $\Delta\nu_M = \Delta\nu_{M'} = \Delta\nu_{M''} = \Delta\nu_{M'''} = 472$ MHz, but the spacing between different modes varies, $\Delta\nu_{M-M'} = 110$ MHz, $\Delta\nu_{M'-M''} = 122.5$ MHz, $\Delta\nu_{M''-M'''} = 121$ MHz, $\Delta\nu_{M'''-M} = 118.5$ MHz.

Figure 7.4 shows the spectrum of the 90° off-axis configuration, and the advantages of this arrangement are immediately clear. Because the input and output coupling mirrors are the same in the semi-confocal arrangement, the signal at the detector is essentially a comparison between on-resonance emission of the cavity and off-resonance direct reflection from the input mirror. In the the 90° off-axis configuration the only signal reaching the detector is that resulting from modes that are efficiently coupled into and out of the cavity. Due to this frequency selective behavior, etalon effects are essentially eliminated giving a flat (near zero) baseline. Higher order modes are also eliminated due to their much higher loss, and the only modes detected are the fundamental TEM_{00} modes. This configuration thus allows a mode filtering similar to what is achieved with perpendicular pairs of L-shaped $\lambda/4$ antennas in modern FTMW machines [83]. The spacing of the modes in the spectrum

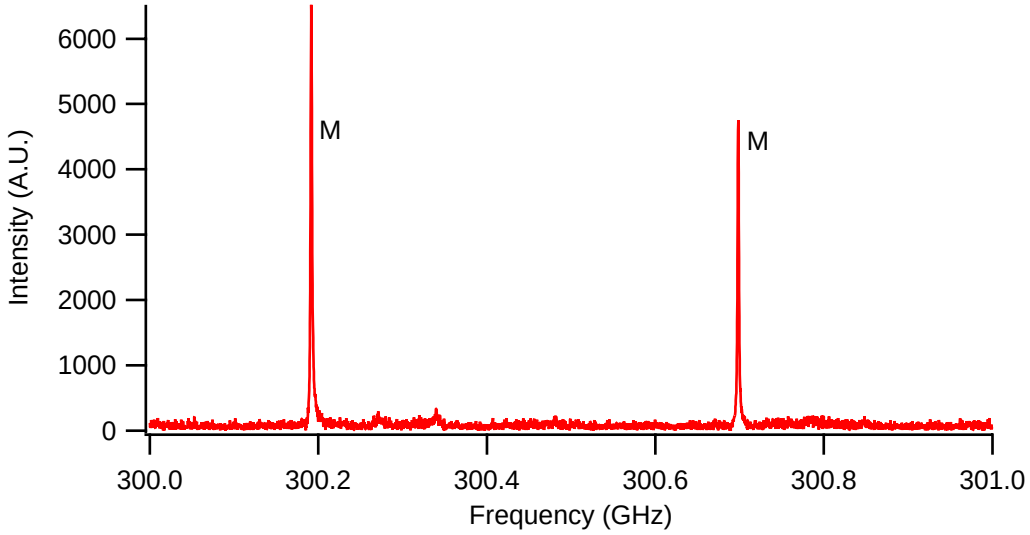

Figure 7.4: AM frequency spectrum corresponding to the cavity arrangement seen in Fig. 7.2. It can be seen that the the 90° off-axis cavity arrangement selectively filters out both higher order TEM_{mn} modes and etalon effects, leaving only the fundamental TEM_{00} modes, labeled M, and a flat baseline. The free spectral range of the modes, $\Delta\nu_M = 506.7$ MHz, and the width of the modes is 2.0 MHz. This corresponds to $Q_L = 1.5 \times 10^5$, which is close to the theoretical limit of Q = 5-6 $\times 10^5$.

is 506.7 MHz, close to the expected spacing $\nu_0 = 492$ MHz based on the 6″ focal length of the off-axis parabolic mirror.

7.5 *Q* Factor and Cavity Limits

The quality factor, Q, of a cavity is proportional to the ratio of the energy stored to the energy lost per second [84]:

$$Q = \frac{2\pi\nu W}{P} \tag{7.4}$$

where W is the energy stored in the cavity, P is the power dissipated, and ν is the frequency of the radiation. The higher the Q factor of the cavity, the more effective it will be as a tool to increase the sensitivity of the spectroscopic setup. The "loaded Q" (including coupling

losses) can be calculated from the cavity spectrum using [85]:

$$Q_L = \frac{\nu}{\Delta\nu} \tag{7.5}$$

where ν is the frequency of the cavity mode, and $\Delta\nu$ is the width of the cavity mode. The ring down time of the cavity can furthermore be calculated using [85]:

$$\tau = \frac{Q_L}{2\pi\nu} \tag{7.6}$$

From the spectrum in Figure 4, we find that the cavity modes have a width, $\Delta\nu$, of 2.0 MHz in the the 90° off-axis configuration. This gives $Q_L = 1.5 \times 10^5$, and $\tau = 0.8$ μs.

The Q factor can be used to calculate further characteristics of the cavity, and it is also a useful measure to assess the fundamental limits of cavities and what can be done to optimize their performance. Since the Q factor is dependent on the angular frequency of the radiation, this somewhat obscures the comparison of cavities between different frequency ranges. Another useful measure therefore is the effective path length of the radiation in the cavity, which is given by [82]:

$$L_{eff} = \frac{\lambda Q_L}{2\pi} \tag{7.7}$$

From equation (7.7), we see that the effective path length is directly proportional to the wavelength of the photons. Since THz photons ($\lambda \sim 0.1$ - 1 mm) have wavelengths approximately two orders of magnitude shorter than those at MW frequencies ($\lambda \sim 1$ - 10 cm), the implication is that an increase in Q of approximately two orders of magnitude is needed to achieve similar path lengths for the two regimes. Indeed, if we calculate the path length in the experiment above, where $\lambda = 1$ mm, and $Q_L = 1.5 \times 10^5$, we find that $L_{eff} = 24$ m.

This is only a factor of a few higher than what is regularly achieved in our flow cell system that is several meters in length, and which can be efficiently double-passed.

To determine how the Q factor, and thus the path length, can be improved compared to the system tested here, we next investigate the aspects of the cavity that limit the Q factor. As mentioned previously, if the optics inside the cavity are chosen with a diameter large compared to that of the beam, diffraction losses can practically be eliminated. In this case, two factors, in principle, limit the quality of the cavity: reflection (and diffraction) losses off the wire-grid polarizers that serve as the input and output coupling mirrors, and power losses due to the finite conductivity of the metal in the mirrors. To examine the effects of each, we will consider the limiting cases where the losses are dominated by only one of the effects. First, the limit where reflection losses are negligible compared to ohmic losses in the metal is considered. In this case the Q factor is given by [85]:

$$Q = \frac{L}{2\delta} \tag{7.8}$$

where δ is the skin depth of the metal, which is a measure of the power loss due to conductance in the surface of the mirror. The skin depth is given by [85]:

$$\delta = \frac{1}{\sqrt{\pi \nu \mu \sigma}} \tag{7.9}$$

where μ is the permeability of the metal, and σ is the conductivity. Gold has a permeability of $4\pi \cdot 10^{-7}$ N/A^2 and a conductivity of $4.4{\cdot}10^7$ $(\Omega\text{m})^{-1}$ (at 300 K) [86], which gives a skin depth at 300 GHz of 1.39×10^{-5} cm. The cavity length of our off-axis configuration is 30.5 cm, giving a theoretical $Q = 1.1 \times 10^6$. In reality this number will be slightly lower in our case, since the polarizer wires are made of tungsten, which has a somewhat lower

conductivity than gold; but this idealized calculations is nonetheless useful for comparative purposes.

Next, we consider the case where the ohmic losses are negligible and the Q factor is dominated by reflection loss of the wire-grid polarizers. In this case the ring down time is give by [87]:

$$\tau = \frac{L}{c(1-R)} \tag{7.10}$$

where R is the reflectivity of the mirror. This equation can be combined with equation (7.6) to give:

$$Q = \frac{2\pi\nu L}{c(1-R)} \tag{7.11}$$

With a reflectivity of 0.999 at 300 GHz, this gives a theoretical limit of $Q = 1.9 \times 10^6$. Again, this is an idealized calculation because we have not included any diffraction caused by the wires themselves.

From these two limiting cases we can calculate the expected total Q factor by:

$$\frac{1}{Q_t} = \frac{1}{Q_C} + \frac{1}{Q_R} \tag{7.12}$$

where the Q_C is that due solely to conductance losses, and the Q_R to reflection losses. Substituting in the numbers we found above gives a theoretical limit on the total quality factor of $Q_t = 7.0 \times 10^5$. As mentioned previously this number is lowered somewhat because the wire-grid polarizers are made from tungsten rather than gold, which brings the total maximum Q into the range of 5-6 $\times$ 10^5. We determined a $Q_L = 1.5 \times 10^5$ from the spectrum in Figure 4, and Q's as high as 3×10^5 have been measured in our system with very careful alignment of the cavity and coupling optics.

These results show that in the current setup it is the conductance losses in the mirror surface that outweigh the reflection losses at the polarizers, although they are similar in magnitude. It should be noted that an increase in frequency causes a rapid decrease in the reflectivity of the polarizer, which corresponds to a decrease in the Q factor. For example, the reflectivity of the G45×10 polarizer in our setup decreases from ∼0.999 at 300 GHz to ∼0.99 at 1 THz, which gives $Q_R = 6.3 \times 10^5$ with this increase in frequency the only change in the system. On the other hand, as we see from equations (7.8) and (7.9), an increase in frequency causes a decrease in the ohmic loss in the metal and a concomitant increase in Q_C, $Q_C \sim \sqrt{\nu}$. At 1 THz, the skin depth of gold decreases to 7.6×10^{-6} cm, and $Q_C = 2.0 \times 10^6$.

Put more generally, for mixed mirror/polarizer cavity designs, at low frequencies the dominant loss term is conductance loss in the metal surfaces of the optics and at high frequencies the dominant loss term is reflection loss at the wire-grid polarizers – with a transition point at several hundred GHz. Increasing the reflectivity of the polarizers will increase the frequency at which this transition point occurs. In principle, it should be possible to increase the reflectivity of the polarizer by decreasing the width and spacing of the wires to the point where ohmic losses always dominate over reflection loss. Because of the relationship in equation (7.12), the reflection loss should be at about an order of magnitude less than the conductance loss for ohmic loss to dominate. Especially at higher THz frequencies this is difficult to achieve with free-standing wire-grid polarizers due to the mechanical challenges of winding very fine wires onto an open aperture under tension. A more promising method for significant increases in reflectivity is therefore the deposition of a wire grid array onto a substrate transparent at THz frequencies, such as high resistivity silicon. This method should allow for the manufacture of a much finer and more closely

spaced array of wires, ensuring that the system will always operate in the regime where conductance loss is the dominant term. The main advantage of operating in this regime is that discussed above, namely that the conductance loss decreases with frequency ($Q_C \sim \sqrt{\nu}$). This partially compensates for the decrease in path length due to the shorter wavelengths at THz frequencies, and would maximize the performance of the cavity.

After decreasing the reflection losses at the wire grid polarizers, the second route to improving the quality factor of the cavity is by decreasing the ohmic loss in the metal surface. Gold wires on high resistivity silicon (a combination that has long been used in THz photomixer designs) would thus lead to an additional gain in the Q factor over free-standing wire grid polarizers as gold is a better conductor than tungsten. In the system we tested here, high reflectivity deposited gold wire grid arrays should increase the Q closer to values near 1.1×10^6 at room temperature. Further gains can be made by cooling the mirrors as the conductivity of metals increases at lower temperatures. For example, at 77 K the conductivity of gold increases to 2.1×10^8 $(\Omega\text{m})^{-1}$, or for aluminum at this temperature the conductivity is 4.2×10^8 $(\Omega\text{m})^{-1}$ [86], resulting in Q_C values of 2.4×10^6 and 3.4×10^6, respectively. Cooling to liquid Helium temperatures (4.2 K) or using superconducting metal wires should allow further improvements, at the cost of considerable experimental complexity of course. Finally, equations (7.8) and (7.11) both show that Q is linearly proportional to the length of the cavity, so larger cavities would result in a further increase in Q.

7.6 Sensitivity of Pulsed FT Systems at THz and Microwave Frequencies

Next we compare the theoretical sensitivity that is attainable in a THz analog of the common FT-MW "Balle-Flygare" systems at the Q levels discussed above. In FT-MW instruments, great increases in sensitivity are achieved by using high quality resonant cavities in combination with a pulsed radiation source and a pulsed molecular beam. In these systems near $\pi/2$ pulses are coupled into the cavity by operating in a regime where the pulse length of the radiation is longer than the cavity ringdown time but significantly shorter than the rotational dephasing time of the coherent electric field in the cavity. Operating in this regime results in maximal polarization of the gas and allows recording of the free induction decay (FID) signal of the molecule in heterodyne mode free of the standing waves which plague frequency scanned spectrometers (see the spectral plots in Chapters 2-5), which allows significantly increased sensitivities beyond those simply resulting from an increased pathlength. To evaluate the sensitivity of a FT-THz system as compared to FT-MW machines, we compare both the levels of the signal power coupling out of the cavity and the noise level of heterodyne detection at both frequencies.

The power of the molecular signal coupling out of the cavity is given by [88]:

$$P_{out} = \frac{16}{9}\pi^2 Q_0 \nu_0 \left(|\langle a|\mu_z|b\rangle|\Delta N_0\right)^2 \pi\omega_0^2 L \left[\left(\frac{1}{\kappa E_0 \tau_p}\right)\int_0^{\kappa E_0 \tau_p} J_1(u)du\right]^2 \tag{7.13}$$

where ν_0 is the frequency of the rotational transition, $\langle a|\mu_z|b\rangle$ is the electric transition dipole moment, ΔN_0 is the number of emitting molecules, ω_0 is the beam waist of the THz field in the cavity, L is the length of the cavity, $\kappa = (2/\hbar)\langle a|\mu_z|b\rangle$, E_0 is half the maximum electric field amplitude in the cavity, and $J_1(u)$ is the first order Bessel function. To compare

between the frequency domains, we simplify equation (7.13) by eliminating terms that can be set to be roughly equivalent. For example, by working in a similar pulse regime (i.e. equal $\kappa E_0 \tau_p$) and at the maximum of the Bessel function, and by further assuming an equivalent transition dipole moment, we find:

$$P_{out} \propto Q_0 \nu_0 \Delta N_0^2 \omega_0^2 L \tag{7.14}$$

Further, from equation (7.3) we can set $\omega_0 = \sqrt{\lambda L / 2\pi}$. Inserting these relationships into equation (7.14) and realizing that $\nu_0 \sim 1/\lambda$ gives the final result:

$$P_{out} \propto Q_0 \Delta N_0^2 L^2 \tag{7.15}$$

Thus, for a transition of similar intrinsic intensity and operating experimentally in the same pulse regime, it is the Q factor, the number of molecules emitting, and the length of the cavity that determines how the output coupled power compares between the THz and MW frequency domains. The cavity in a FT-MW system is generally detuned to increase the width of the mode to a useful value, say 1 MHz, resulting in an operating $Q_L \sim 10^4$ near 10 GHz. The cavity arrangement presented here is capable of achieving an operating $Q_L \sim 10^5$ at THz frequencies, which represents a gain by a factor of ~10 versus microwave frequencies. The last term in equation (7.15) also presents an advantage at THz frequencies, as we know from equation (7.3) that the beamwaist for a given cavity length will be smaller at THz frequencies than at MW frequencies. We can thus choose a THz cavity length similar to MW systems, but use smaller diameter optics.

There are a number of factors where where current MW systems may significantly outperform those at THz frequencies. First among these is the number of molecules emitting.

For pinhole supersonic expansions, the free jet volume can be very large with sufficiently high pumping speeds, leading to an efficient filling of the sizable microwave cavity. One means of improving this situation for FT-THz instruments would be to move to pulsed slit jet expansions such as those employed in tunable far-infrared laser sideband studies of hydrogen bonded clusters [89, 90]. In pulsed slit expansions, the on-axis jet density drops as 1/R, not $1/R^2$, but at the cost of much higher pumping speed requirements and much shorter Mach disk distances. Slit jets would fill only a small fraction of an FT-MW cavity, but could be well matched to an FT-THz instrument and dramatically increase the values of N_0 achievable. The line widths from such jets are also sub-Doppler when the jet axis is orthogonal to the cavity axis, resulting in excellent spectroscopic resolution.

Second, high power, short pulse radiation sources are easily available at MW frequencies, making it simple to excite a large fraction of the molecules in the pulsed molecular beam. At THz frequencies, however, intense sources, especially at the higher frequency end of the spectrum, are severely limited in their tunability and ease of use. What this analysis shows, however, is that as higher power sources become available, cavities at THz frequencies should be capable of operating at similar levels, and eventually even outperform cavities at MW frequencies in terms of output coupling power. For pulsed molecular beam studies, where the duty cycle is dictated primarily by the valve/slit operating characteristics, it may be possible in FT-THz machines to match the frequency characteristics of the radiation source to the cavity. In this case, short pulses of light would not be required and the power in the cavity could be built up to steady state levels before introducing the molecules and switching off the radiation field.

Finally, we compare the noise level of heterodyne receivers at THz frequencies versus MW frequencies. The system temperature for a hot electron bolometer in heterodyne mode

is given by [91]:

$$T_{sys} = \frac{1}{k_B \eta(\nu)} \frac{e^2(\nu)}{R_L} = \frac{NEP^2(\nu)}{2\alpha k_B P_{LO}} \tag{7.16}$$

where k is the Boltzman constant, $\eta(\nu)$ is the quantum efficiency of the mixer, $e(\nu)$ is the noise voltage across the device load, R_L is the resistive load of the device, α is the coupling factor of the radiation to the mixer and P_{LO} is the LO power. The noise equivalent power (NEP) is $NEP(\nu) = e(\nu)/S(\nu)$, where $S(\nu)$ is the voltage responsivity of the detector. The power level of the noise is then simply given by:

$$P_{noise} = kT_{sys}\Delta\nu \tag{7.17}$$

where $\Delta\nu$ is the detection bandwidth.

The system temperature is thus a useful measure to compare noise between MW and THz frequencies. NEP^2 (and thus T_{sys}) of a heterodyne *detector* thus scales with frequency, which represents a significant loss in going from the MW regime to the THz regime. However, the overall *system* temperature must include the thermal radiation (noise) from the cavity. A typical receiver temperature for room temperature Schottky diode mixers at 10 GHz in a FT-MW machine is only $T_{sys} \sim$ 10 - 20 K. Thus, the overall system temperature is dominated by the thermal emission from the cavity. Cooling the cavity mirrors can therefore lead to significant improvements in sensitivity, and the latest generation of FT-MW instruments therefore makes accommodations for either LN_2 or LHe cooled cavities. At THz frequencies, T_{rcvr} values of 350-450 K at 1.1 to 1.25 THz have been achieved with superconducter-insulator-superconductor (SIS) mixers,[92], and approximately 35-40 K has been achieved at 230 GHz for ALMA Band 6 receivers (ALMA Memo #553, see `http://www.alma.nrao.edu`). Thus, when comparing room temperature cavities, the de-

tection systems in FT-MW spectrometers outperform those likely to be available for FT-THz systems, but only by a factor of a few even up to frequencies beyond 1-2 THz. This ratio may well improve as the performance of THz mixers improves. The fundamental quantum limit for heterodyne detection imposes a sensitivity floor of $T_{rcvr} = h\nu/k$, which at 3 THz corresponds to a mixer temperature of ∼150 K.

7.7 Discussion

In summary, we have characterized here the performance of Fabry-Perot cavities at frequencies near 300 GHz using wire-grid polarizers as input and output coupling mirrors in an arrangement in which the cavity acts as a selective filter for only the fundamental TEM_{00} modes. This method of cavity coupling permits designs that are usable across the full THz frequency range without the need for changing optics, and in layouts that are compatible with supersonic jets. We have furthermore achieved Q factors close to the calculated theoretical limit, and show how this is limited by the reflection losses at the polarizers and ohmic losses in the metal surface of the mirror. In terms of using the cavity as a device to increase path length, the current Q factors we achieve do not represent a significant increase versus typical flow cell system path lengths. Using polarizers fabricated by the deposition of fine arrays of narrow gold wires on substrates transparent at THz frequencies should allow path lengths a factor of only a few below the levels achieved in cavity ring down systems in the infrared or in FT-MW machines. Further improvements can then be achieved by cooling the mirrors and increasing the size of the cavity.

Furthermore, comparing the theoretical sensitivity of a pulsed FT-THz system to the sensitivity of current pulsed FT-MW system shows great promise for the use of Fabry-Perot cavities at THz frequencies. At the Q factors measured in this work, we show that THz

cavities should be capable of producing molecule free induction decay signals that match or exceed those from FT-MW systems as higher power THz sources become available. While the receiver noise of heterodyne detectors at THz frequencies is substantially higher than that at MW frequencies, for room temperature cavities it is the thermal emission from the latter that dominates the overall system performance. Thus, in terms of overall sensitivity, FT-MW systems will likely outperform FT-THz instruments, but only by factors of at most a few. A final advantage that a FT-THz system will have versus FT-MW machines is that a Q factor of 10^5 results in cavity modes with a full width half maximum of roughly 10 MHz at 1 THz and 30 MHz at 3 THz, whereas the cavity modes in FT-MW machines are generally around 0.5-1 MHz wide. Furthermore, the cavity dispersion at THz frequencies is much reduced over that in the microwave region, meaning that many cavity modes can in principle be excited (and simultaneously detected) by properly designed frequency combs. These factors should allow for a dramatic increase in scanning speed, offsetting in large measure the decrease in sensitivity.

Chapter 8

Future Directions

This thesis discusses various aspects of the limitations of gas phase spectroscopy at microwave and millimeter wavelengths and the transition to THz spectroscopy as they apply to the study of complex interstellar chemistry. Here we discuss in some further detail the expected gains to be made by transitioning to THz spectroscopy.

Along with the expected decrease in spectral confusion as previously discussed, a major increase in detectivity for large molecules is expected due to the steep frequency dependence in the intensity of THz versus millimeter transitions. Examining this claim more closely, the intrinsic intensity of a transition in local thermodynamic equilibrium is given by [60]:

$$I = \frac{8\pi^3}{3hc}\nu S\mu^2 \frac{\left[e^{-E_l/kT} - e^{-E_u/kT}\right]}{Q_{rs}} \tag{8.1}$$

where S is the quantum mechanical line strength, μ is the dipole moment, E_l and E_u are the lower and upper state energies, and Q_{rs} is the rotation-spin partition function. In the limit where $E_l \ll$ kT (perhaps not a reasonable assumption for the highest J states of complex molecules at hot core temperatures), the numerator in the last term becomes

$[e^{-E_l/kT} - e^{-E_u/kT}] \sim h\nu/kT$. Equation (8.1) then becomes:

$$I = \frac{8\pi^3}{3ckT}\frac{\nu^2 S\mu^2}{Q_{rs}} \tag{8.2}$$

To determine, for example, the absorption strength from the intrinsic intensity, we calculate the optical depth, τ, of the transition, which is given by $\tau = \sigma\rho L$, where σ is the absorption cross-section, ρ is the number density of the absorber and L is the path length. The absorption cross-section of an interstellar absorber integrated over a 1 km/s velocity interval is given by [60]:

$$\sigma = \frac{I}{\nu} \times 2.99792 \times 10^{-9}\text{cm}^2 \tag{8.3}$$

The absorption is then obtained by:

$$Abs = 1 - e^{-\tau} \tag{8.4}$$

which in the limit of low optical depth becomes $Abs \sim \tau$.

Combining the above equations we find:

$$Abs = C \times \frac{\nu S\mu^2}{Q_{rs}T} \times \rho L \tag{8.5}$$

where C is a numerical constant. If we now compare a torsional transition to a rotational transition for the same molecule in the same source, we can simplify equation (8.5) by noting that the number density, path length and temperature will all be equivalent. This gives the final result:

$$Abs \propto \frac{\nu S\mu^2}{Q_{rs}} \tag{8.6}$$

We see that, for transitions of the same molecule, the absorption scales linearly with frequency and quantum mechanical line strength, and to the second power of the dipole moment. If we then compare transitions connecting the same J, K levels from a torsional band and with those in the pure rotational spectrum (which results in an approximately equivalent S), and further assume for the moment that the dipole moments for the transitions are the same, we see that the absorption essentially scales like frequency. Going from a pure rotational transition at 300 GHz to a torsional transition at 3 THz for the same molecule will thus result in a factor 10 increase in intensity. In reality, the dipole moments for the transitions will not be the same; but in many cases the transition dipoles for torsional transitions are significantly larger than those for the pure rotational transitions of complex organic molecules, further increasing this factor.

Above the Earth's atmosphere the only differential sensitivity in the microwave and THz regions arises from the spectrometer performance, and for the High-resolution Instrument for the Far-Infrared (HIFI) aboard Herschel, which operates from 0.48 - 1.91 THz, the relative merits at microwave/THz frequencies combined with the expected decrease in spectral confusion in the THz should lead to an improvement in the detection limits of large molecules with HIFI by an order of magnitude or more.

Another benefit of the THz spectroscopic search for large molecules is that as species increase in size the intense Q-branch features in the torsional modes that are generated by perpendicular transitions become increasingly compact. At some molecular size threshold, the resolving power of the observatory will be comparable to or below the width of the Q-branch, resulting in a summing of the intensities of the individual transitions in a given spectroscopic channel. This effect can at least partially offset the increase in the partition function for large molecules that results in a decrease in absorption as seen in equation (8.6).

In addition to a direct decrease in the detection limit due to going to higher frequencies for the same molecule, this coalescing effect could thus result in significant further increases in detectivity for large molecules. Furthermore, the torsional modes of species such as those studied in this thesis are active in both ices and the gas phase, unlike the pure rotational degrees of freedom. Thus, with instruments such as the Photodetector Array Camera and Spectrometer (PACS) aboard Herschel, which has broader coverage (1.43 - 5.0 THz) than HIFI, but at lower resolution, it will be possible to search for complex organics in both hot cores and in the icy mantles on interstellar dust grains.

Next we consider the effect of the transition to THz spectroscopy on observations of molecular transitions in emission. The radiant power of a collection of excited molecules is given by:

$$P = h\nu N_u A_{ul} \tag{8.7}$$

where N_u is the number of molecules in the upper state and A_{ul} is the Einstein coefficient of spontaneous emission from the upper state. The A-coefficient is given by [60]:

$$A_{ul} = \frac{I\nu^2}{g_u} \frac{Q_{rs}}{\left[e^{-E_l/kT} - e^{-E_u/kT}\right]} \times 2.7964 \times 10^{-16} \tag{8.8}$$

where g_u is the degeneracy of the upper state. Combining with equation (8.1) and eliminating numerical constants gives the following relationship:

$$Ag \propto \nu^3 S\mu^2 \tag{8.9}$$

In the LTE approximation, the integrated intensity of an interstellar transition in emission

is given by [93]:

$$\int_{-\infty}^{\infty} T_b d\nu = \frac{hc^3}{8\pi k\nu^2} A_{ul} g_u \frac{N}{Q_{rs}} e^{-E_u/kT} \tag{8.10}$$

where T_b is the source brightness temperature and N is the column density of the molecular species. This equation can be rewritten to reveal the relationship between the column density and the integrated intensity of the transition:

$$N_T = \int_{-\infty}^{\infty} T_b d\nu \frac{8\pi k\nu^2}{hc^3} \frac{Q_{rs}}{Ag} e^{E_u/kT} \tag{8.11}$$

which allows one to determine the upper limit on the column density at a given noise level. Inserting the relationship for the A-coefficient from equation (8.9) we find the following result:

$$N_T \propto \int_{-\infty}^{\infty} T_b d\nu \frac{Q_{rs} e^{E_u/kT}}{\nu} \tag{8.12}$$

We see that in the LTE approximation the upper limit on detectable signals at a given noise level scales as the inverse of the frequency. This increase in detectivity appears to be offset by an increase in the last term as the energy of upper state, E_u, of the transitions increases by going from a pure rotational to a torsional mode at higher frequencies. However, the LTE approximation underpinning equations (8.10-8.12) may not be correct in this case. As we saw in equation (8.9), the rate of emission by a molecule scales to the third power of the frequency. Thus, by going from 300 GHz to 3 THz, the rate of emission by a molecule is a factor of 1000 higher. The critical density, that is, the particle density of the cloud at which the rate of collisions is similar to the rate of spontaneous emission, increases by a similar factor. As a result, at high THz frequencies, molecular spectra in emission will transition from the domain of LTE conditions to a domain in which scatter of ambient THz

photons (from interstellar dust) dominates.

Since the rate of photon emission scales with the third power of frequency, and, as we saw in the previous chapter, the noise temperature of a heterodyne detector (at given quantum efficiency) scales linearly with frequency, the detectivity in radiative-driven emission will increase significantly for torsional modes of large molecules at high THz frequencies.

Finally, the transition to THz spectroscopy will also be of great benefit to the study of solid state chemistry in dense interstellar clouds. At THz frequencies librational modes, crystal lattice vibrations (phonons), and other intermolecular or low energy modes will be probed, which provides an important complement to the studies of the vibrational spectra of ices at infrared wavelengths. Bands shapes and strengths in the IR have been shown to be strongly dependent on the composition and temperature of the ice, and these effects are likely to be even more pronounced at THz frequencies due to the intermolecular nature of the vibrations at these frequencies. THz studies of ices will thus help in furthering our understanding of the composition and evolution of the icy mantles of dust grains in dense interstellar clouds. Furthermore, it may even be possible to probe torsional modes of larger organic molecules as they sit in the ice on dust grains. Recent waveguide THz Time Doman Spectroscopy (THz-TDS) studies [94] have shown that, when prepared in thin polycrystalline films, various organic compounds show sharp torsional features even in the solid phase. Furthermore, the observed modes showed a narrowing when the samples were cooled to 77 K [94]. It may thus be possible to probe the theoretical formation routes of complex organics by the migration and reaction of larger radical species as grains are heated directly, by using THz observations of the dust in star forming regions of different ages and observing if this effect occurs in 'real time'.

In summary, THz spectroscopy is expected to dramatically expand the opportunities for the spectroscopic studies of the chemical evolution of interstellar clouds, from the cold icy mantles of dust grains in quiescent dense clouds to the warm, turbulent gas near young stars. Both in absorption and emission the detection limits for large molecules in the gas phase are expected to improve significantly, allowing the observations of more complex chemical species; and the comparison of their abundances with other new and known molecules should allow further constraints to be placed on the chemical models of dense interstellar clouds. Beyond the direct lowering of detection limits due to an increase in the intensity of torsional transitions, a coalescing effect of perpendicular Q-branches might allow for a further drop in the detection limits for molecules above a certain size threshold. THz spectroscopy should also increase the direct understanding of the chemistry in the icy mantles of dust grains, both by observing the composition and evolution of the major constituents of the ice and possibly by monitoring larger organic species as they form in the ice but before they evaporate and participate in further gas phase pathways.

Bibliography

[1] "CSO Mauna Kea Atmospheric transmission plotter". http://www.submm.caltech.edu/cso/weather/atplot.shtml.

[2] B.J. Drouin, F.W. Maiwald, J.C. Pearson, "Application of Cascaded Frequency Multiplication to Molecular Spectroscopy", *Rev. Sci. Instr.*, **76**, 093113 (2005).

[3] Galileo Galilei, *"Sidereus Nuncius"* (1610).

[4] Isaac Newton, *"Philosphiae Naturalis Principia Mathematica"* (1687).

[5] A. McKellar, "Evidence for the Molecular Origin of Some Hitherto Unidentified Interstellar Lines", *Publ. Astr. Soc. Pac.*, **52**, 187 (1940).

[6] W.S. Adams, "Some Results with the COUDÉ Spectrograph of the Mount Wilson Observatory", *ApJ*, **93**, 11 (1941).

[7] A.E. Douglas, G. Herzberg, "Note on CH^+ in Interstellar Space and in the Laboratory", *ApJ*, **94**, 38 (1941).

[8] T.P. Snow, B.J. McCall, "Diffuse Atomic and Molecular Clouds", *Ann. Rev. Astron. Astrophys.*, **44**, 367–414 (2006).

[9] E. Herbst, E.F. van Dishoeck, "Complex Organic Interstellar Molecules", *Ann. Rev. Astron. Astrophys.*, **47**, 427–480 (2009).

[10] A.G.G.M Tielens, "Interstellar Polycyclic Aromatic Hydrocarbon Molecules", *Ann. Rev. Astron. Astrophys.*, **46**, 289–337 (2008).

[11] A.C. Cheung, D.M. Rank, C.H. Townes, D.D. Thornton, W.J. Welch, "Detection of NH_3 Molecules in the Interstellar Medium by their Microwave Emission", *Phys. Rev. Lett.*, **21**, 1701–1705 (1968).

[12] A.C. Cheung, D.M. Rank, C.H. Townes, "Detection of Water in Interstellar Regions by its Microwave Radiation", *Nature*, **221**, 626–628 (1969).

[13] L.E. Snyder, D. Buhl, B. Zuckerman, P. Palmer, "Microwave Detection of Interstellar Formaldehyde", *Phys. Rev. Lett.*, **22**, 679–681 (1969).

[14] A.J. Marckwick-Kemper. "astrochemistry.net" (2003). http://astrochemistry.net.

[15] D.E. Woon. "The Astrochymist" (2008). http://www.astrochymist.org.

[16] "The Atacama Large Millimeter Array". http://www.alma.nrao.edu/.

[17] "The Combined Array for Research in Millimeter-wave Astronomy". http://www.mmarray.org/.

[18] "Herschel Space Observatory". http://herschel.esac.esa.int/.

[19] G.A. Blake, "Microwave and Terahertz Spectroscopy", J. Moore, E. Spencer, ed., *"Encyclopedia of Chemical Physics and Physical Chemistry"*, 31–44, Institute of Phys. Publ., Bristol (2000).

[20] E. Herbst, W. Klemperer, "The Formation and Depletion of Molecules in Dense Interstellar Clouds", *ApJ*, **185**, 505 (1973).

[21] S.B. Charnley, A.G.G.M. Tielens, S.D. Rodgers, "Deuterated Methanol in the Orion Compact Ridge", *ApJ*, **482**, L203 (1997).

[22] S.B. Charnley, "Stochastic Theory of Molecule Formation on Dust", *ApJ*, **562**, 99 (2001).

[23] S.B. Charnley, A.G.G.M. Tielens, S.D. Rodgers, "The Molecular Composition of Dense Interstellar Clouds", *ApJ*, **482**, L203 (1997).

[24] C.J. Bennet, R.I. Kaiser, "On the Formation of Glycolaldehyde ($HCOCH_2OH$) and Methyl Formatte ($HCOOCH_3$) in Interstellar Ice Analogs", *ApJ*, **661**, 899 (2007).

[25] G.A. Grieves, T.M. Orlando, "The Importance of Pores in the Electron Stimulated Production of D-2 and O-2 in Low Temperature Ice", *Surf. Sci.*, **593**, 180–186 (2005).

[26] R.T. Garrod, S.L. Widicus Weaver, E. Herbst, "Complex Chemistry in Star-forming Regions: An Expanded Gas-Grain Warm-up Chemical Model", *ApJ*, **682**, 283 (2008).

[27] A. Belloche, R.T. Garrod, H.S.P. Muller, K.M. Menten, C. Comito, P. Schilke, "Increased Complexity in Interstellar Chemistry: Detection and Chemical Modeling of Ethyl Formate and n-Propyl Cyanide in Sagittarius B2(N)", *A&A*, **499**, 215–232 (2009).

[28] R.T. Garrod, E. Herbst, "Formation of methyl formate and other organic species in the warm-up phase of hot molecular cores", *A&A*, **457**, 927 (2006).

[29] C.C. Lin, J.D. Swalen, "Internal Rotation and Microwave Spectroscopy", *Rev. Mod. Phys.*, **31**, 841 (1959).

[30] W. Gordy, R.L. Cook, *"Microwave Molecular Spectra"*, John Wiley & Sons, NY (1984).

[31] L.E. Snyder, F.J. Lovas, J.M. Hollis, D.N. Friedel, P.R. Jewell, A. Remijan, V.V. Ilyushin, E.A. Alekseev, S.F. Dyubko, "A Rigorous Attempt to Verify Interstellar Glycine", *ApJ*, **619**, 914 (2005).

[32] A. Belloche, K.M. Menten, C. Comito, H.S.P. Muller, P. Schilke, J. Ott, S. Thorwirth, C. Hieret, "Detection of amino acetonitrile in Sgr B2(N)", *A&A*, **482**, 179–196 (2008).

[33] L.M. Ziurys, A.J. Apponi, In *"Astrochemistry: Recent Successes and Current Challenges", proceeding of IAU Symp. 231*, D.C. Lis, G.A. Blake, E. Herbst, ed., 207, Cambridge UK: Cambridge Univ. Press (2005).

[34] "Report from the workshop on laboratory spectroscopy in support of Herschel, SOFIA, and ALMA", Pasadena (2006). http://www.submm.caltech.edu/labspec/WorkshopReportFinal.pdf.

[35] F.J. Lovas, R.A. Dragoset, "NIST Recommended Rest Frequencies for Observed Insterstellar Molecular Microwave Transitions" (2002). http://physics.nist.gov/PhysRefData/Micro/Html/contents.html.

[36] D.K. Coles, "Microwave Absorption Line Frequencies of Methyl Alcohol and their Stark Effect", *Phys. Rev.*, **74**, 1194–1195 (1948).

[37] R.H. Hughes, W.E. Good, D.K. Coles, "Microwave Spectrum of Methyl Alcohol", *Phys. Rev.*, **84**, 418–425 (1951).

[38] H.D. Rudolph, H. Dreizler, W. Maier, "Das Mikrowellenspektrum des Methanols von 9 Bis 16 GHz, Aufgenommen mit einem Carcinotron Als Strahlungsquelle", *Zeits. F. Naturforsh. A: Astrophys. & Phys. Chem.*, **15**, 274–275 (1960).

[39] R.M. Lees, J.G. Baker, "Torsion-Vibration-Rotation Interaction in Methanol. I. Millimeter Wave Spectrum", *J. Chem. Phys.*, **48**, 5299–5318 (1968).

[40] F.C. DeLucia, E. Herbst, T. Anderson, P. Helminger, "The Analysis of the Rotational Spectrum of Methanol to Microwave Accuracy", *J. Mol. Spec.*, **134**, 395–411 (1989).

[41] T. Anderson, E. Herbst, F.C. DeLucia, "An Extension of the High-Resolution Millimeter- and Submillimeter-Wave Spectrum of Methanol to High Angular Momentum Quantum Numbers", *ApJSS*, **82**, 405-449 (1992).

[42] L-H. Xu, J.T. Hougen, "Global Fit of Torsional-Rotational Transitions in the Ground and First Excited Torsional States of Methanol", *J. Mol. Spec.*, **173**, 540–551 (1995).

[43] O.I. Baskakov, M.A.O. Pashaev, "Microwave and Submillimeter-wave Rotational Spectrum of Methyl-Alcohol in the Ground Torsional State", *J. Mol. Spec.*, **151**, 282–291 (1992).

[44] S. Tsunekawa, T. Ukai, A. Toyama, K. Takagi, *"Microwave Frequencies of the CH_3OH Molecule in the Frequency Range of 7 to 200 GHz"*, Toyama University, Japan (1992).

[45] G. Moruzzi, B.P. Winnewisser, M. Winnewisser, I. Mukhopahyay, F. Strumia, *"Microwave, Infrared and Laser Transitions of Methanol - Atlas of Assigned Lines from 0 to 1258 cm^{-1}"*, CRC Press, ISBN 0-8493-2478-5 (1995).

[46] S.P. Belov, G. Winnewisser, E. Herbst, "The High-Resolution Rotational Torsional Spectrum of Methanol from 0.55 to 1.2 THz", *J. Mol. Spec.*, **174**, 253–269 (1995).

[47] L-H. Xu, J. Fisher, R.M. Lees, H.Y. Shi, J.T. Hougen, J.C. Pearson, B.J. Drouin, G.A. Blake, R. Braakman, "Torsion-Rotation Global Analysis of the First Three Torsional

States (ν_t = 0, 1, 2) and Terahertz Database for Methanol", *J. Mol. Spec.*, **251**, 305–3113 (2008).

[48] BELGI, at http://info.ifpan.edu.pl/∼kisiel/prospe.htm#introt.

[49] J.M. Hollis, S.N. Vogel, L.E. Snyder, P.R. Jewell, F.J. Lovas, "The Spatial Scale of Glycolaldehyde in the Galactic Center", *ApJ*, **554**, 81 (2001).

[50] J.M. Hollis, F.J. Lovas, P.R. Jewell, "Interstellar Glycolaldehyde: The First Sugar", *ApJ*, **540**, L107 (2000).

[51] J.M. Hollis, F.J. Lovas, P.R. Jewell, A.J. Remijan, "Green Bank Telescope Observations of Interstellar Glycolaldehyde: Low-Temperature Sugar", *ApJ*, **613**, L45 (2004).

[52] S.L. Widicus Weaver, G.A. Blake, "1,3-Dihydroxyacetone in Sagittarius B2(N-LMH): The First Interstellar Ketose", *ApJ*, **624**, L33 (erratum: 63, L163) (2005).

[53] A.J. Apponi, D.T. Halfen, L.M. Ziurys, J.M. Hollis, A.J. Remijan, F.J. Lovas, "Investigating the Limits of Chemical Complexity in Sagittarius B2(N): A Rigorous Attempt to Confirm 1,3-Dihydroxyacetone", *ApJ*, **643**, L29 (2006).

[54] R. Braakman, ed., *"The Search for Hydroxyacetone in the Interstellar Medium"*, MSc Thesis, University of Amsterdam (2003).

[55] R. Braakman, B.J. Drouing, S.L. Widicus Weaver, G.A. Blake, In *60th OSU Int. Symp. Mol. Spec.*, RA07 (2005).

[56] A.J. Apponi, S.S. (Hoy), D.T. Halfen, L.M. Ziurys, M.A. Brewster, "Hydroxyacetone (CH_3COCH_2OH): A Combined Microwave and Millimeter-Wave Laboratory Study and Associated Astronomical Search", *ApJ*, **652**, 1787 (2006).

[57] M. Kattija-Ari, M.D. Harmony, "Internal Rotation and Microwave Spectroscopy", *Int. J. Quant. Chem. Symp.*, **14**, 443 (1980).

[58] J.T. Hougen, I. Kleiner, M. Godefroid, "Selection-rules and Intensity Calculations for a C(s) Asymmetric-Top Molecule Containing a Methyl-Group Internal Rotor", *J. Mol. Spec.*, **163**, 559 (1994).

[59] S.L. Widicus Weaver, R. Braakman, D.R. Kent, G.A. Blake, "The Millimeter and Submillimeter Rotational Spectrum of 1,3-Dihydroxyacetone", *J. Mol. Spec.*, **224**, 101 (2004).

[60] H.M. Pickett, F.L. Poynter, E.A. Cohen, M.L. DeLitsky, J.C. Pearson, H.S.P. Muller, "Submillimeter, Millimeter and Microwave Spectral Line Catalog", *J. Quant. Rad. Trans.*, **60**, 883 (1998).

[61] I.R. Medvedev, M. Winnewisser, B.P. Winnewisser, F.C. DeLucia, E. Herbst, "The Use of CAAARS (Computer Aided Assignment of Asymmetric Rotor Spectra) in the Analysis of Rotational Spectra", *J. Mol. Spec.*, **229**, 742 (2005).

[62] L. Pszczolkowski, E. Bialkowski-Jaworski, Z. Kisiel, "The Millimeter Wave Rotational Spectrum of Lactic Acid", *J. Mol. Spec.*, **234**, 106 (2005).

[63] I. Kleiner, F.J. Lovas, M. Godefroid, "Microwave spectra of molecules of astrophysical interest .23. Acetaldehyde", *J. Phys. Chem. Ref. Data*, **25**, 1113–1210 (1996).

[64] K. Ogata, H. Odashima, K. Takagi, S. Tsunekawa, "Global Fit of Rotational Transitions of Methyl Formate ($HCOOCH_3$) in the Ground and First Excited Torsional States", *J. Mol. Spec.*, **225**, 14 (2004).

[65] V. Mohacek-Grosev, "Vibrational Analysis of Hydroxyacetone", *Spec. Chim. Acta A*, **61**, 477 (2005).

[66] D.T. Halfen, A.J. Apponi, N. Woolf, R. Polt, L.M. Ziurys, "A Systematic Study of Glycolaldehyde in Sagittarius B2(N) at 2 and 3 mm: Criteria for Detecting Large Interstellar Molecules", *ApJ*, **639**, 237 (2006).

[67] I.R. Medvedev, F.C. DeLucia, "An Experimental Approach to the Prediction of Complete Millimeter and Submillimeter Spectra at Astrophysical Temperatures: Applications to Confusion-limited Astrophysical Observations", *ApJ*, **656**, 621 (2007).

[68] R. Braakman, G.A. Blake, "The millimeter-wave spectrum of Methoxyacetonitrile", in preparation.

[69] K.M. Marstokk, H. Mollendal, "Microwave-Spectrum, Conformational Equilibria, Intramolecular Hydrogen-Bonding, Dipole-Moment and Centrifugal-Distortion of 3-Hydroxypropanenitrile, *Act. Chem. Scand. A*, **39**, 15–31.

[70] R. Braakman, G.A. Blake, "The millimeter-wave spectrum of 2-Cyanoethanol", in preparation.

[71] R. Kewley, "Microwave Spectrum of Methoxyacetonitrile", *Can. J. Chem.*, **62**, 509 (1974).

[72] S.W. Charles, F.C. Cullen, G.I.L. Jones, N.L. Owen, "Vibrational Spectra, Barriers to Internal-Rotation and Conformation of Propargyl Methyl-Ether and Methoxyacetontrile", *J. Chem. Soc. Far. Trans. II*, **70**, 758–767 (1974).

[73] W.A. Schutte, A.G.G.M. Tielens, S.A. Sandford, "10 Micron Spectra of Protostars and the Solid Methanol Abundance", *A&A*, **382**, 523–529 (1991).

[74] J.H. Lacy, H. Faraji, L.J. Allamandola, "Unraveling the 10 Micron "Silicate" Feature of Protostars: The Detection of Frozen Interstellar Ammonia", *ApJ*, **501**, 105–109 (1998).

[75] E. Dartois, L. d'Hendecourt, W. Thi, K.M. Pontoppidan, E.F. van Dishoeck, "Combined VLT ISAAC/ISO SWS Spectroscopy of Two Protostellar Sources. The Importance of Minor Solid State Features", *A&A*, **394**, 1057–1068 (2002).

[76] A.C.A. Boogert, K.M. Pontoppidan, C. Knez, F. Lahuis, J. Kessler-Silacci, E.F. van Dishoeck, G.A. Blake, J.C. Augereau, S.E. Bisschop, S. Bottinelli, T.Y. Brooke, J. Brown, A. Crapsi, N.J. Evans, II, H.J. Fraser, V. Geers, T.L. Huard, J.K. Jorgensen, K.I. Oberg, L.E. Allen, P.M. Harvey, D.W. Koerner, L.G. Mundy, D.L. Padgett, A.I. Sargent, K.R. Stapelfeldt, "The c2d Spitzer Spectroscopic Survey of Ices around Low-Mass Young Stellar Objects. I. H_2O and the 5-8 μm Bands", *ApJ*, **678**, 985–1004 (2008).

[77] C. Comito, P. Schilke, T.G. Philips, D.C. Lis, F. Motte, D. Mehringer, "A Molecular Line Survey of Orion KL in the 350 Micron Band", *ApJSS*, **394**, 127–167 (2002).

[78] P.H. Siegel, "Terahertz Technology", *IEEE Trans. Micro. Theory. Tech.*, **50**, 910–928 (2002).

[79] M. Tonouchi, "Cutting-Edge Terahertz Technology", *Nature Photonics*, **1**, 97–105 (2007).

[80] Virginia Diodes. http://www.virginiadiodes.com/multipliers.php.

[81] J.E. Bjarnason, T.L.J. Chan, A.W.M. Lee, E.R. Brown, D.C. Driscoll, M. Hanson,

A.C. Gossard, R.E. Muller, "ErAs:GaAs Photomixer with Two-Decade Tunability and 12 μW Peak Output Power", *Appl. Phys. Lett.*, **85**, 3983-3985 (2004).

[82] P.F. Goldsmith, *"Quasioptical Systems: Gaussian Beam Quasioptical Propagation and Applications"*, IEEE press, NJ (1998).

[83] J.U. Grabow, W. Stahl, H. Dreizler, "A Multioctave Coaxially Oriented Beam-Resonator Arrangement Fourier-Transform Microwave Spectrometer", *Rev. Sci. Instr.*, **67**, 4072–4084 (1996).

[84] R.E. Collin, *"Foundations for Microwave Engineering"*, McGraw-Hill press, NY (1966).

[85] T.J. Balle, W.H. Flygare, "Fabry-Perot Cavity Pulsed Fourier-Transform Microwave Spectrometer with a Pulsed Nozzle Particle Source", *Rev. Sci. Instr.*, **52**, 33–45 (1981).

[86] D.R. Lide (Ed.-in-Ch.), *"CRC Handbook of Chemistry and Physics", 76th Edn*, CRC press, FL (1995).

[87] G. Berden, R. Peeters, G. Meijer, "Cavity Ring-Down Spectroscopy: Experimental Schemes and Applications", *Int. Rev. Phys. Chem.*, **19**, 565–607 (2000).

[88] E.J. Campbell, L.W. Buxton, T.J. Balle, W.H. Flygare, "The Theory of Pulsed Fourier Transform Microwave Spectroscopy carried out in a Fabry-Perot Cavity: Static Gas", *J. Chem. Phys.*, **74**, 813–828 (1980).

[89] K.L. Busarow, G.A. Blake, K.B. Laughlin, R.C. Cohen, Y.T. Lee, R.J. Saykally, "Tunable Far-Infrared Laser Spectroscopy in a Planar Supersonic Jet - The Sigma-Bending Vibration of Ar-H35Cl", *Chem. Phys. Lett.*, **141**, 289–291 (1987).

[90] R. Bumgarner, G.A. Blake, "Microwave Direct Absorption Spectroscopy of Weakly

Bound Clusters in a Planar Supersonic Jet: Spectra of Ar-HCN and (HCN)2 from 17.4 - 76.7 GHz", *Chem. Phys. Lett.*, **161**, 308–314 (1989).

[91] B.S. Karasik, A.I. Elantiev, "Noise temperature limit of a superconducting hot-electron bolometer mixer", *Appl. Phys. Lett.*, **68**, 853–855 (1996).

[92] A. Karpov, D. Miller, F. Rice, J.A. Stern, B. Bumble, H.G. LeDuc, J. Zmuidzinas, "Low Noise 1 THz-1.4 THz Mixers Using Nb/Al-AlN/NbTiN SIS Junctions", *IEEE Trans. Appl. Supercond.*, **17**, 343–346 (2007).

[93] A. Nummelin, J.E. Dickens, P. Bergman, A. Hjalmarson, W.M. Irvine, M. Ikeda, M. Ohishi, "Abundances of Ethylene Oxide and Acetaldehyde in Hot Molecular Cloud Cores", *A&A*, **337**, 275–286 (1998).

[94] N. Laman, S.S. Harsha, D. Grischkowski, J.S. Melinger, "High-Resolution Waveguide THz Spectroscopy of Biological Molecules", *Biophys. J.*, **94**, 1010–1020 (2008).

Appendix A

Observed Transitions of Methoxyacetonitrile

Table A.1: Transitions of the *gauche*-conformer of methoxy acetonitrile observed with the IRAM 30 m telescope toward Sgr B2(N). The horizontal lines mark discontinuities in the observed frequency coverage. Only the transitions associated with a modeled line stronger than 20 mK are listed.

N^a	Transition^b	Frequency (MHz)	Unc.^{c} (kHz)	$E_l{}^d$ (K)	$S\mu^2$ (D^2)	σ^e (mK)	Comments
(1)	(2)	(3)	(4)	(5)	(6)	(7)	(8)
1	$13_{7,7} - 12_{7,6}{}^{\star}$	82088.254	8	44	53.2	19	Blend with C_3H_2 in absorption
3	$13_{6,8} - 12_{6,7}$	82154.546	8	39	58.9	19	**Candidate group**, partial blend with CH_3CH_3CO, v_t=1
4	$13_{6,7} - 12_{6,6}$	82154.817	8	39	58.9	19	**Candidate group**, partial blend with CH_3CH_3CO, v_t=1
5	$13_{3,11} - 12_{3,10}$	82169.999	8	27	70.8	19	Blend with U-line and $HC^{13}CCN$, v_5=1/v_7=3
6	$13_{1,12} - 12_{1,11}$	82170.466	8	25	73.6	19	Blend with U-line and $HC^{13}CCN$, v_5=1/v_7=3
7	$14_{2,13} - 13_{2,12}$	86340.648	8	29	78.6	17	Strong $H^{13}CN$
8	$36_{19,17} - 37_{18,20}{}^{\star}$	87908.039	12	348	4.4	17	Blend with U-line and HNCO, v_6=1
10	$36_{19,17} - 37_{18,19}{}^{\star}$	87908.039	12	348	2.8	17	Blend with U-line and HNCO, v_6=1
12	$14_{1,13} - 13_{1,12}$	87908.911	8	29	79.2	17	Blend with U-line and HNCO, v_6=1
13	$15_{1,15} - 14_{1,14}$	88318.581	9	30	85.7	17	Strong C_2H_5CN
14	$14_{9,5} - 13_{9,4}{}^{\star}$	88353.068	8	61	47.3	17	Blend with U-lines and CH_3OCHO
16	$14_{8,7} - 13_{8,6}{}^{\star}$	88382.293	8	54	54.3	17	Blend with $H^{13}CCCN$, v_6=1 and v_7=1
18	$14_{3,12} - 13_{3,11}$	88419.109	8	31	76.8	17	Blend with U-lines
19	$15_{0,15} - 14_{0,14}$	88424.179	9	30	85.7	17	Blend with C_2H_5OCHO and $CH_2(OH)CHO$
20	$14_{7,8} - 13_{7,7}{}^{\star}$	88431.840	8	48	60.5	17	Blend with U-lines
22	$14_{6,9} - 13_{6,8}$	88516.044	8	43	65.8	17	**Candidate group**, partial blend with C_2H_5CN, v_{13}=1/v_{21}=1 and $H^{13}CCCN$, v_7=1
23	$14_{6,8} - 13_{6,7}$	88516.682	8	43	65.8	17	**Candidate group**, partial blend with C_2H_5CN, v_{13}=1/v_{21}=1 and $H^{13}CCCN$, v_7=1
24	$14_{4,11} - 13_{4,10}$	88818.106	8	34	74.1	21	Blend with U-line, c-C_2H_4O, and a$(CH_2OH)_2$
25	$14_{4,10} - 13_{4,9}$	89147.600	8	34	74.1	16	Blend with C_2H_5CN, v_{13}=1/v_{21}=1
26	$34_{3,32} - 33_{4,30}$	90751.409	29	176	4.5	14	Blend with U-lines
27	$14_{3,11} - 13_{3,10}$	90752.210	9	32	77.0	14	Blend with U-lines
28	$14_{2,12} - 13_{2,11}$	91389.955	8	30	79.0	25	Blend with U-lines
29	$15_{2,14} - 14_{2,13}$	92257.818	8	33	84.4	22	Strong CH_3CN, v_8=1
30	$15_{1,14} - 14_{1,13}$	93582.975	9	33	84.8	24	Strong CH_3CHO
31	$16_{1,16} - 15_{1,15}$	94071.644	9	35	91.5	31	Blend with CH_3CH_3CO, v_t=1 and $^{13}CH_3OH$, v_t=1
32	$16_{0,16} - 15_{0,15}$	94144.155	9	35	91.5	31	Blend with CH_3OCH_3
33	$15_{3,13} - 14_{3,12}$	94632.371	8	36	82.8	26	Blend with CH_3OCHO and CH_3CH_3CO
34	$15_{10,5} - 14_{10,4}{}^{\star}$	94659.674	8	74	48.0	28	Blend with C_2H_3CN, v_{11}=1/v_{15}=1
36	$15_{9,6} - 14_{9,5}{}^{\star}$	94681.673	8	66	55.3	28	Blend with U-lines
38	$17_{6,12} - 17_{5,12}$	94682.930	12	57	8.7	28	Blend with U-lines
39	$15_{8,8} - 14_{8,7}{}^{\star}$	94719.367	8	59	61.8	28	Blend with U-lines
41	$15_{7,9} - 14_{7,8}{}^{\star}$	94781.913	8	52	67.6	28	**Candidate group**
43	$15_{6,10} - 14_{6,9}$	94886.861	8	47	72.6	28	Blend with C_2H_3CN, v_{15}=1 and CH_3NH_2

Table A.1: continued.

N^a	Transition^b	Frequency (MHz)	Unc.^{c} (kHz)	$E_l{}^d$ (K)	$S\mu^2$ (D^2)	σ^e (mK)	Comments
(1)	(2)	(3)	(4)	(5)	(6)	(7)	(8)
44	$26_{2,24} - 26_{2,25}$	94887.224	29	105	2.3	28	Blend with C_2H_3CN, v_{15}=1 and CH_3NH_2
45	$15_{6,9} - 14_{6,8}$	94888.267	8	47	72.6	28	Blend with C_2H_3CN, v_{15}=1 and CH_3NH_2
46	$15_{5,11} - 14_{5,10}$	95059.825	8	42	76.8	28	Blend with C_2H_3CN, v_{15}=1
47	$15_{5,10} - 14_{5,9}$	95096.082	8	42	76.8	28	Blend with C_2H_3CN, v_{15}=1
48	$15_{4,12} - 14_{4,11}$	95212.915	8	39	80.2	28	Strong C_2H_3CN, v=0 and v_{11}=1
49	$27_{6,21} - 27_{5,23}$	95731.786	14	126	11.3	23	Strong CH_3OCH_3
50	$15_{4,11} - 14_{4,10}$	95732.432	8	39	80.2	23	Strong CH_3OCH_3
51	$15_{3,12} - 14_{3,11}$	97580.765	9	36	83.1	20	Strong CH_3OH
52	$15_{2,13} - 14_{2,12}$	97689.045	8	34	84.7	20	Strong $^{13}CH_3CH_2CN$, C_2H_5CN, v_{13}=1/v_{21}=1, and $C_2H_5{}^{13}CN$
53	$16_{2,15} - 15_{2,14}$	98141.361	9	37	90.2	20	Blend with $CH_3{}^{13}CH_2CN$ and U-line
54	$16_{1,15} - 15_{1,14}$	99220.556	9	37	90.5	19	Blend with $HC^{13}C^{13}CN$ and strong H_β recombination line
55	$17_{1,17} - 16_{1,16}$	99819.672	10	39	97.2	14	Blend with $HCC^{13}CN$, v_6=1
56	$17_{0,17} - 16_{0,16}$	99868.953	10	39	97.2	14	Blend with CCS, CH_3OCHO, v_t=1, and NH_2CH_2CN
57	$16_{3,14} - 15_{3,13}$	100805.873	8	40	88.7	20	Blend with CH_3CH_3CO, NH_2CH_2CN, and U-line
58	$16_{13,3} - 15_{13,2}{}^\star$	100962.342	9	107	31.3	20	Partial blend with CH_2CO, uncertain baseline
60	$16_{12,4} - 15_{12,3}{}^\star$	100962.477	9	97	40.3	20	Partial blend with CH_2CO, uncertain baseline
62	$16_{14,2} - 15_{14,1}{}^\star$	100967.473	9	118	21.6	20	Blend with CH_2CO and U-line
64	$23_{15,8} - 24_{14,11}{}^\star$	100968.455	16	173	1.8	20	Blend with CH_2CO and U-line
66	$23_{15,8} - 24_{14,10}{}^\star$	100968.455	16	173	1.1	20	Blend with CH_2CO and U-line
68	$16_{11,5} - 15_{11,4}{}^\star$	100969.367	9	87	48.6	20	Blend with CH_2CO and U-line
70	$27_{3,25} - 27_{1,26}$	100970.875	28	112	2.3	20	Blend with CH_2CO and U-line
71	$16_{10,6} - 15_{10,5}{}^\star$	100985.294	9	78	56.2	21	Blend with C_2H_5OH
73	$16_{9,7} - 15_{9,6}{}^\star$	101013.914	9	70	63.0	21	**Candidate group**, partial blend with U-line and CH_3CH_3CO, v_t=1
75	$31_{5,27} - 30_{6,25}$	101015.693	19	157	6.7	21	**Candidate group**, partial blend with U-line and CH_3CH_3CO, v_t=1
76	$16_{8,9} - 15_{8,8}{}^\star$	101061.412	9	63	69.1	21	Blend with U-lines
78	$16_{7,10} - 15_{7,9}{}^\star$	101138.960	8	57	74.5	21	Strong U-line
80	$16_{6,11} - 15_{6,10}$	101267.615	8	51	79.2	21	**Candidate group**, uncertain baseline
81	$16_{6,10} - 15_{6,9}$	101270.538	8	51	79.2	21	**Candidate group**, uncertain baseline
82	$16_{5,12} - 15_{5,11}$	101471.510	8	47	83.2	16	Blend with CH_3OH, CH_3CH_3CO, and H_2CS
83	$16_{5,11} - 15_{5,10}$	101536.219	9	47	83.2	16	Partial blend with C_2H_5OH, uncertain baseline
84	$16_{4,13} - 15_{4,12}$	101600.336	8	43	86.4	16	**Missing line**, but uncertain baseline?
85	$16_{4,12} - 15_{4,11}$	102384.952	9	43	86.4	30	Blend with U-line
86	$58_{28,30} - 59_{27,33}{}^\star$	103869.273	314	840	8.0	38	Blend with C_2H_5CN and $CH_2{}^{13}CHCN$
88	$58_{28,30} - 59_{27,32}{}^\star$	103869.273	314	840	5.1	38	Blend with C_2H_5CN and $CH_2{}^{13}CHCN$
90	$16_{2,14} - 15_{2,13}$	103870.967	8	39	90.4	38	Blend with C_2H_5CN and $CH_2{}^{13}CHCN$
91	$17_{2,16} - 16_{2,15}$	103994.816	9	42	96.0	38	Blend with C_2H_3CN, v_{11}=1/v_{15}=1, U-line, and $CH_2CH^{13}CN$
92	$16_{3,13} - 15_{3,12}$	104386.983	9	41	89.1	48	Blend with U-line, $^{34}SO_2$, and C_2H_5CN
93	$17_{1,16} - 16_{1,15}$	104845.503	9	42	96.2	25	Blend with U-lines and C_2H_3CN, v_{11}=1/v_{15}=1
94	$18_{1,18} - 17_{1,17}$	105563.935	10	44	103.0	37	Blend with C_2H_5OCHO, CH_3OCH_3, and CH_3CH_3CO
95	$18_{0,18} - 17_{0,17}$	105597.140	10	44	103.0	37	Blend with U-lines
96	$17_{3,15} - 16_{3,14}$	106936.791	9	45	94.6	24	Blend with U-lines and C_2H_5CN, v_{13}=1/v_{21}=1
97	$17_{13,4} - 16_{13,3}{}^\star$	107279.367	9	112	40.7	24	Blend with NH_2CH_2CN and $^{13}C^{17}O$
99	$17_{12,5} - 16_{12,4}{}^\star$	107282.022	9	101	49.1	24	Blend with NH_2CH_2CN and $^{13}C^{17}O$
101	$17_{14,3} - 16_{14,2}{}^\star$	107282.831	9	123	31.5	24	Blend with NH_2CH_2CN and $^{13}C^{17}O$
103	$17_{15,2} - 16_{15,1}{}^\star$	107291.210	9	135	21.7	24	Blend with $^{13}C^{17}O$ and U-line
105	$17_{11,6} - 16_{11,5}{}^\star$	107292.581	9	92	56.9	24	Blend with $^{13}C^{17}O$ and U-line
107	$22_{15,7} - 23_{14,10}{}^\star$	107295.130	16	166	1.5	24	Blend with $^{13}C^{17}O$ and U-line
109	$22_{15,7} - 23_{14,9}{}^\star$	107295.130	16	166	0.9	24	Blend with $^{13}C^{17}O$ and U-line
111	$17_{10,7} - 16_{10,6}{}^\star$	107313.786	9	83	64.0	24	Blend with U-line
113	$17_{9,8} - 16_{9,7}{}^\star$	107350.032	9	75	70.5	24	Blend with CH_3CH_3CO, v=0 and v_t=1, and U-line
115	$32_{6,26} - 31_{7,24}$	107352.941	22	172	7.0	24	Blend with CH_3CH_3CO, v=0 and v_t=1, and U-line
116	$17_{8,10} - 16_{8,9}{}^\star$	107408.769	9	68	76.2	24	Blend with CH_3C_3N and U-line
118	$17_{7,11} - 16_{7,10}$	107503.471	9	62	81.3	24	Strong C_2H_5CN, v=0 and v_{13}=1/v_{21}=1
119	$17_{7,10} - 16_{7,9}$	107503.660	9	62	81.3	24	Strong C_2H_5CN, v=0 and v_{13}=1/v_{21}=1
120	$48_{2,46} - 47_{3,44}$	107506.104	66	343	4.5	24	Strong C_2H_5CN, v=0 and v_{13}=1/v_{21}=1
121	$26_{1,25} - 26_{1,26}$	107656.653	38	99	1.3	24	Blend with U-line
122	$26_{1,25} - 26_{0,26}$	107658.754	38	99	7.6	24	Blend with U-line
123	$17_{6,12} - 16_{6,11}$	107658.861	9	56	85.7	24	Blend with U-line
124	$17_{6,11} - 16_{6,10}$	107664.634	9	56	85.7	24	Blend with $CH_2(OH)CHO$, uncertain baseline
125	$17_{5,13} - 16_{5,12}$	107893.080	9	52	89.5	46	Blend with C_2H_5OH, noisy
126	$17_{4,14} - 16_{4,13}$	107974.255	9	48	92.5	46	Blend with $^{13}CH_2CHCN$ and C_2H_5CN, v_{13}=1/v_{21}=1

Table A.1: continued.

N^a (1)	Transition^b (2)	Frequency (MHz) (3)	Unc.^{c} (kHz) (4)	$E_l{}^d$ (K) (5)	$S\mu^2$ (D^2) (6)	σ^e (mK) (7)	Comments (8)
127	$17_{5,12} - 16_{5,11}$	108003.802	9	52	89.5	46	**Candidate line**, noisy
128	$10_{3,8} - 9_{2,8}$	109109.925	7	15	5.3	29	Strong $O^{13}CS$ and $CH_2(OH)CHO$
129	$17_{4,13} - 16_{4,12}$	109111.540	9	48	92.5	29	Strong $O^{13}CS$ and $CH_2(OH)CHO$
130	$18_{2,17} - 17_{2,16}$	109822.104	9	47	101.8	41	Blend with CH_3CN, v_4=1
131	$29_{3,27} - 29_{2,28}$	109822.607	31	129	15.2	41	Blend with CH_3CN, v_4=1
132	$17_{2,15} - 16_{2,14}$	109927.760	8	44	96.1	41	Blend with CH_3OCHO, v_t=1 and U-line
133	$18_{1,17} - 17_{1,16}$	110474.259	9	47	101.9	32	Blend with $^{13}CH_3CH_2CN$ and U-lines
134	$17_{3,14} - 16_{3,13}$	111139.786	9	46	95.1	25	Blend with U-line and CH_3CH_3CO
135	$19_{1,19} - 18_{1,18}$	111305.372	10	49	108.8	35	Blend with U-line, uncertain baseline
136	$19_{0,19} - 18_{0,18}$	111327.582	10	49	108.8	35	Blend with U-line and C_2H_3CN, v_{11}=2
137	$18_{3,16} - 17_{3,15}$	113023.465	9	50	100.5	40	**Missing line**, but uncertain baseline?
138	$18_{13,5} - 17_{13,4}{}^\star$	113597.618	9	117	49.6	28	Blend with U-line and CH_3COOH
140	$18_{14,4} - 17_{14,3}{}^\star$	113599.057	9	128	41.0	28	Blend with U-line and CH_3COOH
142	$18_{12,6} - 17_{12,5}{}^\star$	113603.246	9	107	57.6	28	Blend with U-line and CH_3COOH
144	$18_{15,3} - 17_{15,2}{}^\star$	113606.135	9	141	31.7	28	Blend with U-line and CH_3COOH
146	$21_{15,6} - 22_{14,9}{}^\star$	113617.691	17	159	1.2	34	Strong $^{13}CH_3CH_2CN$
148	$21_{15,6} - 22_{14,8}{}^\star$	113617.691	17	159	0.8	34	Strong $^{13}CH_3CH_2CN$
150	$18_{16,2} - 17_{16,1}{}^\star$	113617.854	10	153	21.8	34	Strong $^{13}CH_3CH_2CN$
152	$18_{11,7} - 17_{11,6}{}^\star$	113618.062	9	97	65.0	34	Strong $^{13}CH_3CH_2CN$
154	$18_{10,8} - 17_{10,7}{}^\star$	113645.325	9	88	71.7	34	Strong $^{13}CH_3CH_2CN$ and C_2H_5CN
156	$18_{9,10} - 17_{9,9}{}^\star$	113690.267	9	80	77.8	34	Strong $^{13}CH_3CH_2CN$
158	$18_{8,11} - 17_{8,10}{}^\star$	113761.780	9	73	83.2	34	Blend with CH_3OCHO, C_3H_7CN, and U-line
160	$18_{7,12} - 17_{7,11}$	113875.944	9	67	88.0	34	Blend with U-line and C_2H_5OH
161	$18_{7,11} - 17_{7,10}$	113876.354	9	67	88.0	34	Blend with U-line and C_2H_5OH
162	$46_{9,38} - 46_{8,38}$	113878.837	39	358	19.6	34	Blend with U-line and C_2H_5OH
163	$18_{6,13} - 17_{6,12}$	114061.039	9	61	92.2	33	Strong C_2H_3CN, v_{15}=1, C_2H_5OH, and C_2H_3CN
164	$18_{6,12} - 17_{6,11}$	114071.946	9	61	92.2	33	Blend with C_2H_3CN, v_{15}=1 and U-line
165	$18_{5,14} - 17_{5,13}$	114322.597	9	57	95.7	33	Blend with C_2H_5CN, v_{13}=1/v_{21}=1
166	$30_{3,28} - 30_{1,29}$	114323.839	33	137	2.4	33	Blend with C_2H_5CN, v_{13}=1/v_{21}=1
167	$18_{4,15} - 17_{4,14}$	114328.288	9	53	98.5	33	Blend with C_2H_5CN, v_{13}=1/v_{21}=1 and U-line
168	$18_{5,13} - 17_{5,12}$	114504.944	9	57	95.7	37	Blend with $^{13}CH_3CH_2CN$ and U-line
169	$59_{29,30} - 60_{28,33}{}^\star$	114506.465	403	881	7.9	37	Blend with $^{13}CH_3CH_2CN$ and U-line
171	$59_{29,30} - 60_{28,32}{}^\star$	114506.465	403	881	5.0	37	Blend with $^{13}CH_3CH_2CN$ and U-line
173	$19_{2,18} - 18_{2,17}$	115627.251	9	52	107.6	79	Blend with CH_3CHO
174	$18_{2,16} - 17_{2,15}$	115857.429	9	49	101.7	79	Blend with U-line, C_3H_7CN, and $a(CH_2OH)_2$
175	$18_{4,14} - 17_{4,13}{}^\star$	115912.133	9	53	98.6	79	Strong $CH_3{}^{13}CH_2CN$, $C_2H_5{}^{13}CN$, CH_3CHO, and C_2H_5CN, v_{13}=1/v_{21}=1
177	$67_{1,66} - 66_{2,64}$	115912.231	287	642	3.0	79	Strong $CH_3{}^{13}CH_2CN$, $C_2H_5{}^{13}CN$, CH_3CHO, and C_2H_5CN, v_{13}=1/v_{21}=1
178	$23_{15,8} - 22_{15,7}{}^\star$	145190.415	9	171	76.1	25	Blend with $CH_2(OH)CHO$, CH_3NH_2, and U-line
180	$23_{16,7} - 22_{16,6}{}^\star$	145194.470	10	184	68.4	25	Blend with $CH_2(OH)CHO$, CH_3NH_2, and U-line
182	$23_{14,9} - 22_{14,8}{}^\star$	145194.743	9	159	83.4	25	Blend with $CH_2(OH)CHO$, CH_3NH_2, and U-line
184	$23_{13,10} - 22_{13,9}{}^\star$	145209.530	9	147	90.2	25	Blend with C_2H_5CN, v_{13}=1/v_{21}=1 and U-line
186	$23_{18,5} - 22_{18,4}{}^\star$	145222.219	10	212	51.4	25	Blend with U-line and SiS
188	$23_{12,11} - 22_{12,10}{}^\star$	145237.768	9	137	96.4	25	Blend with U-line
190	$23_{11,12} - 22_{11,11}{}^\star$	145283.919	9	127	102.2	25	Blend with NH_2CH_2CN and $HC^{13}CCN$, v_7=1
192	$70_{10,60} - 70_{9,61}$	145285.765	409	799	84.6	25	Blend with NH_2CH_2CN and $HC^{13}CCN$, v_7=1
193	$23_{10,14} - 22_{10,13}{}^\star$	145354.890	8	119	107.5	25	Blend with C_3H_7CN and HC_3N, v_4=1
195	$47_{7,41} - 46_{8,38}$	145355.085	68	358	6.6	25	Blend with C_3H_7CN and HC_3N, v_4=1
196	$23_{9,15} - 22_{9,14}{}^\star$	145461.918	8	111	112.2	25	Blend with CH_3CH_3CO, v_t=1 and $a(CH_2OH)_2$
198	$30_{9,22} - 30_{8,22}$	145462.396	13	168	15.1	25	Blend with CH_3CH_3CO, v_t=1 and $a(CH_2OH)_2$
199	$30_{9,21} - 30_{8,22}$	145465.695	13	168	29.7	25	Blend with CH_3CH_3CO, v_t=1 and $a(CH_2OH)_2$
200	$23_{9,15} - 23_{8,15}{}^\star$	147479.128	12	111	11.5	31	Strong CH_3CN, v_8=1 and $^{13}CH_3CH_2CN$
202	$23_{9,15} - 23_{8,16}{}^\star$	147480.048	12	111	20.8	31	Strong CH_3CN, v_8=1 and $^{13}CH_3CH_2CN$
204	$22_{9,14} - 22_{8,14}{}^\star$	147641.986	12	104	11.0	31	Blend with CH_3OCHO and U-line
206	$22_{9,14} - 22_{8,15}{}^\star$	147642.436	12	104	19.6	31	Blend with CH_3OCHO and U-line
208	$21_{9,13} - 21_{8,13}{}^\star$	147782.439	12	97	10.4	31	Blend with C_2H_5CN
210	$21_{9,13} - 21_{8,14}{}^\star$	147782.652	12	97	18.3	31	Blend with C_2H_5CN
212	$45_{8,38} - 44_{9,35}$	147785.690	24	335	11.1	31	Blend with C_2H_5CN
213	$23_{5,18} - 22_{5,17}$	147803.034	9	88	126.2	31	Blend with CH_3CH_3CO, v_t=1
214	$48_{5,43} - 48_{5,44}$	154482.736	39	365	5.1	112	Strong CH_3CHO, v_t=1 and C_2H_5CN
215	$72_{10,62} - 72_{10,63}$	154485.497	587	843	7.7	112	Strong CH_3CHO, v_t=1 and C_2H_5CN
216	$25_{3,23} - 24_{3,22}$	154486.327	8	94	141.0	112	Strong CH_3CHO, v_t=1 and C_2H_5CN

Table A.1: continued.

N^a	Transition[b]	Frequency (MHz)	Unc.[c] (kHz)	E_l[d] (K)	$S\mu^2$ (D^2)	σ^e (mK)	Comments
(1)	(2)	(3)	(4)	(5)	(6)	(7)	(8)
217	$24_{5,19} - 23_{5,18}$	154670.360	9	95	132.3	112	Strong $^{13}CH_3OH$, HC_3N, v_5=1/v_7=3, and CH_3CHO, v_t=1
218	$27_{2,25} - 26_{2,24}$	166516.847	8	109	152.6	66	Strong $^{13}CH_2CHCN$ and CH_3CN, v_8=2
219	$27_{3,24} - 26_{3,23}$	172476.516	8	113	152.2	44	Strong C_2H_3CN and C_2H_5CN
220	$27_{6,21} - 26_{6,20}$	172860.307	8	122	147.9	44	Strong C_2H_5CN and HC_3N, v_5=1/v_7=3
221	$32_{18,14} - 31_{18,13}$*	202043.346	8	286	126.0	138	Strong CH_3CN and HC_3N, v_5=1/v_7=3
223	$32_{17,15} - 31_{17,14}$*	202045.044	8	271	132.3	138	Strong CH_3CN and HC_3N, v_5=1/v_7=3
225	$24_{4,20} - 23_{3,20}$	202050.783	10	90	15.5	138	Strong HC_3N, v_5=1/v_7=3
226	$32_{19,13} - 31_{19,12}$*	202052.532	8	301	119.4	138	Strong HC_3N, v_5=1/v_7=3
228	$32_{16,16} - 31_{16,15}$*	202059.775	7	257	138.3	138	Strong $CH_3{}^{13}CN$
230	$32_{20,12} - 31_{20,11}$*	202070.978	8	317	112.3	138	Strong $CH_3{}^{13}CN$ and CH_3NH_2
232	$58_{5,53} - 58_{5,54}$	202075.890	64	522	5.5	138	Strong $CH_3{}^{13}CN$ and CH_3NH_2
233	$26_{22,4} - 27_{21,7}$*	202090.368	45	299	0.5	138	Strong H_2CCO
235	$26_{22,4} - 27_{21,6}$*	202090.368	45	299	0.3	138	Strong H_2CCO
237	$32_{15,17} - 31_{15,16}$*	202090.451	7	244	143.8	138	Strong H_2CCO
239	$32_{21,11} - 31_{21,10}$*	202097.438	9	335	105.0	138	Strong H_2CCO
241	$13_{4,10} - 12_{1,11}$	202125.371	15	25	0.2	138	Blend with U-line and CH_3CH_3CO, v_t=1
242	$32_{22,10} - 31_{22,9}$*	202130.942	9	352	97.2	138	Blend with U-line and CH_3CH_3CO, v_t=1
244	$63_{12,51} - 62_{13,49}$	202131.495	82	664	14.0	138	Blend with U-line and CH_3CH_3CO, v_t=1
245	$58_{6,53} - 58_{5,54}$	202140.853	64	522	38.7	138	Blend with CH_3CH_3CO, v_t=1
246	$32_{14,18} - 31_{14,17}$*	202141.090	7	232	149.1	138	Blend with CH_3CH_3CO, v_t=1
248	$58_{6,53} - 58_{4,54}$	202145.016	64	522	5.5	138	Blend with CH_3CH_3CO, v_t=1
249	$32_{24,8} - 31_{24,7}$*	202216.163	9	391	80.7	138	Strong CH_3CN and $CH_3{}^{13}CN$
251	$32_{13,19} - 31_{13,18}$*	202217.402	7	221	154.0	138	Strong CH_3CN and $CH_3{}^{13}CN$
253	$21_{4,18} - 20_{3,18}$	202254.904	12	67	10.0	138	Strong $CH_3{}^{13}CN$ and CH_3CN
254	$32_{26,6} - 31_{26,5}$*	202322.124	10	432	62.7	108	Strong CH_3CN
256	$22_{7,16} - 22_{5,17}$	202323.896	25	88	0.2	108	Strong CH_3CN
257	$32_{12,21} - 31_{12,20}$*	202327.743	7	211	158.4	108	Strong CH_3CN
259	$32_{11,22} - 31_{11,21}$*	202484.841	7	201	162.6	108	Strong $H_2C^{34}S$ and CH_3OCH_3
261	$32_{5,28} - 31_{5,27}$	202596.083	7	162	179.3	108	Blend with CH_3CH_3CO and U-line
262	$26_{2,24} - 26_{1,26}$	202635.551	66	99	0.2	108	Strong CH_3CN, v_8=1 and $H_3C^{13}CN$, v_8=1
263	$32_{4,29} - 31_{3,28}$	202637.864	9	157	30.3	108	Strong CH_3CN, v_8=1 and $H_3C^{13}CN$, v_8=1
264	$21_{3,19} - 20_{2,19}$	202684.856	19	64	7.3	108	Strong C_2H_3CN, v_{15}=1 and $HCONH_2$
265	$17_{6,12} - 16_{5,11}$	202686.732	10	52	12.5	108	Strong C_2H_3CN, v_{15}=1 and $HCONH_2$
266	$17_{6,11} - 16_{5,11}$	202697.901	10	52	10.1	108	Strong $HCONH_2$
267	$32_{10,23} - 31_{10,22}$	202709.010	7	192	166.3	108	Strong CH_3CN, v_8=1
268	$32_{10,22} - 31_{10,21}$	202709.241	7	192	166.3	108	Strong CH_3CN, v_8=1
269	$17_{6,12} - 16_{5,12}$	202824.840	10	52	10.1	138	Strong CH_3CN, v_8=1
270	$17_{6,11} - 16_{5,12}$	202836.010	10	52	12.5	138	Strong CH_3CN, v_8=1
271	$35_{0,35} - 34_{1,34}$*	203000.988	13	167	61.7	138	Blend with $CH_3{}^{13}CH_2CN$, uncertain baseline
273	$35_{0,35} - 34_{0,34}$*	203001.047	13	167	200.9	138	Blend with $CH_3{}^{13}CH_2CN$, uncertain baseline
275	$32_{9,24} - 31_{9,23}$	203033.583	7	184	169.8	138	Strong $H_3C^{13}CN$, v_8=1 and $CH_3{}^{13}CH_2CN$
276	$72_{10,63} - 72_{9,64}$	203034.825	256	833	71.5	138	Strong $H_3C^{13}CN$, v_8=1 and $CH_3{}^{13}CH_2CN$
277	$73_{9,64} - 73_{8,65}$	203035.943	350	855	71.7	138	Strong $H_3C^{13}CN$, v_8=1 and $CH_3{}^{13}CH_2CN$
278	$32_{9,23} - 31_{9,22}$	203037.983	7	184	169.8	138	Strong $H_3C^{13}CN$, v_8=1 and $CH_3{}^{13}CH_2CN$
279	$31_{5,26} - 30_{5,25}$	203038.588	7	154	174.4	138	Strong $H_3C^{13}CN$, v_8=1 and $CH_3{}^{13}CH_2CN$
280	$33_{3,30} - 32_{4,29}$	203044.551	8	167	32.2	138	Strong $H_3C^{13}CN$, v_8=1 and $CH_3{}^{13}CH_2CN$
281	$60_{13,47} - 60_{12,48}$	203046.926	22	617	65.8	138	Strong $H_3C^{13}CN$, v_8=1 and $CH_3{}^{13}CH_2CN$
282	$40_{6,34} - 39_{7,33}$	203492.903	35	258	14.1	161	Strong $^{34}SO_2$ and CH_3CN, v_8=2
283	$66_{37,29} - 67_{36,32}$*	203501.514	1938	1229	6.6	161	Strong $^{34}SO_2$ and CH_3CN, v_8=2
285	$32_{8,25} - 31_{8,24}$	203501.898	7	178	172.8	161	Strong $^{34}SO_2$ and CH_3CN, v_8=2
286	$32_{8,24} - 31_{8,23}$	203564.034	7	178	172.8	161	Strong CH_3CN, v_8=2, CH_3OCH_3, and $^{13}CH_2CHCN$
287	$21_{5,16} - 20_{4,16}$	203599.923	12	71	11.8	161	Strong CH_3OCHO and CH_3CH_3CO
288	$32_{7,26} - 31_{7,25}$	204059.242	7	171	175.5	364	Blend with $H^{13}CCCN$, v_7=2 and U-line
289	$32_{6,27} - 31_{6,26}$	204133.917	7	166	177.7	316	Strong $^{34}SO_2$
290	$9_{9,0} - 8_{8,1}$*	205151.002	11	38	15.9	100	Strong $CH_3{}^{13}CH_2CN$ and C_2H_5CN
292	$9_{9,0} - 8_{8,0}$*	205151.002	11	38	10.5	100	Strong $CH_3{}^{13}CH_2CN$ and C_2H_5CN
294	$22_{5,18} - 21_{4,17}$	205212.879	17	78	11.2	100	Blend with CH_3CH_3CO
295	$69_{6,63} - 68_{7,61}$	205215.743	219	739	11.3	100	Blend with CH_3CH_3CO
296	$33_{3,30} - 32_{3,29}$	205622.877	7	166	186.1	271	Strong U-line and $CH_3{}^{13}CH_2CN$
297	$20_{5,15} - 19_{4,16}$	205902.480	10	64	10.4	271	Strong $C_2H_5{}^{13}CN$ and CH_3OCHO
298	$34_{2,32} - 33_{3,31}$	206130.605	8	171	43.6	280	Strong C_2H_5CN and $H_2{}^{13}CO$
299	$70_{14,57} - 69_{15,54}$	206220.445	177	827	18.4	280	Strong C_2H_5CN
300	$34_{3,32} - 33_{3,31}$	206224.737	8	171	192.7	280	Strong C_2H_5CN

Table A.1: continued.

N^a	Transition^b	Frequency (MHz)	Unc.^{c} (kHz)	$E_l{}^d$ (K)	$S\mu^2$ (D^2)	σ^e (mK)	Comments
(1)	(2)	(3)	(4)	(5)	(6)	(7)	(8)
301	$34_{2,32} - 33_{2,31}$	206267.401	8	171	192.7	280	Strong C_2H_5CN and CH_3OCHO
302	$34_{3,32} - 33_{2,31}$	206361.534	8	171	43.6	280	Strong CH_3OCHO
303	$32_{4,28} - 31_{4,27}$	206409.064	7	161	180.4	106	Strong CH_3NH_2 and C_2H_5CN
304	$12_{8,5} - 11_{7,4}{}^\star$	206649.723	11	41	14.5	106	Strong C_2H_5CN
306	$12_{8,4} - 11_{7,5}{}^\star$	206649.724	11	41	14.5	106	Strong C_2H_5CN
308	$32_{6,26} - 31_{6,25}$	207392.477	7	167	178.0	282	Strong C_2H_5CN, v=0 and v_{13}=1/v_{21}=1
309	$56_{13,43} - 56_{12,44}$	207443.013	16	545	59.8	282	Blend with C_2H_5CN, v_{13}=1/v_{21}=1 and C_2H_5OH
310	$35_{1,34} - 34_{2,33}$	207448.633	10	174	53.8	282	Blend with C_2H_5CN, v_{13}=1/v_{21}=1 and C_2H_5OH
311	$35_{2,34} - 34_{2,33}$	207450.988	10	174	199.6	282	Blend with C_2H_5CN, v_{13}=1/v_{21}=1 and C_2H_5OH
312	$35_{1,34} - 34_{1,33}$	207452.208	10	174	199.6	282	Blend with C_2H_5CN, v_{13}=1/v_{21}=1 and C_2H_5OH
313	$35_{2,34} - 34_{1,33}$	207454.562	10	174	53.8	282	Blend with C_2H_5CN, v_{13}=1/v_{21}=1 and C_2H_5OH
314	$33_{4,30} - 32_{3,29}$	207511.935	8	166	32.3	282	Blend with U-line and C_2H_5CN
315	$22_{5,17} - 21_{4,17}$	208003.035	13	78	12.6	173	Strong $CH_2CH^{13}CN$
316	$51_{3,49} - 51_{2,50}{}^\star$	208012.557	107	381	15.4	173	Blend with $CH_2{}^{13}CHCN$
318	$15_{7,9} - 14_{6,8}{}^\star$	208021.369	10	47	13.6	173	Blend with $CH_2{}^{13}CHCN$
320	$67_{13,54} - 66_{14,52}$	208021.739	135	753	14.7	173	Blend with $CH_2{}^{13}CHCN$
321	$15_{7,9} - 14_{6,9}{}^\star$	208022.437	10	47	10.0	173	Blend with $CH_2{}^{13}CHCN$
323	$29_{4,26} - 29_{1,28}$	208029.081	51	129	0.6	173	Blend with $CH_2{}^{13}CHCN$
324	$23_{5,19} - 22_{4,18}$	208167.623	19	84	11.4	173	Strong $CH_2CH^{13}CN$ and C_2H_5CN
325	$66_{7,59} - 66_{6,60}$	208349.801	125	689	54.8	168	Strong CH_3CH_3CO, $HCC^{13}CN$, and C_2H_5CN
326	$33_{18,15} - 32_{18,14}{}^\star$	208356.192	8	295	133.5	168	Strong CH_3CH_3CO, $HCC^{13}CN$, and C_2H_5CN
328	$25_{4,21} - 25_{1,24}$	208356.829	67	97	0.2	168	Strong CH_3CH_3CO, $HCC^{13}CN$, and C_2H_5CN
329	$33_{17,16} - 32_{17,15}{}^\star$	208361.304	7	281	139.7	168	Strong CH_3CH_3CO, $HCC^{13}CN$, and C_2H_5CN
331	$33_{19,14} - 32_{19,13}{}^\star$	208362.829	8	311	127.1	168	Strong CH_3CH_3CO, $HCC^{13}CN$, and C_2H_5CN
333	$25_{22,3} - 26_{21,6}{}^\star$	208367.020	45	291	0.4	168	Strong CH_3CH_3CO, $HCC^{13}CN$, and C_2H_5CN
335	$73_{10,64} - 73_{8,65}$	208370.355	273	855	7.9	168	Strong CH_3CH_3CO, $HCC^{13}CN$, and C_2H_5CN
336	$33_{20,13} - 32_{20,12}{}^\star$	208379.437	8	327	120.3	168	Strong C_2H_5CN and CH_3CH_3CO
338	$33_{16,17} - 32_{16,16}{}^\star$	208380.527	7	267	145.4	168	Strong C_2H_5CN and CH_3CH_3CO
340	$33_{21,12} - 32_{21,11}{}^\star$	208404.650	8	344	113.1	168	Strong C_2H_5CN
342	$33_{15,18} - 32_{15,17}{}^\star$	208417.056	7	254	150.9	168	Strong C_2H_5CN
344	$33_{22,11} - 32_{22,10}{}^\star$	208437.405	9	362	105.6	168	Strong C_2H_5CN
346	$55_{13,43} - 55_{12,44}$	208469.871	15	528	58.3	168	Strong C_2H_5CN
347	$33_{14,19} - 32_{14,18}{}^\star$	208475.316	7	242	155.9	168	Strong C_2H_5CN
349	$33_{23,10} - 32_{23,9}{}^\star$	208476.862	9	381	97.8	168	Strong C_2H_5CN
351	$55_{13,42} - 55_{12,44}$	208484.222	15	528	26.4	168	Strong C_2H_5CN
352	$33_{13,20} - 32_{13,19}{}^\star$	208561.595	7	231	160.6	168	Blend with U-line
354	$33_{5,29} - 32_{5,28}$	208600.778	7	171	185.1	168	Blend with C_2H_5CN, v_{13}=1/v_{21}=1
355	$33_{12,22} - 32_{12,21}{}^\star$	208685.128	6	220	165.0	168	Strong $CH_2{}^{13}CHCN$
357	$33_{27,6} - 32_{27,5}{}^\star$	208690.017	10	464	62.8	168	Strong $CH_2{}^{13}CHCN$
359	$36_{0,36} - 35_{1,35}{}^\star$	208723.468	14	177	63.6	160	Blend with U-line, CH_3OCHO, and CH_3CHO
361	$36_{0,36} - 35_{0,35}{}^\star$	208723.505	14	177	206.7	160	Blend with U-line, CH_3OCHO, and CH_3CHO
363	$18_{6,13} - 17_{5,12}$	208743.969	10	57	12.7	160	Strong $HCONH_2$ and CH_3CH_3CO
364	$74_{9,65} - 74_{8,66}$	208748.607	372	877	71.7	160	Strong $HCONH_2$ and CH_3CH_3CO
365	$18_{6,12} - 17_{5,12}$	208766.045	10	57	10.5	160	Blend with U-line
366	$33_{11,23} - 32_{11,22}{}^\star$	208860.033	6	211	169.0	160	Strong $HCC^{13}CN$, v_6=1 and v_7=1
368	$18_{6,13} - 17_{5,13}$	208992.799	10	57	10.5	160	Strong $^{13}CH_3OH$ and C_2H_5CN
369	$18_{6,12} - 17_{5,13}$	209014.875	10	57	12.7	160	Strong C_2H_5CN
370	$33_{10,24} - 32_{10,23}$	209108.921	6	202	172.7	160	Strong C_2H_5OH and U-line
371	$33_{10,23} - 32_{10,22}$	209109.335	6	202	172.7	160	Strong C_2H_5OH and U-line
372	$54_{13,42} - 54_{12,42}$	209109.610	15	511	26.0	160	Strong C_2H_5OH and U-line
373	$34_{3,31} - 33_{4,30}$	209323.411	7	176	34.3	58	Strong C_2H_3CN, v_{15}=1
374	$33_{9,25} - 32_{9,24}$	209468.464	6	194	176.0	58	Strong CH_3OCHO
375	$33_{9,24} - 32_{9,23}$	209475.792	6	194	176.0	58	Strong CH_3OCHO
376	$32_{5,27} - 31_{5,26}$	209629.103	7	163	180.3	45	Strong $HC^{13}CCN$, v_7=2, NH_2CH_2CN, and $HCC^{13}CN$, v_7=2
377	$71_{14,57} - 71_{13,58}$	209632.733	110	848	80.9	45	Strong $HC^{13}CCN$, v_7=2, NH_2CH_2CN, and $HCC^{13}CN$, v_7=2
378	$33_{8,26} - 32_{8,25}$	209979.748	6	187	179.0	45	Strong $^{13}CH_3CH_2CN$
379	$74_{6,68} - 73_{7,66}$	210074.514	396	844	11.3	45	Strong NH_2CH_2CN, C_2H_5CN, v_{13}=1/v_{21}=1, $^{13}CH_3CH_2CN$, and CH_3NH_2
380	$33_{8,25} - 32_{8,24}$	210075.681	6	187	179.0	45	Strong NH_2CH_2CN, C_2H_5CN, v_{13}=1/v_{21}=1, $^{13}CH_3CH_2CN$, and CH_3NH_2
381	$25_{4,21} - 24_{3,21}$	210401.571	12	97	15.8	64	Strong CH_3OCHO and $^{13}CH_3OH$
382	$63_{6,57} - 63_{6,58}$	210404.903	92	621	6.3	64	Strong CH_3OCHO and $^{13}CH_3OH$
383	$33_{6,28} - 32_{6,27}$	210450.843	7	176	183.6	64	Strong CH_3OCHO

Table A.1: continued.

N^a	Transition^b	Frequency (MHz)	Unc.^{c} (kHz)	$E_l{}^d$ (K)	$S\mu^2$ (D^2)	σ^e (mK)	Comments
(1)	(2)	(3)	(4)	(5)	(6)	(7)	(8)
384	$15_{4,12} - 14_{2,13}$	210456.934	17	33	0.1	64	Strong CH_3OCHO
385	$33_{7,27} - 32_{7,26}$	210539.691	7	181	181.6	64	Strong C_2H_5OH, CH_3CH_3CO
386	$52_{13,40} - 52_{12,40}$	210541.727	13	479	25.4	64	Strong C_2H_5OH, CH_3CH_3CO
387	$52_{13,39} - 52_{12,40}$	210545.379	13	479	54.0	37	Strong C_2H_5OH, CH_3CH_3CO
388	$22_{4,19} - 21_{3,19}$	210662.566	13	74	10.2	37	Strong C_2H_3CN, v_{11}=3
389	$24_{5,20} - 23_{4,19}$	210668.526	20	92	11.7	37	Strong C_2H_3CN, v_{11}=3
390	$34_{4,31} - 33_{4,30}$	210695.872	7	176	191.8	37	Strong C_2H_3CN, v_{11}=3
391	$51_{13,39} - 51_{12,40}{}^\star$	211209.482	13	463	52.6	33	Strong H_2CO
393	$60_{6,55} - 60_{4,56}$	211211.496	72	556	5.5	33	Strong H_2CO
394	$51_{13,38} - 51_{12,40}$	211211.745	13	463	25.0	33	Strong H_2CO
395	$34_{3,31} - 33_{3,30}$	211212.470	7	176	191.8	33	Strong H_2CO
396	$33_{7,26} - 32_{7,25}$	211390.493	7	181	181.6	33	Strong C_2H_5CN
397	$21_{5,17} - 20_{4,17}$	211410.009	9	71	11.3	33	Strong C_2H_5OH
398	$10_{9,1} - 9_{8,2}{}^\star$	211461.373	11	40	16.0	33	Strong C_2H_3CN
400	$10_{9,1} - 9_{8,1}{}^\star$	211461.373	11	40	10.6	33	Strong C_2H_3CN
402	$35_{2,33} - 34_{3,32}$	211878.109	8	181	45.5	47	Strong C_2H_3CN, v_{15}=1 and $CH_2CH^{13}CN$
403	$35_{3,33} - 34_{3,32}$	211942.630	8	181	198.5	36	Strong $H^{13}CONH_2$, v=0 and v_{12}=1, and CH_3CHO
404	$27_{2,25} - 27_{1,27}$	211968.119	70	107	0.2	36	Strong CH_3CHO
405	$33_{4,29} - 32_{4,28}$	211969.567	8	171	185.9	36	Strong CH_3CHO
406	$19_{3,16} - 18_{2,17}$	211971.500	40	52	1.7	36	Strong CH_3CHO
407	$35_{2,33} - 34_{2,32}$	211972.241	8	181	198.5	36	Strong CH_3CHO
408	$35_{3,33} - 34_{2,32}$	212036.762	8	181	45.5	36	Strong CH_3CHO and C_2H_5CN
409	$23_{5,18} - 22_{4,18}$	212299.989	13	84	13.4	36	Strong CH_3NH_2
410	$34_{4,31} - 33_{3,30}$	212584.930	8	176	34.4	99	Strong CH_3CHO, v_t=1 and C_2H_5OH
411	$25_{5,21} - 24_{4,20}$	212773.838	22	99	12.1	99	Strong $^{13}CH_3OH$
412	$24_{3,21} - 23_{2,21}$	212918.896	24	87	11.4	99	Strong CH_3OCHO and $H^{13}CCCN$, v_7=2
413	$13_{8,6} - 12_{7,5}{}^\star$	212948.896	11	44	14.7	99	Strong $^{13}CH_2CHCN$ and $H^{13}CCCN$, v_7=2
415	$13_{8,6} - 12_{7,6}{}^\star$	212948.898	11	44	10.2	99	Strong $^{13}CH_2CHCN$ and $H^{13}CCCN$, v_7=2
417	$67_{7,60} - 67_{6,61}$	213160.895	138	709	54.8	48	Strong CH_3OH and C_2H_3CN, v_{11}=1
418	$36_{1,35} - 35_{2,34}$	213169.170	10	184	55.7	48	Strong CH_3OH and C_2H_3CN, v_{11}=1
419	$36_{2,35} - 35_{2,34}$	213170.718	10	184	205.4	48	Strong CH_3OH and C_2H_3CN, v_{11}=1
420	$36_{1,35} - 35_{1,34}$	213171.524	10	184	205.4	48	Strong CH_3OH and C_2H_3CN, v_{11}=1
421	$36_{2,35} - 35_{1,34}$	213173.072	10	184	55.7	48	Strong CH_3OH and C_2H_3CN, v_{11}=1
422	$21_{5,16} - 20_{4,17}$	213241.133	10	71	10.2	48	Strong C_2H_3CN, v_{15}=1
423	$16_{7,10} - 15_{6,9}$	214272.062	10	51	13.9	75	Strong $^{13}CH_3CN$
424	$16_{7,9} - 15_{6,9}$	214272.199	10	51	10.3	75	Strong $^{13}CH_3CN$
425	$16_{7,10} - 15_{6,10}$	214274.536	10	51	10.3	75	Strong $^{13}CH_3CN$
426	$16_{7,9} - 15_{6,10}$	214274.673	10	51	13.9	75	Strong $^{13}CH_3CN$
427	$68_{13,56} - 67_{14,54}$	214275.671	134	774	15.1	75	Strong $^{13}CH_3CN$
428	$75_{9,66} - 75_{8,67}$	214276.082	396	900	71.6	75	Strong $^{13}CH_3CN$
429	$55_{3,52} - 55_{3,53}{}^\star$	214280.749	79	452	3.7	75	Strong $^{13}CH_3CN$
431	$55_{4,52} - 55_{3,53}{}^\star$	214281.372	79	452	23.1	75	Strong $^{13}CH_3CN$
433	$46_{6,40} - 45_{7,38}$	214282.870	41	339	14.2	75	Strong $^{13}CH_3CN$
434	$71_{14,57} - 71_{13,59}$	214439.734	45	848	30.6	75	Blend with CH_3CHO
435	$37_{0,37} - 36_{1,36}{}^\star$	214444.812	14	187	65.5	75	Blend with CH_3CHO
437	$37_{0,37} - 36_{0,36}{}^\star$	214444.836	14	187	212.4	75	Blend with CH_3CHO
439	$33_{6,27} - 32_{6,26}$	214447.375	7	177	184.1	75	Blend with CH_3CHO
440	$26_{5,22} - 25_{4,21}$	214558.308	23	107	12.7	75	Strong $HCONH_2$ and C_2H_5CN, v_{13}=1/v_{21}=1
441	$34_{5,30} - 33_{5,29}$	214558.782	7	181	190.8	75	Strong $HCONH_2$ and C_2H_5CN, v_{13}=1/v_{21}=1
442	$34_{18,16} - 33_{18,15}{}^\star$	214668.864	7	305	141.0	75	Strong C_2H_5CN, v_{20}=1 and SO_2
444	$34_{19,15} - 33_{19,14}{}^\star$	214672.698	8	321	134.7	75	Strong C_2H_5CN, v_{20}=1 and SO_2
446	$34_{17,17} - 33_{17,16}{}^\star$	214677.695	7	291	146.9	75	Strong C_2H_5CN, v_{20}=1 and SO_2
448	$34_{20,14} - 33_{20,13}{}^\star$	214687.250	8	337	128.1	75	Strong SO_2
450	$34_{16,18} - 33_{16,17}{}^\star$	214701.776	7	277	152.5	75	Strong SO_2 and C_2H_5OH
452	$34_{21,13} - 33_{21,12}{}^\star$	214711.030	8	354	121.1	75	Strong CH_3CH_3CO and SO_2
454	$19_{6,14} - 18_{5,13}$	214713.444	10	62	12.8	75	Strong CH_3CH_3CO and SO_2
455	$34_{7,27} - 34_{5,30}$	214735.779	35	192	0.5	75	Strong SO_2 and U-line
456	$34_{22,12} - 33_{22,11}{}^\star$	214742.876	8	372	113.9	75	Strong SO_2 and U-line
458	$34_{15,19} - 33_{15,18}{}^\star$	214744.609	7	264	157.8	75	Strong SO_2 and U-line
460	$47_{7,40} - 47_{6,42}$	214754.033	94	358	3.9	75	Strong U-line and CH_3COOH
461	$19_{6,13} - 18_{5,13}$	214755.319	10	62	10.9	75	Strong U-line and CH_3COOH
462	$34_{23,11} - 33_{23,10}{}^\star$	214781.872	8	391	106.2	75	Strong CH_3OCHO
464	$34_{14,20} - 33_{14,19}{}^\star$	214811.050	7	252	162.7	75	Strong CH_3CHO and $H_3{}^{13}CCN$, v_8=1
466	$34_{13,21} - 33_{13,20}{}^\star$	214908.015	6	241	167.3	74	Strong C_2H_5CN and CH_3CH_3CO

Table A.1: continued.

N^a	Transition^b	Frequency (MHz)	Unc.^{c} (kHz)	$E_l{}^d$ (K)	$S\mu^2$ (D^2)	σ^e (mK)	Comments
(1)	(2)	(3)	(4)	(5)	(6)	(7)	(8)
468	$64_{6,58} - 64_{5,59}$	215041.513	100	640	46.7	74	Strong C_2H_5CN
469	$34_{12,23} - 33_{12,22}{}^\star$	215045.689	6	230	171.5	74	Strong C_2H_5CN
471	$64_{7,58} - 64_{6,59}$	215142.583	100	640	46.7	74	Strong $H_2{}^{13}CCO$ and $CH_3{}^{13}CH_2CN$
472	$19_{6,14} - 18_{5,14}$	215144.621	10	62	10.9	74	Strong $H_2{}^{13}CCO$ and $CH_3{}^{13}CH_2CN$
473	$64_{7,58} - 64_{5,59}$	215150.604	100	640	6.3	74	Strong $H_2{}^{13}CCO$ and $CH_3{}^{13}CH_2CN$
474	$42_{13,30} - 42_{12,30}{}^\star$	215150.970	10	334	21.2	74	Strong $H_2{}^{13}CCO$ and $CH_3{}^{13}CH_2CN$
476	$42_{13,30} - 42_{12,31}{}^\star$	215151.342	10	334	40.6	74	Strong $H_2{}^{13}CCO$ and $CH_3{}^{13}CH_2CN$
478	$32_{25,7} - 33_{24,10}{}^\star$	215182.047	134	410	1.1	74	Strong C_2H_5CN, v_{13}=1/v_{21}=1
480	$32_{25,7} - 33_{24,9}{}^\star$	215182.047	134	410	0.7	74	Strong C_2H_5CN, v_{13}=1/v_{21}=1
482	$19_{6,13} - 18_{5,14}$	215186.497	10	62	12.8	74	Strong C_2H_5CN, v_{13}=1/v_{21}=1
483	$34_{11,24} - 33_{11,23}{}^\star$	215239.705	6	221	175.4	74	Strong C_2H_5CN, v_{13}=1/v_{21}=1
485	$41_{13,29} - 41_{12,29}{}^\star$	215441.858	10	321	20.7	74	Strong C_2H_5CN, v_{13}=1/v_{21}=1 and $HCONH_2$, v_{12}=1
487	$41_{13,29} - 41_{12,30}{}^\star$	215442.069	10	321	39.3	74	Strong C_2H_5CN, v_{13}=1/v_{21}=1 and $HCONH_2$, v_{12}=1
489	$35_{3,32} - 34_{4,31}$	215452.995	7	186	36.4	74	Strong $HCONH_2$, v_{12}=1 and C_2H_5CN, v_{13}=1/v_{21}=1
490	$34_{33,1} - 33_{33,0}{}^\star$	215453.545	14	622	11.4	74	Strong $HCONH_2$, v_{12}=1 and C_2H_5CN, v_{13}=1/v_{21}=1
492	$40_{28,12} - 41_{27,15}{}^\star$	215511.622	314	565	2.1	74	Strong C_2H_5CN
494	$40_{28,12} - 41_{27,14}{}^\star$	215511.622	314	565	1.3	74	Strong C_2H_5CN
496	$57_{10,47} - 56_{11,46}$	215514.818	69	536	14.8	74	Strong C_2H_5CN
497	$34_{10,25} - 33_{10,24}$	215515.176	6	212	179.0	74	Strong C_2H_5CN
498	$34_{10,24} - 33_{10,23}$	215515.902	6	212	179.0	74	Strong C_2H_5CN
499	$61_{5,56} - 61_{4,57}$	215703.028	76	574	38.8	74	Strong $^{13}CH_3OH$ and $CH_2{}^{13}CHCN$
500	$40_{13,28} - 40_{12,28}{}^\star$	215709.141	10	309	20.2	74	Strong $^{13}CH_3OH$ and $CH_2{}^{13}CHCN$
502	$40_{13,28} - 40_{12,29}{}^\star$	215709.259	10	309	38.0	74	Strong $^{13}CH_3OH$ and $CH_2{}^{13}CHCN$
504	$34_{9,26} - 33_{9,25}$	215912.049	6	204	182.2	55	Strong C_2H_5OH and U-line
505	$34_{9,25} - 33_{9,24}$	215924.028	6	204	182.2	55	Strong CH_3NH_2 and C_2H_5OH
506	$39_{13,27} - 39_{12,27}{}^\star$	215954.232	10	297	19.7	55	Strong C_2H_5CN
508	$39_{13,27} - 39_{12,28}{}^\star$	215954.297	10	297	36.8	55	Strong C_2H_5CN
510	$33_{5,28} - 32_{5,27}$	216072.921	7	173	186.1	55	Strong C_2H_5CN
511	$15_{4,12} - 14_{1,13}$	216077.016	15	33	0.4	55	Strong C_2H_5CN
512	$27_{5,23} - 26_{4,22}$	216108.001	23	115	13.4	55	Strong $^{13}CH_2CHCN$ and CH_3OCHO
513	$38_{13,26} - 38_{12,26}{}^\star$	216178.463	9	285	19.1	55	Strong U-line and C_2H_5CN
515	$38_{13,26} - 38_{12,27}{}^\star$	216178.498	9	285	35.5	55	Strong U-line and C_2H_5CN
517	$37_{13,25} - 37_{12,25}{}^\star$	216383.098	9	273	18.6	55	Strong $^{13}CH_3OH$ and U-line
519	$37_{13,25} - 37_{12,26}{}^\star$	216383.116	9	273	34.2	55	Strong $^{13}CH_3OH$ and U-line
521	$38_{5,33} - 38_{4,35}$	216438.893	54	230	1.7	55	Blend with CH_3CHO and U-line
522	$35_{4,32} - 34_{4,31}$	216442.748	7	186	197.5	55	Blend with CH_3CHO and U-line
523	$69_{14,55} - 69_{13,57}$	216444.916	36	805	30.5	55	Blend with CH_3CHO and U-line
524	$34_{8,27} - 33_{8,26}$	216465.638	6	197	185.0	55	Strong CH_3CH_3CO, U-line, and $HCONH_2$
525	$36_{13,24} - 36_{12,24}{}^\star$	216569.335	9	262	18.1	55	Strong H_2CO
527	$36_{13,24} - 36_{12,25}{}^\star$	216569.344	9	262	33.0	55	Strong H_2CO
529	$34_{8,26} - 33_{8,25}$	216611.081	6	197	185.0	55	Strong CH_3COOH and U-line
530	$33_{8,26} - 33_{6,27}$	216620.275	32	187	0.5	55	Strong CH_3CHO
531	$24_{5,19} - 23_{4,19}$	216620.997	13	92	14.3	55	Strong CH_3CHO
532	$34_{6,29} - 33_{6,28}$	216724.533	7	186	189.5	55	Strong H_2S and C_2H_5CN, v_{13}=1/v_{21}=1
533	$35_{13,23} - 35_{12,23}{}^\star$	216738.314	9	251	17.5	50	Strong C_2H_5CN
535	$35_{13,23} - 35_{12,24}{}^\star$	216738.319	9	251	31.7	50	Strong C_2H_5CN
537	$35_{3,32} - 34_{3,31}$	216825.455	7	186	197.5	50	Strong CH_3OCHO
538	$34_{13,22} - 34_{12,22}{}^\star$	216891.123	9	241	16.9	50	Strong CH_3CH_3CO and U-line
540	$34_{13,22} - 34_{12,23}{}^\star$	216891.125	9	241	30.5	50	Strong CH_3CH_3CO and U-line
542	$34_{7,28} - 33_{7,27}$	217010.384	6	191	187.5	50	Blend with $CH_2{}^{13}CHCN$ and U-line
543	$33_{13,20} - 33_{12,21}{}^\star$	217028.798	9	230	29.2	50	Blend with CH_3CH_3CO and ^{13}CN
545	$33_{13,21} - 33_{12,22}{}^\star$	217028.800	9	230	29.2	50	Blend with CH_3CH_3CO and ^{13}CN
547	$32_{13,19} - 32_{12,20}{}^\star$	217152.333	9	220	28.0	50	Strong C_2H_5CN and $H_2{}^{13}CCO$
549	$32_{13,20} - 32_{12,21}{}^\star$	217152.333	9	220	28.0	50	Strong C_2H_5CN and $H_2{}^{13}CCO$
551	$68_{14,55} - 68_{13,56}$	217260.750	34	784	75.9	50	Strong $C_2H_5{}^{13}CN$ and ^{13}CN
552	$31_{13,18} - 31_{12,19}{}^\star$	217262.674	9	211	26.8	50	Strong $C_2H_5{}^{13}CN$ and ^{13}CN
554	$31_{13,19} - 31_{12,20}{}^\star$	217262.674	9	211	26.8	50	Strong $C_2H_5{}^{13}CN$ and ^{13}CN
556	$15_{4,11} - 14_{1,13}$	217358.142	16	33	0.2	50	Blend with CH_3OCH_3, U-line, and ^{13}CN in absorption
557	$30_{13,17} - 30_{12,18}{}^\star$	217360.731	9	201	25.5	50	Blend with CH_3OCH_3, U-line, and ^{13}CN in absorption
559	$30_{13,18} - 30_{12,19}{}^\star$	217360.731	9	201	25.5	50	Blend with CH_3OCH_3, U-line, and ^{13}CN in absorption
561	$29_{13,16} - 29_{12,17}{}^\star$	217447.373	9	192	24.3	50	Blend with U-line and ^{13}CN in absorption
563	$29_{13,17} - 29_{12,18}{}^\star$	217447.373	9	192	24.3	50	Blend with U-line and ^{13}CN in absorption
565	$75_{10,66} - 75_{8,67}$	217451.078	339	900	8.1	50	Blend with $CH_2CH^{13}CN$ and ^{13}CN in absorption
566	$34_{4,30} - 33_{4,29}$	217456.631	8	181	191.5	50	Blend with $CH_2CH^{13}CN$ and ^{13}CN in absorption

Table A.1: continued.

N^a	Transition^b	Frequency (MHz)	Unc.^{c} (kHz)	$E_l{}^d$ (K)	$S\mu^2$ (D^2)	σ^e (mK)	Comments
(1)	(2)	(3)	(4)	(5)	(6)	(7)	(8)
567	$28_{5,24} - 27_{4,23}$	217516.877	23	124	14.3	50	Strong U-line and $HC^{13}CCN$, v_5=1/v_7=3
568	$28_{13,15} - 28_{12,16}{}^\star$	217523.434	9	183	23.0	50	Strong U-line and $HC^{13}CCN$, v_5=1/v_7=3
570	$28_{13,15} - 28_{12,17}{}^\star$	217523.434	9	183	13.3	50	Strong U-line and $HC^{13}CCN$, v_5=1/v_7=3
572	$27_{13,14} - 27_{12,15}{}^\star$	217589.713	9	175	21.8	50	Strong U-line and $CH_2CH^{13}CN$
574	$27_{13,14} - 27_{12,16}{}^\star$	217589.713	9	175	12.6	50	Strong U-line and $CH_2CH^{13}CN$
576	$36_{2,34} - 35_{3,33}$	217614.389	8	191	47.4	50	Strong $CH_3{}^{13}CH_2CN$ and $CH_2CH^{13}CN$
577	$26_{13,13} - 26_{12,14}{}^\star$	217646.977	9	167	20.5	50	Strong $CH_2CH^{13}CN$, CH_3OH, v_t=1, and $CH_2{}^{13}CHCN$
579	$26_{13,13} - 26_{12,15}{}^\star$	217646.977	9	167	12.0	50	Strong $CH_2CH^{13}CN$, CH_3OH, v_t=1, and $CH_2{}^{13}CHCN$
581	$36_{3,34} - 35_{3,33}$	217658.455	8	191	204.2	50	Strong U-line and CH_3NH_2
582	$36_{2,34} - 35_{2,33}$	217678.909	8	191	204.2	50	Strong U-line and CH_3NH_2
583	$61_{36,25} - 62_{35,28}{}^\star$	217690.479	1634	1101	5.4	50	Strong U-line and $CH_2CH^{13}CN$
585	$25_{13,12} - 25_{12,13}{}^\star$	217695.958	9	159	19.2	50	Strong U-line and $CH_2CH^{13}CN$
587	$25_{13,12} - 25_{12,14}{}^\star$	217695.958	9	159	11.3	50	Strong U-line and $CH_2CH^{13}CN$
589	$45_{30,15} - 46_{29,18}{}^\star$	217699.153	506	678	2.8	50	Strong U-line and $CH_2CH^{13}CN$
591	$45_{30,15} - 46_{29,17}{}^\star$	217699.153	506	678	1.8	50	Strong U-line and $CH_2CH^{13}CN$
593	$36_{3,34} - 35_{2,33}$	217722.975	8	191	47.4	50	Strong U-line and $C_2H_5{}^{13}CN$
594	$24_{13,11} - 24_{12,12}{}^\star$	217737.362	9	151	17.9	50	Strong U-line, CH_3CH_3CO, v_t=1, and $HC^{13}CCN$, v_6=1
596	$24_{13,11} - 24_{12,13}{}^\star$	217737.362	9	151	10.6	50	Strong U-line, CH_3CH_3CO, v_t=1, and $HC^{13}CCN$, v_6=1
598	$23_{4,20} - 22_{3,20}$	219325.535	14	80	10.4	92	Strong C_2H_5CN, v_{13}=1/v_{21}=1 and C_2H_3CN, v_{11}=1
599	$34_{26,8} - 35_{25,11}{}^\star$	219476.990	182	452	1.2	92	Strong NH_2CN and HC_3N, v_6=v_7=1
601	$34_{26,8} - 35_{25,10}{}^\star$	219476.990	182	452	0.8	92	Strong NH_2CN and HC_3N, v_6=v_7=1
603	$26_{4,22} - 25_{3,22}$	219481.624	15	105	15.9	92	Strong NH_2CN and HC_3N, v_6=v_7=1
604	$30_{5,26} - 29_{4,25}$	220313.796	22	142	16.7	98	Strong HNCO, v_6=1 and CH_3CN
605	$35_{5,31} - 34_{5,30}$	220473.189	7	192	196.6	98	Blend with ^{13}CO in absorption, CH_3CH_3CO, and CH_3CN
606	$65_{14,52} - 65_{13,53}$	220501.379	24	723	71.2	98	Blend with ^{13}CO in absorption, C_2H_3CN, v_{11}=3, and $H^{13}CCCN$, v_5=1/v_7=3
607	$17_{7,11} - 16_{6,10}$	220504.995	10	56	14.1	98	Blend with ^{13}CO in absorption, C_2H_3CN, v_{11}=3, and $H^{13}CCCN$, v_5=1/v_7=3
608	$17_{7,10} - 16_{6,10}$	220505.321	10	56	10.7	98	Blend with ^{13}CO in absorption, C_2H_3CN, v_{11}=3, and $H^{13}CCCN$, v_5=1/v_7=3
609	$17_{7,11} - 16_{6,11}$	220510.391	10	56	10.7	98	Blend with ^{13}CO in absorption, C_2H_3CN, v_{11}=3, and $H^{13}CCCN$, v_5=1/v_7=3
610	$17_{7,10} - 16_{6,11}$	220510.718	10	56	14.1	98	Blend with ^{13}CO in absorption, C_2H_3CN, v_{11}=3, and $H^{13}CCCN$, v_5=1/v_7=3
611	$20_{6,15} - 19_{5,14}$	220565.304	10	68	13.0	98	Strong C_2H_3CN and $CH_3{}^{13}CN$
612	$20_{6,14} - 19_{5,14}$	220641.848	10	68	11.3	98	Strong $CH_3{}^{13}CN$ and CH_3CN
613	$41_{29,12} - 42_{28,15}{}^\star$	225934.410	402	600	2.1	278	Blend with C_3H_7CN, uncertain baseline
615	$41_{29,12} - 42_{28,14}{}^\star$	225934.410	402	600	1.3	278	Blend with C_3H_7CN, uncertain baseline
617	$26_{5,21} - 25_{4,21}$	225940.684	11	107	16.3	278	Blend with C_3H_7CN, uncertain baseline
618	$33_{5,29} - 32_{4,28}$	225950.608	17	171	21.8	278	Blend with C_3H_7CN, uncertain baseline
619	$21_{6,16} - 20_{5,15}$	226260.603	10	74	13.1	278	Strong C_2H_3CN and C_2H_5OH
620	$36_{5,32} - 35_{5,31}$	226347.783	7	202	202.4	278	Blend with CN in absorption and CH_3OCH_3
621	$21_{6,15} - 20_{5,15}$	226395.881	10	74	11.8	278	Strong C_2H_3CN and C_2H_5OH
622	$18_{7,12} - 17_{6,11}$	226716.305	10	61	14.3	96	Strong CH_3OCHO
623	$18_{7,11} - 17_{6,11}$	226717.041	10	61	11.1	96	Strong CH_3OCHO
624	$18_{7,12} - 17_{6,12}$	226727.474	10	61	11.1	96	Blend with CN in absorption
625	$18_{7,11} - 17_{6,12}$	226728.211	10	61	14.3	96	Blend with CN in absorption
626	$37_{4,33} - 36_{5,32}$	227117.159	9	213	29.9	96	Blend with C_2H_5OH and C_2H_5CN, uncertain baseline
627	$62_{11,51} - 61_{12,50}$	227121.239	119	635	16.1	96	Blend with C_2H_5OH and C_2H_5CN, uncertain baseline
628	$21_{6,16} - 20_{5,16}$	227427.532	10	74	11.8	85	Strong HC_3N, v_5=1/v_7=3 and $^{13}CH_3CH_2CN$
629	$36_{24,12} - 35_{24,11}{}^\star$	227433.216	8	431	115.2	85	Strong HC_3N, v_5=1/v_7=3 and $^{13}CH_3CH_2CN$
631	$70_{8,63} - 70_{7,64}$	227478.641	185	769	54.9	85	Strong $^{13}CH_3CH_2CN$ and CH_3NH_2
632	$36_{25,11} - 35_{25,10}{}^\star$	227484.640	8	452	107.4	85	Strong $^{13}CH_3CH_2CN$ and CH_3NH_2
634	$36_{14,22} - 35_{14,21}{}^\star$	227487.197	6	273	176.0	85	Strong $^{13}CH_3CH_2CN$ and CH_3NH_2
636	$70_{8,63} - 70_{6,64}$	227493.347	185	769	7.1	85	Strong $^{13}CH_3CH_2CN$ and CH_3NH_2
637	$21_{6,15} - 20_{5,16}$	227562.811	10	74	13.0	85	Strong CH_3OCHO
638	$36_{27,9} - 35_{27,8}{}^\star$	227604.924	8	495	90.7	85	Strong $HCONH_2$ and C_2H_5OH
640	$36_{13,24} - 35_{13,23}{}^\star$	227607.804	6	262	180.4	85	Strong $HCONH_2$ and C_2H_5OH
642	$36_{12,25} - 35_{12,24}{}^\star$	227776.778	6	251	184.4	85	Strong C_2H_5CN
644	$22_{4,18} - 21_{3,19}$	227779.414	31	74	4.3	85	Strong C_2H_5CN
645	$62_{37,25} - 63_{36,28}{}^\star$	227781.682	1931	1149	5.3	85	Strong C_2H_5CN
647	$56_{14,43} - 56_{13,43}$	227785.671	14	555	27.4	85	Strong C_2H_5CN
648	$37_{4,34} - 36_{4,33}$	227902.473	7	208	209.0	85	Strong $CH_3{}^{13}CH_2CN$ and C_2H_3CN

Table A.1: continued.

N^a	Transition^b	Frequency (MHz)	Unc.^{c} (kHz)	$E_l{}^d$ (K)	$S\mu^2$ (D^2)	σ^e (mK)	Comments
(1)	(2)	(3)	(4)	(5)	(6)	(7)	(8)
649	$36_{31,5} - 35_{31,4}{}^\star$	227904.401	11	591	53.6	85	Strong $CH_3{}^{13}CH_2CN$ and C_2H_3CN
651	$27_{5,22} - 26_{4,22}$	231234.499	9	115	17.3	183	Strong $^{13}CH_2CHCN$ and C_2H_3CN, v_{15}=1
652	$49_{14,36} - 49_{13,36}{}^\star$	231236.821	11	442	24.5	183	Strong $^{13}CH_2CHCN$ and C_2H_3CN, v_{15}=1
654	$49_{14,36} - 49_{13,37}{}^\star$	231237.660	11	442	48.5	183	Strong $^{13}CH_2CHCN$ and C_2H_3CN, v_{15}=1
656	$35_{5,31} - 34_{4,30}$	231556.381	14	191	25.9	40	Strong C_2H_5OH
657	$40_{0,40} - 39_{1,39}{}^\star$	231601.730	16	219	71.1	40	Strong CH_3NH_2
659	$40_{0,40} - 39_{0,39}{}^\star$	231601.736	16	219	229.7	40	Strong CH_3CHO and CH_3NH_2
661	$48_{14,35} - 48_{13,35}{}^\star$	231604.344	11	428	24.1	40	Strong CH_3CHO and CH_3NH_2
663	$48_{14,35} - 48_{13,36}{}^\star$	231604.845	11	428	47.2	40	Strong CH_3CHO and CH_3NH_2
665	$64_{38,26} - 65_{37,29}{}^\star$	231745.751	2269	1218	5.6	40	Strong C_2H_5CN and CH_3CHO
667	$50_{8,42} - 49_{9,41}$	231747.991	60	407	14.3	40	Strong C_2H_5CN and CH_3CHO
668	$22_{6,17} - 21_{5,16}$	231750.187	11	81	13.2	40	Strong C_2H_5CN and CH_3CHO
669	$24_{5,20} - 23_{4,20}$	232536.063	9	91	12.5	19	Strong C_2H_5CN and C_2H_5OH
670	$44_{14,31} - 44_{13,31}{}^\star$	232827.023	10	371	22.2	19	Strong $H_3{}^{13}CCN$, v_8=1 and CH_3CH_3CO, v_t=1
672	$44_{14,31} - 44_{13,32}{}^\star$	232827.078	10	371	42.1	19	Strong $H_3{}^{13}CCN$, v_8=1 and CH_3CH_3CO, v_t=1
674	$28_{14,14} - 28_{13,15}{}^\star$	235000.218	9	194	22.0	131	Strong C_2H_5OH, CH_3CH_3CO, v_t=1, and U-line
676	$28_{14,14} - 28_{13,16}{}^\star$	235000.218	9	194	12.8	131	Strong C_2H_5OH, CH_3CH_3CO, v_t=1, and U-line
678	$36_{5,32} - 35_{4,31}$	235001.335	12	202	28.1	131	Strong C_2H_5OH, CH_3CH_3CO, v_t=1, and U-line
679	$27_{14,13} - 27_{13,14}{}^\star$	235043.321	9	185	20.7	131	Strong CH_3OCHO
681	$27_{14,13} - 27_{13,15}{}^\star$	235043.321	9	185	12.2	131	Strong CH_3OCHO
683	$26_{14,12} - 26_{13,13}{}^\star$	235079.665	9	177	19.4	131	Strong C_2H_5OH and U-line
685	$26_{14,12} - 26_{13,14}{}^\star$	235079.665	9	177	11.5	131	Strong C_2H_5OH and U-line
687	$25_{14,11} - 25_{13,12}{}^\star$	235109.820	9	169	18.1	131	Strong c-C_2H_4O
689	$25_{14,11} - 25_{13,13}{}^\star$	235109.820	9	169	10.7	131	Strong c-C_2H_4O
691	$24_{14,10} - 24_{13,11}{}^\star$	235134.333	10	162	16.8	131	Strong C_2H_5OH
693	$24_{14,10} - 24_{13,12}{}^\star$	235134.333	10	162	10.0	131	Strong C_2H_5OH
695	$23_{14,9} - 23_{13,10}{}^\star$	235153.730	10	154	15.5	131	Strong SO_2 and C_2H_5OH
697	$23_{14,9} - 23_{13,11}{}^\star$	235153.730	10	154	9.3	131	Strong SO_2 and C_2H_5OH
699	$22_{14,8} - 22_{13,9}{}^\star$	235168.517	10	147	14.1	131	Blend with C_2H_5OH, CH_3CH_3CO, and U-line
701	$22_{14,8} - 22_{13,10}{}^\star$	235168.517	10	147	8.5	131	Blend with C_2H_5OH, CH_3CH_3CO, and U-line
703	$11_{10,1} - 10_{9,2}{}^\star$	235173.718	11	51	17.8	131	Blend with C_2H_5OH, CH_3CH_3CO, and U-line
705	$11_{10,1} - 10_{9,1}{}^\star$	235173.718	11	51	11.8	131	Blend with C_2H_5OH, CH_3CH_3CO, and U-line
707	$14_{14,0} - 14_{13,1}{}^\star$	235174.407	12	103	1.9	131	Blend with C_2H_5OH, CH_3CH_3CO, and U-line
709	$14_{14,0} - 14_{13,2}{}^\star$	235174.407	12	103	1.2	131	Blend with C_2H_5OH, CH_3CH_3CO, and U-line
711	$21_{14,7} - 21_{13,8}{}^\star$	235179.176	10	141	12.8	131	Blend with U-line and CH_3OCHO
713	$21_{14,7} - 21_{13,9}{}^\star$	235179.176	10	141	7.7	131	Blend with U-line and CH_3OCHO
715	$15_{14,1} - 15_{13,2}{}^\star$	235180.867	12	107	3.6	131	Blend with U-line and CH_3OCHO
717	$15_{14,1} - 15_{13,3}{}^\star$	235180.867	12	107	2.2	131	Blend with U-line and CH_3OCHO
719	$16_{14,2} - 16_{13,3}{}^\star$	235185.998	12	112	5.3	131	Blend with U-line and CH_3OCHO
721	$16_{14,2} - 16_{13,4}{}^\star$	235185.998	12	112	3.2	131	Blend with U-line and CH_3OCHO
723	$20_{14,6} - 20_{13,7}{}^\star$	235186.169	11	134	11.4	131	Blend with U-line and CH_3OCHO
725	$20_{14,6} - 20_{13,8}{}^\star$	235186.169	11	134	6.9	131	Blend with U-line and CH_3OCHO
727	$17_{14,3} - 17_{13,4}{}^\star$	235189.463	12	117	6.9	131	Blend with U-line and CH_3OCHO
729	$17_{14,3} - 17_{13,5}{}^\star$	235189.463	12	117	4.2	131	Blend with U-line and CH_3OCHO
731	$19_{14,5} - 19_{13,6}{}^\star$	235189.938	11	128	9.9	131	Blend with U-line and CH_3OCHO
733	$19_{14,5} - 19_{13,7}{}^\star$	235189.938	11	128	6.0	131	Blend with U-line and CH_3OCHO
735	$18_{14,4} - 18_{13,5}{}^\star$	235190.902	11	123	8.4	131	Blend with U-line and CH_3OCHO
737	$18_{14,4} - 18_{13,6}{}^\star$	235190.902	11	123	5.1	131	Blend with U-line and CH_3OCHO
739	$37_{6,32} - 36_{6,31}$	235253.326	7	218	207.1	131	Strong C_2H_5CN, v_{13}=1/v_{21}=1
740	$37_{9,29} - 36_{9,28}$	235296.303	6	236	200.6	131	Blend with CH_3CHO, U-line, and CH_3CH_3CO, v_t=1
741	$49_{7,42} - 48_{8,40}$	235297.456	26	387	16.4	131	Blend with CH_3CHO, U-line, and CH_3CH_3CO, v_t=1
742	$37_{9,28} - 36_{9,27}$	235343.403	6	236	200.6	131	Blend with CH_3CH_3CO and $^{13}CH_3OH$, v_t=1
743	$27_{8,20} - 27_{6,21}{}^\star$	235394.633	26	130	0.3	131	Blend with $^{13}CH_3OH$, v_t=1, U-line, and C_2H_5CN
745	$37_{8,30} - 36_{8,29}$	235954.472	6	229	203.2	131	Strong $^{13}CH_3OH$
746	$26_{3,23} - 25_{2,23}$	235999.134	25	101	11.2	131	Strong CH_3CHO and $^{13}CH_3OH$
747	$42_{30,12} - 43_{29,15}{}^\star$	236302.555	507	637	2.0	37	Strong C_2H_5OH and $^{13}CH_3CH_2CN$
749	$42_{30,12} - 43_{29,14}{}^\star$	236302.555	507	637	1.3	37	Strong C_2H_5OH and $^{13}CH_3CH_2CN$
751	$37_{7,31} - 36_{7,30}$	236307.982	6	224	205.5	37	Strong C_2H_5OH and $^{13}CH_3CH_2CN$
752	$37_{8,29} - 36_{8,28}$	236410.585	6	229	203.2	37	Strong $HC^{13}CCN$, v_7=1, CH_3NH_2, and C_2H_5CN, v_{13}=1/v_{21}=1
753	$66_{11,56} - 65_{12,53}$	236411.188	59	713	15.3	37	Strong $HC^{13}CCN$, v_7=1, CH_3NH_2, and C_2H_5CN, v_{13}=1/v_{21}=1
754	$38_{11,28} - 37_{11,27}$	240806.888	6	264	200.6	216	Strong $CH_3{}^{13}CH_2CN$
755	$38_{11,27} - 37_{11,26}$	240807.233	6	264	200.6	216	Strong $CH_3{}^{13}CH_2CN$

Table A.1: continued.

N^a	Transition^b	Frequency (MHz)	Unc.^{c} (kHz)	$E_l{}^d$ (K)	$S\mu^2$ (D^2)	σ^e (mK)	Comments
(1)	(2)	(3)	(4)	(5)	(6)	(7)	(8)
756	$39_{4,35} - 38_{5,34}$	240932.302	7	236	34.4	216	Strong SO_2
757	$38_{10,29} - 37_{10,28}$	241209.162	6	255	203.8	216	Strong CH_3OH, v_t=1 and CH_3NH_2
758	$38_{10,28} - 37_{10,27}$	241214.867	6	255	203.8	216	Strong CH_3OH, v_t=1 and CH_3NH_2
759	$18_{8,11} - 17_{7,10}{}^\star$	244337.755	10	67	15.9	46	Strong CH_3OH, v_t=1 and C_2H_5OH
761	$18_{8,11} - 17_{7,11}{}^\star$	244338.081	10	67	11.8	46	Strong CH_3OH, v_t=1 and C_2H_5OH
763	$69_{12,58} - 68_{13,56}$	244347.274	135	784	16.5	46	Strong CH_3OH, v_t=1 and C_2H_5OH
764	$39_{4,35} - 38_{4,34}$	244747.400	7	235	219.7	39	Strong CH_3CH_3CO, v_t=1
765	$40_{3,37} - 39_{4,36}$	244862.776	7	241	46.3	39	Strong $^{13}CH_3CH_2CN$
766	$40_{4,37} - 39_{4,36}$	245039.786	7	241	226.2	39	Strong CH_3CHO
767	$40_{3,37} - 39_{3,36}$	245114.964	7	241	226.2	72	Strong CH_2NH
768	$57_{1,56} - 57_{0,57}{}^\star$	245117.740	240	461	7.7	72	Strong CH_2NH
770	$57_{2,56} - 57_{1,57}{}^\star$	245117.740	240	461	7.7	72	Strong CH_2NH
772	$21_{7,15} - 20_{6,14}$	245166.228	10	79	14.9	72	Strong CH_3CHO and $HCC^{13}CN$, v_7=1
773	$21_{7,14} - 20_{6,14}$	245172.645	10	79	12.3	72	Strong CH_3CHO and $HCC^{13}CN$, v_7=1
774	$21_{7,15} - 20_{6,15}$	245242.772	10	79	12.3	72	Strong C_2H_3CN, v_{15}=1
775	$21_{7,14} - 20_{6,15}$	245249.189	10	79	14.9	72	Strong C_2H_3CN, v_{15}=1
776	$40_{4,37} - 39_{3,36}$	245291.974	7	241	46.3	72	Strong CH_3CH_3CO
777	$38_{5,33} - 37_{5,32}$	245912.486	7	228	214.2	53	Strong $CH_2CH^{13}CN$ and $CH_2{}^{13}CHCN$
778	$52_{7,45} - 51_{8,43}$	245922.351	49	435	16.5	53	Strong $CH_2CH^{13}CN$ and $CH_2{}^{13}CHCN$
779	$24_{6,19} - 23_{5,19}$	245999.489	9	94	13.2	53	Strong C_2H_5CN and $CH_2{}^{13}CHCN$
780	$39_{35,4} - 38_{35,3}{}^\star$	247203.868	14	733	43.7	68	Strong HC_3N, v_7=2 and C_2H_5CN
782	$54_{7,47} - 53_{8,45}$	247209.367	64	467	15.7	68	Strong HC_3N, v_7=2 and C_2H_5CN
783	$39_{11,29} - 38_{11,28}$	247211.820	6	276	206.8	68	Strong HC_3N, v_7=2 and C_2H_5CN
784	$39_{11,28} - 38_{11,27}$	247212.409	6	276	206.8	68	Strong HC_3N, v_7=2 and C_2H_5CN
785	$25_{6,19} - 24_{5,19}$	247346.153	12	102	13.9	68	Strong CH_3CHO
786	$39_{6,34} - 38_{6,33}$	247349.240	7	241	218.7	68	Strong CH_3CHO
787	$40_{4,36} - 39_{5,35}$	247433.054	7	247	36.5	68	Strong CH_3CHO and t-HCOOH

Notes: ^{a} Numbering of the observed transitions associated with a modeled line stronger than 20 mK. ^{b} Transitions marked with a * are double with a frequency difference less than 0.1 MHz. The quantum numbers of the second one are not shown. ^{c} Frequency uncertainty. ^{d} Lower energy level in temperature units (E_l/k_B). ^{e} Calculated rms noise level in T_{mb} scale.

Appendix B

Observed Transitions of Cyanoethanol

Table B.1: Transitions of the *gauche*-conformer of 2-cyanoethanol observed with the IRAM 30 m telescope toward Sgr B2(N). The horizontal lines mark discontinuities in the observed frequency coverage. Only the transitions associated with a modeled line stronger than 20 mK are listed.

N^a	Transition^b	Frequency (MHz)	Unc.^{c} (kHz)	$E_l{}^d$ (K)	$S\mu^2$ (D^2)	σ^e (mK)	Comments
(1)	(2)	(3)	(4)	(5)	(6)	(7)	(8)
1	$14_{0,14} - 13_{1,13}$	80867.350	7	26	78.0	33	Blend with U-lines, noisy
2	$14_{1,14} - 13_{0,13}$	81204.029	7	26	78.1	18	Blend with C_2H_5CN, v_{13}=1/v_{21}=1
3	$15_{0,15} - 14_{1,14}$	86552.902	8	30	84.6	17	**Candidate group**, blend with C_2H_5OH, uncertain baseline
4	$25_{17,8} - 26_{16,11}{}^\star$	86554.133	15	199	5.8	17	**Candidate group**, blend with C_2H_5OH, uncertain baseline
6	$15_{0,15} - 14_{0,14}$	86683.774	8	30	50.6	17	Blend with U-lines
7	$15_{1,15} - 14_{0,14}$	86766.281	8	30	84.6	16	Blend with $H^{13}CO^+$ in absorption
8	$14_{8,7} - 13_{8,6}{}^\star$	87827.230	6	51	32.1	17	Blend with C_2H_5OCHO and C_3H_7CN
10	$14_{7,8} - 13_{7,7}{}^\star$	87900.707	6	45	35.7	17	Blend with HNCO and $HN^{13}CO$
12	$14_{6,9} - 13_{6,8}$	88023.553	6	41	38.9	19	Blend with U-line
13	$24_{2,22} - 24_{1,23}$	88024.743	18	88	46.2	19	Blend with U-line
14	$14_{6,8} - 13_{6,7}$	88026.016	6	41	38.9	19	Blend with U-line
15	$15_{1,14} - 14_{2,13}$	88755.890	7	32	57.9	21	Strong C_2H_5CN
16	$14_{2,13} - 13_{1,12}$	88957.447	7	28	52.0	21	Blend with U-lines, uncertain baseline
17	$14_{2,12} - 13_{2,11}$	90627.495	6	30	46.4	20	Blend with U-line and C_2H_5CN, v_{13}=1/v_{21}=1
18	$15_{2,14} - 14_{2,13}$	90767.536	7	32	49.7	14	Blend with U-lines and SiS
19	$14_{3,11} - 13_{3,10}$	91039.698	7	31	45.5	14	Blend with HC_3N, v_5=1/v_7=3
20	$15_{1,14} - 14_{1,13}$	91606.811	7	32	49.9	24	Blend with C_2H_5CN, v_{13}=1/v_{21}=1 and CH_3CH_3CO
21	$16_{0,16} - 15_{1,15}$	92216.172	8	34	91.1	27	Blend with CH_3CN, v_8=1
22	$16_{1,16} - 15_{1,15}$	92267.808	8	34	53.9	22	Blend with CH_3CN, v_8=1
23	$16_{0,16} - 15_{0,15}$	92298.679	8	34	54.0	22	Blend with $H_3C^{13}CN$, v_8=1, U-line, and C_2H_5CN
24	$16_{1,16} - 15_{0,15}$	92350.315	8	34	91.1	22	Blend with CH_3CN, v_8=1
25	$24_{7,17} - 24_{6,18}$	93134.179	11	104	86.9	22	**Missing line**, but noisy and uncertain baseline?
26	$15_{2,14} - 14_{1,13}$	93618.458	8	32	58.7	24	Blend with $^{13}CH_3OH$
27	$15_{3,13} - 14_{3,12}$	93675.025	7	35	48.8	24	Blend with CH_3OCHO and U-line
28	$15_{13,2} - 14_{13,1}{}^\star$	94014.420	7	93	12.7	31	**Missing group**, uncertain baseline?
30	$28_{7,22} - 28_{6,23}$	94014.809	11	136	105.8	31	**Missing group**, uncertain baseline?
31	$15_{12,3} - 14_{12,2}{}^\star$	94015.384	7	84	18.4	31	**Missing group**, uncertain baseline?
33	$15_{9,7} - 14_{9,6}{}^\star$	94078.329	7	61	32.7	31	Blend with U-line and C_2H_5CN, v_{13}=1/v_{21}=1
35	$19_{15,4} - 20_{14,7}{}^\star$	94132.098	16	134	2.5	31	Noisy
37	$27_{7,21} - 27_{6,22}$	94132.140	11	128	101.0	31	Noisy
38	$15_{8,8} - 14_{8,7}{}^\star$	94135.150	7	55	36.5	31	Noisy
40	$15_{7,9} - 14_{7,8}$	94227.567	7	49	39.9	26	**Missing group**, but uncertain baseline?
41	$15_{7,8} - 14_{7,7}$	94227.738	7	49	39.9	26	**Missing group**, but uncertain baseline?
42	$23_{7,16} - 23_{6,17}$	94279.886	10	97	81.9	26	Strong C_2H_3CN and C_2H_5OH
43	$15_{6,10} - 14_{6,9}$	94380.043	7	45	42.9	26	Blend with CH_3OCHO and C_2H_5OH

Table B.1: continued.

N^a	Transition^b	Frequency (MHz)	Unc.^{c} (kHz)	$E_l{}^d$ (K)	$S\mu^2$ (D^2)	σ^e (mK)	Comments
(1)	(2)	(3)	(4)	(5)	(6)	(7)	(8)
44	$26_{7,20} - 26_{6,21}$	94381.365	10	119	96.2	26	Blend with CH_3OCHO and C_2H_5OH
45	$15_{5,11} - 14_{5,10}$	94611.332	7	41	45.3	26	Blend with C_2H_5OCHO and CH_3CH_3CO
46	$15_{4,12} - 14_{4,11}$	94694.932	7	38	47.4	28	Blend with C_2H_5OH
47	$15_{5,10} - 14_{5,9}$	94717.620	7	41	45.3	28	Blend with U-lines
48	$25_{7,19} - 25_{6,20}$	94722.525	10	111	91.3	28	Blend with U-line
49	$16_{1,15} - 15_{2,14}$	95099.808	8	37	65.0	28	Blend with C_2H_3CN, v_{15}=1 and C_2H_5CN
50	$24_{7,18} - 24_{6,19}$	95119.889	10	104	86.5	28	Blend with U-line and C_2H_3CN, v_{15}=1
51	$22_{7,15} - 22_{6,16}$	95189.303	10	90	77.0	28	Strong C_2H_3CN, v_{15}=1
52	$23_{7,17} - 23_{6,18}$	95543.182	10	97	81.7	23	Blend with U-line, $CH_2(OH)CHO$, and C_2H_5OH
53	$15_{4,11} - 14_{4,10}$	95803.931	7	38	47.4	23	Blend with $^{13}CH_3CH_2CN$ and C_2H_5CN, v_{13}=1/v_{21}=1
54	$21_{7,14} - 21_{6,15}$	95911.879	10	83	72.3	23	Strong C_2H_5OH and CH_3OH
55	$22_{7,16} - 22_{6,17}$	95968.197	10	90	76.9	23	Blend with C_2H_5CN, v_{13}=1/v_{21}=1
56	$21_{7,15} - 21_{6,16}$	96376.821	10	83	72.2	32	Blend with $H_2{}^{13}CO$ and CH_3OH, v_t=2
57	$20_{7,13} - 20_{6,14}$	96488.321	10	77	67.6	32	Strong CH_3OH, v_t=1
58	$16_{2,15} - 15_{2,14}$	96491.686	7	37	53.1	32	Strong CH_3OH, v_t=1
59	$9_{3,7} - 8_{2,7}$	96492.244	6	12	0.6	32	Strong CH_3OH, v_t=1
60	$15_{2,13} - 14_{2,12}$	96622.339	7	34	49.8	29	Blend with CH_3CHO, v_t=1 and $H^{13}C^{13}CCN$
61	$21_{16,5} - 22_{15,8}{}^\star$	96623.120	16	158	3.2	29	Blend with CH_3CHO, v_t=1 and $H^{13}C^{13}CCN$
63	$20_{7,14} - 20_{6,15}$	96756.587	10	77	67.6	29	Strong CH_3OH
64	$19_{7,12} - 19_{6,13}$	96950.611	10	70	63.0	29	Blend with CH_3CH_3CO, v_t=1, $CH_3{}^{13}CH_2CN$, and $H_2{}^{13}CCO$
65	$19_{7,13} - 19_{6,14}$	97099.887	10	70	63.0	21	**Candidate line**, blend with U-line?
66	$16_{1,15} - 15_{1,14}$	97111.454	7	37	53.2	21	Blend with U-line and C_3H_7CN
67	$18_{7,11} - 18_{6,12}$	97323.168	10	65	58.5	21	Blend with C_3H_7CN and U-lines
68	$18_{7,12} - 18_{6,13}$	97403.039	10	65	58.5	20	Blend with CH_3CH_3CO and U-line, uncertain baseline
69	$17_{7,11} - 17_{6,11}$	97622.760	10	59	1.0	20	Blend with C_2H_3CN, v_{11}=2
70	$17_{7,10} - 17_{6,11}$	97624.376	10	59	54.0	20	Blend with C_2H_3CN, v_{11}=2
71	$17_{7,11} - 17_{6,12}$	97665.313	10	59	54.0	20	Blend with C_2H_5CN, v_{13}=1/v_{21}=1
72	$17_{7,10} - 17_{6,12}$	97666.929	10	59	1.0	20	Blend with C_2H_5CN, v_{13}=1/v_{21}=1
73	$15_{3,12} - 14_{3,11}$	97806.800	7	35	49.1	20	**Candidate line**, blend with C_2H_5CN, v_{13}=1/v_{21}=1 and C_2H_5OH
74	$17_{0,17} - 16_{1,16}$	97864.630	8	38	97.7	20	**Missing group**, blend with C_3H_7CN
75	$16_{7,10} - 16_{6,10}$	97867.370	11	54	0.9	20	**Missing group**, blend with C_3H_7CN
76	$16_{7,9} - 16_{6,10}$	97868.051	11	54	49.5	20	**Missing group**, blend with C_3H_7CN
77	$16_{7,10} - 16_{6,11}$	97888.054	11	54	49.5	20	Blend with CH_3OCHO, v_t=1, $HCONH_2$, and U-line
78	$16_{7,9} - 16_{6,11}$	97888.735	11	54	0.9	20	Blend with CH_3OCHO, v_t=1, $HCONH_2$, and U-line
79	$17_{1,17} - 16_{1,16}$	97896.744	8	38	57.4	20	Blend with $a(CH_2OH)_2$ and CH_3OCHO, v_t=1
80	$17_{0,17} - 16_{0,16}$	97916.266	8	38	57.4	20	Blend with $HCONH_2$, U-line, and $CH_2(OH)CHO$
81	$17_{1,17} - 16_{0,16}$	97948.381	8	38	97.7	20	Blend with CH_3CH_3CO, v_t=1, uncertain baseline
82	$15_{7,9} - 15_{6,9}$	98064.412	11	49	0.9	20	Blend with U-line and $C_2H_5{}^{13}CN$
83	$15_{7,8} - 15_{6,9}$	98064.681	11	49	45.1	20	Blend with U-line and $C_2H_5{}^{13}CN$
84	$15_{7,9} - 15_{6,10}$	98073.943	11	49	45.1	20	Strong $CH_3{}^{13}CH_2CN$ and $C_2H_5{}^{13}CN$
85	$15_{7,8} - 15_{6,10}$	98074.212	11	49	0.9	20	Strong $CH_3{}^{13}CH_2CN$ and $C_2H_5{}^{13}CN$
86	$14_{7,8} - 14_{6,8}{}^\star$	98222.287	11	45	0.8	18	Blend with U-line and C_2H_5CN, v_{13}=1/v_{21}=1
88	$75_{24,51} - 74_{25,50}{}^\star$	98223.780	72	1060	54.1	18	Blend with U-line and C_2H_5CN, v_{13}=1/v_{21}=1
90	$14_{7,8} - 14_{6,9}{}^\star$	98226.419	11	45	40.6	18	Strong C_2H_5CN, v_{13}=1/v_{21}=1
92	$13_{7,7} - 13_{6,7}{}^\star$	98347.596	11	41	0.7	18	**Missing group**, blend with U-line and CH_3CH_3CO, uncertain baseline
94	$13_{7,7} - 13_{6,8}{}^\star$	98349.265	11	41	36.1	18	**Missing group**, blend with U-line and CH_3CH_3CO, uncertain baseline
96	$12_{7,6} - 12_{6,6}{}^\star$	98445.704	11	37	0.6	18	Blend with CH_3OCHO and U-lines
98	$12_{7,6} - 12_{6,7}{}^\star$	98446.323	11	37	31.6	18	Blend with CH_3OCHO and U-lines
100	$16_{2,15} - 15_{1,14}$	98503.332	8	37	65.4	18	Blend with U-lines
101	$30_{6,25} - 30_{4,26}$	98519.710	13	149	1.9	18	Strong C_2H_5CN
102	$11_{7,5} - 11_{6,5}{}^\star$	98521.110	11	33	0.6	18	Strong C_2H_5CN
104	$11_{7,5} - 11_{6,6}{}^\star$	98521.318	11	33	27.0	18	Strong C_2H_5CN
106	$10_{7,3} - 10_{6,4}{}^\star$	98577.690	11	30	22.2	18	Blend with C_2H_5CN, v_{13}=1/v_{21}=1
108	$9_{7,2} - 9_{6,3}{}^\star$	98618.836	11	27	17.3	18	Strong C_2H_5CN, v_{13}=1/v_{21}=1 and v=0
110	$5_{5,1} - 4_{4,0}{}^\star$	99648.441	8	9	29.0	19	Strong $HC^{13}CCN$

Table B.1: continued.

N^a	Transition^b	Frequency (MHz)	Unc.^{c} (kHz)	$E_l{}^d$ (K)	$S\mu^2$ (D^2)	σ^e (mK)	Comments
(1)	(2)	(3)	(4)	(5)	(6)	(7)	(8)
112	$5_{5,1} - 4_{4,1}{}^\star$	99648.486	8	9	0.7	19	Strong $HC^{13}CCN$
114	$16_{3,14} - 15_{3,13}$	99688.953	7	39	52.3	19	Blend with C_2H_5CN and U-line
115	$16_{14,2} - 15_{14,1}{}^\star$	100293.808	7	107	12.8	24	Strong CH_3OCHO
117	$16_{12,4} - 15_{12,3}{}^\star$	100294.984	7	89	23.8	24	Strong CH_3OCHO
119	$16_{11,5} - 15_{11,4}{}^\star$	100308.588	7	80	28.7	24	Strong CH_3OCHO and CH_3CH_3CO
121	$16_{10,6} - 15_{10,5}{}^\star$	100334.865	7	73	33.2	24	Blend with $a(CH_2OH)_2$ and CH_3CH_3CO, v_t=1
123	$16_{9,8} - 15_{9,7}{}^\star$	100379.093	7	66	37.2	24	**Candidate group**, blend with CH_3CH_3CO, v_t=1, uncertain baseline
125	$16_{8,9} - 15_{8,8}{}^\star$	100450.235	7	59	40.8	24	Blend with $HCC^{13}CN$, v_5=1/v_7=3 and C_2H_5OH
127	$16_{7,10} - 15_{7,9}$	100564.513	7	54	44.0	20	**Missing group**, uncertain baseline?
128	$16_{7,9} - 15_{7,8}$	100564.925	7	54	44.0	20	**Missing group**, uncertain baseline?
129	$16_{6,11} - 15_{6,10}$	100750.402	7	49	46.8	20	Blend with U-line, uncertain baseline
130	$16_{6,10} - 15_{6,9}$	100761.554	7	49	46.8	20	Strong C_2H_5CN, v_{13}=1/v_{21}=1
131	$16_{4,13} - 15_{4,12}$	101009.913	7	42	51.0	21	Blend with U-line
132	$16_{5,12} - 15_{5,11}$	101012.281	7	45	49.1	21	Blend with U-line
133	$16_{5,11} - 15_{5,10}$	101199.587	7	45	49.1	21	Blend with $CH_2CH^{13}CN$ and CH_3OCHO, v_t=1
134	$17_{1,16} - 16_{2,15}$	101240.925	8	41	71.9	21	Blend with U-line and C_2H_5OH
135	$27_{3,25} - 27_{1,26}$	102186.982	19	110	1.6	30	Blend with C_2H_5CN, v_{13}=1/v_{21}=1, U-line, and CH_3OCH_3
136	$17_{2,16} - 16_{2,15}$	102188.335	8	41	56.5	30	Blend with C_2H_5CN, v_{13}=1/v_{21}=1, U-line, and CH_3OCH_3
137	$16_{2,14} - 15_{2,13}$	102456.406	7	39	53.1	30	**Candidate line**, partial blend with CH_3CH_3CO
138	$16_{4,12} - 15_{4,11}$	102622.206	7	42	51.0	37	**Candidate line**
139	$17_{1,16} - 16_{1,15}$	102632.803	8	41	56.6	37	Blend with U-line and C_2H_5CN, v_{13}=1/v_{21}=1
140	$58_{17,42} - 57_{18,39}{}^\star$	102634.748	14	615	44.7	37	Blend with U-line and C_2H_5CN, v_{13}=1/v_{21}=1
142	$31_{8,23} - 31_{7,24}$	103290.278	12	168	117.1	25	Blend with CH_3CH_3CO, v_t=1, $HCONH_2$, and U-line
143	$8_{4,4} - 7_{3,5}$	103293.008	7	12	24.7	25	Blend with $HCONH_2$ and U-line
144	$25_{1,24} - 25_{1,25}$	103294.207	20	90	0.9	25	Blend with $HCONH_2$ and U-line
145	$25_{1,24} - 25_{0,25}$	103294.827	20	90	23.2	25	Blend with $HCONH_2$ and U-line
146	$18_{0,18} - 17_{1,17}$	103503.257	8	43	104.2	27	Blend with U-line and C_2H_5CN, v_{13}=1/v_{21}=1
147	$18_{1,18} - 17_{1,17}$	103523.122	8	43	60.8	27	Strong $HCONH_2$ and C_2H_5OH
148	$43_{11,32} - 42_{12,31}$	103534.233	14	325	35.6	27	Blend with CH_3CH_3CO, v_t=1 and U-line, uncertain baseline
149	$18_{0,18} - 17_{0,17}$	103535.372	8	43	60.8	27	Blend with CH_3CH_3CO, v_t=1 and U-line, uncertain baseline
150	$18_{1,18} - 17_{0,17}$	103555.237	8	43	104.2	27	**Candidate line**, noisy
151	$17_{2,16} - 16_{1,15}$	103580.213	8	41	72.2	27	Blend with C_2H_3CN and U-line
152	$16_{3,13} - 15_{3,12}$	104475.290	7	40	52.6	48	Blend with C_3H_7CN and U-lines
153	$18_{2,16} - 17_{3,15}$	104511.568	10	49	48.3	25	Blend with C_2H_3CN, v_{11}=1
154	$13_{3,11} - 12_{2,10}$	104897.724	8	26	28.1	25	Blend with $CH_3{}^{13}CH_2CN$
155	$30_{8,22} - 30_{7,23}$	105171.268	12	159	111.7	28	Blend with U-lines
156	$17_{3,15} - 16_{3,14}$	105646.146	7	44	55.7	37	Blend with $a(CH_2OH)_2$ and C_2H_3CN, v_{11}=2
157	$6_{5,2} - 5_{4,1}{}^\star$	105908.750	8	10	29.2	43	Blend with C_3H_7CN, uncertain baseline
159	$6_{5,2} - 5_{4,2}{}^\star$	105909.154	8	10	0.7	43	Blend with C_3H_7CN, uncertain baseline
161	$17_{13,4} - 16_{13,3}{}^\star$	106568.770	8	102	24.0	34	Noisy, blend with C_2H_5CN
163	$17_{14,3} - 16_{14,2}{}^\star$	106569.152	8	112	18.6	34	Noisy, blend with C_2H_5CN
165	$17_{15,2} - 16_{15,1}{}^\star$	106576.263	8	123	12.8	34	Noisy
167	$17_{12,5} - 16_{12,4}{}^\star$	106576.848	7	93	29.0	34	Noisy
169	$17_{11,6} - 16_{11,5}{}^\star$	106595.949	7	85	33.6	34	Blend with U-line and C_2H_5OCHO
171	$17_{10,7} - 16_{10,6}{}^\star$	106630.022	7	77	37.8	34	Blend with CH_3OH, v_t=1 and CH_3OCHO
173	$28_{3,26} - 28_{1,27}$	106630.998	19	118	1.6	34	Blend with CH_3OH, v_t=1 and CH_3OCHO
174	$17_{9,9} - 16_{9,8}{}^\star$	106685.426	7	70	41.6	34	**Missing group**, blend with CH_3CH_3CO, uncertain baseline
176	$29_{8,21} - 29_{7,22}$	106711.320	11	150	106.4	34	Blend with U-line and $CH_2(OH)CHO$
177	$17_{8,10} - 16_{8,9}{}^\star$	106772.990	7	64	45.0	34	Strong CH_3OCH_3
179	$17_{7,11} - 16_{7,10}$	106912.263	7	59	48.0	24	Strong $HOCO^+$
180	$17_{7,10} - 16_{7,9}$	106913.198	7	59	48.0	24	Strong $HOCO^+$
181	$17_{6,12} - 16_{6,11}$	107135.004	7	54	50.6	24	Blend with C_2H_5CN, v_{20}=1 and U-line
182	$17_{6,11} - 16_{6,10}$	107156.873	7	54	50.6	24	Strong CH_3OH
183	$18_{1,17} - 17_{2,16}$	107226.905	8	46	78.8	24	Blend with C_2H_5CN, v_{13}=1/v_{21}=1 and CH_3CH_3CO
184	$32_{8,25} - 32_{7,26}$	107255.747	12	178	121.1	24	Strong C_2H_5CN, v_{13}=1/v_{21}=1
185	$17_{4,14} - 16_{4,13}$	107290.752	7	47	54.6	24	Blend with $^{13}C^{17}O$
186	$17_{5,13} - 16_{5,12}$	107419.323	7	50	52.8	24	Strong $H_3{}^{13}CCN$, v_8=1 and C_2H_5CN, v_{13}=1/v_{21}=1
187	$31_{8,24} - 31_{7,25}$	107678.486	12	168	116.1	24	Blend with C_2H_5CN, v_{20}=1
188	$17_{5,12} - 16_{5,11}$	107734.687	7	50	52.8	46	Strong C_2H_5CN, v=0 and v_{13}=1/v_{21}=1
189	$18_{2,17} - 17_{2,16}$	107863.000	8	46	59.9	46	**Candidate line**, blend with C_3H_7CN, noisy
190	$28_{8,20} - 28_{7,21}$	107966.919	11	141	101.3	46	Blend with CH_3CH_3CO
191	$14_{3,12} - 13_{2,11}$	108027.175	9	30	31.3	46	Partial blend with $CH_3{}^{13}CH_2CN$, noisy

Table B.1: continued.

N^a	Transition^b	Frequency (MHz)	Unc.^{c} (kHz)	$E_l{}^d$ (K)	$S\mu^2$ (D^2)	σ^e (mK)	Comments
(1)	(2)	(3)	(4)	(5)	(6)	(7)	(8)
192	$17_{2,15} - 16_{2,14}$	108140.530	7	44	56.3	48	Blend with U-lines, noisy
193	$18_{1,17} - 17_{1,16}$	108174.315	8	46	60.0	48	Noisy
194	$30_{8,23} - 30_{7,24}$	108176.244	11	159	111.0	48	Noisy
195	$29_{8,22} - 29_{7,23}$	108716.054	11	149	106.0	20	Strong C_2H_5CN
196	$18_{2,17} - 17_{1,16}$	108810.410	8	46	79.0	20	Blend with ^{13}CN in absorption, C_3H_7CN, and C_2H_3CN
197	$34_{8,26} - 34_{7,28}$	108945.062	14	198	1.7	29	Strong C_2H_5CN
198	$9_{4,6} - 8_{3,5}$	108945.793	7	14	25.4	29	Strong C_2H_5CN
199	$27_{8,19} - 27_{7,20}$	108991.589	11	132	96.3	29	Partial blend with NH_2CH_2CN, noisy
200	$19_{0,19} - 18_{1,18}$	109135.309	9	48	110.7	29	Strong CH_3OH
201	$19_{1,19} - 18_{1,18}$	109147.539	9	48	64.2	29	Blend with $CH_3{}^{13}CH_2CN$ and CH_3OH
202	$19_{0,19} - 18_{0,18}$	109155.174	9	48	64.1	29	Strong CH_3OH and C_2H_5CN, v_{13}=1/v_{21}=1
203	$19_{16,3} - 20_{15,6}{}^\star$	109165.795	16	145	1.7	29	Strong $^{13}CH_3OH$ and HC_3N
205	$19_{1,19} - 18_{0,18}$	109167.404	9	48	110.7	29	Strong $^{13}CH_3OH$ and HC_3N
206	$28_{8,21} - 28_{7,22}$	109270.428	11	141	101.1	36	Blend with CH_3CH_3CO, v_t=1 and U-line
207	$17_{4,13} - 16_{4,12}$	109519.258	8	47	54.6	36	Blend with CH_3CH_3CO, v_t=1 and U-line
208	$9_{4,5} - 8_{3,6}$	109631.846	7	14	25.2	36	Blend with U-line
209	$27_{8,20} - 27_{7,21}$	109817.656	11	132	96.2	41	Blend with CH_3CN, v_4=1
210	$51_{8,43} - 51_{8,44}$	109830.189	34	425	4.3	41	Strong HNCO
211	$26_{8,18} - 26_{7,19}$	109831.610	11	124	91.5	41	Strong HNCO
212	$26_{8,19} - 26_{7,20}$	110341.630	11	124	91.4	24	Blend with U-line and CH_3CN
213	$25_{8,17} - 25_{7,18}$	110524.761	11	116	86.7	32	Blend with CH_3OCHO
214	$25_{8,18} - 25_{7,19}$	110831.299	11	116	86.6	25	Blend with U-line and C_2H_3CN
215	$17_{3,14} - 16_{3,13}$	111018.412	7	45	56.1	25	Blend with CH_3CH_3CO and CH_3CN, v_8=2
216	$29_{3,27} - 29_{2,28}$	111073.611	19	126	46.3	25	Blend with NH_2CH_2CN and $^{13}CH_2CHCN$, uncertain baseline
217	$15_{3,13} - 14_{2,12}$	111074.706	9	34	35.2	25	Blend with NH_2CH_2CN and $^{13}CH_2CHCN$, uncertain baseline
218	$24_{8,16} - 24_{7,17}$	111100.763	11	108	81.9	25	Blend with CH_3COOH and $CH_2(OH)CHO$, uncertain baseline
219	$24_{8,17} - 24_{7,18}$	111279.906	11	108	81.9	35	Blend with U-line and C_2H_5OH
220	$18_{3,16} - 17_{3,15}$	111547.945	8	49	59.2	35	Blend with CH_3COOH and C_2H_3CN, v_{11}=1
221	$23_{8,15} - 23_{7,16}$	111582.487	11	101	77.3	35	Blend with a$(CH_2OH)_2$ and $^{13}CH_2CHCN$
222	$23_{8,16} - 23_{7,17}$	111684.126	11	101	77.3	29	Blend with CH_3OCHO and U-line
223	$22_{8,15} - 22_{7,15}$	111984.533	11	94	1.3	29	Blend with U-line
224	$22_{8,14} - 22_{7,15}$	111987.349	11	94	72.7	29	Blend with U-line
225	$22_{8,15} - 22_{7,16}$	112043.223	11	94	72.7	42	Blend with C_2H_5CN, v_{13}=1/v_{21}=1 and C_2H_5OH
226	$13_{2,11} - 12_{1,11}$	112143.318	9	24	0.9	42	Blend with $^{13}CH_3OH$
227	$19_{2,17} - 18_{3,16}$	112144.262	9	55	55.6	42	Blend with $^{13}CH_3OH$
228	$27_{2,26} - 27_{0,27}$	112160.508	21	105	0.9	42	Blend with U-line, $CH_2{}^{13}CHCN$, and CH_3CH_3CO
229	$7_{5,3} - 6_{4,2}{}^\star$	112163.322	8	12	29.7	42	Blend with U-line, $CH_2{}^{13}CHCN$, and CH_3CH_3CO
231	$7_{5,3} - 6_{4,3}{}^\star$	112165.334	8	12	0.7	42	Blend with U-line, $CH_2{}^{13}CHCN$, and CH_3CH_3CO
233	$21_{8,14} - 21_{7,14}$	112327.272	11	88	1.3	42	Blend with U-line and a$(CH_2OH)_2$
234	$21_{8,13} - 21_{7,14}$	112328.607	11	88	68.2	42	Blend with U-line and a$(CH_2OH)_2$
235	$21_{8,14} - 21_{7,15}$	112358.297	11	88	68.2	42	Strong $C^{17}O$
236	$21_{8,13} - 21_{7,15}$	112359.632	11	88	1.3	42	Strong $C^{17}O$
237	$20_{8,13} - 20_{7,13}$	112615.845	11	81	1.2	31	Blend with U-line and CH_3CH_3CO
238	$20_{8,12} - 20_{7,13}$	112616.451	11	81	63.7	31	Blend with U-line and CH_3CH_3CO
239	$20_{8,13} - 20_{7,14}$	112631.657	11	81	63.7	31	Blend with U-lines, $^{13}CH_3CH_2CN$, and $CH_3{}^{13}CH_2CN$
240	$20_{8,12} - 20_{7,14}$	112632.263	11	81	1.2	31	Blend with U-lines, $^{13}CH_3CH_2CN$, and $CH_3{}^{13}CH_2CN$
241	$18_{13,5} - 17_{13,4}{}^\star$	112848.515	8	108	29.3	40	Blend with C_2H_3CN, U-line, and CH_3OCHO
243	$18_{15,3} - 17_{15,2}{}^\star$	112850.688	8	128	18.7	40	Blend with C_2H_3CN, U-line, and CH_3OCHO
245	$19_{8,12} - 19_{7,12}$	112858.588	11	75	1.1	40	**Missing group**, uncertain baseline?
246	$19_{8,11} - 19_{7,12}$	112858.852	11	75	59.2	40	**Missing group**, uncertain baseline?
247	$18_{12,6} - 17_{12,5}{}^\star$	112861.107	8	98	34.0	40	**Missing group**, uncertain baseline?
249	$18_{16,2} - 17_{16,1}{}^\star$	112861.973	8	139	12.9	40	**Missing group**, uncertain baseline?
251	$19_{8,12} - 19_{7,13}$	112866.330	11	75	59.2	40	Blend with CH_3OCHO and U-line
252	$19_{8,11} - 19_{7,13}$	112866.594	11	75	1.1	40	Blend with CH_3OCHO and U-line
253	$18_{11,7} - 17_{11,6}{}^\star$	112886.550	8	90	38.4	40	Blend with c-C_2H_4O and U-line
255	$18_{10,8} - 17_{10,7}{}^\star$	112929.547	7	82	42.3	40	Blend with CH_3CH_3CO, v_t=1 and U-lines
257	$18_{9,10} - 17_{9,9}{}^\star$	112997.686	7	76	45.9	40	Strong CH_3OCH_3
259	$18_{8,11} - 18_{7,11}$	113062.084	11	69	1.1	40	Blend with CH_3OCH_3
260	$18_{8,10} - 18_{7,11}$	113062.193	11	69	54.7	40	Blend with CH_3OCH_3
261	$18_{8,11} - 18_{7,12}$	113065.710	11	69	54.7	40	Blend with CH_3OCH_3 and U-line
262	$18_{8,10} - 18_{7,12}$	113065.819	11	69	1.1	40	Blend with CH_3OCH_3 and U-line
263	$19_{1,18} - 18_{2,17}$	113098.433	8	52	85.6	40	Strong C_2H_5OH
264	$18_{8,11} - 17_{8,10}{}^\star$	113103.934	7	69	49.1	40	Blend with U-line and C_2H_3CN, v_{11}=1
266	$17_{8,10} - 17_{7,10}{}^\star$	113231.688	11	64	1.0	28	Blend with CN in absorption

Table B.1: continued.

N^a	Transition^b	Frequency (MHz)	Unc.^{c} (kHz)	$E_l{}^d$ (K)	$S\mu^2$ (D^2)	σ^e (mK)	Comments
(1)	(2)	(3)	(4)	(5)	(6)	(7)	(8)
268	$17_{8,10} - 17_{7,11}{}^\star$	113233.304	11	64	50.3	28	Blend with CN in absorption
270	$18_{7,12} - 17_{7,11}$	113271.528	7	64	52.0	28	Blend with CH_3OCH_3 and CH_3CH_3CO, v_t=1
271	$18_{7,11} - 17_{7,10}$	113273.538	7	64	52.0	28	Blend with CH_3OCH_3 and CH_3CH_3CO, v_t=1
272	$16_{8,9} - 16_{7,9}{}^\star$	113371.896	11	59	0.9	28	Blend with $CH_2{}^{13}CHCN$ and C_2H_3CN, v_{11}=2
274	$16_{8,9} - 16_{7,10}{}^\star$	113372.577	11	59	45.8	28	Blend with $CH_2{}^{13}CHCN$ and C_2H_3CN, v_{11}=2
276	$15_{8,8} - 15_{7,8}{}^\star$	113486.586	11	54	0.8	28	Blend with CN in absorption
278	$15_{8,8} - 15_{7,9}{}^\star$	113486.855	11	54	41.3	28	Blend with CN in absorption
280	$19_{2,18} - 18_{2,17}$	113520.598	8	52	63.3	28	Blend with CN in absorption
281	$18_{4,15} - 17_{4,14}$	113529.090	8	52	58.1	28	Blend with CN in absorption
282	$18_{6,13} - 17_{6,12}$	113533.802	7	59	54.4	28	Blend with CN in absorption
283	$18_{6,12} - 17_{6,11}$	113574.746	7	59	54.4	28	Blend with CN in absorption
284	$14_{8,7} - 14_{7,7}{}^\star$	113579.173	11	49	0.7	28	Blend with CN in absorption
286	$14_{8,7} - 14_{7,8}{}^\star$	113579.272	11	49	36.8	28	Blend with CN in absorption
288	$13_{8,6} - 13_{7,6}{}^\star$	113652.717	11	45	0.7	34	Strong $^{13}CH_3CH_2CN$
290	$13_{8,6} - 13_{7,7}{}^\star$	113652.750	11	45	32.2	34	Strong $^{13}CH_3CH_2CN$
292	$18_{2,16} - 17_{2,15}$	113702.100	8	49	59.6	34	Blend with $^{13}CH_3CH_2CN$ and U-line
293	$12_{8,5} - 12_{7,5}{}^\star$	113709.978	12	41	0.6	34	Blend with U-line and CH_3CH_3CO
295	$12_{8,5} - 12_{7,6}{}^\star$	113709.988	12	41	27.5	34	Blend with U-line and CH_3CH_3CO
297	$19_{1,18} - 18_{1,17}$	113734.528	8	52	63.4	34	Blend with HNCO
298	$47_{12,36} - 46_{13,33}$	113736.855	13	387	39.0	34	Blend with HNCO
299	$11_{8,4} - 11_{7,4}{}^\star$	113753.467	12	38	0.5	34	Strong CH_3OCHO
301	$11_{8,4} - 11_{7,5}{}^\star$	113753.470	12	38	22.6	34	Strong CH_3OCHO
303	$10_{8,2} - 10_{7,3}{}^\star$	113785.464	12	34	17.5	34	Blend with C_2H_5OCHO and U-line
305	$9_{8,1} - 9_{7,2}{}^\star$	113808.040	12	31	12.2	34	Blend with CH_3CH_3CO and C_2H_3CN, v_{15}=1
307	$18_{5,14} - 17_{5,13}$	113826.898	8	55	56.5	34	Blend with U-line and C_2H_3CN
308	$16_{3,14} - 15_{2,13}$	114141.320	9	39	39.8	33	Blend with U-line
309	$19_{2,18} - 18_{1,17}$	114156.693	8	52	85.7	33	Blend with U-line and C_3H_7CN
310	$18_{5,13} - 17_{5,12}$	114335.717	8	55	56.5	33	Blend with C_2H_3CN, v_{11}=1
311	$21_{3,18} - 20_{4,17}$	114607.784	14	69	38.3	37	Strong C_2H_3CN, v_{11}=2 and $H^{13}CCCN$
312	$10_{4,7} - 9_{3,6}$	114702.942	7	17	26.0	37	Blend with CH_3OCH_3
313	$20_{0,20} - 19_{1,19}$	114762.875	9	53	117.2	37	Blend with C_2H_5CN
314	$20_{1,20} - 19_{1,19}$	114770.374	9	53	67.5	37	Blend with C_2H_5CN and U-line
315	$20_{0,20} - 19_{0,19}$	114775.106	9	53	67.6	37	Blend with $^{13}CH_3CH_2CN$, U-line, and CH_3CH_3CO, v_t=1
316	$20_{1,20} - 19_{0,19}$	114782.604	9	53	117.2	37	Blend with U-lines
317	$23_{2,22} - 22_{2,21}$	136051.289	9	75	76.9	28	Blend with U-line and C_2H_5CN, v_{13}=1/v_{21}=1
318	$23_{1,22} - 22_{1,21}$	136093.077	9	75	76.9	28	Blend with U-line and C_2H_5CN, v_{13}=1/v_{21}=1
319	$23_{2,22} - 22_{1,21}$	136168.212	9	75	112.2	28	Blend with U-lines
320	$37_{10,27} - 37_{9,28}$	136440.827	12	242	135.3	28	Blend with $CH_3{}^{13}CH_2CN$ and U-line
321	$38_{10,29} - 38_{9,30}$	136480.175	13	254	140.3	28	Strong HC_3N, v_5=1/v_7=3 and C_2H_5CN, v_{13}=1/v_{21}=1
322	$14_{2,13} - 13_{1,13}$	136480.836	10	26	0.4	28	Strong HC_3N, v_5=1/v_7=3 and C_2H_5CN, v_{13}=1/v_{21}=1
323	$24_{2,22} - 23_{3,21}$	145126.300	9	86	91.9	25	Strong CH_3OH
324	$23_{7,17} - 22_{7,16}$	145259.787	8	94	71.0	25	Blend with C_2H_5OH, uncertain baseline
325	$54_{13,42} - 53_{14,40}$	145260.626	14	503	1.2	25	Blend with C_2H_5OH, uncertain baseline
326	$23_{7,16} - 22_{7,15}$	145308.454	8	94	71.0	25	Strong $HCC^{13}CN$, v_7=1 and C_2H_3CN, v_{15}=1
327	$54_{10,45} - 54_{8,46}$	154331.413	24	479	3.4	112	Strong CH_3OCHO
328	$37_{11,26} - 37_{10,27}$	154332.966	12	249	129.8	112	Strong CH_3OCHO
329	$37_{11,27} - 37_{10,28}$	154406.602	12	249	129.8	112	Strong HNCO
330	$26_{11,16} - 25_{11,15}{}^\star$	163350.130	8	142	72.6	38	**Missing group**, blend with C_2H_5OCHO, uncertain baseline?
332	$27_{3,25} - 26_{2,24}$	163373.443	8	107	112.5	38	Blend with SiS and CH_3COOH
333	$26_{10,17} - 25_{10,16}{}^\star$	163514.580	8	134	75.4	38	Blend with CH_3OCHO and C_2H_5OH
335	$26_{6,20} - 25_{6,19}$	166608.848	8	112	83.7	66	Blend with $^{13}CH_2CHCN$ and CH_3CN, v_8=2
336	$32_{12,21} - 32_{11,21}{}^\star$	172614.055	10	203	1.9	44	Strong HC_3N, v_4=1
338	$32_{12,21} - 32_{11,22}{}^\star$	172614.293	10	203	102.3	44	Strong HC_3N, v_4=1
340	$31_{12,20} - 31_{11,20}{}^\star$	172849.978	9	193	1.8	44	Strong HC_3N and C_2H_5CN
342	$31_{12,20} - 31_{11,21}{}^\star$	172850.097	9	193	97.8	44	Strong HC_3N and C_2H_5CN
344	$28_{4,25} - 27_{4,24}$	172878.566	8	120	92.5	44	Strong C_2H_5OH
345	$18_{2,17} - 17_{1,17}$	175993.210	13	43	0.4	365	Blend with $^{13}CH_2CHCN$, noisy
346	$32_{5,27} - 31_{6,26}$	175993.594	17	164	49.5	365	Blend with $^{13}CH_2CHCN$, noisy
347	$53_{11,43} - 52_{12,40}$	176010.436	18	469	45.3	365	Blend with CH_3OCHO and CH_3CH_3CO, noisy
348	$28_{11,18} - 27_{11,17}{}^\star$	176011.654	8	158	80.6	365	Blend with CH_3OCHO and CH_3CH_3CO, noisy
350	$65_{40,25} - 66_{39,28}{}^\star$	176213.351	2104	1215	17.6	365	Noisy
352	$28_{5,24} - 27_{5,23}$	176215.901	8	124	91.8	365	Noisy

Table B.1: continued.

N^a	Transition^b	Frequency (MHz)	Unc.^{c} (kHz)	$E_l{}^d$ (K)	$S\mu^2$ (D^2)	σ^e (mK)	Comments
(1)	(2)	(3)	(4)	(5)	(6)	(7)	(8)
353	$28_{10,19} - 27_{10,18}$	176223.832	8	150	83.1	365	Blend with CH_3CH_3CO, v_t=1, noisy
354	$28_{10,18} - 27_{10,17}$	176224.012	8	150	83.1	365	Blend with CH_3CH_3CO, v_t=1, noisy
355	$42_{8,34} - 41_{9,33}$	176228.045	19	290	37.9	365	Blend with CH_3CH_3CO, v_t=1, noisy
356	$28_{4,25} - 27_{3,24}$	176230.732	9	119	90.3	365	Blend with CH_3CH_3CO, v_t=1, noisy
357	$57_{8,50} - 57_{6,51}$	176361.135	22	514	4.6	365	Blend with CH_3NH_2
358	$54_{13,42} - 54_{12,43}$	176362.805	15	501	204.8	365	Blend with CH_3NH_2
359	$27_{5,22} - 26_{5,21}$	176363.288	8	117	89.0	365	Blend with CH_3NH_2
360	$31_{6,25} - 30_{6,24}$	201857.105	7	155	101.8	138	Strong ^{34}SO
361	$41_{14,28} - 41_{13,28}{}^\star$	201870.297	11	321	2.4	138	Strong $^{13}CH_3CH_2CN$
363	$41_{14,28} - 41_{13,29}{}^\star$	201870.480	11	321	135.2	138	Strong $^{13}CH_3CH_2CN$
365	$49_{35,14} - 50_{34,17}{}^\star$	201872.733	568	802	8.0	138	Strong $^{13}CH_3CH_2CN$
367	$40_{14,27} - 40_{13,27}{}^\star$	202165.086	10	309	2.4	138	Strong CH_3CN
369	$40_{14,27} - 40_{13,28}{}^\star$	202165.184	10	309	130.7	138	Strong CH_3CN
371	$34_{2,32} - 33_{3,31}$	202173.430	7	168	158.9	138	Strong CH_3CN
372	$34_{3,32} - 33_{3,31}$	202187.335	7	168	113.5	138	Strong $^{13}CH_2CHCN$
373	$34_{2,32} - 33_{2,31}$	202195.058	7	168	113.5	138	Strong $CH_3{}^{13}CN$
374	$25_{8,18} - 25_{6,19}$	202199.834	21	112	0.2	138	Strong $CH_3{}^{13}CN$
375	$34_{3,32} - 33_{2,31}$	202208.962	7	168	158.9	138	Strong CH_3CN
376	$32_{9,24} - 31_{9,23}$	202216.762	7	179	100.3	138	Strong $CH_3{}^{13}CN$
377	$32_{9,23} - 31_{9,22}$	202249.232	7	179	100.2	138	Strong $CH_3{}^{13}CN$
378	$39_{14,26} - 39_{13,26}{}^\star$	202434.793	10	296	2.3	108	Strong C_2H_5CN
380	$39_{14,26} - 39_{13,27}{}^\star$	202434.844	10	296	126.1	108	Strong C_2H_5CN
382	$32_{6,27} - 31_{6,26}$	202442.339	7	164	104.8	108	Strong C_2H_5CN and t-HCOOH
383	$38_{14,25} - 38_{13,25}{}^\star$	202680.967	10	285	2.2	108	Strong C_2H_3CN, v_{15}=1
385	$38_{14,25} - 38_{13,26}{}^\star$	202680.994	10	285	121.6	108	Strong C_2H_3CN, v_{15}=1
387	$32_{8,25} - 31_{8,24}$	202844.933	7	173	102.0	138	Strong C_2H_3CN, v_{15}=2 and $H_3C^{13}CN$, v_8=1
388	$37_{14,24} - 37_{13,24}{}^\star$	202905.073	10	273	2.2	138	Strong $CH_3CN.v_8$=1
390	$37_{14,24} - 37_{13,25}{}^\star$	202905.087	10	273	117.1	138	Strong $CH_3CN.v_8$=1
392	$36_{14,23} - 36_{13,23}{}^\star$	203108.494	9	262	2.1	138	Blend with C_2H_5OCHO and C_2H_3CN, v_{11}=1/v_{15}=1
394	$36_{14,23} - 36_{13,24}{}^\star$	203108.501	9	262	112.6	138	Blend with C_2H_5OCHO and C_2H_3CN, v_{11}=1/v_{15}=1
396	$32_{8,24} - 31_{8,23}$	203181.927	7	173	102.0	138	Strong C_2H_3CN, v_{11}=2
397	$66_{8,58} - 66_{7,59}$	203183.009	24	687	192.4	138	Strong C_2H_3CN, v_{11}=2
398	$76_{16,60} - 76_{15,61}$	203265.387	43	965	304.8	161	Strong $H^{13}CCCN$, v_7=1 and C_2H_3CN, v_{11}=1
399	$32_{7,26} - 31_{7,25}$	203267.671	7	168	103.6	161	Strong $H^{13}CCCN$, v_7=1 and C_2H_3CN, v_{11}=1
400	$85_{16,70} - 85_{15,71}$	203276.210	69	1185	353.7	161	Strong $H^{13}CCCN$, v_7=1 and C_2H_3CN, v_{11}=1
401	$35_{14,22} - 35_{13,22}{}^\star$	203292.542	9	251	2.0	161	Strong C_2H_5OCHO and CH_3CN, v_8=2
403	$35_{14,22} - 35_{13,23}{}^\star$	203292.545	9	251	108.2	161	Strong C_2H_5OCHO and CH_3CN, v_8=2
405	$35_{1,34} - 34_{2,33}$	203356.562	7	171	190.4	161	Blend with CH_3CN, v_8=2
406	$35_{2,34} - 34_{2,33}$	203356.834	7	171	117.7	161	Blend with CH_3CN, v_8=2
407	$35_{1,34} - 34_{1,33}$	203357.003	7	171	117.7	161	Blend with CH_3CN, v_8=2
408	$35_{2,34} - 34_{1,33}$	203357.276	7	171	190.4	161	Blend with CH_3CN, v_8=2
409	$31_{5,27} - 30_{4,26}$	203378.234	10	149	79.6	161	Strong CH_3OCH_3
410	$34_{14,20} - 34_{13,21}{}^\star$	203458.463	9	241	103.7	161	Strong CH_3CN, v_8=2
412	$34_{14,21} - 34_{13,22}{}^\star$	203458.464	9	241	103.7	161	Strong CH_3CN, v_8=2
414	$33_{14,19} - 33_{13,20}{}^\star$	203607.444	9	230	99.3	161	Blend with CH_3CH_3CO and $^{13}CH_2CHCN$
416	$33_{14,20} - 33_{13,21}{}^\star$	203607.444	9	230	99.3	161	Blend with CH_3CH_3CO and $^{13}CH_2CHCN$
418	$32_{14,18} - 32_{13,19}{}^\star$	203740.616	8	220	94.8	364	Blend with $H^{13}CONH_2$, uncertain baseline
420	$32_{14,19} - 32_{13,20}{}^\star$	203740.616	8	220	94.8	364	Blend with $H^{13}CONH_2$, uncertain baseline
422	$31_{14,17} - 31_{13,18}{}^\star$	203859.059	8	211	90.4	364	Strong CH_3OCHO
424	$31_{14,18} - 31_{13,19}{}^\star$	203859.059	8	211	90.4	364	Strong CH_3OCHO
426	$32_{8,24} - 32_{6,27}$	203863.737	24	173	0.4	364	Strong CH_3OCHO
427	$30_{14,16} - 30_{13,17}{}^\star$	203963.805	8	201	85.9	364	Strong U-line
429	$30_{14,16} - 30_{13,18}{}^\star$	203963.805	8	201	1.7	364	Strong U-line
431	$29_{14,15} - 29_{13,16}{}^\star$	204055.841	8	192	81.5	364	Strong $H^{13}CCCN$, v_7=2
433	$29_{14,16} - 29_{13,16}{}^\star$	204055.841	8	192	1.6	364	Strong $H^{13}CCCN$, v_7=2
435	$28_{14,14} - 28_{13,15}{}^\star$	204136.111	8	184	77.0	316	Strong $^{34}SO_2$
437	$28_{14,14} - 28_{13,16}{}^\star$	204136.111	8	184	1.5	316	Strong $^{34}SO_2$
439	$12_{9,3} - 11_{8,4}{}^\star$	204144.855	10	43	55.6	316	Strong CH_3OCH_3
441	$12_{9,3} - 11_{8,3}{}^\star$	204144.855	10	43	1.3	316	Strong CH_3OCH_3
443	$27_{14,13} - 27_{13,14}{}^\star$	204205.520	8	175	72.5	316	Strong C_2H_3CN, v_{11}=1 and $CH_3{}^{13}CH_2CN$
445	$27_{14,13} - 27_{13,15}{}^\star$	204205.520	8	175	1.5	316	Strong C_2H_3CN, v_{11}=1 and $CH_3{}^{13}CH_2CN$
447	$36_{9,28} - 36_{7,29}$	204211.440	26	221	0.5	316	Strong C_2H_3CN, v_{11}=1 and $CH_3{}^{13}CH_2CN$
448	$26_{14,12} - 26_{13,13}{}^\star$	204264.935	8	167	68.0	316	Strong U-line and CH_3CH_3CO

Table B.1: continued.

N^a	Transition^b	Frequency (MHz)	Unc.^{c} (kHz)	$E_l{}^d$ (K)	$S\mu^2$ (D^2)	σ^e (mK)	Comments
(1)	(2)	(3)	(4)	(5)	(6)	(7)	(8)
450	$26_{14,12} - 26_{13,14}{}^\star$	204264.935	8	167	1.4	316	Strong U-line and CH_3CH_3CO
452	$33_{7,26} - 33_{5,29}$	204313.845	34	179	0.3	316	Strong C_2H_5CN
453	$25_{14,11} - 25_{13,12}{}^\star$	204315.184	9	159	63.4	316	Strong C_2H_5CN
455	$25_{14,11} - 25_{13,13}{}^\star$	204315.184	9	159	1.3	316	Strong C_2H_5CN
457	$24_{14,10} - 24_{13,11}{}^\star$	204357.063	9	152	58.8	316	Strong U-line, CH_3CH_3CO, and C_2H_5OCHO
459	$24_{14,10} - 24_{13,12}{}^\star$	204357.063	9	152	1.2	316	Strong U-line, CH_3CH_3CO, and C_2H_5OCHO
461	$23_{14,9} - 23_{13,10}{}^\star$	204391.333	9	145	54.1	316	Strong SO_2 and $H^{13}CCCN$, v_5=1/v_7=3
463	$23_{14,9} - 23_{13,11}{}^\star$	204391.333	9	145	1.1	316	Strong SO_2 and $H^{13}CCCN$, v_5=1/v_7=3
465	$22_{14,8} - 22_{13,9}{}^\star$	204418.719	9	138	49.4	316	Strong $^{13}CH_3CH_2CN$ and U-line
467	$22_{14,8} - 22_{13,10}{}^\star$	204418.719	9	138	1.0	316	Strong $^{13}CH_3CH_2CN$ and U-line
469	$21_{14,7} - 21_{13,8}{}^\star$	204439.919	10	131	44.6	316	Strong U-line
471	$21_{14,7} - 21_{13,9}{}^\star$	204439.919	10	131	0.9	316	Strong U-line
473	$63_{15,49} - 63_{14,49}$	204441.015	15	680	3.4	316	Strong U-line
474	$20_{14,6} - 20_{13,7}{}^\star$	204455.597	10	125	39.6	316	Strong U-line and CH_3CH_3CO
476	$20_{14,6} - 20_{13,8}{}^\star$	204455.597	10	125	0.8	316	Strong U-line and CH_3CH_3CO
478	$19_{14,5} - 19_{13,6}{}^\star$	204466.385	10	119	34.6	316	Strong CH_3CH_3CO
480	$19_{14,5} - 19_{13,7}{}^\star$	204466.385	10	119	0.7	316	Strong CH_3CH_3CO
482	$14_{14,0} - 14_{13,1}{}^\star$	204467.046	12	93	6.5	316	Strong CH_3CH_3CO
484	$15_{14,1} - 15_{13,2}{}^\star$	204472.257	12	98	12.7	316	Strong CH_3CH_3CO and $^{13}CH_3OH$
486	$15_{14,1} - 15_{13,3}{}^\star$	204472.257	12	98	0.3	316	Strong CH_3CH_3CO and $^{13}CH_3OH$
488	$18_{14,4} - 18_{13,5}{}^\star$	204472.887	11	113	29.4	316	Strong CH_3CH_3CO and $^{13}CH_3OH$
490	$18_{14,4} - 18_{13,6}{}^\star$	204472.887	11	113	0.6	316	Strong CH_3CH_3CO and $^{13}CH_3OH$
492	$45_{8,37} - 44_{9,35}$	204475.101	16	330	1.5	316	Strong CH_3CH_3CO and $^{13}CH_3OH$
493	$16_{14,2} - 16_{13,3}{}^\star$	204475.295	11	102	18.5	316	Strong CH_3CH_3CO and $^{13}CH_3OH$
495	$16_{14,2} - 16_{13,4}{}^\star$	204475.295	11	102	0.4	316	Strong CH_3CH_3CO and $^{13}CH_3OH$
497	$17_{14,3} - 17_{13,4}{}^\star$	204475.676	11	108	24.0	316	Strong CH_3CH_3CO and $^{13}CH_3OH$
499	$17_{14,3} - 17_{13,5}{}^\star$	204475.676	11	108	0.5	316	Strong CH_3CH_3CO and $^{13}CH_3OH$
501	$36_{0,36} - 35_{1,35}{}^\star$	204565.243	7	174	221.0	316	Blend with CH_3OCH_3
503	$36_{0,36} - 35_{0,35}{}^\star$	204565.246	7	174	122.0	316	Blend with CH_3OCH_3
505	$33_{5,29} - 32_{5,28}$	205352.174	7	169	108.9	100	Strong $^{13}CH_3CH_2CN$ and $C_2H_5{}^{13}CN$
506	$32_{7,25} - 31_{7,24}$	205454.628	7	168	103.7	100	Strong C_2H_5OH and CH_3CH_3CO, v_t=1
507	$20_{6,15} - 19_{5,14}$	205722.264	8	67	42.3	271	Blend with C_2H_5CN
508	$62_{15,47} - 62_{14,48}$	205729.216	14	661	233.3	271	Blend with C_2H_5CN
509	$65_{14,52} - 64_{15,49}$	206418.149	25	709	56.3	106	Strong C_2H_5CN
510	$34_{3,31} - 33_{4,30}$	206424.485	7	173	132.0	106	Strong C_2H_5CN
511	$43_{7,36} - 42_{8,34}$	206670.752	15	299	1.7	106	Strong $^{13}CH_2CHCN$ and C_2H_5CN, v_{13}=1/v_{21}=1 and v_{20}=1
512	$34_{4,31} - 33_{4,30}$	206676.705	7	173	112.8	106	Strong $^{13}CH_2CHCN$ and C_2H_5CN, v_{13}=1/v_{21}=1 and v_{20}=1
513	$22_{4,19} - 21_{3,19}$	206710.148	11	72	1.2	106	Strong C_2H_5CN, v_{13}=1/v_{21}=1 and CH_3OCHO
514	$35_{5,30} - 34_{6,29}$	206714.221	12	194	71.7	106	Strong C_2H_5CN, v_{13}=1/v_{21}=1 and CH_3OCHO
515	$16_{6,11} - 16_{3,14}$	206723.846	26	44	0.2	106	Strong OCS
516	$20_{4,16} - 19_{3,17}$	206729.759	21	60	12.3	106	Strong OCS
517	$10_{10,0} - 9_{9,1}{}^\star$	206745.688	11	43	61.3	106	Strong OCS
519	$10_{10,0} - 9_{9,0}{}^\star$	206745.688	11	43	1.4	106	Strong OCS
521	$33_{4,29} - 32_{4,28}$	206790.348	7	168	109.0	106	Blend with CH_3OCHO
522	$34_{3,31} - 33_{3,30}$	206798.603	7	173	112.9	106	Blend with CH_3OCHO, uncertain baseline
523	$32_{5,28} - 31_{4,27}$	206805.634	9	159	87.0	106	Blend with U-line
524	$61_{15,47} - 61_{14,47}$	206812.570	13	642	3.4	106	Blend with U-line
525	$21_{5,16} - 20_{4,17}$	206832.347	11	69	28.3	106	Blend with CH_3OCHO and C_2H_5CN, v_{13}=1/v_{21}=1
526	$70_{10,61} - 70_{9,62}$	206967.151	28	778	218.0	117	Blend with C_2H_5CN and U-line
527	$33_{19,14} - 32_{19,13}{}^\star$	206967.887	9	290	75.0	117	Blend with C_2H_5CN and U-line
529	$33_{18,15} - 32_{18,14}{}^\star$	206969.999	9	277	78.9	117	Blend with C_2H_5CN and U-line
531	$33_{20,13} - 32_{20,12}{}^\star$	206979.482	9	304	71.0	117	Strong C_2H_5CN
533	$33_{17,16} - 32_{17,15}{}^\star$	206988.373	8	264	82.5	117	Strong C_2H_5CN
535	$78_{16,63} - 78_{15,64}$	207002.346	36	1012	315.5	117	Strong $H^{13}CONH_2$, v_{12}=1 and U-line
536	$33_{21,12} - 32_{21,11}{}^\star$	207002.831	9	319	66.8	117	Strong $H^{13}CONH_2$, v_{12}=1 and U-line
538	$48_{9,39} - 47_{10,38}$	207003.431	22	378	43.0	117	Strong $H^{13}CONH_2$, v_{12}=1 and U-line
539	$33_{16,17} - 32_{16,16}{}^\star$	207026.416	8	252	85.9	117	Strong U-line
541	$33_{22,11} - 32_{22,10}{}^\star$	207036.420	9	335	62.4	117	Strong U-line and CH_3OCHO
543	$34_{4,31} - 33_{3,30}$	207050.822	7	173	132.1	117	Strong U-line and $C_2H_5{}^{13}CN$
544	$70_{10,61} - 70_{8,62}$	207056.374	28	778	5.6	117	Strong U-line and $C_2H_5{}^{13}CN$
545	$33_{23,10} - 32_{23,9}{}^\star$	207079.056	9	351	57.7	117	Strong CH_3OCHO and $H^{13}CONH_2$
547	$61_{11,50} - 61_{10,52}$	207086.087	82	610	1.1	117	Strong C_2H_5CN
548	$33_{15,18} - 32_{15,17}{}^\star$	207088.763	8	241	89.1	117	Strong C_2H_5CN

Table B.1: continued.

N^a	Transition^b	Frequency (MHz)	Unc.^{c} (kHz)	$E_l{}^d$ (K)	$S\mu^2$ (D^2)	σ^e (mK)	Comments
(1)	(2)	(3)	(4)	(5)	(6)	(7)	(8)
550	$33_{14,19} - 32_{14,18}{}^\star$	207181.880	7	230	92.0	117	Strong U-line and C_2H_5OCHO
552	$33_{25,8} - 32_{25,7}{}^\star$	207187.848	10	386	47.8	117	Strong U-line and C_2H_5OCHO
554	$33_{13,21} - 32_{13,20}{}^\star$	207315.052	7	220	94.8	117	Blend with C_2H_5CN and U-line
556	$33_{27,6} - 32_{27,5}{}^\star$	207323.559	10	423	37.1	117	Blend with C_2H_5CN and U-line
558	$33_{12,22} - 32_{12,21}{}^\star$	207502.107	7	211	97.4	282	Strong U-line and C_2H_5CN
560	$32_{5,27} - 31_{5,26}$	207615.024	7	162	106.0	282	Strong C_2H_5OH
561	$15_{8,8} - 14_{7,7}{}^\star$	207714.323	9	49	51.7	282	Blend with U-line, uncertain baseline
563	$15_{8,8} - 14_{7,8}{}^\star$	207714.422	9	49	1.3	282	Blend with U-line, uncertain baseline
565	$65_{14,51} - 64_{15,49}$	207755.688	27	709	1.6	282	Blend with C_2H_5OH, uncertain baseline
566	$33_{32,1} - 32_{32,0}{}^\star$	207758.192	15	529	6.7	282	Blend with C_2H_5OH, uncertain baseline
568	$33_{11,23} - 32_{11,22}$	207764.581	7	203	99.8	282	Blend with C_2H_5OH, uncertain baseline
569	$33_{11,22} - 32_{11,21}$	207764.809	7	203	99.8	282	Blend with C_2H_5OH, uncertain baseline
570	$35_{2,33} - 34_{3,32}$	207773.375	7	177	165.4	282	Blend with C_2H_5OCHO, uncertain baseline
571	$35_{3,33} - 34_{3,32}$	207782.285	7	177	116.9	282	Strong C_2H_5OH and $CH_2{}^{13}CHCN$
572	$35_{2,33} - 34_{2,32}$	207787.280	7	177	116.9	173	Strong C_2H_5OH and $CH_2{}^{13}CHCN$
573	$35_{3,33} - 34_{2,32}$	207796.189	7	177	165.4	173	Strong C_2H_5OH and C_2H_5CN
574	$20_{6,14} - 19_{5,15}$	208022.760	8	67	41.9	173	Blend with $CH_2{}^{13}CHCN$
575	$67_{9,59} - 67_{7,60}$	208136.493	24	707	5.2	173	Blend with C_2H_5OCHO, $CH_2CH^{13}CN$, and C_2H_3CN, v_{11}=1
576	$33_{10,24} - 32_{10,23}$	208137.019	7	196	102.0	173	Blend with C_2H_5OCHO, $CH_2CH^{13}CN$, and C_2H_3CN, v_{11}=1
577	$33_{10,23} - 32_{10,22}$	208141.014	7	196	102.0	173	Blend with C_2H_5OCHO, $CH_2CH^{13}CN$, and C_2H_3CN, v_{11}=1
578	$34_{4,30} - 33_{5,29}$	208246.884	8	179	101.3	168	Strong $CH_2CH^{13}CN$ and C_2H_5CN
579	$33_{6,28} - 32_{6,27}$	208485.086	7	173	108.2	168	Strong C_2H_5CN and $^{13}CH_3OH$
580	$33_{9,25} - 32_{9,24}$	208665.980	7	189	103.9	168	Strong $^{13}CH_3OH$
581	$33_{9,24} - 32_{9,23}$	208719.238	7	189	103.9	160	Blend with C_2H_5OCHO, CH_3OCHO, and CH_3CHO
582	$32_{6,26} - 31_{6,25}$	208774.753	7	165	105.4	160	Blend with U-line and CH_3OCHO
583	$36_{1,35} - 35_{2,34}$	208955.532	7	181	196.9	160	Blend with C_2H_3CN
584	$36_{2,35} - 35_{2,34}$	208955.700	7	181	121.1	160	Blend with C_2H_3CN
585	$36_{1,35} - 35_{1,34}$	208955.805	7	181	121.1	160	Blend with C_2H_3CN
586	$36_{2,35} - 35_{1,34}$	208955.972	7	181	196.9	160	Blend with C_2H_3CN
587	$83_{14,70} - 83_{12,71}$	209319.456	74	1115	5.8	58	Strong C_2H_3CN, v_{15}=1
588	$33_{8,26} - 32_{8,25}$	209323.723	7	183	105.7	58	Strong C_2H_3CN, v_{15}=1
589	$29_{27,2} - 30_{26,5}{}^\star$	209631.213	47	385	0.7	45	Blend with $HC^{13}CCN$, v_7=2, NH_2CH_2CN, and $HCC^{13}CN$, v_7=2
591	$33_{7,27} - 32_{7,26}$	209633.837	7	178	107.1	45	Blend with $HC^{13}CCN$, v_7=2, NH_2CH_2CN, and $HCC^{13}CN$, v_7=2
592	$59_{12,47} - 58_{13,46}$	209828.069	23	578	50.8	45	Strong $^{13}CH_3CH_2CN$
593	$33_{8,25} - 32_{8,24}$	209830.234	7	183	105.7	45	Strong $^{13}CH_3CH_2CN$
594	$41_{7,34} - 40_{8,33}$	209842.879	19	272	47.3	45	Strong $^{13}CH_3CH_2CN$
595	$24_{4,20} - 24_{1,23}$	210160.111	50	88	0.5	64	Blend with C_2H_3CN, v_{11}=2
596	$37_{0,37} - 36_{1,36}{}^\star$	210165.324	7	184	227.4	64	Blend with C_2H_3CN, v_{11}=2
598	$37_{0,37} - 36_{0,36}{}^\star$	210165.327	7	184	125.4	64	Blend with C_2H_3CN, v_{11}=2
600	$13_{9,5} - 12_{8,4}{}^\star$	210406.053	10	47	56.1	64	Blend with CH_3OCHO and $^{13}CH_3OH$
602	$13_{9,4} - 12_{8,5}{}^\star$	210406.053	10	47	56.1	64	Blend with CH_3OCHO and $^{13}CH_3OH$
604	$60_{12,49} - 60_{10,50}$	210664.306	41	596	1.9	37	Strong C_2H_3CN, v_{11}=3
605	$33_{5,29} - 32_{4,28}$	210672.911	8	168	94.4	37	Strong C_2H_3CN, v_{11}=3
606	$21_{6,16} - 20_{5,15}$	210739.812	9	73	42.4	37	Blend with C_3H_7CN
607	$18_{7,12} - 17_{6,11}$	210894.288	9	59	48.0	37	Strong HC_3N, v_5=1/v_7=3
608	$18_{7,11} - 17_{6,11}$	210897.914	9	59	1.4	37	Strong HC_3N, v_5=1/v_7=3
609	$18_{7,12} - 17_{6,12}$	210936.841	9	59	1.4	37	Strong $H^{13}CONH_2$
610	$18_{7,11} - 17_{6,12}$	210940.467	9	59	48.0	37	Strong $H^{13}CONH_2$
611	$54_{3,51} - 54_{3,52}{}^\star$	210944.999	20	428	2.5	37	Strong $H^{13}CONH_2$
613	$54_{4,51} - 54_{3,52}{}^\star$	210945.044	20	428	70.7	37	Strong $H^{13}CONH_2$
615	$34_{5,30} - 33_{5,29}$	211042.886	7	179	112.3	33	Blend with U-line and C_2H_5OCHO
616	$38_{6,32} - 37_{7,31}$	211930.232	16	231	57.6	36	Strong $H^{13}CCCN$, v_6=1 and $H^{13}CONH_2$
617	$35_{3,32} - 34_{4,31}$	212101.379	7	183	138.8	36	Strong $H^{13}CCCN$, v_7=1 and $HCONH_2$, v_{12}=1
618	$63_{13,51} - 62_{14,49}$	212104.718	22	661	1.6	36	Strong $H^{13}CCCN$, v_7=1 and $HCONH_2$, v_{12}=1
619	$34_{4,30} - 33_{4,29}$	212129.447	7	178	112.3	36	Strong CH_3CHO and $H^{13}CONH_2$
620	$35_{4,32} - 34_{4,31}$	212270.421	7	183	116.2	36	Strong $H^{13}CONH_2$ and $HCONH_2$
621	$62_{7,56} - 62_{6,57}$	212350.714	18	592	142.8	36	Blend with C_2H_3CN and U-line
622	$62_{7,56} - 62_{5,57}$	212351.431	18	592	4.4	36	Blend with C_2H_3CN and U-line
623	$35_{3,32} - 34_{3,31}$	212353.599	7	183	116.2	36	Blend with C_2H_3CN and U-line
624	$35_{4,32} - 34_{3,31}$	212522.641	7	183	138.8	99	Partial blend with C_3H_7CN, very uncertain baseline
625	$68_{8,60} - 68_{8,61}$	212524.945	24	726	5.3	99	Partial blend with C_3H_7CN, very uncertain baseline
626	$33_{7,26} - 32_{7,25}$	212526.081	7	178	107.3	99	Partial blend with C_3H_7CN, very uncertain baseline

Table B.1: continued.

N^a	Transition^b	Frequency (MHz)	Unc.^{c} (kHz)	$E_l{}^d$ (K)	$S\mu^2$ (D^2)	σ^e (mK)	Comments
(1)	(2)	(3)	(4)	(5)	(6)	(7)	(8)
627	$75_{10,65} - 75_{10,66}$	213011.737	41	895	6.0	99	Blend with $C_2H_5{}^{13}CN$, uncertain baseline
628	$11_{10,1} - 10_{9,2}{}^\star$	213015.569	10	46	61.4	99	Blend with $C_2H_5{}^{13}CN$, uncertain baseline
630	$11_{10,1} - 10_{9,1}{}^\star$	213015.569	10	46	1.4	99	Blend with $C_2H_5{}^{13}CN$, uncertain baseline
632	$34_{19,15} - 33_{19,14}{}^\star$	213233.303	8	300	79.5	48	Strong C_2H_3CN, v_{15}=1
634	$34_{18,16} - 33_{18,15}{}^\star$	213239.756	8	287	83.2	48	Strong C_2H_3CN, v_{15}=1
636	$34_{20,14} - 33_{20,13}{}^\star$	213241.613	9	314	75.6	48	Strong C_2H_3CN, v_{15}=1
638	$34_{21,13} - 33_{21,12}{}^\star$	213262.551	9	329	71.5	48	Blend with $H_2{}^{13}CCO$ and CH_3CHO
640	$34_{17,17} - 33_{17,16}{}^\star$	213263.771	8	274	86.7	48	Blend with $H_2{}^{13}CCO$ and CH_3CHO
642	$33_{5,28} - 32_{5,27}$	213267.112	7	172	109.2	48	Blend with $H_2{}^{13}CCO$ and CH_3CHO
643	$34_{22,12} - 33_{22,11}{}^\star$	213294.461	9	345	67.2	48	Strong $H_2{}^{13}CO$
645	$34_{16,18} - 33_{16,17}{}^\star$	213309.084	8	262	90.1	48	Blend with C_2H_3CN, v_{11}=1/v_{15}=1 and $H^{13}CONH_2$
647	$34_{23,11} - 33_{23,10}{}^\star$	213336.039	9	361	62.7	48	Blend with U-line and $C_2H_5{}^{13}CN$
649	$36_{2,34} - 35_{3,33}$	213370.000	7	187	172.0	48	Strong CH_3OH
650	$36_{3,34} - 35_{3,33}$	213375.691	7	187	120.3	48	Strong CH_3OH
651	$36_{2,34} - 35_{2,33}$	213378.910	7	187	120.3	48	Strong CH_3OH
652	$34_{15,19} - 33_{15,18}{}^\star$	213380.789	7	251	93.2	48	Strong CH_3OH
654	$36_{3,34} - 35_{2,33}$	213384.601	7	187	172.0	48	Strong CH_3OH
655	$34_{24,10} - 33_{24,9}{}^\star$	213386.248	9	378	58.0	48	Strong CH_3OH
657	$34_{14,20} - 33_{14,19}{}^\star$	213486.003	7	240	96.0	48	Blend with $C_2H_5{}^{13}CN$
659	$57_{4,53} - 57_{4,54}{}^\star$	213494.205	17	485	3.2	48	Blend with $C_2H_5{}^{13}CN$ and U-line
661	$57_{5,53} - 57_{4,54}{}^\star$	213494.501	17	485	94.6	48	Blend with $C_2H_5{}^{13}CN$ and U-line
663	$34_{13,22} - 33_{13,21}{}^\star$	213634.983	7	230	98.7	48	Blend with CH_3CH_3CO, v_t=1 and C_2H_5CN, v_{13}=1/v_{21}=1
665	$34_{12,23} - 33_{12,22}{}^\star$	213843.076	7	221	101.3	48	Blend with U-line and C_2H_5OH
667	$21_{6,16} - 20_{5,16}$	213928.431	8	73	1.5	48	Blend with C_2H_5CN and U-line
668	$54_{38,16} - 55_{37,19}{}^\star$	213936.215	1303	958	9.3	48	Blend with U-line and CH_3CH_3CO
670	$16_{8,9} - 15_{7,8}{}^\star$	213936.821	9	54	52.4	48	Blend with U-line and CH_3CH_3CO
672	$16_{8,9} - 15_{7,9}{}^\star$	213937.090	9	54	1.4	48	Blend with U-line and CH_3CH_3CO
674	$34_{33,1} - 33_{33,0}{}^\star$	214126.826	16	563	6.7	75	Strong $C_2H_5{}^{13}CN$
676	$34_{11,24} - 33_{11,23}$	214134.294	7	213	103.6	75	Strong $C_2H_5{}^{13}CN$
677	$34_{11,23} - 33_{11,22}$	214134.718	7	213	103.6	75	Strong $C_2H_5{}^{13}CN$
678	$75_{11,65} - 75_{10,66}$	214423.572	39	895	244.3	75	Strong $CH_3{}^{13}CH_2CN$
679	$21_{6,15} - 20_{5,16}$	214424.398	8	73	41.7	75	Strong $CH_3{}^{13}CH_2CN$
680	$72_{16,57} - 72_{15,58}$	214459.694	22	875	280.5	75	Strong CH_3OCH_3
681	$34_{6,29} - 33_{6,28}$	214462.215	7	183	111.6	75	Strong CH_3OCH_3
682	$34_{10,25} - 33_{10,24}$	214546.802	7	206	105.6	75	Blend with $HCONH_2$
683	$37_{1,36} - 36_{2,35}$	214552.844	6	191	203.4	75	Blend with $HCONH_2$
684	$37_{2,36} - 36_{2,35}{}^\star$	214552.948	6	191	124.5	75	Blend with $HCONH_2$
686	$37_{2,36} - 36_{1,35}$	214553.115	6	191	203.4	75	Blend with $HCONH_2$
687	$34_{10,24} - 33_{10,23}$	214553.725	7	206	105.7	75	Blend with $HCONH_2$
688	$85_{14,72} - 85_{12,73}$	214555.338	99	1165	6.2	75	Blend with $HCONH_2$
689	$35_{4,31} - 34_{5,30}$	214711.926	7	189	108.7	75	Strong U-line and CH_3CH_3CO
690	$50_{15,36} - 50_{14,36}$	214722.921	11	456	2.9	75	Strong U-line and CH_3CH_3CO
691	$50_{15,35} - 50_{14,36}$	214723.034	11	456	172.8	75	Strong U-line and CH_3CH_3CO
692	$50_{15,36} - 50_{14,37}$	214724.767	11	456	172.8	75	Strong U-line and CH_3CH_3CO
693	$50_{15,35} - 50_{14,37}$	214724.881	11	456	2.9	75	Strong U-line and CH_3CH_3CO
694	$72_{16,56} - 72_{15,58}$	214725.686	22	875	3.8	75	Strong U-line and CH_3CH_3CO
695	$56_{11,45} - 55_{12,44}$	214921.197	25	518	48.1	74	Strong CH_2NH
696	$34_{5,30} - 33_{4,29}$	214925.449	7	178	101.8	74	Strong CH_2NH
697	$34_{9,26} - 33_{9,25}$	215125.927	7	199	107.6	74	Strong C_2H_5CN
698	$49_{15,35} - 49_{14,35}{}^\star$	215171.154	11	441	2.9	74	Strong C_2H_5CN
700	$49_{15,35} - 49_{14,36}{}^\star$	215172.235	11	441	168.1	74	Strong C_2H_5CN
702	$34_{9,25} - 33_{9,24}$	215211.497	7	199	107.6	74	Strong C_2H_5CN and SO
703	$22_{6,17} - 21_{5,16}$	215331.698	9	79	42.3	74	Blend with $H^{13}CONH_2$, v_{12}=1 and C_2H_5CN, v_{20}=1
704	$33_{6,27} - 32_{6,26}$	215540.916	7	175	108.9	74	Strong C_2H_5CN, v_{13}=1/v_{21}=1
705	$48_{15,34} - 48_{14,34}{}^\star$	215587.071	11	426	2.8	74	Strong C_2H_5CN, v_{20}=1 and v_{13}=1/v_{21}=1
707	$48_{15,34} - 48_{14,35}{}^\star$	215587.694	11	426	163.3	74	Strong C_2H_5CN, v_{20}=1 and v_{13}=1/v_{21}=1
709	$66_{11,56} - 65_{12,53}$	215591.127	80	704	27.4	74	Strong C_2H_5CN, v_{20}=1 and v_{13}=1/v_{21}=1
710	$71_{16,56} - 71_{15,57}$	215693.984	20	853	274.8	74	Strong $HCONH_2$ and C_2H_5CN, v_{13}=1/v_{21}=1
711	$36_{5,31} - 35_{6,30}$	215695.264	11	204	79.9	74	Strong $HCONH_2$ and C_2H_5CN, v_{13}=1/v_{21}=1
712	$38_{0,38} - 37_{1,37}{}^\star$	215763.718	6	194	233.9	74	Blend with CH_3CH_3CO, v_t=1
714	$38_{0,38} - 37_{0,37}{}^\star$	215763.719	6	194	128.8	74	Blend with CH_3CH_3CO, v_t=1
716	$34_{8,27} - 33_{8,26}$	215799.240	7	193	109.2	74	Blend with C_2H_5CN, v_{13}=1/v_{21}=1

Table B.1: continued.

N^a	Transition^b	Frequency (MHz)	Unc.^{c} (kHz)	$E_l{}^d$ (K)	$S\mu^2$ (D^2)	σ^e (mK)	Comments
(1)	(2)	(3)	(4)	(5)	(6)	(7)	(8)
717	$66_{14,52} - 65_{15,50}$	215807.944	30	729	1.7	55	Blend with C_2H_5CN, v_{13}=1/v_{21}=1
718	$34_{7,28} - 33_{7,27}$	215955.868	7	188	110.6	55	Strong C_2H_5CN
719	$22_{1,21} - 21_{0,21}$	215962.601	15	65	0.4	55	Strong C_2H_5CN
720	$66_{14,52} - 65_{15,51}$	215966.443	30	729	57.2	55	Strong C_2H_5CN
721	$70_{16,54} - 70_{15,55}$	215971.934	19	832	269.3	55	Strong C_2H_5CN
722	$47_{15,33} - 47_{14,33}{}^\star$	215972.573	11	411	2.8	55	Strong C_2H_5CN
724	$47_{15,33} - 47_{14,34}{}^\star$	215972.927	11	411	158.7	55	Strong C_2H_5CN
726	$72_{10,63} - 72_{8,64}$	216323.949	28	819	5.7	55	Strong U-line
727	$63_{13,50} - 62_{14,48}$	216328.757	26	661	1.6	55	Strong U-line
728	$46_{15,32} - 46_{14,32}{}^\star$	216329.423	11	397	2.7	55	Strong U-line
730	$46_{15,32} - 46_{14,33}{}^\star$	216329.621	11	397	154.0	55	Strong U-line
732	$22_{5,17} - 21_{4,18}$	216510.483	14	76	25.9	55	Strong CH_3CH_3CO, v_t=1 and C_2H_5CN, v_{13}=1/v_{21}=1
733	$34_{8,26} - 33_{8,25}$	216543.456	7	193	109.3	55	Strong C_2H_5CN, v_{13}=1/v_{21}=1
734	$53_{2,51} - 53_{1,52}{}^\star$	216543.675	26	402	47.2	55	Strong C_2H_5CN, v_{13}=1/v_{21}=1
736	$53_{3,51} - 53_{2,52}{}^\star$	216543.677	26	402	47.2	55	Strong C_2H_5CN, v_{13}=1/v_{21}=1
738	$60_{9,52} - 59_{10,50}$	216655.291	31	573	1.5	55	Blend with C_3H_7CN, uncertain baseline
739	$45_{15,31} - 45_{14,31}{}^\star$	216659.262	11	383	2.7	55	Blend with C_3H_7CN, uncertain baseline
741	$45_{15,31} - 45_{14,32}{}^\star$	216659.372	11	383	149.4	55	Blend with C_3H_7CN, uncertain baseline
743	$14_{9,6} - 13_{8,5}{}^\star$	216662.858	10	51	56.6	55	Blend with C_3H_7CN, uncertain baseline
745	$14_{9,5} - 13_{8,6}{}^\star$	216662.858	10	51	56.6	55	Blend with C_3H_7CN, uncertain baseline
747	$61_{12,50} - 60_{13,48}$	216696.181	21	614	1.7	55	Strong H_2S
748	$35_{5,31} - 34_{5,30}$	216702.601	7	189	115.6	55	Strong H_2S
749	$19_{7,13} - 18_{6,12}$	216962.523	9	65	48.6	50	Strong CH_3OCHO
750	$44_{15,30} - 44_{14,30}{}^\star$	216963.629	11	370	2.6	50	Strong CH_3OCHO
752	$44_{15,30} - 44_{14,31}{}^\star$	216963.689	11	370	144.9	50	Strong CH_3OCHO
754	$19_{7,12} - 18_{6,12}$	216970.265	9	65	1.4	50	Strong CH_3OCHO
755	$19_{7,13} - 18_{6,13}$	217046.020	9	65	1.4	50	Strong C_2H_5OCHO and U-line
756	$19_{7,12} - 18_{6,13}$	217053.762	9	65	48.5	50	Strong C_2H_5OCHO and U-line
757	$43_{15,29} - 43_{14,29}{}^\star$	217243.972	10	356	2.5	50	Strong $CH_2{}^{13}CHCN$
759	$43_{15,29} - 43_{14,30}{}^\star$	217244.003	10	356	140.3	50	Strong $CH_2{}^{13}CHCN$
761	$42_{15,28} - 42_{14,28}{}^\star$	217501.656	10	343	2.5	50	Strong C_2H_5CN, v_{13}=1/v_{21}=1 and U-line
763	$42_{15,28} - 42_{14,29}{}^\star$	217501.673	10	343	135.8	50	Strong C_2H_5CN, v_{13}=1/v_{21}=1 and U-line
765	$35_{4,31} - 34_{4,30}$	217507.928	7	189	115.7	50	Strong C_2H_5CN, v_{13}=1/v_{21}=1 and U-line
766	$41_{15,27} - 41_{14,27}{}^\star$	217737.976	10	331	2.4	50	Strong U-line and CH_3CH_3CO, v_t=1
768	$41_{15,27} - 41_{14,28}{}^\star$	217737.985	10	331	131.3	50	Strong U-line and CH_3CH_3CO, v_t=1
770	$36_{3,33} - 35_{4,32}$	217746.768	7	194	145.5	50	Strong CH_3CH_3CO, v_t=1 and $HC^{13}CCN$, v_6=1
771	$12_{10,2} - 11_{9,3}{}^\star$	219284.427	10	49	61.6	92	Strong C_2H_3CN, v_{11}=1
773	$12_{10,2} - 11_{9,2}{}^\star$	219284.427	10	49	1.5	92	Strong C_2H_3CN, v_{11}=1
775	$29_{15,14} - 29_{14,15}{}^\star$	219303.582	8	202	77.7	92	Strong C_2H_5CN, v_{13}=1/v_{21}=1 and C_2H_3CN, v_{11}=1/v_{15}=1
777	$29_{15,14} - 29_{14,16}{}^\star$	219303.582	8	202	1.6	92	Strong C_2H_5CN, v_{13}=1/v_{21}=1 and C_2H_3CN, v_{11}=1/v_{15}=1
779	$23_{2,21} - 22_{1,21}$	219349.374	15	75	0.8	92	Strong $^{34}SO_2$ and $CH_3{}^{13}CH_2CN$
780	$28_{15,13} - 28_{14,14}{}^\star$	219356.277	8	193	73.2	92	Strong $^{34}SO_2$ and $CH_3{}^{13}CH_2CN$
782	$28_{15,13} - 28_{14,15}{}^\star$	219356.277	8	193	1.5	92	Strong $^{34}SO_2$ and $CH_3{}^{13}CH_2CN$
784	$27_{15,12} - 27_{14,13}{}^\star$	219400.708	8	185	68.6	92	Strong C_2H_3CN
786	$27_{15,12} - 27_{14,14}{}^\star$	219400.708	8	185	1.4	92	Strong C_2H_3CN
788	$23_{6,18} - 22_{5,17}$	219412.564	10	86	42.3	92	Strong HC_3N, v_6=v_7=1
789	$26_{15,11} - 26_{14,12}{}^\star$	219437.556	9	177	64.0	92	Strong HC_3N, v_6=v_7=1 and CH_3NH_2
791	$26_{15,11} - 26_{14,13}{}^\star$	219437.556	9	177	1.3	92	Strong HC_3N, v_6=v_7=1 and CH_3NH_2
793	$25_{15,10} - 25_{14,11}{}^\star$	219467.473	9	169	59.3	92	Strong C_2H_5CN
795	$25_{15,10} - 25_{14,12}{}^\star$	219467.473	9	169	1.2	92	Strong C_2H_5CN
797	$24_{15,9} - 24_{14,10}{}^\star$	219491.090	9	162	54.6	92	Strong HC_3N, v_6=v_7=1
799	$24_{15,9} - 24_{14,11}{}^\star$	219491.090	9	162	1.1	92	Strong HC_3N, v_6=v_7=1
801	$35_{19,16} - 34_{19,15}{}^\star$	219498.018	8	310	84.0	92	Strong HC_3N, v_6=v_7=1 and C_2H_5CN
803	$35_{5,31} - 34_{4,30}$	219498.602	7	189	109.1	92	Strong HC_3N, v_6=v_7=1 and C_2H_5CN
804	$35_{20,15} - 34_{20,14}{}^\star$	219502.729	8	324	80.2	92	Strong HC_3N, v_6=v_7=1 and C_2H_5CN
806	$75_{12,64} - 74_{13,61}$	219503.613	148	905	21.8	92	Strong HC_3N, v_6=v_7=1 and C_2H_5CN
807	$23_{15,8} - 23_{14,9}{}^\star$	219509.009	9	154	49.8	92	Strong C_2H_5CN
809	$23_{15,8} - 23_{14,10}{}^\star$	219509.009	9	154	1.0	92	Strong C_2H_5CN
811	$35_{18,17} - 34_{18,16}{}^\star$	219509.185	8	297	87.6	92	Strong C_2H_5CN
813	$15_{15,0} - 15_{14,1}{}^\star$	219511.616	12	107	6.5	92	Strong C_2H_5CN
815	$16_{15,1} - 16_{14,2}{}^\star$	219520.465	12	112	12.7	92	Strong HC_3N, v_6=v_7=1
817	$16_{15,1} - 16_{14,3}{}^\star$	219520.465	12	112	0.3	92	Strong HC_3N, v_6=v_7=1
819	$35_{21,14} - 34_{21,13}{}^\star$	219520.987	8	339	76.2	92	Strong HC_3N, v_6=v_7=1

Table B.1: continued.

N^a	Transition^b	Frequency (MHz)	Unc.^{c} (kHz)	$E_l{}^d$ (K)	$S\mu^2$ (D^2)	σ^e (mK)	Comments
(1)	(2)	(3)	(4)	(5)	(6)	(7)	(8)
821	$22_{15,7} - 22_{14,8}{}^\star$	219521.808	10	147	44.9	92	Strong HC_3N, v_6=v_7=1
823	$22_{15,7} - 22_{14,9}{}^\star$	219521.808	10	147	0.9	92	Strong HC_3N, v_6=v_7=1
825	$17_{15,2} - 17_{14,3}{}^\star$	219527.577	11	117	18.6	92	Strong HC_3N, v_6=v_7=1
827	$17_{15,2} - 17_{14,4}{}^\star$	219527.577	11	117	0.4	92	Strong HC_3N, v_6=v_7=1
829	$21_{15,6} - 21_{14,7}{}^\star$	219530.043	10	141	40.0	92	Strong HNCO, v_5=1 and v=0
831	$21_{15,6} - 21_{14,8}{}^\star$	219530.043	10	141	0.8	92	Strong HNCO, v_5=1 and v=0
833	$18_{15,3} - 18_{14,4}{}^\star$	219532.538	11	123	24.2	92	Strong HNCO, v_5=1 and v=0
835	$18_{15,3} - 18_{14,5}{}^\star$	219532.538	11	123	0.5	92	Strong HNCO, v_5=1 and v=0
837	$20_{15,5} - 20_{14,6}{}^\star$	219534.242	10	134	34.9	92	Strong HNCO, v_5=1 and v=0
839	$20_{15,5} - 20_{14,7}{}^\star$	219534.242	10	134	0.7	92	Strong HNCO, v_5=1 and v=0
841	$19_{15,4} - 19_{14,5}{}^\star$	219534.913	11	128	29.6	92	Strong HNCO, v_5=1 and v=0
843	$19_{15,4} - 19_{14,6}{}^\star$	219534.913	11	128	0.6	92	Strong HNCO, v_5=1 and v=0
845	$35_{17,18} - 34_{17,17}{}^\star$	219539.290	8	284	91.0	92	Strong HNCO, v_5=1 and v=0
847	$67_{44,23} - 68_{43,26}{}^\star$	219540.490	5076	1373	14.6	92	Strong HNCO, v_5=1 and v=0
849	$35_{22,13} - 34_{22,12}{}^\star$	219550.985	9	355	72.0	92	Strong HNCO and $C^{18}O$
851	$35_{23,12} - 34_{23,11}{}^\star$	219591.305	9	371	67.7	92	Strong $C_2H_5{}^{13}CN$ and CH_3CN, v_4=1
853	$35_{16,19} - 34_{16,18}{}^\star$	219592.420	7	272	94.2	92	Strong $C_2H_5{}^{13}CN$ and CH_3CN, v_4=1
855	$35_{24,11} - 34_{24,10}{}^\star$	219640.815	9	388	63.1	92	Strong CH_3CN, v_4=1 and C_2H_3CN, v_{11}=2
857	$56_{3,53} - 56_{3,54}{}^\star$	219641.434	20	459	2.5	92	Strong CH_3CN, v_4=1 and C_2H_3CN, v_{11}=2
859	$56_{4,53} - 56_{3,54}{}^\star$	219641.453	20	459	70.9	92	Strong CH_3CN, v_4=1 and C_2H_3CN, v_{11}=2
861	$64_{13,52} - 63_{14,50}$	219647.573	23	680	1.7	92	Strong CH_3CN, v_4=1 and C_2H_3CN, v_{11}=2
862	$34_{7,27} - 33_{7,26}$	219657.438	7	188	110.9	92	Strong HNCO
863	$28_{5,23} - 28_{2,26}$	219660.298	50	123	1.2	92	Strong HNCO
864	$58_{10,49} - 57_{11,47}$	219666.987	26	545	1.6	92	Strong HC_3N, v_7=2
865	$35_{15,20} - 34_{15,19}{}^\star$	219674.159	7	261	97.2	92	Strong HC_3N, v_7=2
867	$35_{14,22} - 34_{14,21}{}^\star$	219792.332	7	250	100.0	92	Strong HNCO
869	$35_{6,30} - 34_{6,29}$	220375.475	6	194	115.1	98	Strong CH_3CH_3CO and ^{13}CO
870	$35_{34,1} - 34_{34,0}{}^\star$	220501.747	18	597	6.7	98	Strong C_2H_3CN, v_{11}=3
872	$35_{11,25} - 34_{11,24}$	220511.092	6	223	107.3	98	Strong $H^{13}CCCN$, v_5=1/v_7=3 and C_2H_3CN, v_{11}=3
873	$35_{11,24} - 34_{11,23}$	220511.865	6	223	107.3	98	Strong $H^{13}CCCN$, v_5=1/v_7=3 and C_2H_3CN, v_{11}=3
874	$21_{4,17} - 20_{3,18}$	220626.556	24	66	10.4	98	Strong $CH_3{}^{13}CN$
875	$36_{15,21} - 35_{15,20}{}^\star$	225968.903	7	271	101.2	278	Partial blend with $CH_3{}^{13}CH_2CN$, noisy
877	$36_{14,23} - 35_{14,22}{}^\star$	226100.931	7	261	103.9	278	Blend with C_2H_5CN
879	$36_{6,31} - 35_{6,30}$	226228.268	6	204	118.5	278	Blend with C_3H_7CN
880	$71_{8,63} - 71_{8,64}$	226277.715	23	787	5.4	278	Blend with CN in absorption
881	$71_{8,63} - 71_{7,64}$	226282.848	23	787	192.8	278	Blend with CN in absorption
882	$36_{13,24} - 35_{13,23}{}^\star$	226284.976	6	251	106.5	278	Blend with CN in absorption
884	$38_{32,6} - 39_{31,9}{}^\star$	226289.953	215	583	2.4	278	Blend with CN in absorption
886	$18_{8,11} - 17_{7,10}$	226335.622	9	64	53.8	278	Strong CN in absorption
887	$18_{8,10} - 17_{7,10}$	226335.730	9	64	1.5	278	Strong CN in absorption
888	$68_{7,61} - 68_{7,62}$	226336.960	20	716	4.9	278	Strong CN in absorption
889	$18_{8,11} - 17_{7,11}$	226337.238	9	64	1.5	278	Strong CN in absorption
890	$18_{8,10} - 17_{7,11}$	226337.346	9	64	53.8	278	Strong CN in absorption
891	$68_{7,61} - 68_{6,62}$	226338.056	20	716	167.8	278	Strong CN in absorption
892	$71_{9,63} - 71_{8,64}$	226340.580	23	787	192.8	278	Strong CN in absorption
893	$71_{9,63} - 71_{7,64}$	226345.713	23	787	5.4	278	Strong CN in absorption
894	$36_{30,6} - 35_{30,5}{}^\star$	226345.942	11	516	37.4	278	Strong CN in absorption
896	$36_{12,25} - 35_{12,24}{}^\star$	226539.875	6	242	108.8	278	Blend with CH_2NH
898	$36_{32,4} - 35_{32,3}{}^\star$	226545.826	13	560	25.7	278	Blend with CH_2NH
900	$35_{7,28} - 34_{7,27}$	226807.961	7	199	114.5	96	Strong CN in absorption and CH_3CH_3CO
901	$59_{16,44} - 59_{15,45}$	226808.419	11	615	211.4	96	Strong CN in absorption and CH_3CH_3CO
902	$59_{16,43} - 59_{15,45}$	226809.328	11	615	3.4	96	Strong CN in absorption and CH_3CH_3CO
903	$36_{11,26} - 35_{11,25}$	226895.311	6	234	111.0	96	Strong CN in absorption and $CH_2CH^{13}CN$
904	$36_{11,25} - 35_{11,24}$	226896.689	6	234	111.0	96	Strong CN in absorption and $CH_2CH^{13}CN$
905	$69_{8,61} - 68_{9,59}$	226898.751	36	746	1.5	96	Strong CN in absorption and $CH_2CH^{13}CN$
906	$40_{0,40} - 39_{1,39}{}^\star$	226955.259	6	215	246.8	96	Strong CN in absorption and $CH_2CH^{13}CN$
908	$40_{0,40} - 39_{0,39}{}^\star$	226955.259	6	215	135.6	96	Strong CN in absorption and $CH_2CH^{13}CN$
910	$37_{4,33} - 36_{5,32}$	226971.342	6	210	123.3	96	Strong CN in absorption and $CH_3{}^{13}CH_2CN$
911	$36_{10,26} - 35_{10,25}$	227415.910	6	227	113.0	85	Strong HC_3N
912	$58_{16,43} - 58_{15,43}$	227421.409	11	598	3.4	85	Strong HC_3N
913	$58_{16,42} - 58_{15,43}$	227421.956	11	598	206.4	85	Strong HC_3N
914	$28_{6,23} - 27_{5,22}$	231128.031	15	125	44.9	183	Blend with $H_2{}^{13}CS$ and U-line
915	$50_{16,35} - 50_{15,35}{}^\star$	231145.553	10	466	3.0	183	Strong $H_2{}^{13}CS$, C_2H_3CN, v_{11}=1, and CH_3CHO, v_t=1

Table B.1: continued.

N^a	Transition^b	Frequency (MHz)	Unc.^{c} (kHz)	$E_l{}^d$ (K)	$S\mu^2$ (D^2)	σ^e (mK)	Comments
(1)	(2)	(3)	(4)	(5)	(6)	(7)	(8)
917	$50_{16,35} - 50_{15,36}{}^\star$	231145.667	10	466	168.3	183	Strong $H_2{}^{13}CS$, C_2H_3CN, v_{11}=1, and CH_3CHO, v_t=1
919	$40_{1,39} - 39_{2,38}{}^\star$	231334.439	6	223	222.9	40	Blend with CH_3CHO and $^{13}CH_2CHCN$
921	$40_{1,39} - 39_{1,38}{}^\star$	231334.478	6	223	134.7	40	Blend with CH_3CHO and $^{13}CH_2CHCN$
923	$49_{16,34} - 49_{15,34}{}^\star$	231479.706	10	451	2.9	40	Strong CH_3NH_2 and CH_3CHO
925	$49_{16,34} - 49_{15,35}{}^\star$	231479.769	10	451	163.6	40	Strong CH_3NH_2 and CH_3CHO
927	$37_{14,24} - 36_{14,23}{}^\star$	232411.870	6	272	107.8	19	Strong CH_3OH
929	$37_{28,9} - 36_{28,8}{}^\star$	232419.456	9	485	53.8	19	Strong CH_3OH
931	$19_{8,12} - 18_{7,11}$	232505.685	9	69	54.4	19	Blend with $CH_3{}^{13}CH_2CN$, $^{13}CH_3CH_2CN$, and U-line
932	$19_{8,11} - 18_{7,11}$	232505.949	9	69	1.5	19	Blend with $CH_3{}^{13}CH_2CN$, $^{13}CH_3CH_2CN$, and U-line
933	$37_{29,8} - 36_{29,7}{}^\star$	232506.276	9	505	48.5	19	Blend with $CH_3{}^{13}CH_2CN$, $^{13}CH_3CH_2CN$, and U-line
935	$19_{8,12} - 18_{7,12}$	232509.311	9	69	1.5	19	Blend with $CH_3{}^{13}CH_2CN$, $^{13}CH_3CH_2CN$, and U-line
936	$19_{8,11} - 18_{7,12}$	232509.574	9	69	54.4	19	Blend with $CH_3{}^{13}CH_2CN$, $^{13}CH_3CH_2CN$, and U-line
937	$41_{0,41} - 40_{1,40}{}^\star$	232548.316	6	226	253.4	19	Blend with C_2H_5OH, uncertain baseline
939	$41_{0,41} - 40_{0,40}{}^\star$	232548.316	6	226	138.9	19	Blend with C_2H_5OH, uncertain baseline
941	$45_{16,30} - 45_{15,30}{}^\star$	232587.148	10	394	2.7	19	Strong $^{13}CH_2CHCN$
943	$45_{16,30} - 45_{15,31}{}^\star$	232587.154	10	394	145.4	19	Strong $^{13}CH_2CHCN$
945	$37_{13,25} - 36_{13,24}{}^\star$	232615.284	6	262	110.3	19	Strong CH_3CH_3CO, v_t=1 and U-line
947	$74_{16,58} - 73_{17,57}$	232616.645	63	918	64.2	19	Strong CH_3CH_3CO, v_t=1 and U-line
948	$30_{6,25} - 29_{5,24}$	232767.849	16	143	49.6	19	Strong $H_3{}^{13}CCN$, v_8=1 and CH_3CH_3CO
949	$44_{16,29} - 44_{15,29}{}^\star$	232812.598	10	380	2.6	19	Strong $H_3{}^{13}CCN$, v_8=1
951	$44_{16,29} - 44_{15,30}{}^\star$	232812.600	10	380	140.9	19	Strong $H_3{}^{13}CCN$, v_8=1
953	$64_{12,53} - 63_{13,50}$	232867.048	28	671	49.6	19	Strong CH_3CH_3CO, $H_3{}^{13}CCN$, v_8=1, and C_2H_5CN, v_{13}=1/v_{21}=1
954	$38_{4,34} - 37_{5,33}$	232871.416	6	221	130.4	19	Strong CH_3CH_3CO, $H_3{}^{13}CCN$, v_8=1, and C_2H_5CN, v_{13}=1/v_{21}=1
955	$37_{12,26} - 36_{12,25}$	232896.137	6	253	112.6	19	Strong $H_3{}^{13}CCN$, v_8=1
956	$37_{12,25} - 36_{12,24}$	232896.279	6	253	112.6	19	Strong $H_3{}^{13}CCN$, v_8=1
957	$37_{8,30} - 36_{8,29}$	235140.453	6	225	120.0	131	Strong SO_2
958	$71_{17,55} - 71_{16,55}$	235260.476	17	863	3.9	131	Strong C_2H_5CN, v_{13}=1/v_{21}=1
959	$24_{6,18} - 23_{5,19}$	235267.230	9	93	39.2	131	Strong C_2H_5CN, v_{13}=1/v_{21}=1
960	$22_{7,15} - 21_{6,16}$	235271.104	8	83	49.6	131	Strong C_2H_5CN, v_{13}=1/v_{21}=1
961	$71_{17,54} - 71_{16,55}$	235278.986	17	863	266.8	131	Strong C_2H_5CN, v_{13}=1/v_{21}=1
962	$17_{9,9} - 16_{8,8}{}^\star$	235393.076	9	64	58.6	131	Blend with $^{13}CH_3OH$, v_t=1
964	$17_{9,9} - 16_{8,9}{}^\star$	235393.091	9	64	1.5	131	Blend with $^{13}CH_3OH$, v_t=1
966	$83_{12,72} - 83_{10,73}$	235424.334	76	1093	6.5	131	Blend with $^{13}CH_3OH$, v_t=1 and C_2H_5CN, v_{13}=1/v_{21}=1
967	$22_{4,18} - 21_{3,19}$	235431.021	27	72	8.8	131	Blend with $^{13}CH_3OH$, v_t=1 and C_2H_5CN, v_{13}=1/v_{21}=1
968	$43_{7,36} - 42_{8,35}$	235592.247	17	297	58.5	131	Blend with CH_3CH_3CO and U-line
969	$40_{2,38} - 39_{3,37}$	235732.962	6	230	198.1	131	Blend with CH_3NH_2
970	$40_{3,38} - 39_{3,37}$	235733.886	6	230	133.9	131	Blend with CH_3NH_2
971	$40_{2,38} - 39_{2,37}$	235734.422	6	230	133.9	131	Blend with CH_3NH_2
972	$40_{3,38} - 39_{2,37}$	235735.346	6	230	198.1	131	Blend with CH_3NH_2
973	$34_{6,29} - 33_{5,28}$	236128.934	13	182	68.7	37	Strong $^{13}CH_3CH_2CN$
974	$37_{7,30} - 36_{7,29}$	240957.398	6	221	121.8	216	Strong CH_3OH, v_t=1
975	$38_{9,30} - 37_{9,29}$	241042.260	5	242	122.0	216	Strong CH_3OH
976	$38_{8,30} - 37_{8,29}$	244246.675	6	237	123.6	46	Strong SO_2
977	$16_{10,7} - 15_{9,6}{}^\star$	244333.630	9	66	63.5	46	Strong CH_3OH, v_t=0 and v_t=1
979	$16_{10,6} - 15_{9,7}{}^\star$	244333.630	9	66	63.5	46	Strong CH_3OH, v_t=0 and v_t=1
981	$40_{4,36} - 39_{5,35}$	244397.903	6	243	144.3	46	Strong C_2H_5CN
982	$70_{14,57} - 69_{15,55}$	244404.271	40	810	1.9	46	Strong C_2H_5CN
983	$39_{20,19} - 38_{20,18}{}^\star$	244536.107	7	368	97.8	91	Strong U-line and $H^{13}CONH_2$
985	$39_{21,18} - 38_{21,17}{}^\star$	244540.816	7	383	94.2	91	Strong U-line and $H^{13}CONH_2$
987	$39_{19,20} - 38_{19,19}{}^\star$	244549.115	7	354	101.2	39	Strong $H^{13}CONH_2$
989	$39_{22,17} - 38_{22,16}{}^\star$	244560.740	7	399	90.5	39	Strong $HC^{13}CCN$
991	$39_{18,21} - 38_{18,20}{}^\star$	244583.086	7	341	104.4	39	Strong CH_3OCHO, C_2H_5OH, and $HCC^{13}CN$
993	$39_{23,16} - 38_{23,15}{}^\star$	244593.917	7	415	86.5	39	Strong C_2H_5OH, $HCC^{13}CN$, and CH_3OCHO
995	$39_{24,15} - 38_{24,14}{}^\star$	244638.791	7	432	82.4	39	Blend with C_2H_5OH, uncertain baseline
997	$39_{17,22} - 38_{17,21}{}^\star$	244642.302	7	328	107.5	39	Blend with C_2H_5OH, uncertain baseline
999	$26_{4,23} - 25_{3,23}$	244644.897	14	100	1.2	39	Blend with C_2H_5OH, uncertain baseline
1000	$40_{5,36} - 39_{5,35}$	244718.677	5	243	132.5	39	Strong H_2CCO and $H_2C^{13}CO$

Table B.1: continued.

N^a	Transition^b	Frequency (MHz)	Unc.^{c} (kHz)	$E_l{}^d$ (K)	$S\mu^2$ (D^2)	σ^e (mK)	Comments
(1)	(2)	(3)	(4)	(5)	(6)	(7)	(8)
1001	$39_{16,23} - 38_{16,22}{}^\star$	244732.521	6	316	110.3	39	Strong U-line, C_2H_3CN, and $HCC^{13}CN$, v_5=1/v_7=3
1003	$35_{32,3} - 36_{31,6}{}^\star$	244732.708	213	548	0.9	39	Strong U-line, C_2H_3CN, and $HCC^{13}CN$, v_5=1/v_7=3
1005	$39_{26,13} - 38_{26,12}{}^\star$	244758.856	7	468	73.7	39	Blend with NH_2CH_2CN
1007	$21_{8,14} - 20_{7,13}$	244767.169	9	81	55.6	39	Blend with NH_2CH_2CN
1008	$21_{8,13} - 20_{7,13}$	244768.504	9	81	1.6	39	Blend with NH_2CH_2CN
1009	$21_{8,14} - 20_{7,14}$	244782.981	9	81	1.6	39	Strong $^{13}CH_3CH_2CN$ and CH_3CHO
1010	$21_{8,13} - 20_{7,14}$	244784.316	9	81	55.6	39	Strong $^{13}CH_3CH_2CN$ and CH_3CHO
1011	$39_{15,25} - 38_{15,24}{}^\star$	244861.684	6	305	113.1	39	Strong $^{13}CH_3CH_2CN$
1013	$40_{4,36} - 39_{4,35}$	244866.424	5	243	132.6	39	Strong $^{13}CH_3CH_2CN$
1014	$39_{14,26} - 38_{14,25}{}^\star$	245041.053	6	294	115.6	39	Strong CH_3CHO, $C_2H_5{}^{13}CN$, and C_2H_3CN
1016	$80_{18,62} - 80_{17,63}$	245045.143	36	1081	307.9	39	Strong CH_3CHO, $C_2H_5{}^{13}CN$, and C_2H_3CN
1017	$39_{5,34} - 38_{5,33}$	245048.879	6	237	128.8	39	Strong CH_3CHO, $C_2H_5{}^{13}CN$, and C_2H_3CN
1018	$40_{5,36} - 39_{4,35}$	245187.198	5	243	144.3	72	Strong CH_3CH_3CO, v_t=1
1019	$39_{13,27} - 38_{13,26}{}^\star$	245287.203	6	285	117.9	72	Strong $C_2H_5{}^{13}CN$ and CH_3CH_3CO
1021	$80_{18,62} - 80_{17,64}$	245621.039	34	1081	4.3	53	Strong HC_3N, v_5=1/v_7=3 and $CH_2{}^{13}CHCN$
1022	$39_{12,28} - 38_{12,27}$	245625.584	5	276	120.1	53	Strong HC_3N, v_5=1/v_7=3 and $CH_2{}^{13}CHCN$
1023	$39_{12,27} - 38_{12,26}$	245626.050	5	276	120.1	53	Strong HC_3N, v_5=1/v_7=3 and $CH_2{}^{13}CHCN$
1024	$41_{3,38} - 40_{4,37}$	245750.386	5	249	178.8	53	Strong CH_3OCHO
1025	$38_{6,33} - 37_{5,32}$	245752.313	8	226	97.6	53	Strong CH_3OCHO
1026	$41_{4,38} - 40_{4,37}$	245764.311	5	249	136.6	53	Strong HC_3N, v_5=1/v_7=3 and CH_3NH_2
1027	$41_{3,38} - 40_{3,37}$	245771.695	5	249	136.6	53	Strong CH_3NH_2 and CH_3OCHO
1028	$69_{10,60} - 68_{11,58}$	245772.831	37	755	1.7	53	Strong CH_3NH_2 and CH_3OCHO
1029	$41_{4,38} - 40_{3,37}$	245785.620	5	249	178.8	53	Strong C_2H_5CN, v_{13}=1/v_{21}=1
1030	$39_{36,3} - 38_{36,2}{}^\star$	245793.648	20	691	19.6	53	Strong C_2H_5CN, v_{13}=1/v_{21}=1
1032	$24_{7,18} - 23_{6,17}$	245869.123	8	97	50.0	53	Blend with $CH_2CH^{13}CN$ and CH_3OCHO
1033	$40_{5,35} - 39_{6,34}$	245958.716	6	249	112.2	53	Blend with CH_3CH_3CO, v_t=1
1034	$51_{39,12} - 52_{38,15}{}^\star$	245962.097	1680	936	5.8	53	Blend with CH_3CH_3CO, v_t=1
1036	$67_{5,62} - 67_{5,63}{}^\star$	245964.390	16	673	3.9	53	Blend with CH_3CH_3CO, v_t=1
1038	$67_{6,62} - 67_{5,63}{}^\star$	245964.481	16	673	119.4	53	Blend with CH_3CH_3CO, v_t=1
1040	$14_{11,3} - 13_{10,4}{}^\star$	246945.998	10	64	68.3	68	Blend with C_2H_3CN
1042	$14_{11,3} - 13_{10,3}{}^\star$	246945.998	10	64	1.6	68	Blend with C_2H_3CN
1044	$50_{17,34} - 50_{16,34}{}^\star$	247211.238	9	477	3.0	68	Strong HC_3N, v_7=2 and C_2H_5CN
1046	$50_{17,34} - 50_{16,35}{}^\star$	247211.244	9	477	164.1	68	Strong HC_3N, v_7=2 and C_2H_5CN
1048	$24_{7,17} - 23_{6,18}$	247430.134	8	97	49.8	68	Blend with CH_3CHO and t-HCOOH
1049	$59_{11,48} - 58_{12,46}$	247431.373	31	570	1.8	68	Blend with CH_3CHO and t-HCOOH

Notes: ^{a} Numbering of the observed transitions associated with a modeled line stronger than 20 mK. ^{b} Transitions marked with a * are double with a frequency difference less than 0.1 MHz. The quantum numbers of the second one are not shown. ^{c} Frequency uncertainty. ^{d} Lower energy level in temperature units (E_l/k_B). ^{e} Calculated rms noise level in T_{mb} scale.